

ISSN: 0120-1425 • Junio de 2022

SERVICIO  
GEOLÓGICO  
COLOMBIANO



volumen **49**  
número 1

# Boletín Geológico

<https://revistas.sgc.gov.co/index.php/boletingeo>



*Boletín Geológico*  
Vol. 49, n.º 1, 2022  
Periodicidad semestral  
ISSN impreso: 0120-1425  
ISSN digital: 2711-1318  
Servicio Geológico Colombiano

Oscar Paredes Zapata  
Director general

Mario Andrés Cuéllar  
Director de Geociencias Básicas

Héctor Mora páez  
Director de Geoamenazas (e)

Gloria Prieto Rincón  
Directora de Recursos Minerales

Hernán Olaya Dávila  
Director de Asuntos Nucleares

Humberto Andrés Fuenzalida  
Director de Hidrocarburos

Hernando Camargo  
Director de Laboratorios

Victoria Díaz Acosta  
Directora de Gestión de Información

#### Servicio Geológico Colombiano

Diagonal 53 n.º 34-53  
Bogotá, Colombia  
Teléfono: (601) 220 0200, ext.: 3048  
boletingeologico@sgc.gov.co

Mario Maya  
Editor  
Boletín Geológico

#### Comité editorial

Germán Alonso Bayona Chaparro  
Cooperación Geológica Ares  
Bogotá – Colombia

Matthias Bernet  
Université Grenoble Alpes  
Francia

Antoni Camprubí Cano  
Universidad Nacional Autónoma de México  
México

Iván Darío Correa Arango  
Consultor  
Medellín – Colombia

Thomas Heinrich Cramer  
Universidad Nacional de Colombia  
Bogotá – Colombia

Tobias Fischer  
The University of New Mexico  
Estados Unidos

Carlos Jaramillo  
Instituto Smithsonian de Investigaciones  
Tropicales  
Panamá

John Makario Londoño  
Servicio Geológico Colombiano  
Manizales - Colombia

María Isabel Marín Cerón  
Universidad EAFIT  
Medellín – Colombia

Camilo Montes Rodríguez  
Universidad del Norte  
Barranquilla - Colombia

Héctor Mora Páez  
Servicio Geológico Colombiano  
Manizales - Colombia

Natalia Pardo  
Universidad de los Andes  
Bogotá – Colombia

Germán A. Prieto  
Universidad Nacional de Colombia  
Bogotá – Colombia

Yamirka Rojas Agramonte  
Universität Kiel  
Alemania

John Jairo Sánchez  
Universidad Nacional de Colombia  
Medellín – Colombia

Luigi Solari  
Universidad Nacional Autónoma de México  
México

Carlos Augusto Zuluaga Castrillón  
Universidad Nacional de Colombia  
Bogotá – Colombia

#### Corrección de estilo en español

Leonardo Paipilla  
Fernando Carretero

#### Traducción y corrección de estilo en inglés

American Journal Experts

#### Diseño y diagramación

Leonardo Cuéllar V.

#### Diseño GIS

Cristian Hernández

#### Editora general

Carolina Hernández O.

#### Foto de cubierta

Cerro Machín Volcano,  
Central Cordillera, Colombia.  
Fotografía de Ricardo Arturo Méndez  
Fajuri, Servicio Geológico Colombiano.

#### Incluida en los siguientes índices y bases de datos:

Ulrich  
REDIB  
GeoRef  
Periódica  
Google Scholar  
Doaj  
Sherpa Romeo

#### Página web:

<https://revistas.sgc.gov.co/index.php/boletingeo>

Esta obra está bajo licencia  
internacional Creative Commons  
Reconocimiento 4.0



#### Impresión

Imprenta Nacional de Colombia  
Carrera 66 N.º 24-09  
PBX: (601) 457 8000  
[www.imprensa.gov.co](http://www.imprensa.gov.co)  
Bogotá, D. C., Colombia

Junio, 2022

---

## CONTENIDO

---

### 3 Editorial

Mario **Maya**

Research article

### 7 Petrographic, chemical and geochronological characteristics of the Onzaga Metarhyolite and its correlation with Ordovician magmatic events in the northern Andes, Colombia

Características petrográficas, químicas y geocronológicas de la Metariorlita de Onzaga y su correlación con eventos magmáticos ordovícicos en los Andes del norte, Colombia

Gabriel **Rodríguez García**

Research article

### 29 Determination of a potentially optimal zone to perform hydraulic fracturing work, Upper Magdalena Valley basin, Colombia

Determinación de una zona potencialmente óptima para realizar trabajos de fracturamiento hidráulico, Valle Superior del Magdalena, Colombia

Carlos Fabián **Sánchez**, Indira **Molina**, Gabriel Ángel **Molina**

Research article

### 41 Interpretation of Palaeozoic geofoms with the use of seismic attributes in a region of the Eastern Plains, Colombia

Interpretación de geofomas paleozoicas con el uso de atributos sísmicos en una localidad de los Llanos Orientales, Colombia

Laura Carolina **Esquivel**, Fanny **Villamizar**, Indira **Molina**

Research article

### 55 Gravity Studies at the Cerro Machín volcano, Colombia

Estudios gravimétricos en el volcán Cerro Machín, Colombia

Nicolás Felipe **Pedraza**, Juan Diego **Velásquez**, Indira **Molina**, Andrés **Pedraza**

Case study article

**67** Hydrogeological potential in soft formations and hard rocks:

A case study in the Cauca River Canyon, Antioquia, Colombia

Potencial hidrogeológico en formaciones blandas y rocas duras:

Un estudio de caso en el cañón del río Cauca, Antioquia, Colombia

Paola Andrea **Palacio**, Rodrigo Alonso **Díaz**, María Alejandra **Vela**, Juliana **Ossa**

Case study article

**77** Region-scale estimation of potential groundwater recharge in soft and hard rock formations through a distributed water balance in the area of influence of the tropical dry forest in the Cauca River canyon, Antioquia, Colombia

Estimaciones regionales de recarga potencial de aguas subterráneas en formaciones blandas y rocas duras, mediante un balance hídrico distribuido en zona de influencia del bosque seco tropical en el cañón del río Cauca, Antioquia, Colombia

Breiner Dan **Bastidas**, Juliana **Ossa**, Cristina **Martínez**, María Alejandra **Vela**, Teresita **Betancur**, Arbei **Osorio**

Research article

**103** Magnetic fabric of deformed Quaternary sediments: contributions to the understanding of the neotectonic activity in the surroundings in the Aburrá Valley, Central Cordillera, Colombia

Fábrica magnética de sedimentos cuaternarios deformados: contribuciones para entender la actividad neotectónica en los alrededores del Valle de Aburrá, Colombia

Santiago **Noriega-Londoño**, Duván **Jaraba**, María Paula **Ruiz**, María Isabel **Marín-Cerón**, Sergio Andrés **Restrepo-Moreno**

**124** Editorial Policy and Author Guidelines

---

## EDITORIAL

---

**B**oletín Geológico publishes Issue 49(1), June 2022, with the following articles (Figure 1):

[Rodríguez et al.](#) describe the macroscopic, microscopic, and chemical characteristics, as well as the crystallization age, of the Onzaga Metarhyolite unit. The spatiotemporal relationships among the magmatic events that occurred during the Ordovician in the Santander, La Floresta and Quetame massifs and in the Mérida Mountain range are analyzed. Additionally, a correlation is made with plutonic bodies that have crystallization ages within this same period. The analytical results indicate crystallization ages that vary between  $450.9 \pm 2.5$  Ma and  $449.9 \pm 5.9$  Ma, with a second population between  $475.9 \pm 5.4$  Ma and  $469.8 \pm 4.0$  Ma. These ages are interpreted as magmatic zircons inherited from a lower to middle Ordovician igneous event.

[Sánchez et al.](#) analyze electrical logs from twelve wells located in the Upper Magdalena Valley to obtain a correlation between the area of interest located in the Monserrate Formation and each of the wells under study. The petrophysical properties are calculated by using gamma ray, resistivity, neutron, and density logs to determine the shale volume, effective porosity, total porosity, water saturation and permeability in each well. Additionally, the production history of each of the wells and the calculations are used to suggest a new site where hydraulic fracturing could also be successful.

[Esquivel et al.](#) analyze seismostratigraphic sequences, gamma ray well logs, and seismic interpretation of possible geological structures at depth using a seismic cube, four 2D seismic lines, and four wells. The results suggest a possible shallow marine depositional environment in the Ordovician and a slightly deeper shallow marine environment in the Cambrian. The information is integrated and analyzed to generate maps of geoforms corresponding to the Middle Ordovician, Lower Ordovician and Cambrian sequences.

[Pedraza et al.](#) perform a gravity study at the Cerro Machin volcano, Colombia. Bouguer anomalies range between -87 mGal and -29 mGal. The Oasis Montaj density model reveals an elongated dacitic complex at the top of the distribution with a mean density of  $2300 \text{ kg/m}^3$ , with the presence of a volcanic conduit of  $2400 \text{ kg/m}^3$  at the base. The seismicity in the area suggests that the gravimetric anomaly caused by the dome and its surrounding materials may be related to a weakened zone at the interface between the volcanic edifice and the metamorphic basement, provoked by fault activity, interaction with the hydrothermal system and the ascent of hot fluid material to the surface.

[Palacio et al.](#) evaluate the hydrogeological potential in tropical dry forest areas associated with the Cauca River Canyon, Antioquia, Colombia. Based on the lithostructural evaluation of the area, hypotheses are established by which conditions of greater or lesser aquifer potential are assigned according to the diverse types of geological materials present. This finding provides new

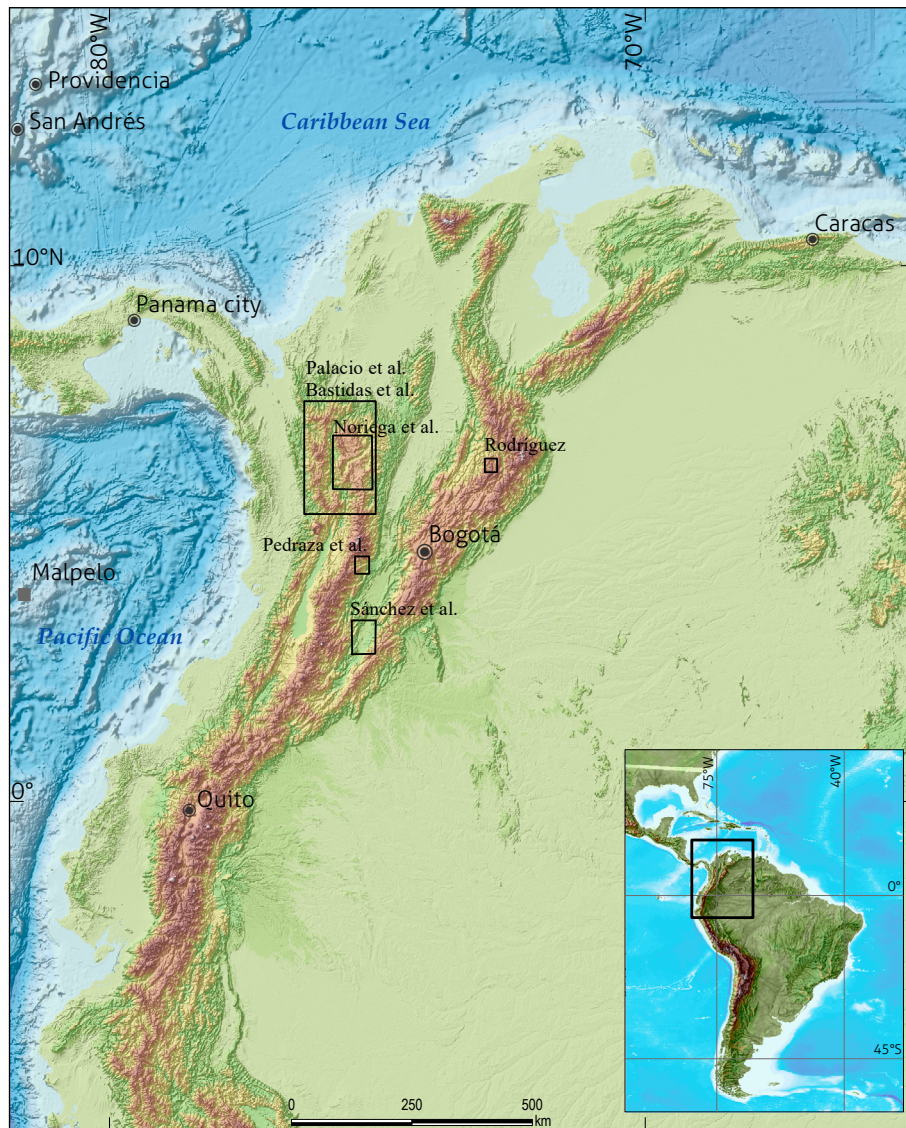


Figure 1. Locations of the areas with contributions presented in *Boletín Geológico*, 49(1), 2022.

research perspectives on fractured environments and presents groundwater as a main and alternative source to meet the needs of the population, in addition to playing a fundamental role in terms of the ecosystem sustainability of the tropical dry forest.

**Bastidas et al.** estimate recharge through a distributed soil water balance model at a daily time step, which efficiently incorporates the spatiotemporal variability of the meteorological conditions of the region, as well as the spatial variability of the surface properties, such as soils, land cover and topography. The recharge behavior in the area favors regional flows between hydrogeological units and confirms the considerable hydrogeological potential of various units of fractured hard rocks.

**Noriega et al.** contribute to the understanding of the Aburrá Valley Neotectonic framework using the anisotropy of magnetic susceptibility and structural analysis. The authors measure the magnetic fabric ellipsoid shape of faulted sediments and compare them with the geometry and kinematics of fault planes to determine their relationship with the present-day stress field and the regional fault architecture. This work identifies the AMS technique as a powerful tool for understanding the neotectonic framework along urban areas and surrounding areas.

*Boletín Geológico* acknowledges the collaboration of the following reviewers and their commitment to the peer-review process involved in this issue:

Alejandro Escalona, University of Stavanger, Norway  
Anabel Gómez, Universidad de Buenos Aires, Argentina  
Anderson Costa dos Santos, Universidad Federal do Rio de Janeiro, Brazil  
Andreas Kammer, Universidad Nacional de Colombia, Colombia  
Angela Maria Gomez, Universidad Nacional de Colombia, Colombia  
Bogdan Nitescu, Universidad de los Andes, Colombia  
Carolina Ortiz, Universidad Nacional de Colombia, Colombia  
César Mora, Kuenka S.A.S., Colombia  
Claudia Lalinde, Integral S.A.S., Colombia  
Daniela Marchionni, Universidad Nacional de la Plata, Argentina  
Edier Aristizábal, Universidad Nacional de Colombia, Colombia  
Emperatriz López, Universidad Industrial de Santander, Colombia  
Francis Aury, Universidad de los Andes, Colombia  
Francisco Velandia, Universidad Industrial de Santander, Colombia  
Gemma Acosta, Universidad Nacional de San Juan, Argentina  
Guillermo Alzate, Universidad Nacional de Colombia, Colombia  
Gustavo Neira, Universidad Nacional de Colombia, Colombia  
Héctor Mario Herrera, Carsucre, Colombia  
Ivan Olaya, Consulting, Colombia  
Janeth Calderón, Universidad Nacional de Colombia, Colombia  
Jean Baptiste Tary, Universidad de los Andes, Colombia  
John Fernando Escobar, Agencia Nacional de Hidrocarburos, Colombia  
Lisbeth Fog, Consulting, Colombia  
Luz Mary Toro, Universidad de Caldas, Colombia  
Nora Rubinstein, Universidad de Buenos Aires, Argentina  
Tania Arboleda, Consulting, Colombia  
Thomas Cramer, Universidad Nacional de Colombia, Colombia

**Mario Maya**

**Editor**

[mmaya@sgc.gov.co](mailto:mmaya@sgc.gov.co)

[boletingeologico@sgc.gov.co](mailto:boletingeologico@sgc.gov.co)



Morfología del Batolito de Mogotés, correspondiente al magmatismo Triásico-Jurásico del Macizo de Santander y valle aluvial en los alrededores del municipio de Mogotés, Santander.  
Fotografía de Gabriel Rodríguez.



Research article

# Petrographic, chemical and geochronological characteristics of the Onzaga Metarhyolite and its correlation with Ordovician magmatic events in the northern Andes, Colombia

Características petrográficas, químicas y geocronológicas de la Metariolita de Onzaga y su correlación con eventos magmáticos ordovícicos en los Andes del norte, Colombia

Gabriel Rodríguez García<sup>1</sup>

<sup>1</sup> Servicio Geológico Colombiano, Special Geological Studies Group, Medellín, Colombia.

**Corresponding author:** [grodriguez@sgc.gov.co](mailto:grodriguez@sgc.gov.co)

## ABSTRACT

The macroscopic, microscopic, and chemical characteristics as well as crystallization age of the Onzaga Metarhyolite unit are described. The spatiotemporal relationships among the magmatic events that occurred during the Ordovician in the Santander, La Floresta and Quetame massifs and in the Mérida Mountain range are analyzed. Additionally, a correlation is made with plutonic bodies that have crystallization ages within this same period of time.

The Onzaga Metarhyolite outcrops in the Santander massif in the surroundings of the municipality of Onzaga-Santander, with an approximate area of 155 km<sup>2</sup>; it is composed of metavolcanic rocks that are chemically classified as rhyolites, which were affected by metamorphism in green schist facies to low amphibolite. The metarhyolites are composed of quartz porphyroclasts, plagioclase and alkali feldspar, and some retain the textures and relict forms of the phenocrysts, which are found within a microcrystalline matrix, with local development of quartz mosaics and oriented sheets of white mica and biotite.

The rocks of the Onzaga Metarhyolite have high contents of SiO<sub>2</sub> (76.9% to 79.3%), K<sub>2</sub>O (4.03% to 5.66%) and Al<sub>2</sub>O<sub>3</sub> (11.5% to 14.3%) and low contents of Fe<sub>2</sub>O<sub>3</sub>, TiO<sub>2</sub>, CaO, MnO and MgO. The rocks have alkali values (Na<sub>2</sub>O + K<sub>2</sub>O) between 5.3% and 7.9% and K<sub>2</sub>O/Na<sub>2</sub>O > 2. They are classified within the calc-alkaline rocks high in K, peraluminous, and related to magmas that generate type S granites. In the multielement diagrams, Nb has a weak negative anomaly, as does Zr, while the negative anomalies of Ti and Sr are pronounced. Higher values of lithophilic elements of high ionic radius (LILE) Cs, Ba and Th indicate a continental crust

affinity. The  $\text{Eu}/\text{Eu}^*$  values are low, between 0.12 and 0.74. The normalized values of  $(\text{La}/\text{Yb})_N$  vary between 4 and 24.4,  $(\text{La}/\text{Sm})_N$  varies between 2.2 and 2.5, and  $(\text{Eu}/\text{Yb})_N$  varies between 0.2 and 2.1.

Two samples of Onzaga Metarhyolite were analyzed by the LA-ICP-MS U-Pb method in zircon. The results analysis indicates a crystallization age that varies between  $450.9 \pm 2.5$  Ma and  $449.9 \pm 5.9$  Ma, with a second population between  $475.9 \pm 5.4$  Ma and  $469.8 \pm 4.0$ ; these ages are interpreted as magmatic zircons inherited from a lower to middle Ordovician igneous event. The zircons have xenocrysts and inherited nuclei of  $555 \pm 11$  Ma and  $565.7 \pm 9$  Ma and populations of  $617 \pm 16$  Ma ( $n = 3$ ) and  $644.5 \pm 6.5$  ( $n = 3$ ), respectively, and three inheritances between  $1071 \pm 48$  Ma and  $1171 \pm 37$  Ma.

**Keywords:** U-Pb geochronology, Santander Massif, volcanism, Ordovician.

## RESUMEN

Se describen las características macroscópicas, microscópicas, químicas y la edad de cristalización de la unidad. Se analiza la relación espacio-temporal con los eventos magmáticos que ocurrieron durante el Ordovícico en los macizos de Santander, La Floresta y Quetame, y en la cordillera de Mérida. Adicionalmente, se hace una correlación con cuerpos plutónicos que tienen edades de cristalización en este mismo periodo de tiempo.

La Metariolita de Onzaga aflora en el macizo de Santander, en los alrededores del municipio de Onzaga-Santander, con un área aproximada de  $155 \text{ km}^2$ ; está constituida por rocas metavolcánicas que clasifican químicamente como riolitas, las cuales fueron afectadas por metamorfismo en facies esquisto verde a probablemente anfibolita baja. Las metariolitas están constituidas por porfidoclastos de cuarzo, plagioclasa y feldespato alcalino, algunos conservan las texturas y formas relictas de los fenocristales; estos se encuentran dentro de una matriz microcristalina, con desarrollo local de mosaicos de cuarzo y láminas orientadas de mica blanca y biotita.

Las rocas de la Metariolita de Onzaga presentan altos contenidos de  $\text{SiO}_2$  (76,9 % a 79,3 %),  $\text{K}_2\text{O}$  (4,03 % a 5,66 %) y  $\text{Al}_2\text{O}_3$  (11,5 % a 14,3 %), y bajos contenidos de  $\text{Fe}_2\text{O}_3$ ,  $\text{TiO}_2$ ,  $\text{CaO}$ ,  $\text{MnO}$  y  $\text{MgO}$ . Tienen valores de álcalis ( $\text{Na}_2\text{O} + \text{K}_2\text{O}$ ) entre 5,3 % y 7,9 % y  $\text{K}_2\text{O}/\text{Na}_2\text{O} > 2$ . Se clasifican dentro de las rocas calcoalcalinas altas en K, peraluminosas, afines a los magmas que generan granitos Tipo S. En los diagramas multielementales el Nb presenta una débil anomalía negativa, al igual que el Zr, mientras las anomalías negativas de Ti y Sr son pronunciadas. Los mayores valores de los elementos litófilos de alto radio iónico (LILE) Cs, Ba y Th indican una afinidad de corteza continental. Los valores  $\text{Eu}/\text{Eu}^*$  son bajos entre 0,12 y 0,74. Los valores normalizados de  $(\text{La}/\text{Yb})_N$  varían entre 4 y 24,4;  $(\text{La}/\text{Sm})_N$  varían entre 2,2 y 2,5, y  $(\text{Eu}/\text{Yb})_N$  entre 0,2 y 2,1.

Se analizaron dos muestras de la Metariolita de Onzaga por el método LA-ICP-MS U-Pb en circón. El análisis de los resultados indica una edad de cristalización que varía entre  $450,9 \pm 2,5$  Ma y  $449,9 \pm 5,9$  Ma, con una segunda población entre  $475,9 \pm 5,4$  Ma y  $469,8 \pm 4,0$ ; estas edades se interpretan como circones magmáticos heredados de un evento ígneo Ordovícico inferior a medio. Los circones presentan xenocristales y núcleos heredados de  $555 \pm 11$  Ma y  $565,7 \pm 9$  Ma, poblaciones de  $617 \pm 16$  Ma ( $n = 3$ ) y  $644,5 \pm 6,5$  ( $n = 3$ ) y tres herencias entre  $1071 \pm 48$  Ma y  $1171 \pm 37$  Ma.

**Palabras clave:** geocronología U-Pb, Macizo de Santander, vulcanismo, Ordovícico.

## 1. INTRODUCTION

The first descriptions of this unit were made by Vargas et al. (1976, 1981), who named it Riolitas de Onzaga. The rhyolitic body outcrops in the surroundings of the municipality of Onzaga-Santander and extends south toward the Páramo de Canutos. The unit occupies an area of approximately  $155 \text{ km}^2$  and is present in a strip with an average width of 4.5 km and an average length of 35 km. The directional tendency is mainly

N-S, and in its southwestern portion, it presents a NE-SW directional tendency. The Onzaga Metarhyolite has been considered an effusive product of the granitic bodies of Mogotes and Santa Rosita of Jurassic-Triassic age (Vargas et al., 1981).

This article presents new data from petrography (7 analyses), total rock chemistry (4 analyses) and U-Pb geochronology in zircon (2 analyses) for the metavolcanic rocks of the unit called Onzaga Metarhyolite. The mineralogy and characteristics of the metamorphism that affect the unit are described. The name On-

zaga Metarhyolite is proposed, considering the metamorphism on tax. Crystallization ages of the Upper Ordovician were obtained, and these ages relate the unit to magmatic events of the Paleozoic in the Santander Massif and subsequently to the main event of the Famatinian orogeny of *ca.* 470 Ma.

## **2. REGIONAL GEOLOGICAL FRAMEWORK**

The Santander Massif (MS) is located in the Eastern Cordillera of Colombia and is part of a regional block limited by the Santa Marta-Bucaramanga faults on the western side, the Oca fault on the northern side and the Boconó fault on the side (Cediel et al., 2003; Mantilla et al., 2013; van der Lelij et al., 2016).

The MS is formed by a metamorphic basement represented by the Bucaramanga gneiss, the Silgará Formation and granitic orthogneisses (Ward et al., 1973). The Bucaramanga gneiss consists of sillimanite-cordierite gneiss with garnet, amphibolic gneiss, feldspathic quartz granofels and amphibolites with migmatitic structures (Ward et al., 1973), with metamorphism ages of approximately 477 Ma (van der Lelij, 2013, van der Lelij et al., 2016). Overlying the Bucaramanga gneiss is the Silgará Formation (Ward et al., 1973), called the Silgará schist by Mantilla et al. (2016), composed of schists, phyllites, meta-lodolites, meta-sandstones and marbles of Paleozoic age (Clavijo et al., 2008; Mantilla et al., 2012; Ordóñez-Cardona et al., 2006; Ríos et al., 2003; van der Lelij et al., 2016; Zuluaga et al., 2017). Ordovician deformed granitoids (“Unit of orthogneisses”, according to Ward et al., 1973) intrude the Bucaramanga gneiss and the Silgará Formation. The three units mentioned above record a common event of Ordovician metamorphism that affected the entire basement of the MS (Mantilla et al., 2012, 2013; Restrepo-Pace et al., 1997; van der Lelij et al., 2016; Zuluaga et al., 2017).

In the MS, there is a record of Paleozoic and Mesozoic magmatism. The first is represented by orthogneiss, plutons and volcanics, which originated from magmatic events before and after the Famatinian orogeny, and most of them are associated with a continental arc environment. The igneous bodies are Ordovician, Silurian, Lower Devonian and Carboniferous; among them are orthogneiss from Berlin and monzogranite from Cáchira (Leal-Mejía, 2011; Mantilla et al., 2012; Restrepo-Pace, 1995; Ulloa and Rodríguez, 1982; van der Lelij, 2013; van der Lelij et al., 2016, Zapata et al., 2017). Mesozoic magmatism is mainly from the late Triassic to the Upper Jurassic and includes batholiths and stocks located in the core and along the western edge of the MS (Rodríguez et al., 2017, 2020a). Small

bodies of Albian-Cenomanian dikes intrude the Triassic-Jurassic granitoids (Correa-Martínez et al., 2017).

The Onzaga Metarhyolite is limited to the west, with metasedimentary rocks of the Silgará Formation and granitic intrusion by the Canutos Stock. To the east, the unit is in contact with Cretaceous and Devonian sediments. The Silgará Formation is crossed by dikes and rhyolitic silos that correlate with the Onzaga metarhyolite, which presents xenoliths of metamorphic rocks. To the south, contact with the Canutos Stock granite was described as likely transitional (Figure 1).

## **3. METHODS**

In this research, regional sampling was performed to cover the entire MS, including the Onzaga Metarhyolite on the eastern side of the massif.

### **3.1. Petrography**

Two petrographic analyses were compiled in cartography projects by the Colombian Geological Survey (previously Ingeominas). Five new thin sections were elaborated in Bogotá, which were analyzed in the Petrography Laboratory of the Colombian Geological Service in the Medellín region using Leitz and Olympus petrographic microscopes for the analysis; the classification was made from 300 counting points using Streckeisen triangles (1978) and following the recommendations of the Subcommittee on Metamorphic Rocks (Schmid et al., 2007).

### **3.2. Chemical analysis of total rock**

Four chemical analyses of total rock were carried out in the Analytical Geochemistry Laboratory of the Colombian Geological Service, Bogotá. The major oxides and minor elements were analyzed with a Panalytical AXIOS Mineral X-ray fluorescence spectrometer; the former were quantified from samples fused with lithium metaborate and tetraborate, while the latter were quantified in pressed samples. For the analysis of trace elements, a mass spectrometer with inductively coupled plasma ICP-MS, Perkin Elmer NEXION, was used.

Petrographic and geochemical diagrams were obtained using the software GCDkit by Janoušek et al. (2006).

### **3.3. Geochronology**

Two samples of metarhyolites were dated by the U-Pb method using laser ablation, together with inductive plasma-coupled mass spectrometry (LA-ICP-MS) in zircon. The zircons were concen-

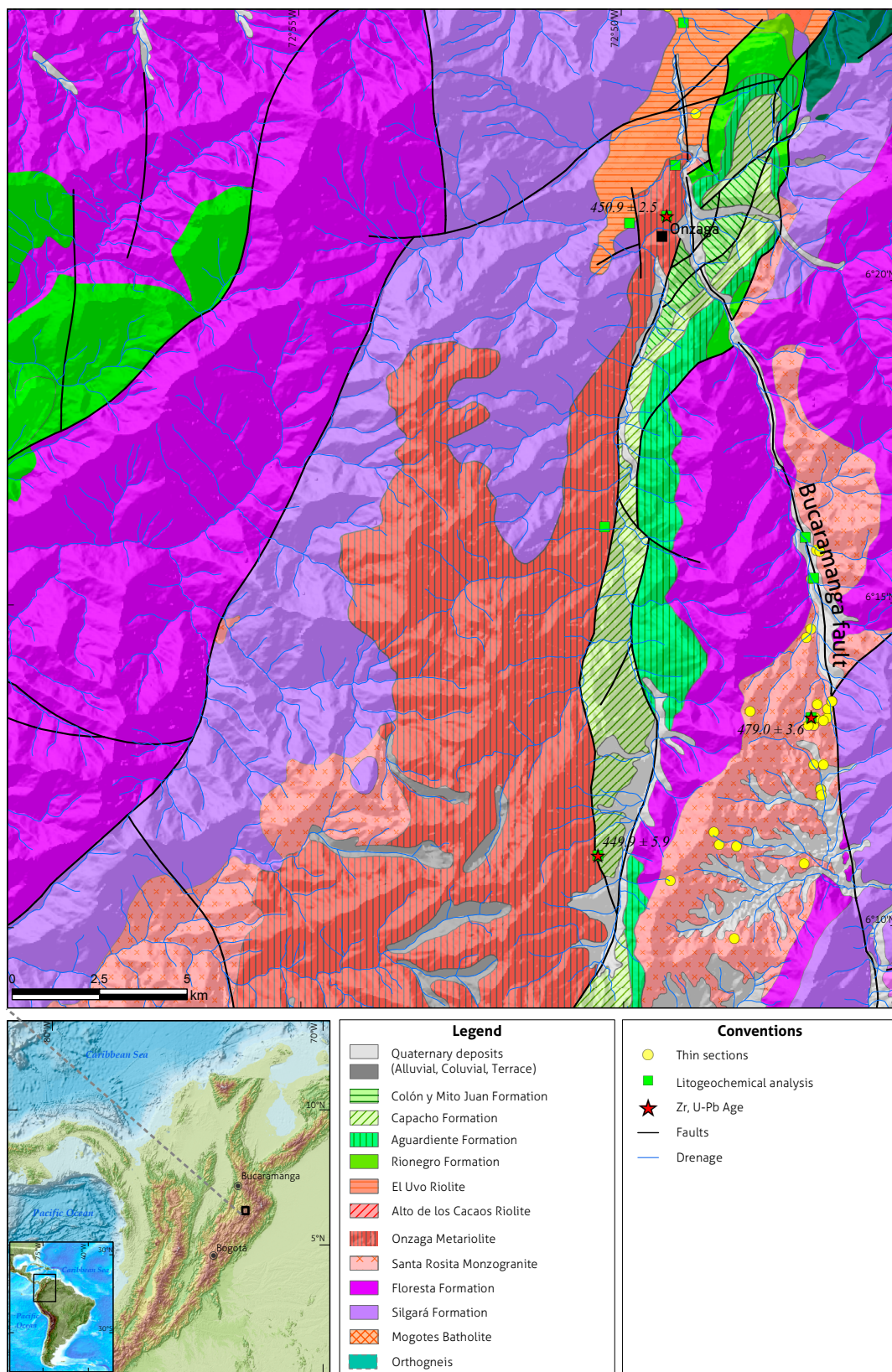


**Figure 1.** Geological map of the Onzaga Metarhyolite. Distribution of petrography, geochronology and total rock chemistry samples. Source: Vargas et al. (1987), Ulloa et al. (1998), and this work.

trated in the Chemical Laboratory of the Colombian Geological Service, Medellín, using hydrodynamic and magnetic separation. Then, they were manually selected with an Olympus binocular magnifying glass in the Petrography Laboratory at the Medellín headquarters. Cathodoluminescence (LC) images were acquired from the zircon grain assemblies by means of luminoscopes.

A sample was analyzed in the Laboratory of Isotopic Studies (LEI) at the Geosciences Center of the National Autonomous University of Mexico (UNAM), Juriquilla campus, using a Thermo X series QICPMS coupled to a Resonetics, Excimer Laser Workstation Resolution M050; the procedures and equipment are described in Solari et al. (2010). The analyzed points were 23  $\mu\text{m}$ ; the propagated 2-sigma uncertainties were achieved according to Paton et al. (2010). The  $^{207}\text{Pb}/^{206}\text{Pb}$  ratios, ages and errors were calculated according to Petrus and Kamber (2012). The concentrations of U and Th were calculated using an external standard zircon according to Paton et al. (2010).

The second sample was analyzed in the laboratories of the Colombian Geological Survey. The rock samples were crushed, pulverized and sieved following the separation procedures of Castaño et al. (2018) and analyzed by LA-ICP-MS according to the procedures described in Peña et al. (2018). The zircons were concentrated in the Chemical Laboratory of the Colombian Geological Service, Medellín, using hydrodynamic and magnetic separation and by batting for some samples in the field. Then, they were manually selected with an Olympus binocular magnifying glass in the Petrography Laboratory of the Medellín headquarters. Cathodoluminescence (LC) images were acquired from the zircon grain assemblies.

The analyses were performed in photon machine ablation equipment with a 193-nm excimer laser coupled to an Element 2-type mass spectrometer. The isotopes used for manual integration are  $^{238}\text{U}$ ,  $^{206}\text{Pb}$  and  $^{204}\text{Pb}$ . As reference standards, Plešovice (Sláma et al., 2008), FC-1 (Coyner et al., 2004), Zircón 91500 (Wiedenbeck et al., 1995, 2004) and Mount Dromedary (Renne et al., 1998) were used. The analyzed points in the zircons were 20 microns in diameter. Plešovice (Sláma

et al., 2008), 91500 (Wiedenbeck et al., 2004) and mount dromedary (Renne et al., 1998) were used as reference standards. Data reduction was performed using the Iolite v2.5 program in IGORPro 6.3.6.4 (Paton et al., 2010; Hellstrom et al., 2008). The correction for common lead was performed according to the evolution model from Stacey and Kramers (1975). The final results correspond to the mean of the data obtained after applying data discrimination to two standard deviations.

## 4. RESULTS

### 4.1. Macroscopic and microscopic description

Figure 2c shows the Streckeisen diagram (1978) and the classification based on the phenocrysts of the rock protolith. Table 1 summarizes the petrographic results.

The rocks presented as banded, and the mineral orientation showed development of schistosity (Figure 2, a and b); the rocks are composed of metarhyolites, metadacites and metaquartzites of light pinkish brown to light greenish brown color, where quartz, plagioclase and feldspar porphyroclasts, (old phenocrysts) are recognized as alkaline in a pinkish-brown, aphanitic matrix. The porphyroclasts are 1 to 2.5 mm, with some rounded and others elongated in the manner of augens, and in some samples, they conserve the primary form of the volcanic rock (Figure 3). The rocks have relict textures of the porphyritic protolith. The matrix is lepidoblastic microgranoblastic, marked by sheets of muscovite and biotite together with polygonal microgranular mosaics of quartz and feldspars. It presents recrystallization of subgrains at the edges of feldspar and quartz porphyroclasts, as well as orientation of the micas, and relict textures are recognized in the old quartz phenocrysts, such as bays and paste drops in the matrix. It consists of porphyroclasts (phenocrysts) of plagioclase, feldspar and quartz, and in the matrix, it is composed of mosaics of quartz feldspars and thin sheets of white mica and biotite. Zircon, titanite, and opaque minerals are used as accessory minerals, and sericite from plagioclase and clay group minerals are used as alteration minerals.

Table 1. Modal composition of rocks of the Onzaga Metarhyolite

IGM	N field	X	And	Qtz	Pl	Fsp	Bt	Ms	Chl	Op	Zrn	Ttn	Matrix	Other	Petrographic classification
900893	GR-6733	1137174	1185242	13.5	9.4	11.5	2.1	15.0		TR	TR	TR	48.5		Meta Riolite
900913	JGB-467	1139441	1194628	22.7	16.3	5.7	TR		1	TR			53	1.3	Meta Dacite
900928	LMC-076	1138952	1194129	16	7	12		30		TR	TR		34	1	Meta Rhyolite
900968	TCR382	1139194	1195574	53.3	5	12		27		2	0.2	0.5			Meta Rhyolite
900992	JGB-483	1136986	1175847	6.1	3.4	5.4		TR		TR	TR		85.1		Meta Rhyolite
74832	OP-675	1121220	1164130	2.1	7	5.3	TR		TR	TR	TR		85.6	TR	Pheno quartzlatite

Qtz: quartz, Pl: plagioclase, Fsp: alkaline feldspar, Bt: biotite, Ms: muscovite (white mica), Chl: chlorite, Op: opaque minerals, Zrn: zircon, Ttn: titanite, TR: traces.

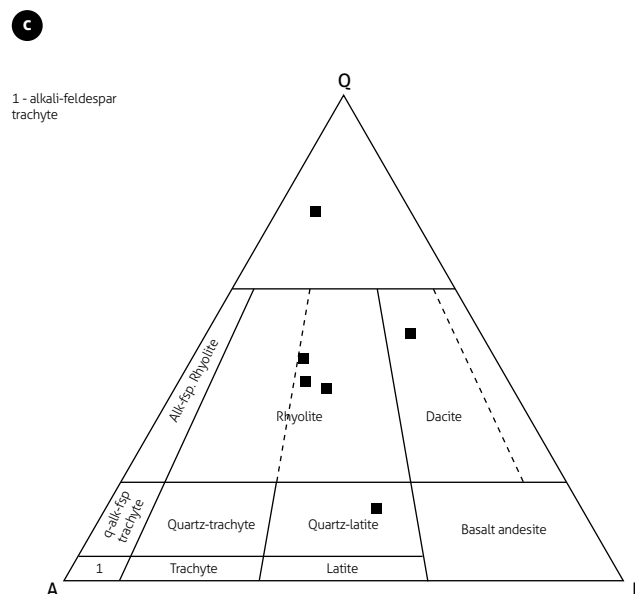
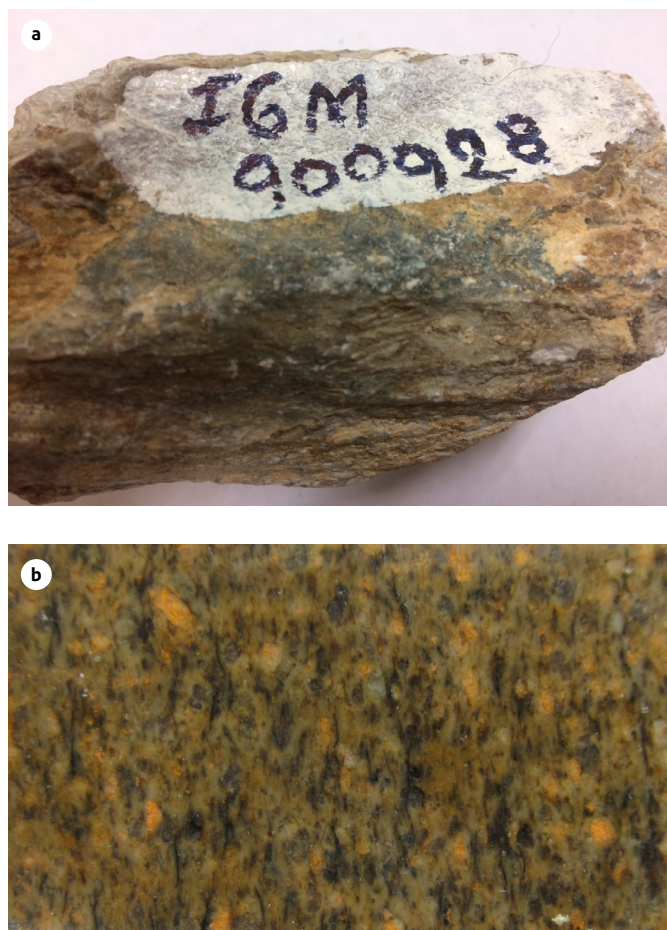
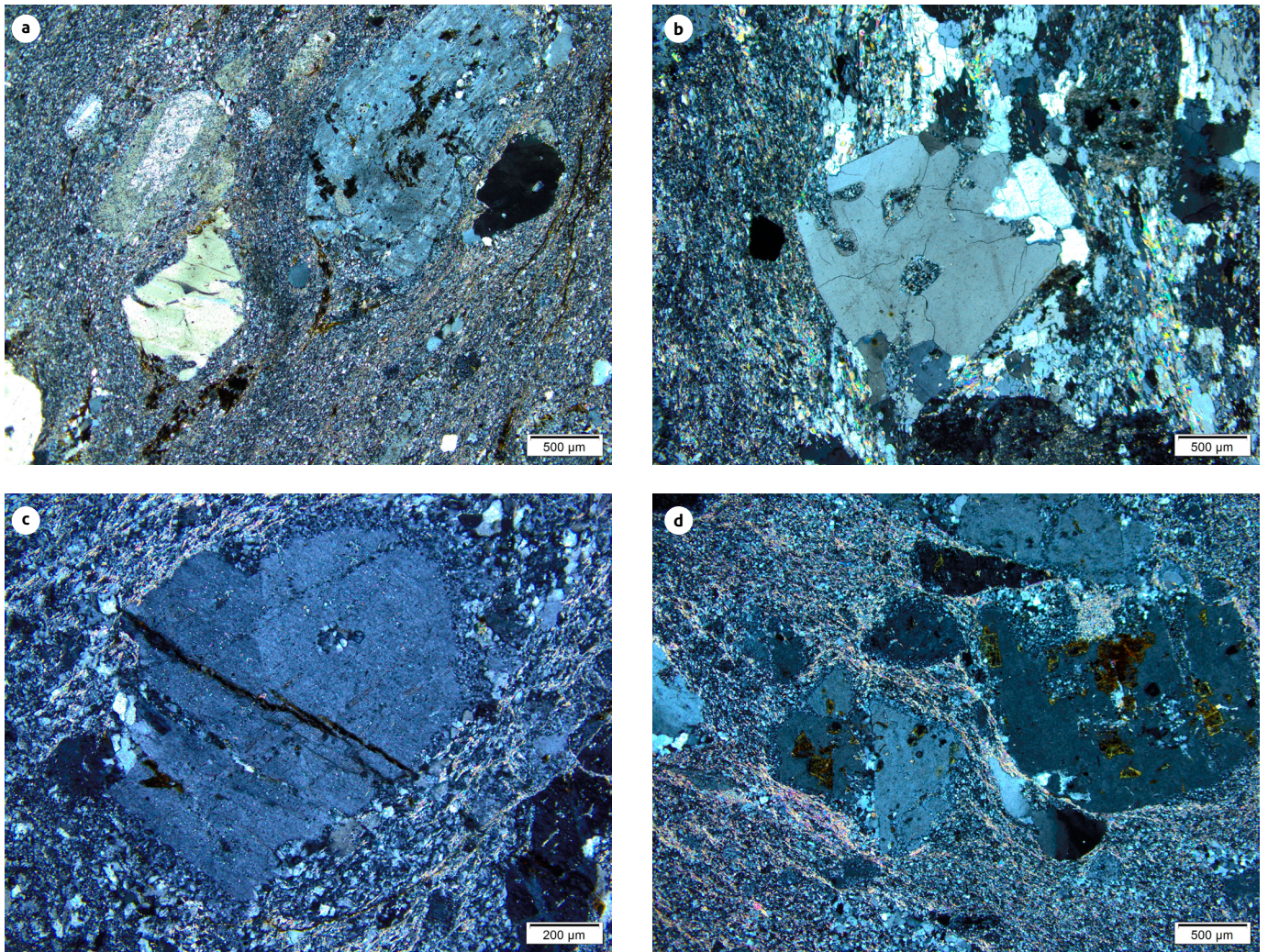


Figure 2. Macroscopic aspect of rocks of the Onzaga Metarhyolite and modal classification a) Sample LMC-076, b) Sample GR-6733 and c) Classification triangle (Streckeisen, 1978).

Quartz, plagioclase and alkaline feldspar appear as partially deformed porphyroclasts inherited from phenocrysts of the volcanic protolith (Figure 3, a, b, c and d). Porphyroclasts are oriented in the direction of the metamorphic foliation. The quartz crystals can retain the relict bipyramidal form, the corrosion bays of the matrix and the recrystallized paste droplets (Figure 3, a and b). They are of sizes between 0.5 mm and 2.5 mm, with marked wavelike extinctions, some with recrystallization to subgrains at the edges and along the lamellae that cross the phenocrysts. Plagioclase is albite to sodium oligoclase type, which occurs in euhedral to subhedral crystals of sizes between 0.75 mm and 2 mm; they are partially recrystallized subgrains at the edges with local patches inside the crystals and may or may not have twins of inherited albite and albite *Carlsbad* types (Figure 3, a and d). The alkaline feldspar presents poorly developed microcline twins and occasionally *Carlsbad*,

and they are euhedral to subhedral (Figure 3, a, c and d), with wave extinctions; their specimens present recrystallization of microcrystalline mosaics at the edges and occasionally inside the crystals, have asymmetric pressure shadows caused by dynamic metamorphism, are powdered by biotite inclusions and alteration to clay, and may be fractured and recrystallized micromosaics or preserve the relict forms of the volcanic protolith.

The biotite is of metamorphic origin, synkinematic, corresponds to microsheets of sizes smaller than 0.07 mm, brown in color, oriented in a lepidoblastic manner, and can appear in the limits of quartz mosaics, limiting the crystals, or in bands that indicate the schistosity of the rock. White mica is present in microcrystalline aggregates forming bands with biotite, developed by metamorphic recrystallization, or with the micromosaics of quartz and feldspars in the matrix.



**Figure 3.** Microscopic aspect of quartz (Qz), plagioclase (Pl) and alkaline feldspar (Fsp) porphyroclasts within a microcrystalline matrix (M) Petrographic samples of the Onzaga Metarhyolite: a) Sample IGM-900893, porphyroclasts with development of augen forms and asymmetric tails. b) Sample IGM-900968, quartz porphyroclasts with bays and edges corroded by the matrix inherited from the protolith. c) Sample IGM-900913, alkaline feldspar porphyroclast with slight recrystallization at the edges and inside the crystal. d) Sample IGM-900928, deformed and recrystallized porphyroclasts along the edges.

The rock matrix presents different degrees of metamorphic recrystallization, depending on the rock. The matrix consists of felsitic microcrystalline mosaics of quartz, plagioclase and alkaline feldspar, with oriented microsheets of white mica and biotite in some rocks, which can form oriented bands that mark the schistosity of the rock. In some rock samples, the fluid structure of the vitreous protolith of rhyolitic composition is preserved but recrystallized to granoblastic micromosaics (Figure 4).

The rock preserves the porphyritic texture of the igneous protolith and some characteristics of the phenocrysts, but the-

se rocks have been deformed and locally recrystallized by dynamic metamorphism, especially at the edges, in addition to being oriented in the direction of the metamorphic foliation. The recrystallization of feldspars and quartz and the formation of biotite and white mica by blastesis suggest that this rock probably reached the low amphibolite facies. The rock has a schist metamorphic structure marked by biotite and white mica. The original matrix of the protolith recrystallized to a microgranoblastic felsitic mosaic, and oriented micaceous minerals with lepidoblastic texture were formed.

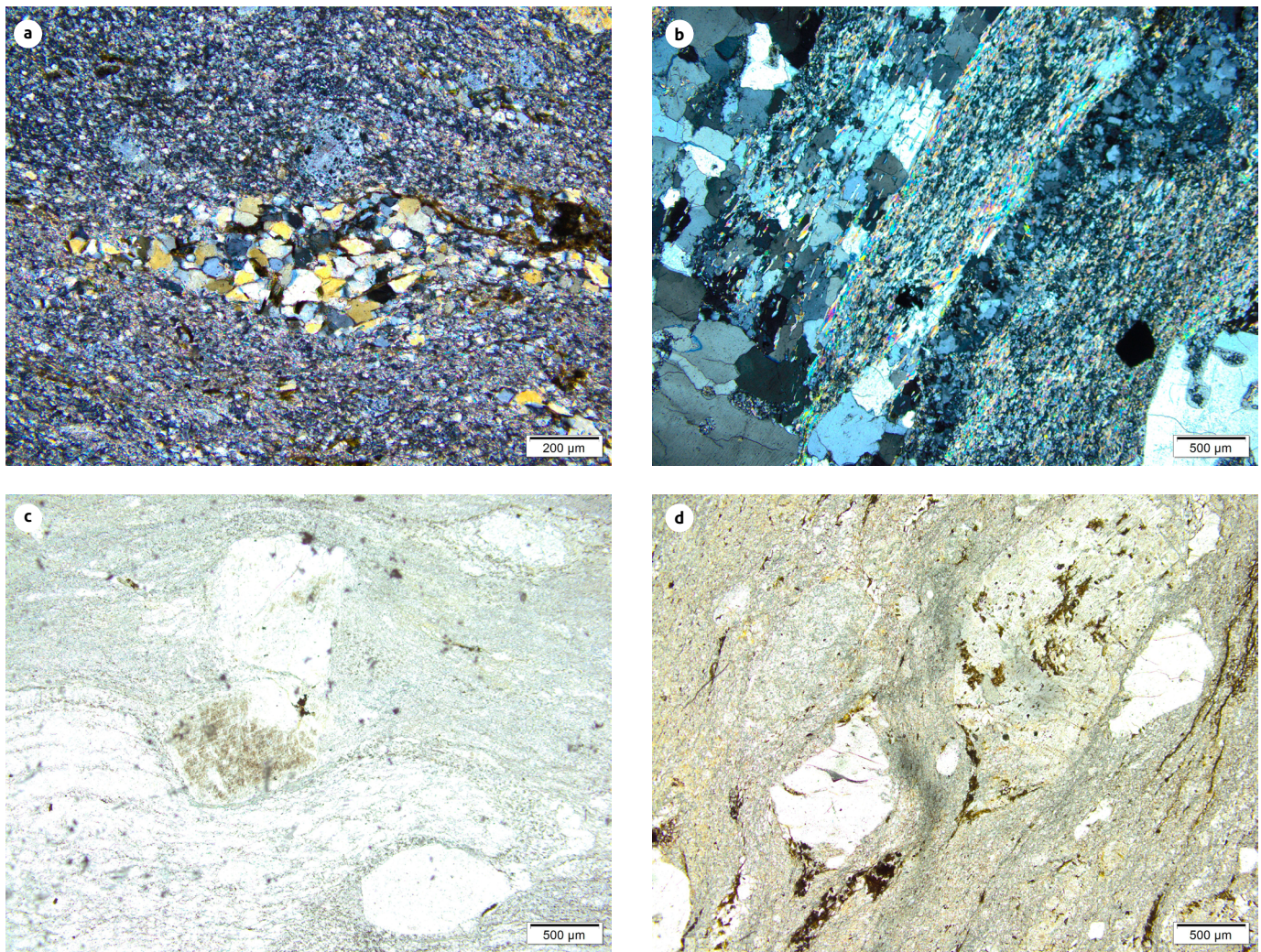


**Figure 4.** Characteristics of the rock matrix of the Onzaga Metarhyolite a) Sample IGM-900893, quartz augen with polygonal microcrystals and oriented muscovite microsheets. b) Sample IGM-900968, fine bands in the recrystallized matrix with oriented muscovite interspersed with granoblastic bands of quartz and feldspars. c) Sample IGM-900992 and d) Sample IGM-900893, development of porphyroclasts in the form of asymmetric augens and slightly banded microcrystalline matrix.

#### 4.2. Geochemistry

The geochemical analysis was performed on four rock samples distributed spatially in the body and classified petrographically as metarhyolite, metadacite and metaquartzlatite. The results are presented in Table 2, and the spatial distribution is shown in Figure 1.

The four samples have high  $\text{SiO}_2$  contents, with values between 76.9% and 79.3%, low  $\text{Fe}_2\text{O}_3$ ,  $\text{TiO}_2$ ,  $\text{CaO}$ ,  $\text{MnO}$  and  $\text{MgO}$  contents, and high  $\text{K}_2\text{O}$  values between 4.03% and 5.66% (Table 2). High values of  $\text{Al}_2\text{O}_3$  (11.5% to 14.3%) and low values of  $\text{Fe}_2\text{O}_3 + \text{TiO}_2 + \text{MgO}$  (1.18% to 2.04%) correspond to metar-

hyolites with few ferromagnesian. Losses on ignition (LOIs) are less than 1.62%, which suggests that they are slightly altered rocks, as shown in the petrographic analysis. The Onzaga Metarhyolite was subjected to metamorphism after crystallization, with the possibility of mobilizing major elements (Si, K, Na, Ca, Mg, and Fe) and large ion lithophiles (LILEs), such as Rb, Ba and Sr. In contrast, trace elements of small ionic radius, rare earths (REEs) and some transition metals (Ti, V, and Cr) have been considered immobile in postmagmatic conditions, such as metamorphism (Hastie et al., 2007; Winchester and Floyd, 1977).

**Table 2.** Content of major oxides in rocks of the Onzaga Metarhyolite

IGM	FIELD No.	SiO <sub>2</sub>	TiO <sub>2</sub>	Al <sub>2</sub> O <sub>3</sub>	Fe <sub>2</sub> O <sub>3</sub>	MgO	CaO	Na <sub>2</sub> O	K <sub>2</sub> O	P <sub>2</sub> O <sub>5</sub>	MnO	LOI
900893	GR-6733	76.86	0.13	13.17	1.70	0.05	0.23	2.35	5.40	0.10	0.005	0.95
900928	LMC-076	78.15	0.04	14.26	1.00	0.22	0.05	1.31	4.97	0.00	0	1.62
900968	TCR382	78.70	0.15	13.24	1.91	0.00	0.55	1.30	4.03	0.11	0.01	1.12
900992	JGB-483	79.32	0.07	11.53	1.12	0.00	0.00	2.30	5.66	0.00	0.002	0.54

The rocks of the Onzaga Metarhyolite plot in the rhyolite field in the diagram of Winchester and Floyd (1977) (Figure 5a). In the diagram of Th vs. Co, Hastie et al. (2007) plot in the field of andesites, departing from the petrographic classification, and correspond to calc-alkaline rocks with high K (Figure 5b). They have alkali values (Na<sub>2</sub>O + K<sub>2</sub>O) between 5.3% and 7.9% and K<sub>2</sub>O/Na<sub>2</sub>O > 2. They are classified within

peraluminous rocks, with values of A/CNK > 1 and A/NK values between 1 and 2 (Shand diagram, 1943) (Figure 5c). The high contents of K<sub>2</sub>O and moderate values of Na<sub>2</sub>O correspond to magmas related to those that generate S-type granites, as shown in the diagram of Chappell and White (1974) (Figure 5d). The mineralogy of the rocks shows the development of white mica and subordinate biotite.

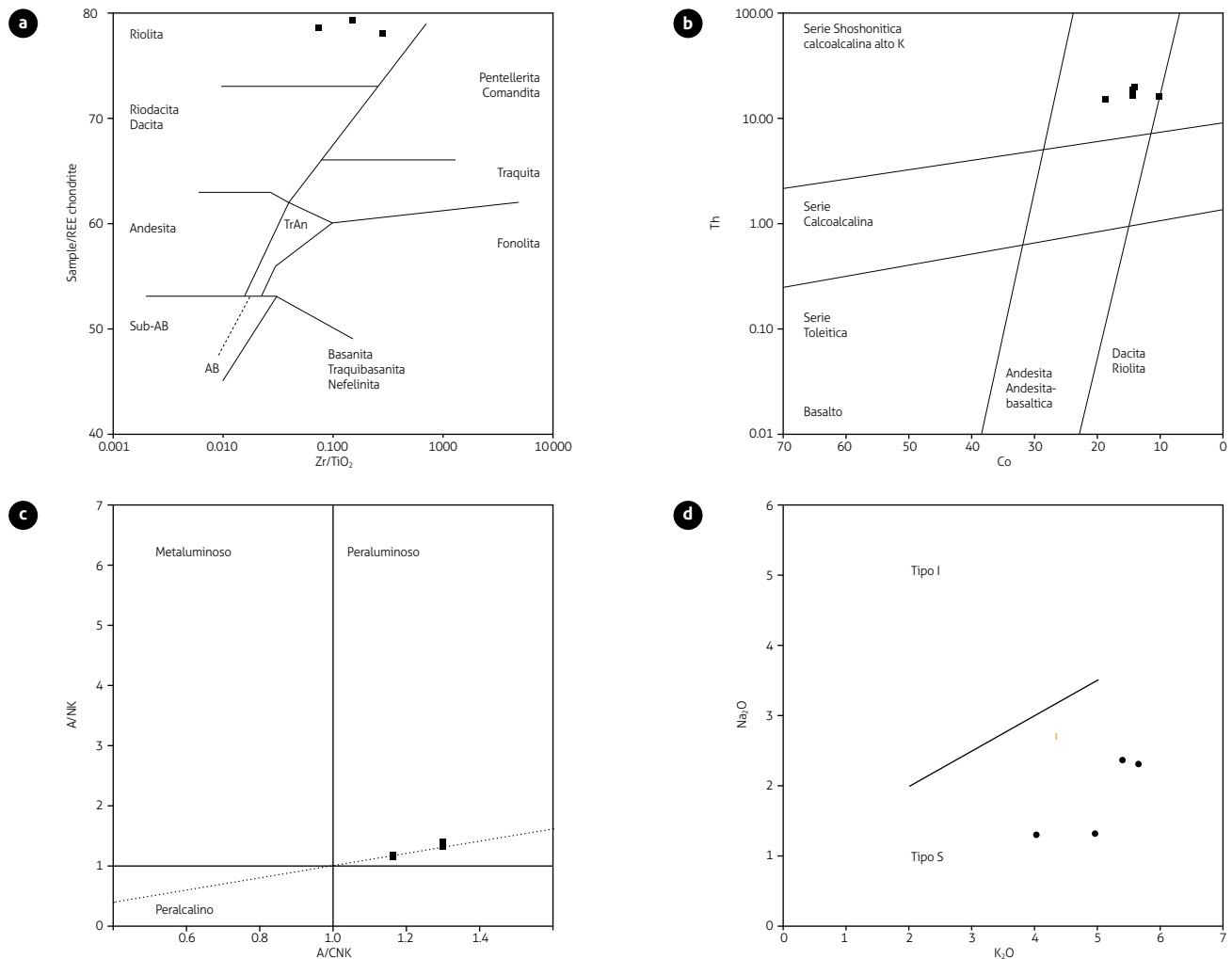


**Figure 5.** Classification diagram of volcanic rocks of the Onzaga Metarhyolite a) Diagram of Zr/TiO<sub>2</sub> vs. SiO<sub>2</sub> (Winchester and Floyd, 1977). b) Co vs. Th diagram (Hastie et al., 2007). c) Shand classification diagram (1943). d) Diagram K<sub>2</sub>O vs. Na<sub>2</sub>O by Chappell and White (1974) to discriminate between type I and type S granites.

Table 3 summarizes the values of the trace elements. The contents of Rb, Sr, Ba and Zr vary from 218-256 ppm, 26-56 ppm, 167-1113 ppm and 105-114 ppm, respectively. The rocks are characterized by high Rb/Zr ratios (between 1.9 and 2.2), Rb/Ba ratios <0.29, except for sample JGB-483, which has a value of 2, and high Rb/Sr values (between 3.8 and 9.8).

The multielement diagram of trace elements normalized to the upper continental crust (Figure 6a) (Taylor and McLennan,

**Table 3.** Results of trace elements and rare earth elements in rocks of the Onzaga Metarhyolite

IGM N field	900893 GR-6733	900928 LMC-076	900968 TCR382	900992 JGB-483
Li	15	7.3	17	3.8
Be	5.9	3.2	6.6	4.6
Sc	11	14	15	7.9
V	4.2	5.0	9.0	4.8
Cr	2.1	2.1	2.0	3.5
Mn	273	204	377	126
Co	10	14	19	14
Nor	1.7	2.5	3.621	<0.5
Cu	6.6	4.2	5.3	6.3
Zn	62	23	52	46
Ga	21	22	25	14
As	6.4	2.7	3.1	1.9
Rb	245	256	218	231
Sr	53	26	56	25
Y				26
Cd	0.14	<0.08	0.15	0.10
In	0.12	0.13	0.15	0.040
Cs	5.1	3.2	2.4	2.6
Ba	1167	856	991	113
La	44	33	39	25
Ce	79	74	75	58
Pr	12	9.9	9.9	7.7
Nd	45	31	36	27
Sm	12	8.2	9.6	6.3
Eu	1.6	0.98	1.9	0.23
Gd	9.2	4.3	6.5	5.2
Tb	2.3	0.57	1.5	0.88
Dy	15	1.9	6.6	4.8
Ho	2.9	0.33	1.2	0.94
Er	8.5	1.1	3.2	2.8
Tm	1.18	0.12	0.41	0.40
Yb	7.3	0.91	2.7	2.7
Lu	0.96	0.14	0.42	0.39
Tl	1.5	1.4	1.0	1.2
Pb	24	15	25	27
Bi	0.23	0.43	0.70	0.055
Th	16	17	15	20
U	3.1	2.7	4.0	4.1
Zr	109	114	111	105
Nb	27	27	23	25
W	37	43	68	63

1995) in rocks of the Onzaga Metarhyolite shows negative anomalies of Sr and Ti that are related to minerals, such as plagioclase and Fe-Ti opaques, respectively (McDonough and Sun, 1995). Sample JGB-484 shows a negative Ba (113 ppm) anomaly. The negative anomalies of Ba, Sr and Eu may be related to the low modal proportion of plagioclase observed (Table 1), and it is likely that in the source, the plagioclase was in a slightly abundant phase. The other elements present values close to those of the upper continental crust.

The diagram of rare earth elements (REEs) normalized to chondrite according to the values of Nakamura (1974) (Figure 6b) presents enrichment in light rare earth elements (LREEs) of approximately 80 to 100 times with respect to the value of chondrite, with a pattern that is progressively impoverished toward heavy rare earth elements (HREEs). Additionally, they have negative Eu anomalies, with low Eu/Eu\* values between 0.12 and 0.74. The negative Eu anomaly can be caused by early fractionation of plagioclase in the magma or fusion of previous

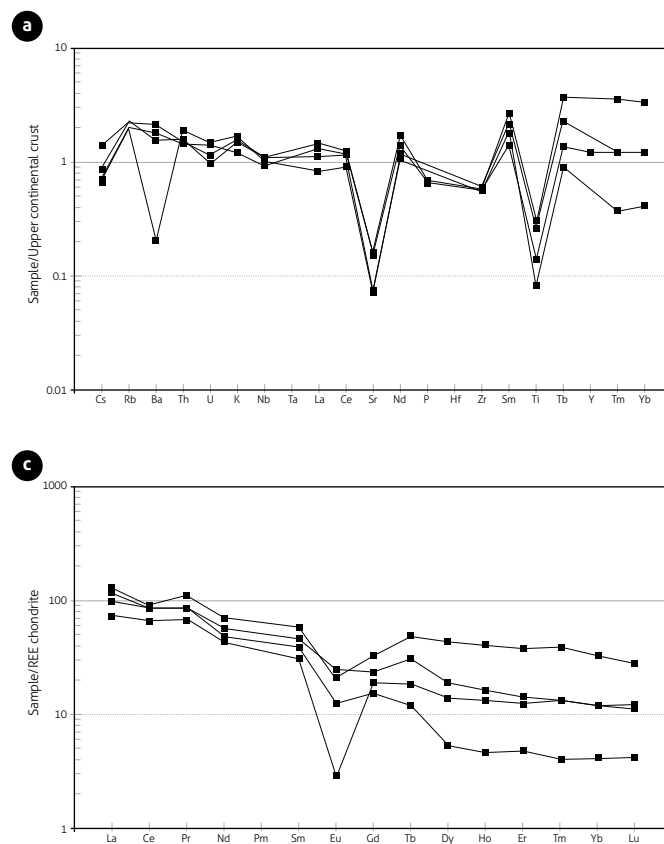


**Figure 6.** Multielement diagrams for rocks of the Onzaga Metarhyolite a) Diagram of trace elements normalized to the upper crust (Taylor and McLennan, 1995); b) Rare earth element diagram (REE) normalized to the Nakamura chondrite (1974).

igneous rocks with negative Eu anomalies; however, it is not easy to determine the reasons for the behavior of the plagioclase in the source area or the subsequent removal of plagioclase phenocrysts from the melt. When comparing the average value of  $Eu/Eu^*$  (0.56) in rocks of the Onzaga Metarhyolite with the average values obtained by Tang et al. (2015) for the upper crust ( $0.67 \pm 0.01$ ), the values are slightly lower but close to the average value of the upper crust. The normalized values of  $(La/Yb)_N$  vary between 4 and 24.4;  $(La/Sm)_N$  varies between 2.2 and 2.5; and  $(Eu/Yb)_N$  varies between 0.2 and 2.1.

### 4.3. Geochronology

For the geochronological analysis of the Onzaga Metarhyolite, two rocks were analyzed by the U-Pb LA-ICPMS method in zircons. The ages are summarized in Table 4, the spatial location is shown in Figure 1, and the results are presented in Supplementary Data. The reported ages are calculated with the  $Pb^{206}/U^{238}$  ratio. In the calculation of the crystallization age of each rock, the presence or absence of populations is considered

according to the probability density diagram and the distribution in the concord diagram.

Sample JGB-483 was chemically classified as a rhyolite with quartz, plagioclase and sanidine porphyroclasts that correspond to 14.9% of the rock. The matrix is microgranoblastic and occupies the remaining 85.1%. The rock partially preserves the flow structure of the volcanic protolith, being constituted by cryptocrystals and microcrystals of quartz, feldspars and sericite, with schist structure and thicker recrystallized sectors with polygonal textures combined with thinner bands. Most of the zircons in the sample are short and prismatic, with pyramidal ends smaller than  $50 \mu m$ . The cathodoluminescence images are of very low quality and do not allow us to define the internal structure of each zircon or the presence of inherited nuclei, but in some cases, the concentric structure of igneous zircons is recognized. The ablations were advanced in the zircon nuclei. To determine ages, a total of 47 analyses were performed; 5 analyses had discordances  $> 5$ , and 12 analyses did not touch the concord curve and were eliminated (Figure 7).

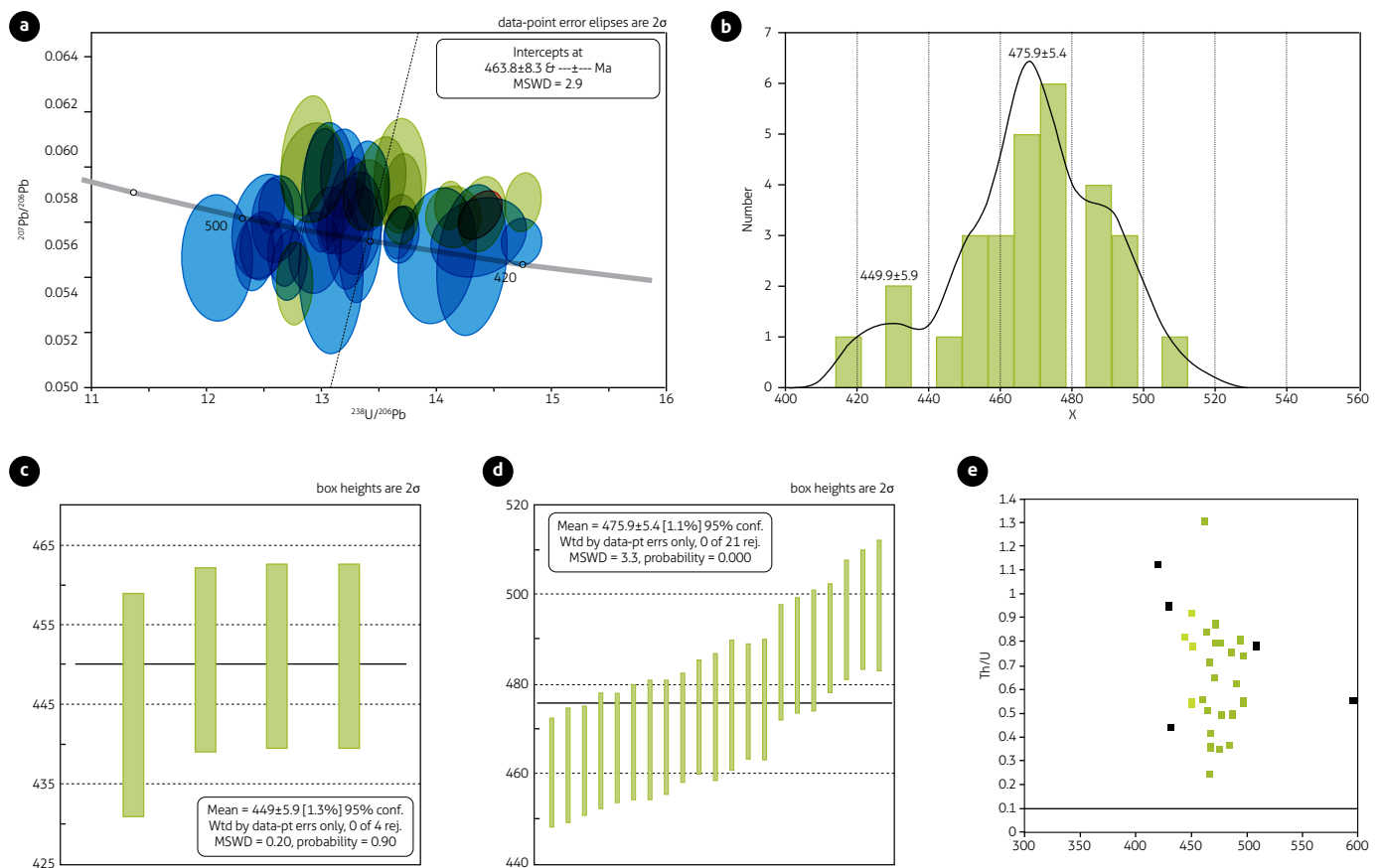


**Figure 7.** Results of U-Pb dating in zircon of sample JGB-483 a) Concordia Tera-Wasserburg; blue is accepted data, green is deleted data; b) Probability density diagram; c) Weighted average age. e) Age-Th/U relationship.

The accepted analyses show a wide dispersion between  $419.5 \pm 11.06$  Ma and  $509.1 \pm 15.8$  Ma. A weighted average age was obtained from four concordant analyses that yielded  $449.9 \pm 5.9$  Ma with an MSWD=0.20, which is interpreted as the age of rock crystallization, and an inherited age was obtained from 21 accepted analyses, with  $Pb^{206}/U^{238}$  values that yielded an age of  $475.9 \pm 5.4$  Ma and MSWD=3.3. Additionally, in the range of all the results between  $445 \pm 14$  and  $497.7 \pm 14.6$  Ma, an integrated age of  $471.2 \pm 6$  Ma was obtained with MSWD=5.3. The Th/U ratio > 0.1 for all accepted zircons suggests that they correspond to zircons formed from a melt (Rubatto, 2002).

A second sample (LMC-076) was analyzed, which corresponds to a metarhyolite with quartz porphyroclasts, plagioclase and alkali feldspar and recrystallization at the edges. The porphyroclasts are distributed within the oriented microcrystalline matrix, which is mainly composed of quartz and sericite. The zircons are prismatic, elongated and short, and some are small, rounded, and lilac. They are located in the rock matrix and are smaller than 50  $\mu$ m. The cathodoluminescence images show a concentric structure of igneous zircons, with some inherited dark-gray nuclei and more luminescent light-gray edges.

To determine ages, 60 analyses were performed (Supplementary Data), of which 8 were eliminated with discordances > 5 and errors > 4.5 (Figure 8). A zircon crystal is presented with two analyses that yield results of  $188.4 \pm 4$  Ma and  $190.3 \pm 5$  Ma, which is interpreted as a contaminating zircon that is probably associated with the Triassic-Jurassic magmatism of the Santander massif. A population is presented with ages between  $430.5 \pm 9$  Ma and  $458.3 \pm 7$  Ma that determine the average age of rock crystallization as  $450.9 \pm 2.5$  Ma, MSWD=2.5 (n=29). A second population of xenocrysts, with ages between  $462.4 \pm 8$  Ma and  $479 \pm 10$  Ma, showed an average age of  $469.8 \pm 4.0$  Ma, MSWD=4 (n=9) and presents xenocrysts and inherited nuclei of the Neoproterozoic, with two data points of  $555 \pm 11$  Ma and  $565.7 \pm 9$  Ma, a population of three data points with an average age of  $617 \pm 16$  Ma and MSWD=1.7. A population of three data points, with an average age of  $644, 5 \pm 6.5$  Ma and MSWD=0.067 and three heritages, occurred between  $1071 \pm 48$  Ma and  $1171 \pm 37$  Ma. The Th/U ratio of these heritages is greater than 0.1, which suggests that the inherited zircons are igneous (Rubatto, 2002).

## 5. DISCUSSION

### 5.1. Correlations and Ordovician magmatism

Two populations of Ordovician igneous ages were found in the two analyzed samples from the Onzaga Metarhyolite: in sample JGB-483, the youngest average age yielded a value of  $449.9 \pm 5.9$  Ma (n=4), and the second population showed an average age of  $475.9 \pm 5.4$  Ma (n=21); in the LMC-076 sample, the average age of rock crystallization is  $450.9 \pm 2.5$  Ma (n=29), and the second igneous population is  $469.8 \pm 4.0$  (n=9). The results in both samples are comparable and suggest that the crystallization age of the rhyolitic lavas occurred at approximately 450 Ma (Upper Ordovician), while the second age corresponds to a population of inherited magmatic zircons with ages of approximately 470-475 Ma (Lower-Middle Ordovician limit), which is interpreted as zircons contributing to the rhyolitic magma, possibly as a result of the fusion of crustal rocks that crystallized during the Lower-Middle Ordovician.

Figure 9 shows a correlation graph of U-Pb ages for different Ordovician units of the Santander and Floresta massifs and the Mérida Mountain range, and Table 4 summarizes the ages with which the figure was made.

In the Santander massif, the Onzaga Metarhyolite presents ages slightly older than the crystallization of the Durania, Timotes and Tarra granites and agrees with the K-Ar age in muscovite of a pegmatite that cuts the Bucaramanga gneiss to the east of the town of Chitagá, with  $457 \pm 13$  Ma (Goldsmith et al., 1971), as well as with a gabbro unit that outcrops near Pamplona, which yields a K-Ar age in total rock of  $456 \pm 23$  Ma (Boinet et al., 1985); this age is slightly younger than the U-Pb age reported for the Santa Rosita Monzogranite of  $460.2 \pm 4.6$  Ma (Zapata et al., 2017) and that of a granofels that corresponds to a xenolith of an orthogneiss within the Monzogranite of La Corcova, which gave a U/Pb crystallization age of  $462.7 \pm 3.1$  Ma (Rodríguez et al., 2017a, 2020). The Berlin orthogneiss has a similar U/Pb crystallization age of  $451.5 \pm 1.3$  Ma (van der Lelij et al., 2016) (Table 4, Figure 9).

In the Mérida Mountain range, the Onzaga Metarhyolite is geochronologically correlated with the Verdálito, Macanas, Chapolo, Miraflores, Carmania and La Puerta granitoids, with the orthogneiss units of La Raya, Micarache and La Playita, with the Iglesias Complex and with the Bailadores rhyolite. All these units, with similar U/Pb ages, were reported by van der Lelij et al. (2016) and Tazzo et al. (2018) (Table 4, Figure 9). The Onzaga Metarhyolite has slightly younger ages than the

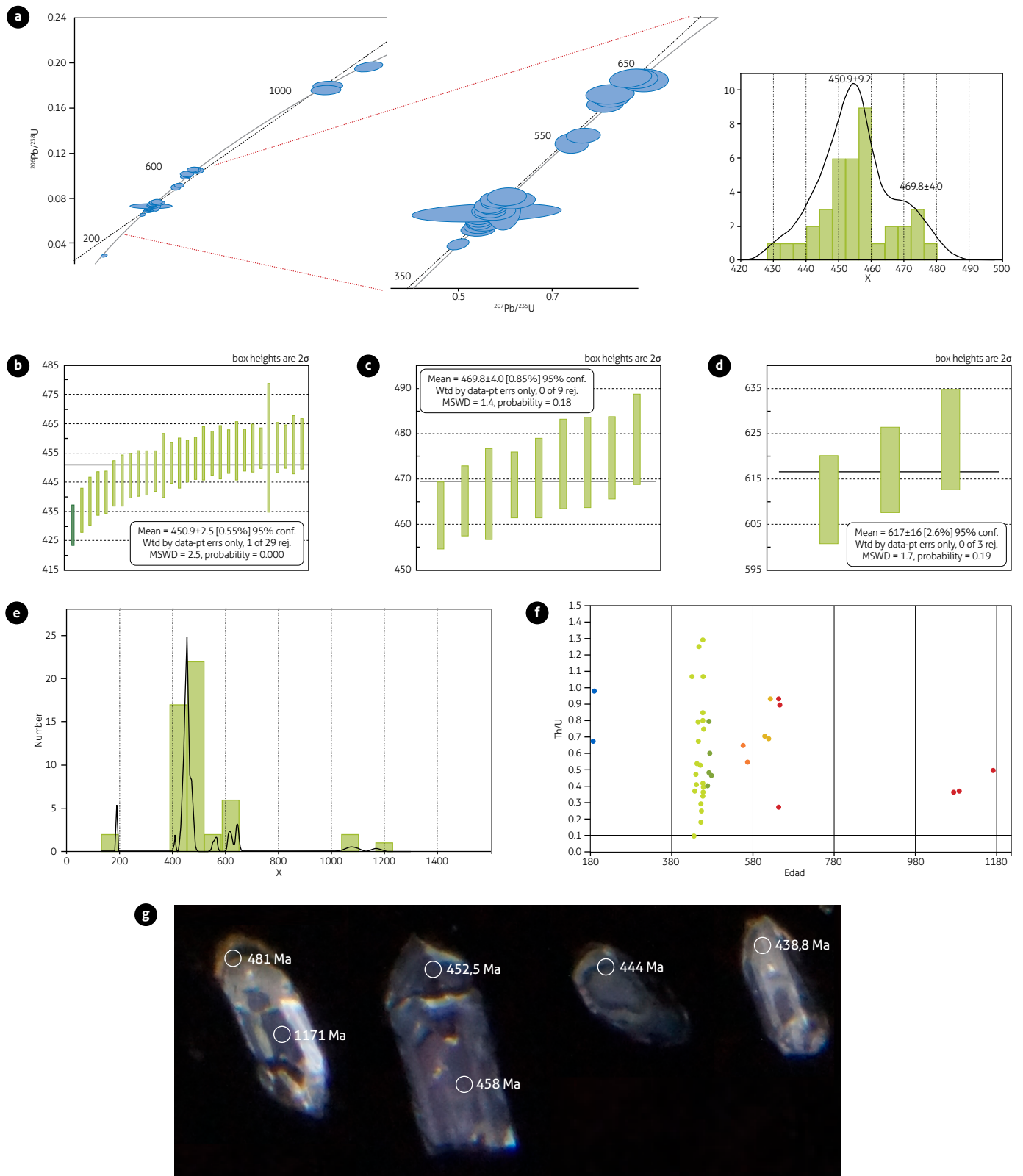


**Figure 8.** Results of U-Pb dating in the zircon of sample LMC-076  
a) Concordia Tera-Wasserburg; b) Probability density diagram; c) Weighted average age diagrams; e) Diagram of probability density in inherited zircons; f) Age-Th/U relationship; g) Cathodoluminescence images of zircons from sample LMC-076.

Mitisus gneiss. In the Floresta massif, the ages reported for the Santa Rosita Monzogranite are slightly older than those of the Onzaga Metarhyolite but could be related to the same magmatism (Table 4, Figure 9).

The Ordovician ages inherited from the Onzaga Metarhyolite (*ca.* 470–475 Ma, lower-middle Ordovician limit) are comparable with ages obtained in the Santander massif in nonfoliated granitoid rocks of 471 ± 7 Ma (Restrepo-Pace and Cediel, 2010).

Within the foliated bodies, there are U/Pb ages of 473.5 ± 2.5 Ma and 472.5 ± 3.4 Ma in the orthogneiss of Berlin, 479 ± 10 and 471 ± 11 in the gneiss of Bucaramanga (van der Lelij et al., 2016; García Ramírez et al., 2017), and an age of 477.0 ± 5.3 in a paragneiss migmatite (van der Lelij, 2013; van der Lelij et al., 2016). Although they are foliated rocks, the U-Pb ages in zircon presented by the aforementioned authors were interpreted as those of crystallization and have Th/U ratios > 0.1.

Table 4. U-Pb ages in zircon for different Ordovician bodies of the Santander, Floresta, Quetame and Mérida Mountain ranges

No. field	Coordinates		Unity	Age U/Pb (Ma)	MSWD	Source
	West (m)	North				
<b>Mérida Mountain range</b>						
08VDL03	8° 28' 49"	71° 34' 13"	Verdalite granodiorite	449.3 ± 2.5	2	Van der Lelij et al. (2016)
08VDL11	8° 41' 41"	70° 53' 31"	Micarache orthogneiss	454.0 ± 10.0	2.5	Van der Lelij et al. (2016)
08VDL15	8° 11' 51"	71° 50' 09"	Alkali rhyolite dancers	452.6 ± 2.7	2.7	Van der Lelij et al. (2016)
08VDL21	8° 08' 28"	71° 56' 15"	La Grita Diorite	471.8 ± 4.0	2	Van der Lelij et al. (2016)
08VDL22	8° 11' 38"	71° 53' 02"	La Playita orthogneiss	449.7 ± 4.4	9.3	Van der Lelij et al. (2016)
08VDL36	8° 27' 53"	71° 26' 50"	Puente Real augen gneiss	472.3 ± 3.4	4.1	Van der Lelij et al. (2016)
08VDL38	8° 20' 19"	71° 37' 21"	Macanas alkali granite	454.8 ± 4.2	1.5	Van der Lelij et al. (2016)
08VDL41	8° 55' 55"	70° 47' 31"	Chapolo Granite	454.5 ± 3.1	1	Van der Lelij et al. (2016)
08VDL44	9° 10' 42"	70° 38' 08"	Miraflores granodiorite	447.9 ± 2.5	1.4	Van der Lelij et al. (2016)
08VDL47	9° 15' 59"	70° 38' 18"	Carmania monzodiorite	450.4 ± 2.5	1.5	Van der Lelij et al. (2016)
08VDL49	9° 07' 11"	70° 42' 39"	La Puerta Granodiorite	453.1 ± 1.8	2.1	Van der Lelij et al. (2016)
QG-25	8° 41' 37"	70° 56' 23"	Complex churches	451.4 ± 3.6	0.69	Tazzo et al. (2018)
QM-02	8° 44' 23"	70° 53' 49"	Complex churches	435.5 ± 5.9	0.81	Tazzo et al. (2018)
GLR-02c	8° 54' 0"	70° 37' 43"	The hornblende-gneiss ray	458.0 ± 3.4	0.53	Tazzo et al. (2018)
SB-0405	8° 52' 7"	70° 35' 30"	Mitisus gneiss	466.8 ± 3.7	0.69	Tazzo et al. (2018)
SDB-01	8° 52' 38"	70° 38' 4"	Complex churches	487.2 ± 7.0	0.97	Tazzo et al. (2018)
CM-01	8° 42' 20"	70° 50' 15"	Sierra Nevada	445 ± 31	0.64	Tazzo et al. (2018)
<b>Santander Massif</b>						
10VDL49	7° 29' 20"	72° 42' 16"	Fm Silgará	479.8 ± 3.1	1.7	Van der Lelij et al. (2016)
10VDL47	7° 28' 23"	72° 41' 44"	Gabbrodiorite	483.7 ± 5.9	0.7	Van der Lelij et al. (2016)
10VDL46	7° 16' 29"	72° 39' 55"	Durania granite	439.2 ± 4.7	8	Van der Lelij et al. (2016)
08VDL50	9° 00' 52"	70° 44' 25"	Timotes granite	445.2 ± 3.9	8.2	Van der Lelij et al. (2016)
GE-58-M1	7° 23' 27.6"	72° 53' 28.7"	Foliate metadiorites	477.0 ± 4.1	2.9	Mantilla et al. (2012)
GH-72-M2	7° 23' 27.6"	72° 53' 28.7"	Foliate metadiorites	477 ± 2	4.7	Mantilla et al. (2012)
GI-60-M2	7° 23' 27.6"	72° 53' 28.7"	Foliate metadiorites	481.9 ± 6.1	4.1	Mantilla et al. (2012)
10VDL50	7° 15' 22"	72° 53' 45"	Migmatite from paragneiss	477.0 ± 5.3	7.5	Van der Lelij et al. (2016)
10VDL23	6° 56' 35"	72° 58' 00"	Bucaramanga gneiss	461 ± 2.1	2.6	Van der Lelij et al. (2016)
VR-7-2	7° 10' 29.40"	72° 42' 07.15"	Bucaramanga gneiss	479 ± 10		García Ramírez et al. (2017)
VR-22-1	7° 12' 11.95"	72° 46' 49.22"	Bucaramanga gneiss	471 ± 11		García Ramírez et al. (2017)
10VDL51	7° 15' 17"	72° 53' 48"	Orthogneiss of Berlin	472.5 ± 3.4	11.5	Van der Lelij et al. (2016)
10VDL37	7° 11' 24"	72° 58' 41"	Orthogneiss of Berlin	451.5 ± 1.3	1	Van der Lelij et al. (2016)
10VDL44	7° 20' 40"	72° 42' 59"	Orthogneiss of Berlin	473.5 ± 2.5	4.6	Van der Lelij et al. (2016)
10VDL55	8° 03' 10"	73° 04' 31"	Tarra granodiorite	443.4 ± 3.2	3.8	Van der Lelij et al. (2016)
AMC-0128A	7° 08' 12.59"	73° 02' 17.97"	Xenolith-granofels of Qtz-Pl-Kfs	462.7 ± 3.1	1.7	Rodríguez et al. (2020)
JGB-483	6° 11' 05.98"	72° 50' 23.61"	Onzaga Metarhyolite	449.9 ± 5.9	0.2	This work
LMC-076	6° 21' 00.88"	72° 49' 18.27"	Onzaga Metarhyolite	450.9 ± 2.5	2.5	This work
<b>Massif of Floresta and Quetame</b>						
RH1	4° 23' 1085"	73° 17' 24.95"	Granodiorite mine	483 ± 10	4.2	Horton et al. (2010)
FS11A	5° 50' 55.53"	72° 51' 52.12"	Otengá stock	482 ± 15	6.5	Horton et al. (2010)
1308080	5° 58' 54.44"	72° 48' 45.84"	Otengá stock	477 ± 11	28	Horton et al. (2010)
GZ-6837	6° 13' 13.93"	72° 47' 04.91"	Monzogranite from Santa Rosita	479.0 ± 3.6	1.2	Zapata et al. (2017)
JGB-482	6° 00' 50.37"	72° 52' 35.16"	Monzogranite from Santa Rosita	460.6 ± 4.6		Zapata et al. (2017)

Source: Rodríguez et al. (2020), Horton et al. (2010), Mantilla et al. (2012), van der Lelij et al. (2016), Zapata et al. (2017), García Ramírez et al. (2017), and Tazzo et al. (2018).

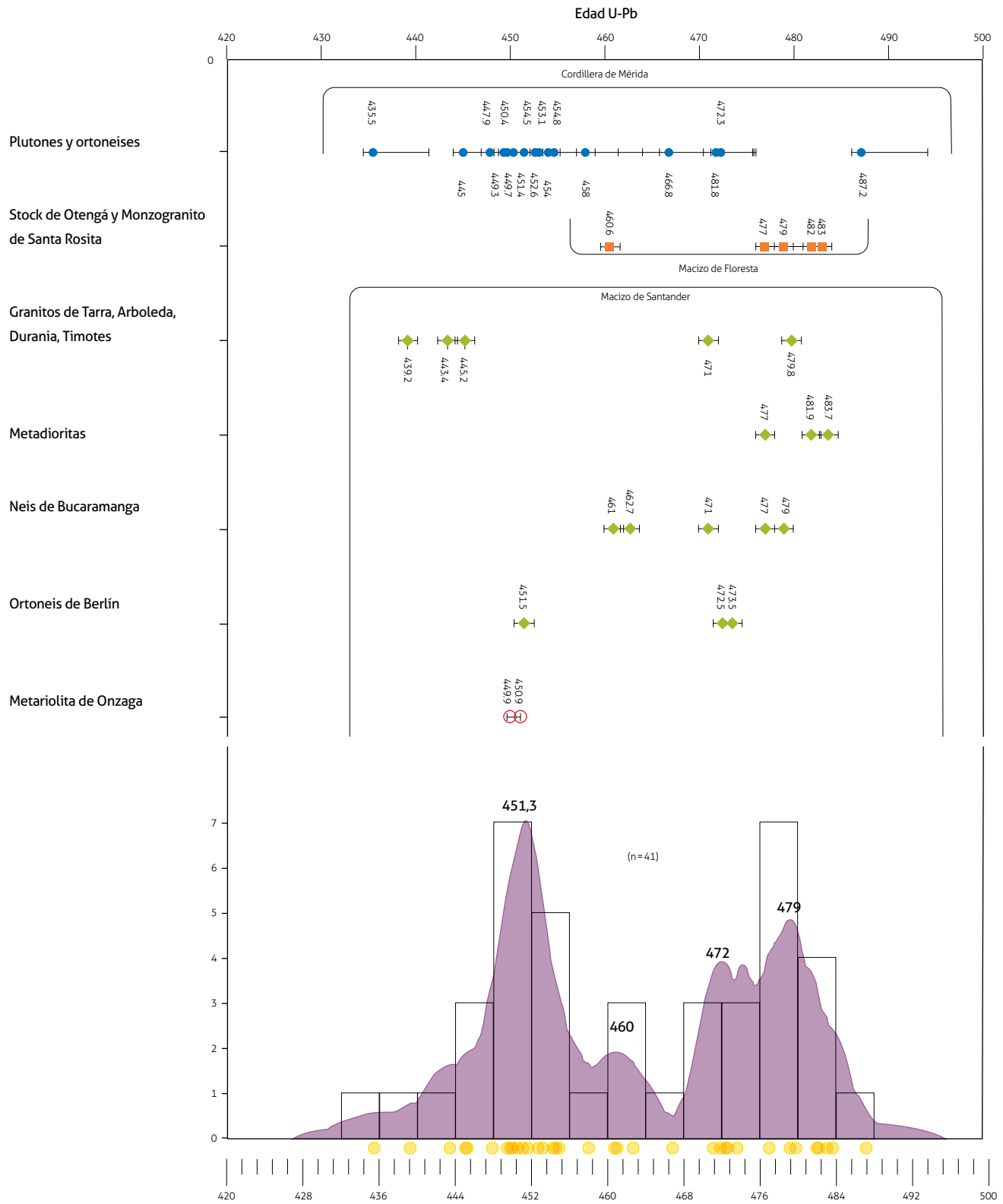


**Figure 9.** Compilation of U-Pb ages of different Ordovician bodies of the Santander, Floresta, Quetame and Mérida Mountain ranges and kernel density estimation diagram for crystallization ages of Ordovician units  
Source: Rodríguez et al. (2020), Horton et al. (2010), Mantilla et al. (2012), van der Lelij et al. (2016), Zapata et al. (2017), García Ramírez et al. (2017), and Tazzo et al. (2018).

Some units have slightly older ages, such as the Otengá Stock in the Floresta massif with U-Pb ages of  $477 \pm 11$  Ma and  $482 \pm 15$  Ma (Horton et al., 2010); the bodies of metadiorites and gabbrodiorites give U/Pb ages of  $477.0 \pm 4.1$  Ma,  $477 \pm 2$  Ma,  $481.9 \pm 6.1$  Ma and  $483.7 \pm 5.9$  Ma (Mantilla et al., 2012; van der Lelij et al., 2016), which represents a more basic magmatism than that of orthogneiss and nonfoliated granites, which are younger.

Further west, in the Central Cordillera of Colombia, Martens et al. (2014) recorded igneous U-Pb ages of the La Miel gneiss of  $479 + 15/-1$  Ma ( $n=7$ ) and  $443 \pm 8$  Ma ( $n=8$ ), the latter in the zircon magmatic edges, associated with the Anacona terrain, which for these authors represents a portion of the Ordovician magmatic belt that bordered Gondwana in the early Paleozoic. As potential regional correlations, Martens et al. (2014), van der Lelij et al. (2016) and Tazzo et al. (2018) consider similarities with the first Paleozoic component of the Marañón Complex of Peru, the Acatlán Complex of the Mixtec terrain in southern Mexico and the Maya Block of Central America.

When analyzing Figure 9 and Table 4, it can be concluded that the magmatism of the Santander, La Floresta, Quetame and Mérida Mountain ranges presents at least four main crystallization events in the Ordovician, which can be grouped at approximately 479-472 Ma, *ca.* 460 Ma and *ca.* 451 Ma. In the interval between 479-472 Ma, basic to intermediate magmatism is recognized in the Santander massif at approximately 479 Ma (diiorites and gabbrodiorites), which formed small calc-alkaline intrusions and have been interpreted by Mantilla et al. (2012) as plutons formed from magmas derived from the mantle; this finding is possibly associated with a suprasubduction event related to the beginning of the closure of the Lapetus Ocean. In this same interval but approximately 472 Ma, felsic bodies, calc-alkaline high in K, peraluminous and migmatitic gneiss (orthogneiss of Berlin and gneiss of Bucaramanga) were formed; these formations have been explained by partial fusion of continental crust, producing felsic magmatic rocks, likely facilitated by the heat transfer of basic magmas at the base of the crust (Huppert and Sparks, 1988; Cochrane et al., 2014; van der Lelij, 2016) and by the existence of an active continental margin. This process occurred between *ca.* 495 Ma and *ca.* 415 Ma (van der Lelij et al., 2016). These rocks are part of the Famatinian Arc that crops out south of the continent. Subsequently, a discrete crystallization event of approximately 460 Ma is recognized (Santa Rosita Monzogranite, Qtz-Fsp-Pl granofels

xenolith within the La Corcova Monzogranite and an age in the Bucaramanga gneiss), which continues to be magmatic, high calc-alkaline K and peraluminous. At approximately 451 Ma, one of the largest magmatism and crystallization events occurred, with the formation of volcanic rocks (Onzaga Metarhyolite) that were probably fissurally extruded along faults based on the shape of the body, which is elongated and thin and has a N-S orientation. Contemporaneous with the volcanism, the intrusion of granite bodies (granites of Durania, Timotes and Tarra) occurred, being of acid magmatism, calc-alkaline high in K, peraluminous and of type S, with abundant contribution of zircons inherited from the igneous event of *ca.* 472-475 Ma, as evidenced by the geochronological results of the Onzaga Metarhyolite.

Trace elements in granitic magmas are dictated not only by the composition of the source but also by magmatic processes, such as partial melting and fractional crystallization. Therefore, they have little capacity to identify the nature of the source of the granites (Gao et al., 2016). The rocks of the Onzaga Metarhyolite and the Santa Rosita Monzogranite are distributed in the La/Sm vs. La diagram (Figure 10a) in the fields of partial fusion and fractional crystallization, while the samples of the Durania Granite plot in the rock field, as they were formed by partial fusion. The metasedimentary protolith granites can show compositional variations similar to the so-called peraluminous type I granites. The chemistry of these three units corresponds to peraluminous magmas, which plot in conventional diagrams in the field of S-type granites (Figure 10b), with two micas but whose source does not necessarily correspond to the melting of sediments or metasediments.

The presence of an abundant population of zircons with ages between 460 Ma and 497 Ma, Th/U ratios  $> 0.1$  and a concentric structure suggests that the source of the Onzaga Metarhyolite corresponds to igneous rocks, with crystallization ages between 470 Ma and 475 Ma. The inheritances of xenocrysts and zircon nuclei with the Neoproterozoic results (Tonian, Cryogenian and Ediacarian) could be contributed by igneous sources rather than by the fusion of metasedimentary rocks. Considering that peraluminous magmas have a low capacity to melt zircons, this finding is attributable to the following factors: (1) the relatively high abundance of zircons in the case that they come from clastic metasedimentary rocks; (2) the relatively low temperatures for magmas with S-type granitics (Chappell et al., 2004); (3) the low solubility of zircon in peraluminous melts (Watson and Harrison, 1983); and (4) the

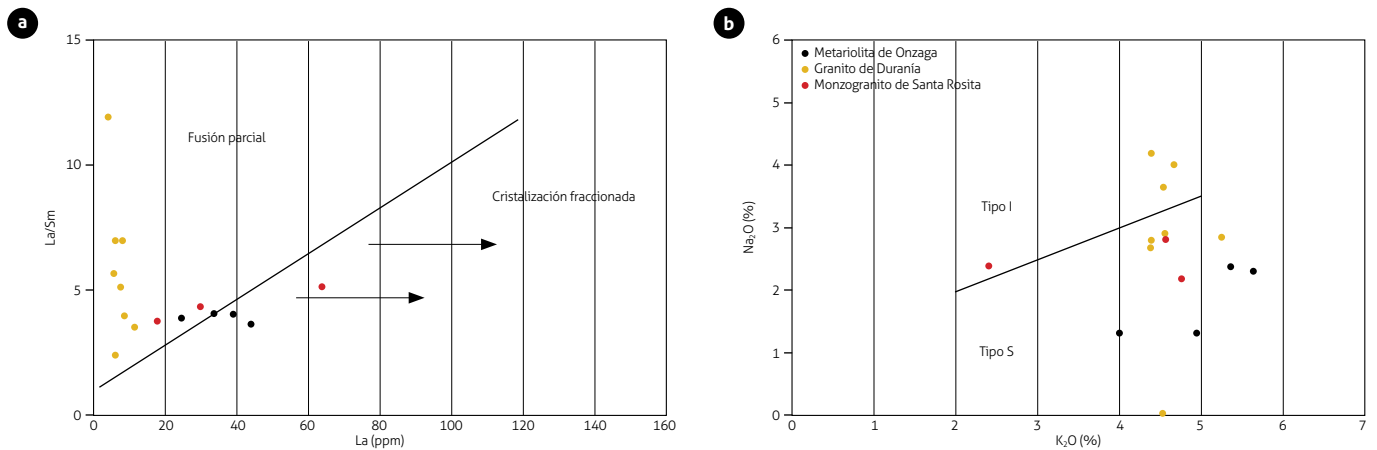


**Figure 10.** La-La/Sm diagram (Jiang et al., 2005): evolution of the magmas of the Onzaga Metarhyolite, Santa Rosita Monzogranite and Durania Granite by partial fusion. K<sub>2</sub>O-Na<sub>2</sub>O diagram of granite type classification (Chappell and White, 1992)

rapid migration of granitic magmas from the melting regions to the sites of emplacement (Clemens, 2003). Therefore, information on the nature of the source of the granites can be obtained by comparing magmatic zircons with inherited zircons (Jeon et al., 2012). In this sense, the inheritances of zircons in the Onzaga Metarhyolite point to an igneous source with magmatic zircons with average ages between ~ 470 and ~ 475 Ma, similar to the ages reported for the orthogneiss of Berlin and the gneiss of Bucaramanga.

## 6. CONCLUSIONS

New U-Pb LA-ICPMS geochronology data in zircons indicate volcanism *ca.* 451 Ma (Onzaga Metarhyolite) in the Santander massif, contemporaneous with plutonic bodies that crystallized in the Mérida Mountain range and the Santander massif itself. The volcanism results are acidic, high in K, peraluminous and of type S, with abundant contributions of zircons inherited from an igneous event *ca.* 472-475 Ma, which suggests the fusion of igneous rocks with these ages in the development of the magma that gave rise to the protolith of the metarhyolites.

In the Santander, La Floresta, Quetame and Mérida Mountain ranges, at least four crystallization events occurred during the Ordovician period, grouped *ca.* 479-472 Ma, *ca.* 460 Ma, and *ca.* 451 Ma, plus basic to intermediate magmatism at approximately 479 Ma. The crystallization of the Onzaga Metarhyolite is associated with rocks from *ca.* 451 Ma.

The volcanic rocks of the Onzaga Metarhyolite, after magmatic crystallization, were subjected to metamorphism that

reached the green schist facies and probably reached the low amphibolite facies, as indicated by recrystallization of the edges of the quartz phenocrysts, plagioclase and alkali feldspar in some rocks. The metamorphism had a dynamic component, with the development of porphyroclasts with asymmetric tails and was generated by blastesis microsheets of biotites and white mica that mark the foliation of the rocks.

## ACKNOWLEDGMENTS

Thank you to the following people and organizations: the Servicio Geológico Colombiano, who financed the study; the chemistry, thin section and geochronology laboratories of the Servicio Geológico Colombiano; geologists Gilberto Zapata, Tomás Correa, Lina Cetina and José Gilberto Bermúdez for their help with field sampling; and Tomás Correa for translation of the abstract and to the anonymous reviewers for their comments, which allowed us to improve the manuscript.

## SUPPLEMENTARY DATA

Supplementary data for this article can be found online at <https://doi.org/10.32685/0120-1425/bol.geol.48.2.2021.571>

## REFERENCES

Boinet, T., Bourgois, J., Bellon, H., & Toussaint, J. (1985). Age et repartition du Age et repartition du magmatisme Pré-mésozoïque des Andes de Colombie=Age and distribution

- of the Premesozoic magmatism of the Andes of Columbia. *Comptes-rendus des séances de L'Académie des Sciences. Serie 2, Mécanique- Physique, Chimie, Sciences des Univers, Sciences de la Terre*, 300(2), 445-450.
- Castaño, J. M., Rodríguez F., & García, C. A. (2018). Caracterización de parámetros en la concentración de circones para andesitas, monzogranitos, riolitas, cuarcitas y cuarzomonzonitas. *Boletín Geológico*, (44), 25-38. <https://doi.org/10.32685/0120-1425/boletingeo.44.2018.6>
- Cediel, F., Shaw, R. P., & Caceres, C. (2003). Tectonic assembly of the Northern Andean Block. In C. Bartolini, R. T. Buffler, & J. Blickwede (eds.), *The Circum-Gulf of Mexico and the Caribbean: Hydrocarbon Habitats, Basin Formation, and Plate Tectonics* (vol. 79, pp. 815-848). AAPG Memoir.
- Chappell, B. W., & White, A. J. R. (1974). Two contrasting granite types. *Pacific Geology*, 8(2), 173-174.
- Chappell, B. W., & White, A. J. R. (1992). I- and S-type granites in the Lachlan Fold Belt. *Earth and Environmental Science Transactions of the Royal Society of Edinburgh*, 83(1-2), 1-26. <https://doi.org/10.1017/S0263593300007720>
- Chappell, B. W., White, A. J. R., Williams, I. S., & Wyborn, D. (2004). Low- and high-temperature granites. *Transactions of the Royal Society of Edinburgh: Earth Sciences*, 95, 125-140. <https://doi.org/10.1017/S0263593300000973>
- Clavijo, J., Mantilla, F. L. C., Pinto, J., Bernal, L., & Pérez, A. (2008). Evolución geológica de la serranía de San Lucas, norte del valle medio del Magdalena y noroeste de la cordillera Oriental. *Boletín de Geología*, 30(1), 45-62.
- Clemens, J. D. (2003). S-type granitic magmas-petrogenetic issues, models and evidence. *Earth-Science Reviews*, 61(1-2), 1-18. [https://doi.org/10.1016/S0012-8252\(02\)00107-1](https://doi.org/10.1016/S0012-8252(02)00107-1)
- Cochrane, R., Spikings, R., Gerdes, A., Winkler, W., Ulianov, A., Mora, A., & Chiaradia, M. (2014). Distinguishing between in-situ and accretionary growth of continents along active margins. *Lithos*, 202-203, 382-394. <https://doi.org/10.1016/j.lithos.2014.05.031>
- Correa-Martínez, A. M., Rodríguez, G., Arango, M. I., Zapata, G., & Bermúdez J. G. (2017). *Catálogo de unidades litoestratigráficas de Colombia. Batolito de Mogotes*. Servicio Geológico Colombiano.
- Coyner, S. J., Kamenov, G. D., Mueller, P. A., Rao, V., & Foster, D. A. (2004). FC-1: A zircon reference standard for the determination of Hf isotopic compositions via laser ablation ICP-MS. *American Geophysical Union, Fall Meeting Abstracts*.
- Frost, B., & Frost. D. (2008). A geochemical classification for feldspathic igneous rocks. *Journal of Petrology*, 49(11), 1955-1969. <https://doi.org/10.1093/petrology/egn054>
- Gao, P., Fei Zheng, Y., & Fu Zhao, Z. (2016). Distinction between S-type and peraluminous I-type granites: Zircon versus whole-rock geochemistry. *Lithos*, 258-259, 77-91. <https://doi.org/10.1016/j.lithos.2016.04.019>
- García Ramírez, C., Rey-León, V., & Valencia, V. (2017). Ortonaises en la Franja Silos-Babega, macizo de Santander, Colombia: evidencias de la orogenia famatiniana en los Andes del norte. *Andean Geology*, 44(3), 307-327. <https://doi.org/10.5027/andgeov44n3-a04>
- Goldsmith, R., Marvin, R. F., & Maner, H. H. (1971). *Radio-metric ages in the Santander Massif, Eastern Cordillera, Colombian Andes*. U.S. Geological Survey Professional Paper 750-D, D44-D49.
- Hastie, A. R., Kerr, A. C., Pearce, J. A., & Mitchell, S. F. (2007). Classification of altered volcanic island arc rocks using immobile trace elements: development of the Th Co discrimination diagram. *Journal of Petrology*, 48(12), 2341-2357. <https://doi.org/10.1093/petrology/egm062>
- Hellstrom, J., Paton, C., Woodhead, J. D., & Hergt, J. M. (2008). Lolite: Software for spatially resolved LA- (quad and MC) ICP-MS analysis. In P. Sylvester (ed.), *Laser Ablation ICP-MS in the Earth sciences: Current practices and outstanding issues* (pp. 343-348). Mineralogical Association of Canada.
- Horton, B. K., Saylor, J. E., Nie, J., Mora, A., Parra, M., Reyes-Harker, A., & Stockli, D. F. (2010). Linking sedimentation in the northern Andes to basement configuration, Mesozoic extension, and Cenozoic shortening: evidence from detrital zircon U-Pb ages, Eastern Cordillera, Colombia. *GSA Bulletin*, 122(9-10), 1423-1442. <https://doi.org/10.1130/B30118.1>
- Huppert, H. E., & Sparks, R. S. J. (1988). The generation of granitic magmas by intrusion of basalt into continental crust. *Journal of Petrology*, 29, 599-624. <https://doi.org/10.1093/petrology/29.3.599>
- wwJanoušek, V., Farrow, C. M., & Erban, V. (2006). Interpretation of whole-rock geochemical data in igneous geochemistry: Introducing Geochemical Data Toolkit (GC-Dkit). *Journal of Petrology*, 47(6), 1255-1259. <https://doi.org/10.1093/petrology/egl013>
- Jeon, H., Williams, I. S., & Chappell, B. W. (2012). Magma to mud to magma: rapid crustal recycling by Permian granite magmatism near the eastern Gondwana margin. *Earth and*

- Planetary Science Letters*, 319-320, 104-117. <https://doi.org/10.1016/j.epsl.2011.12.010>
- Jiang, Y. H., Ling, H. F., Jiang, S. Y., Fan, H. H., Shen, W. Z., & Ni, P. (2005). Petrogenesis of a Late Jurassic Peraluminous Volcanic complex and its high-Mg, potassic, quenched enclaves at Xiangshan, Southeast China. *Journal of Petrology*, 46(6), 1121-1154. <https://doi.org/10.1093/petrology/egi012>
- Leal-Mejía, H. (2011). *Phanerozoic gold metallogeny in the Colombian Andes: A tectono-magmatic approach* [Ph.D. Thesis]. University of Barcelona.
- Mantilla, L. C., Bissig, T., Cottle, J. M., & Hart, C. J. (2012). Remains of early Ordovician mantle-derived magmatism in the Santander Massif (Colombian Eastern Cordillera). *Journal of South American Earth Sciences*, 38, 1-12. <https://doi.org/10.1016/j.jsames.2012.03.001>
- Mantilla, L. C., Bissig, T., Valencia, V., & Hart, C. (2013). The magmatic history of the Vetás-California Mining District, Santander Massif Eastern Cordillera, Colombia. *Journal of South American Earth Sciences*, 45, 235-249. <https://doi.org/10.1016/j.jsames.2013.03.006>
- Mantilla, L. C., García-Ramírez, C. A., & Valencia, V. A. (2016). Propuesta de escisión de la denominada 'formación Silgará' (macizo de Santander, Colombia), a partir de edades U-Pb en circones detríticos. *Boletín de Geología*, 38(1), 33-50. <https://doi.org/10.18273/revbol.v38n1-2016002>
- Martens, U., Restrepo, J. J., Ordoñez-Carmona, O., & Correa-Martínez, A. M. (2014). The Tahamí and Anacona terranes of the Colombian Andes: missing links between the South American and Mexican Gondwana margins. *Journal of Geology*, 122(5), 507-530. <https://doi.org/10.1086/677177>
- McDonough, W. F., & Sun, S. S. (1995). The composition of the earth. *Chemical Geology*, 120(3-4), 223-253. [https://doi.org/10.1016/0009-2541\(94\)00140-4](https://doi.org/10.1016/0009-2541(94)00140-4)
- Nakamura, N. (1974). Determination of REE, Ba, Fe, Mg, Na and K in carbonaceous and ordinary chondrites. *Geochimica et Cosmochimica Acta*, 38(5), 757-775. [https://doi.org/10.1016/0016-7037\(74\)90149-5](https://doi.org/10.1016/0016-7037(74)90149-5)
- Ordóñez-Cardona, O., Restrepo Álvarez, J. J., & Pimentel, M. M. (2006). Geochronological and isotopic review of pre-Devonian crustal basement of the Colombian Andes. *Journal of South American Earth Sciences*, 21(4), 372-382. <https://doi.org/10.1016/j.jsames.2006.07.005>
- Paton, C., Woodhead, J. D., Hellstrom, J. C., Hergt, J. M., Greig, A., & Maas, R. (2010). Improved laser ablation U-Pb zircon geochronology through robust downhole fractionation correction. *Geochemistry, Geophysics, Geosystems*, 11(3), 1-36. <https://doi.org/10.1029/2009GC002618>
- Peña, M. L., Muñoz Rocha, J. A., & Urueña, C. L. (2018). Laboratorio de Geocronología en el Servicio Geológico Colombiano: avances sobre datación U-Pb en circones mediante la técnica LA-ICP-MS. *Boletín Geológico*, (44), 39-56. <https://doi.org/10.32685/0120-1425/boletingeo.44.2018.7>
- Petrus, J. A., & Kamber, B. S. (2012). VizualAge: A novel approach to laser ablation ICP-MS U-Pb geochronology data reduction. *Geostandards and Geoanalytical Research*, 36(3), 247-270. <https://doi.org/10.1111/j.1751-908X.2012.00158.x>
- Renne, P. R., Swisher, C. C., Deino, A. L., Karner, D. B., Owens, T. L., & De Paolo, D. J. (1998). Intercalibration of standards, absolute ages and uncertainties in  $^{40}\text{Ar}/^{39}\text{Ar}$  dating. *Chemical Geology*, 145(1-2), 117-152. [https://doi.org/10.1016/S0009-2541\(97\)00159-9](https://doi.org/10.1016/S0009-2541(97)00159-9)
- Restrepo-Pace, P. (1995). *Late Precambrian to Early Mesozoic Tectonic Evolution of the Colombian Andes based on new geochronological, geochemical and isotopic date* [Ph.D. Thesis]. The University of Arizona.
- Restrepo-Pace, P., Ruiz, J., Gehrels, G., & Cosca, M. (1997). Geochronology and Nd isotopic data of Grenville-age rocks in Colombian Andes: new constraints for Late Proterozoic Early Paleozoic paleocontinental reconstructions of Americans. *Earth and Planetary Science Letters*, 150(3-4), 427-441. [https://doi.org/10.1016/S0012-821X\(97\)00091-5](https://doi.org/10.1016/S0012-821X(97)00091-5)
- Restrepo-Pace, P., & Cediél, F. (2010). Northern South America basement tectonics and implications for paleocontinental reconstructions of the Americas. *Journal of South American Earth Sciences*, 29(4), 764-771. <https://doi.org/10.1016/j.jsames.2010.06.002>
- Ríos, C., García, C., & Takusa, A. (2003). Tectono-metamorphic evolution of the Silgara Formation metamorphic rocks in the Southwestern Santander Massif, Colombian Andes. *Journal of South American Earth Sciences*, 16(2), 133-154. [https://doi.org/10.1016/S0895-9811\(03\)00025-7](https://doi.org/10.1016/S0895-9811(03)00025-7)
- Rodríguez, G., Zapata, G., Correa, A. M., & Arango, M. I. (2017). *Caracterización petrográfica, química y geocronológica del magmatismo Triásico-Jurásico del macizo de Santander-Colombia*. XVI Congreso Colombiano de Geología y III Simposio de Exploradores, Geología, Sociedad y Territorio. Santa Marta, Colombia.
- Rodríguez, G., Correa, A. M., Zapata, G., & Arango, M. I. (2017a). *Catálogo Monzogranito de La Corcova, cordillera*

- Oriental, departamento de Santander*. Servicio Geológico Colombiano.
- Rodríguez, G., Correa, A. M., Arango, M. I., Zapata, G., & Bermúdez, J. G. (2020). *Catálogos de las unidades litoestratigráficas de Colombia: Macizo de Santander* (Vol. 1). Servicio Geológico Colombiano. <https://doi.org/10.32685/9789585279445>
- Rodríguez, G., Correa, A. M., Zapata, G., Arango, M. I., Obando-Erazo, G., Zapata-Villada, J. P., & Bermúdez, J. G. (2020a). Diverse Jurassic magmatic arcs of the Colombian Andes: Constraints from petrography, geochronology and geochemistry. In J. Gómez, & A. O. Pinilla Pachón (eds.), *The Geology of Colombia* (vol. 2, pp. 117-170). Publicaciones Geológicas Especiales 36. Servicio Geológico Colombiano. <https://doi.org/10.32685/pub.esp.36.2019.04>
- Rubatto, D. (2002). Zircon trace element geochemistry: Partitioning with garnet and the link between U-Pb ages and metamorphism. *Chemical Geology*, 184(1-2), 123-138. [https://doi.org/10.1016/S0009-2541\(01\)00355-2](https://doi.org/10.1016/S0009-2541(01)00355-2)
- Shand, S. J. (1943). *Eruptive rocks: Their genesis, composition, classification, and their relation to ore-deposits with a chapter on meteorite*. John Wiley & Sons.
- Sláma, J., Košler, J., Condon, D. J., Crowley, J. L., Gerdes, A., Hanchar, J. M., Horstwood, M. S. A., Morris, G. A., Nasdala, L., Norberg, N., Schaltegger, U., Schoene, B., Tubrett, M. N., & Whitehouse, M. J. (2008). Plešovice zircon - A new natural reference material for U-Pb and Hf isotopic microanalysis. *Chemical Geology*, 249(1-2), 1-35. <https://doi.org/10.1016/j.chemgeo.2007.11.005>
- Solari, L., Gómez Tuena, A., Bernal, J., Pérez Arvizu, O., & Tanner, M. (2010). U-Pb zircon geochronology with an integrated LA-ICP-MS microanalytical workstation: Achievements in precision and accuracy. *Geostandards and Geoanalytical Research*, 34(1), 5-18. <https://doi.org/10.1111/j.1751-908X.2009.00027.x>
- Stacey, J. S., & Kramers, J. D. (1975). Approximation of terrestrial lead isotope evolution by a two-stage model. *Earth and Planetary Science Letters*, 26(2), 207-221. [https://doi.org/10.1016/0012-821X\(75\)90088-6](https://doi.org/10.1016/0012-821X(75)90088-6)
- Schmid, R., Fettes, D., Harte, B. N., Davis, E. A., Desmons, J. (2007). How to name a metamorphic rock. Recommendations by the IUGS Subcommittee on the Systematics of Metamorphic Rocks: Web version 01/02/07. <http://www.bgs.ac.uk/SCMR>
- Streckeisen, A. (1978). IUGS Subcommittee on the Systematics of Igneous Rocks: Classification and nomenclature of volcanic rocks, lamprophyres, carbonatites and melilitic rocks; recommendation and suggestions. *Neues Jahrbuch für Mineralogie - Abhandlungen*, 134, 1-14.
- Tang, M., Rudnick, R., McDonough W., Gaschnig R., & Huang, Y. (2015). Europium anomalies constrain the mass of recycled lower continental crust. *Geology*, 43(8), 703-706. <https://doi.org/10.1130/G36641.1>
- Taylor, S. R., & McLennan, S. M. (1995). The geochemical evolution of the continental crust. *Reviews of Geophysics*, 33(2), 241-265. <https://doi.org/10.1029/95RG00262>
- Tazzo, D., Weber, B., González-Guzmán, R., Valencia, V., Frei, D., Schaaf, P., & Solari, L. (2018). Multiple metamorphic events in the Palaeozoic Mérida Andes basement, Venezuela: insights from U-Pb geochronology and Hf-Nd isotope systematics. *International Geology Review*, 61(13), 1557-1593. <https://doi.org/10.1080/00206814.2018.1522520>
- Ulloa, C., & Rodríguez, G. I. (1982). *Intrusivos ácidos Ordovícicos y post - Devónicos en la Floresta (Boyacá)*. VI Congreso Colombiano de Geología, Cali.
- Ulloa, C., Guerra, A., & Escovar, R. (1998). *Geología de la Plancha 172 Paz de Río. Escala 1:100.000* [Map]. Ingeominas.
- Van der Lelij, R. (2013). *Reconstructing North-Western Gondwana with implications for the evolution of the Iapetus and Rheic Oceans: A geochronological, thermochronological and geochemical study* [Ph.D. Thesis]. Université de Genève.
- Van der Lelij, R., Spikings, R., Ulianov, A., Chiaradia, M., & Mora, A. (2016). Palaeozoic to Early Jurassic history of the Northwestern corner of Gondwana, and implications for the evolution of the Iapetus, Rheic and Pacific Oceans. *Gondwana Research*, 31, 271-294. <https://doi.org/10.1016/j.gr.2015.01.011>
- Vargas, R., Arias, A., Jaramillo, L., & Téllez, N. (1976). *Geología de la plancha 136, Málaga. Escala: 1:100.000* [Map]. Ingeominas.
- Vargas, R., Arias, A., Jaramillo, L., & Téllez, N. (1981). *Geología de las planchas 136-Málaga y 152-Soatá, cuadrángulo I-13. Escala 1:100.000. Boletín Geológico*, 24(3).
- Vargas, R., Arias, A., Jaramillo, L., & Téllez, N. (1987). *Geología de la Planchas 152 Soatá. Escala 1:100.000* [Map, version 2009]. Ingeominas.
- Ward, D. E., Goldsmith, R., Jimeno, A., Cruz, J., Restrepo, H., & Gómez, E. (1973). *Cuadrángulo H-12, Bucaramanga. Planchas 109, Rionegro, y 120, Bucaramanga. Cuadrángulo H-13, Pamplona. Planchas 110, Pamplona, y 121, Cerrito. Escala 1:100.000. Boletín Geológico*, 21(1-3).

- Watson, E. B., & Harrison, T. M. (1983). Zircon saturation revisited: temperature and composition effects in a variety of crustal magma types. *Earth and Planetary Science Letters*, 64(2), 295-304. [https://doi.org/10.1016/0012-821X\(83\)90211-X](https://doi.org/10.1016/0012-821X(83)90211-X)
- Wiedenbeck, M., Allé, P., Corfu, F., Griffin, W. L., Meier, M., Oberli, F., Von Quadt, A., Roddick, J. C., & Spiegel, W. (1995). Three natural zircon standards for U-Th-Pb, Lu-Hf, trace element and REE analyses. *Geostandards Newsletter*, 19(1), 1-23. <https://doi.org/10.1111/j.1751-908X.1995.tb00147.x>
- Wiedenbeck, M., Hancher, J. M., Peck, W. H., Sylvester, P., Valley, J., Whitehouse, M., & Zheng, Y. F. (2004). Further characterisation of the 91500 zircon crystal. *Geostandards and Geoanalytical Research*, 28(1), 9-39. <https://doi.org/10.1111/j.1751-908X.2004.tb01041.x>
- Winchester, J. A., & Floyd, P. A. (1977). Geochemical discrimination of different magma series and their differentiation products using immobile elements. *Chemical Geology*, 20, 325-343. [https://doi.org/10.1016/0009-2541\(77\)90057-2](https://doi.org/10.1016/0009-2541(77)90057-2)
- Zapata, G. Correa, A. M., Rodríguez, G., & Arango, M. I. (2017). *Monzogranito de Santa Rosita, cordillera Oriental, departamentos de Santander y Boyacá*. Servicio Geológico Colombiano.
- Zuluaga, C. A., Amaya S., Uruña, C., & Bernet, M. (2017). Migmatization and low-pressure overprinting metamorphism as record of two pre-Cretaceous tectonic episodes in the Santander Massif of the Andean basement in northern Colombia (NW South America). *Lithos*, 274-275, 123-146. <https://doi.org/10.1016/j.lithos.2016.12.036>



Cañón del río Páez a través de Cuarzomonzodiorita de Páez y del Granito de La Plata  
Fotografía de Gabriel Rodríguez



This work is distributed under the Creative Commons Attribution 4.0 License.

Received: May 15, 2020

Revision received: October 3, 2021

Accepted: October 27, 2021

Published online: January 24, 2022

## Research article

# Determination of a potentially optimal zone to perform hydraulic fracturing work, Upper Magdalena Valley basin, Colombia

Determinación de una zona potencialmente óptima para realizar trabajos de fracturamiento hidráulico, Valle Superior del Magdalena, Colombia

Carlos Fabián Sánchez<sup>1</sup>, Indira Molina<sup>2</sup>, Gabriel Ángel Molina<sup>3</sup>

<sup>1</sup> Universidad de los Andes, Bogotá, Colombia

<sup>2</sup> Universidad de los Andes, Bogotá, Colombia. Now at Servicio Geológico Colombiano, Bogotá, Colombia, [cmolinap@sgc.gov.co](mailto:cmolinap@sgc.gov.co)

<sup>3</sup> Consultant, Bogotá, Colombia

**Corresponding author:** Carlos Fabián Sánchez, [cf.sanchez@uniandes.edu.co](mailto:cf.sanchez@uniandes.edu.co)

## ABSTRACT

The present study was carried out for an oil field located in the upper Magdalena Valley basin, Colombia, in which successful hydraulic fracturing was carried out in a well, which we denote *fractured*. The main objective is to replicate this technique in an existing well in the same field. For this work, electrical logs from twelve wells, including the fractured well, were analyzed to obtain a correlation between the area of interest, located in the Monserrate Formation, and each of the wells under study. By using *gamma ray*, resistivity, neutron and density logs, the petrophysical properties were calculated to determine the shale volume, effective porosity, total porosity, water saturation and permeability in each well. Additionally, the production history of each of the wells and the calculations described above were used to suggest a new site where hydraulic fracturing could also be successful. Two candidates were proposed in this study, one based on the similarity of its petrophysical properties, and another based on the consideration of additional production data. Notably, this well stimulation technique has global importance and has produced positive impacts on increased oil production where it has been implemented. The purpose of this study is to provide technical support for the decision to replicate this procedure in a new area of the field.

**Keywords:** Hydraulic fracturing, petrophysics, electrical logs, correlation.

## RESUMEN

El presente estudio fue realizado para un campo petrolero ubicado en la cuenca del valle superior del Magdalena, Colombia, en el cual se realizaron trabajos exitosos de fracturamiento hidráulico en un pozo, al cual denominaremos *fracturado*. Como objetivo principal, se busca replicar esta técnica en un nuevo pozo ya existente en el mismo campo. Para el desarrollo de este trabajo se analizaron los registros eléctricos provenientes de doce pozos, incluyendo el fracturado, con el fin de obtener una correlación de la zona de interés,

ubicada en la Formación Monserrate, con cada uno de los pozos en estudio. Gracias a los registros de *gamma ray*, resistividad, neutrón y densidad, se realizaron los cálculos de las propiedades petrofísicas, determinándose los volúmenes de shale, las porosidades efectiva y total, las saturaciones de agua y la permeabilidad en cada pozo. Adicionalmente, se utilizó la historia de producción de cada uno de los pozos, y los cálculos explicados anteriormente para sugerir un nuevo sitio donde el fracturamiento hidráulico podría ser exitoso también. Dos candidatos fueron propuestos en este estudio, uno a partir de la similitud en sus propiedades petrofísicas y otro integrando datos adicionales de producción. Cabe destacar la importancia que ha tenido esta técnica de estimulación de pozos a nivel mundial y su impacto positivo en el incremento en la producción de petróleo donde se ha implementado. La finalidad de este estudio radica en soportar, con argumentos técnicos, la decisión de replicar este procedimiento en una nueva zona del campo.

**Palabras clave:** Fracturamiento hidráulico, petrofísica, registros eléctricos, correlación.

### 1. INTRODUCTION

Hydraulic fracturing is a well stimulation technique used in the oil industry to increase production. It consists of injecting, at a certain depth, a mixture of fluids at high pressure, composed mostly of water (usually more than 95% of the mixture) and, to a lesser extent, chemicals and proppants that are responsible for keeping fractures open at the end of the procedure

(Rutqvist, 2000). This injection method is applied mainly in low-permeability rocks since generating fractures via stimulation can increase the area of rock in contact with high-permeability channels and thus increase the production of the well (Atkinson, 2015). This technique was used for the first time in the United States in 1948 (Hubbert and Willis, 1957). Since the beginning of the new millennium, a derivative of this technique known as *fracking* began to be applied in unconventional

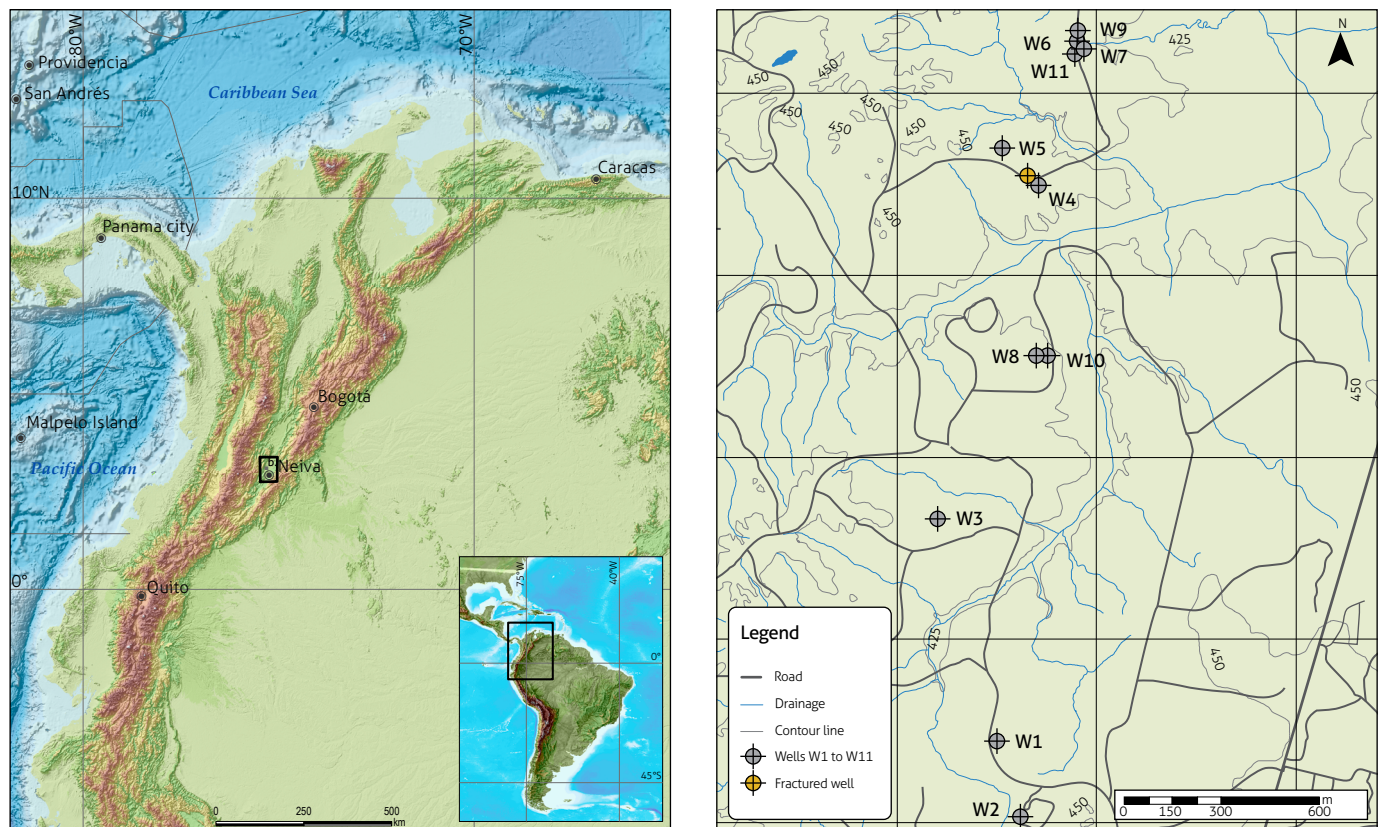


Figure 1. a) General location of the area. b) Distribution of wells in the field of the Upper Magdalena Valley basin, Colombia

deposits. These deposits correspond to formations of very low permeability that are rich in organic matter and are utilized with an extraction method that requires greater complexity and investment than conventional production techniques. In the case of fracking, horizontal wells are drilled, and stimulation is performed in a multistage manner on a larger scale, different from the procedure performed in this work, which consisted of the stimulation of an approximately vertical well.

The study area is located in the upper Magdalena Valley basin (Figure 1), which is one of the most important oil sources in Colombia, with three of the main reservoirs in the Honda, Caballos and Monserrate formations (Kairuz *et al.*, 2000). The formation under study is Monserrate, mainly composed of sandstones and Cretaceous clays. The fractured well is vertical with slight deviations and an artificial lift system of progressive cavity pumping. This well was stimulated toward the end of 2016 (Figure 2) in three intervals of interest (3775-3780', 3794-3799' and 3811-3816') in the Monserrate Formation. Fracturing was performed to improve the permeability of channels in the formation and increase the production of the well. A total of 903 bbl of fracture fluid was pumped with 39,320 lb of 20/40 carbolite as the proppant. The stimulation effectively increased the productivity of the well, given that by the end of 2016, the well produced approximately 40 barrels of oil per day (BOPD), and after applying the technique, daily production amounts above 100 BOPD were reached, leaving fractures with an average width of 0.04 in and conductivity of 1500 mD\*ft.

The increase in production was reflected immediately after applying hydraulic fracturing. During the first semester of 2017, a decrease in production was observed, which is why maintenance was performed at the wellhead in July of that same year, which again resulted in an increase.

## 2. METHODOLOGY AND DATA

Given that all resources are found in the subsoil, it is not possible to obtain a real view of the structure and properties of the deposit; however, through exploration techniques, structural approximations can be generated, and petrophysical properties can be determined. In this work, well logging data was used; this technique consists of sending active signals and/or capturing passive signals to a formation (Beck, 1981) to obtain its resistivity, natural radioactivity, spontaneous potential, porosity and density. The *gamma ray* tool measures the natural emission of gamma rays by the formation, which is proportional to the presence of

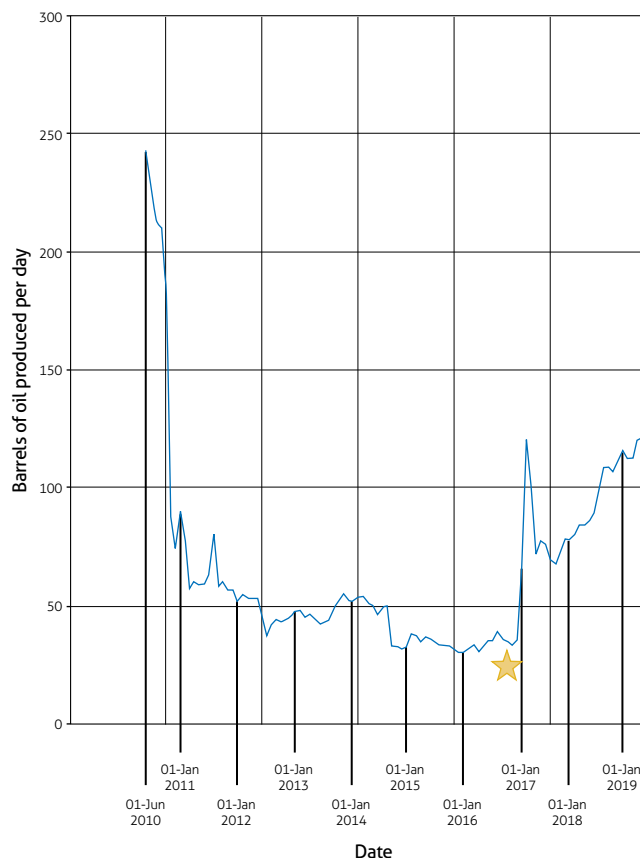


Figure 2. Production history of the fractured well from its inception in 2010 to April 2019

The star indicates the moment when hydraulic fracturing was performed at the end of 2016.

U, Th and K, which are elements associated with the clay content in a formation. The resistivity tool emits electrical currents through the rock to obtain resistivity data, which are related to the type of fluid stored in the pores since high resistivity values correspond to hydrocarbons, and low values correspond to water (Bendeck, 1992). The neutron tool provides an estimate of the porosity of the formation based on the emission of neutrons toward the reservoir, measuring the attenuation by hydrogen as they advance in the medium; the fewer neutrons are detected, the greater the porosity. Finally, the density tool emits gamma rays toward the rock and records how many return to the sensor to estimate the density of the formation (Glover, 2000).

Once the petrophysical properties are obtained, they can be correlated to obtain a spatial mapping. In this work, logs from eleven wells drilled in the Monserrate Formation were used to correlate their properties with those of the fractured

well; further reliance on historical production data and drilled and current well conditions obtained directly from the field in question made it possible to support an operational decision based on technical criteria.

### 2.1. Lithostratigraphic correlation

Due to operational decisions, wells P1 and P2 were not considered for the analysis because they are too old and do not have enough log information. Data processing was performed with Techlog software (Schlumberger, 2017). To obtain the correlation, the gamma ray and formation resistivity logs of the fractured well were used to identify the interval of interest corresponding to the wells drilled where hydraulic fracturing was performed. Once this area of interest was identified, the aforementioned logs from wells P3 to P11 were analyzed to identify the Monserrate Formation in each of them. In most of the wells, resistivity and gamma ray patterns were identified that allowed easy correlation of this formation. However, in wells P10 and P11, there were no similar patterns, so it was necessary to use the drilled well holes as a guide to locate the area of interest.

### 2.2. Petrophysical property calculations

Petrophysical properties reveal the interaction of the rock with the fluids that are stored in it. Using gamma ray, resistivity, neutron and density logs, the following properties were obtained: shale volume, total and effective porosity, water saturation and permeability. Each calculation was performed using the aforementioned Techlog software (Schlumberger, 2017), as will be described below.

#### 2.2.1. Shale volume

Shale is a type of sedimentary rock that has three main attributes: clay minerals that constitute its structure, pore sizes and permeability values on a nanometric scale, and water adsorbed on its surface or between its sheets (Katahara, 2008). In a conventional petroleum system, the shale corresponds to the parent rock, where organic matter is stored and from which hydrocarbons are released, and can sometimes act as a seal, capable of generating an impermeable barrier that prevents the migration of fluids. In addition, shale can occupy the porous spaces of sedimentary rocks such as sandstones and carbonates, and this volume can be calculated from well logs. The most commonly used method for this calculation is the gamma ray technique; however, this method can present limitations when the rock contains clayey minerals that increase and overesti-

mate the value obtained. Therefore, to perform this calculation, the method of Poupon and Gaymard (1970) was chosen, which used neutron porosity and density logs as input parameters. The resulting data was input into Techlog to generate the volume curve of shale, calculated from the following equation:

$$Vsh = \frac{\Phi_{NFL} - \Phi_{DFL}}{\Phi_{NMA} - \Phi_{DMA}} \quad (1)$$

where

$Vsh$  = volume of shale in  $ft^3/ft^3$

$\Phi_{NFL}$  = neutron porosity reading, 100% fluid

$\Phi_{NMA}$  = neutron porosity reading, 100% rock matrix

$\Phi_{DFL}$  = porosity density reading, 100% fluid

$\Phi_{DMA}$  = porosity density reading, 100% rock matrix

The subscripted terms  $\Phi_N$  and  $\Phi_D$  refer to the porosity values recorded by the neutron tool and density tool, respectively.

#### 2.2.2. Effective and total porosity

Porosity is the property of rock that relates its porous or “void” volume ( $V_{porous}$ ) to the total volume ( $V_{total}$ ); that is:

$$\Phi_{total} = \frac{V_{porous}}{V_{total}} \quad (2)$$

Porosity calculations were performed in Techlog from the neutron and density logs and using the generated shale volume curve as follows (Atlas, 1979):

$$\Phi_D = \left( \frac{\rho_b - \rho_{MA}}{\rho_f - \rho_{MA}} \right) \quad (3)$$

where

$\Phi_D$  = porosity density in  $ft^3/ft^3$

$\rho_b$  = apparent density in  $g/cm^3$

$\rho_{MA}$  = density of the matrix (sandstone = 2.65  $g/cm^3$ ; limestone = 2.71  $g/cm^3$ ; dolomite = 2.87  $g/cm^3$ ; anhydrite = 2.90  $g/cm^3$ ; salt = 2.15  $g/cm^3$ )

$\rho_f$  = density of the fluid (by default, a density of 1  $g/cm^3$  is used, associated with sludge filtering)

To obtain all the parameters of Equation 3, Techlog makes the following considerations:

- » If  $\Phi_N \leq \Phi_D$ , a limestone/sandstone combination is chosen
- » If  $\Phi_N > \Phi_D$ , a limestone/dolomite combination is chosen

» If  $\Phi_N > \Phi_D$ ,  $2.91 \leq \rho_b \leq 3.5$  and  $\Phi_E \leq 0.04$ , anhydrite is chosen

where  $\Phi_N$  = neutron porosity, obtained from log data, and  $\Phi_E$  = effective porosity.

Finally, the following equation is used to determine the total porosity (Kamel and Mabrouk, 2003):

$$\Phi_{Total} = \frac{\Phi_N + \Phi_D}{2} \quad (4)$$

By substituting Equation 3 in 4, the total porosity is obtained in terms of density and neutron porosity (Atlas, 1979):

$$\Phi_{Total} = \frac{1}{2} \left[ \Phi_N + \left( \frac{\rho_b - \rho_{MA}}{\rho_f - \rho_{MA}} \right) \right] \quad (5)$$

Equation 5 is then used to calculate the effective porosity ( $\Phi_E$ ) as follows (Tenchov, 1998):

$$\Phi_E = \Phi_{Total} (1 - V_{sh}) = \frac{1}{2} \left[ \Phi_N + \left( \frac{\rho_b - \rho_{MA}}{\rho_f - \rho_{MA}} \right) \right] (1 - V_{sh}) \quad (6)$$

### 2.2.3. Water saturation

Every reservoir stores a significant amount of water, which must be considered when estimating original oil volumes. This water (irreducible or connate) is stored in the formation, occupying porous spaces or stored in clays, and can be estimated from well logs and supported by correlations. Based on the petrophysical properties and lithological configuration of a reservoir, different models have been formulated for the calculation of water saturation. These models may or may not consider the amount of clay present and its distribution in the rock. The Archie model is the most used model globally but does not take into account the amount of clay present in the deposit, while the models of Simandoux (1963) and Schlumberger and Indonesia do. The Simandoux model was established experimentally with artificial sand and clay data, and the Schlumberger model is based on the Simandoux model and is less accurate due to not considering the cementation factor (Pinas and Acosta, 2019). In the present work, the Indonesia model (Equation 7) was used, as proposed by Leveaux and Poupon (1971), which assumes that clay is distributed in the formation in a random or dispersed way. This model, obtained from field data in Indonesia, seems to be the most complete:

$$Sw = \frac{1}{Rt} \left( \frac{\sqrt{aR_w R_{sh}}}{V_{sh} \sqrt{aR_w} + \Phi_{Total}^m \sqrt{R_{sh}}} \right)^{n/2} \quad (7)$$

where

$S_w$  = water saturation, in percentage (%)

$R_i$  = true resistivity of the formation ( $\Omega m$ )

$R_w$  = resistivity of brine water at the formation temperature ( $\Omega m$ )

$R_{sh}$  = average value of deep resistivity measured in shale ( $\Omega m$ )

$a$  = tortuosity factor

$n$  = saturation exponent

$m$  = cementation factor

### 2.2.4. Permeability

Permeability is one of the most important petrophysical properties of a reservoir since it measures the ability of a rock to allow the passage of a fluid through it. The fluid has a certain viscosity depending on the pressure and temperature at which it is found, and this property is also affected by the porosity of the rock, the tortuosity, the radius of the pores and the volume of clay (Ekpoudom et al., 2004).

It is possible to determine the permeability directly from rock cores obtained from the drilling of the well, but when such cores are not available, it is possible to obtain the value using well logs. For this calculation, the model of Coates and Dumanoir (1973) was used, which is based on a correlation of effective porosity and irreducible water saturation to obtain the permeability of the rock (Equation 8).

$$K = k_c * \Phi_E^4 * \left( \frac{1 - S_{wirr}}{S_{wirr}} \right)^2 \quad (8)$$

where

$K$  = permeability in mD

$k_c$  = empirical permeability constant, with a value of 10,000

$S_{wirr}$  = irreducible or connate water saturation, in percentage (%)

The value of  $S_{wirr}$  is obtained by finding the lowest water saturation value in the curve generated with Equation 7, a value that is manually entered in Techlog to perform the permeability calculation with Equation 8.

## 3. RESULTS

### 3.1. Lithostratigraphic correlation

The interval of interest identified for the fractured well corresponds to the zone in which hydraulic fracturing was perfor-

med, between 3775' and 3825'. The Monserrate Formation is identified as a sandstone rock interval with some clay intercalations whose resistivity values are high in areas with stored oil. Thicknesses within this interval were located where the gamma ray and resistivity values in the other wells correspond to the same or approximate values as those found in the fractured well. From these values, the correlation in Figure 3 was obtained, where the gamma ray logs of the wells are shown and the depths are plotted as the "length of the well" or *measured depth* (MD). From this correlation, one can identify that the Monserrate Formation is found at variable depths between 3400 'and 4450' for the wells considered in this study.

### 3.2. Petrophysical properties

Figure 4 shows the log data used and the petrophysical properties calculated for the fractured well. The intervals with drillings in the area of interest (3775-3780', 3794-3799' and 3811-3816') have gamma ray values below 130 gAPI and resistivities above 20 ohm\*m. In addition, in the density and neutron logs, crosslinking is observed in the drilled intervals, indicating lower values in both logs. These data together reflect the presence of hydrocarbons stored in this area. From this information, shale volumes between 0 and 20%, effective porosities close to 16%, irreducible water saturations of 16% and permeabilities of 5 mD were found for the fractured well.

In the same way, the petrophysical properties of each well under study were calculated; Table 1 compares the estimated values for each parameter in the corresponding units.

These values are approximations of the calculations performed in Techlog and interpretation of the logs.

## 4. DISCUSSION

Of the eleven initial wells (P1 to P11), P1 and P2 were discarded because these wells are too old and lack enough data.

From the results obtained, it was possible to identify two possible candidates for hydraulic fracturing: one was identified based on the lithostratigraphic correlation and the comparative petrophysical properties results obtained in Table 1; the second was identified by considering the above criteria together with production information and the drilling intervals in each well.

According to the results obtained in Table 1, the first candidate was well P6, whose petrophysical properties have values very similar to those of the fractured well.

In this case, we did not find the target formation in the well, so it was recommended to proceed with perforations and stimulation in the intervals identified in Figure 5 (4285-4290', 4303-4308' and 4322- 4327' in MD). Thus, stimulation should be performed in 15 ft of the Monserrate Formation located in well P6 at the aforementioned depths; the intent is to proceed

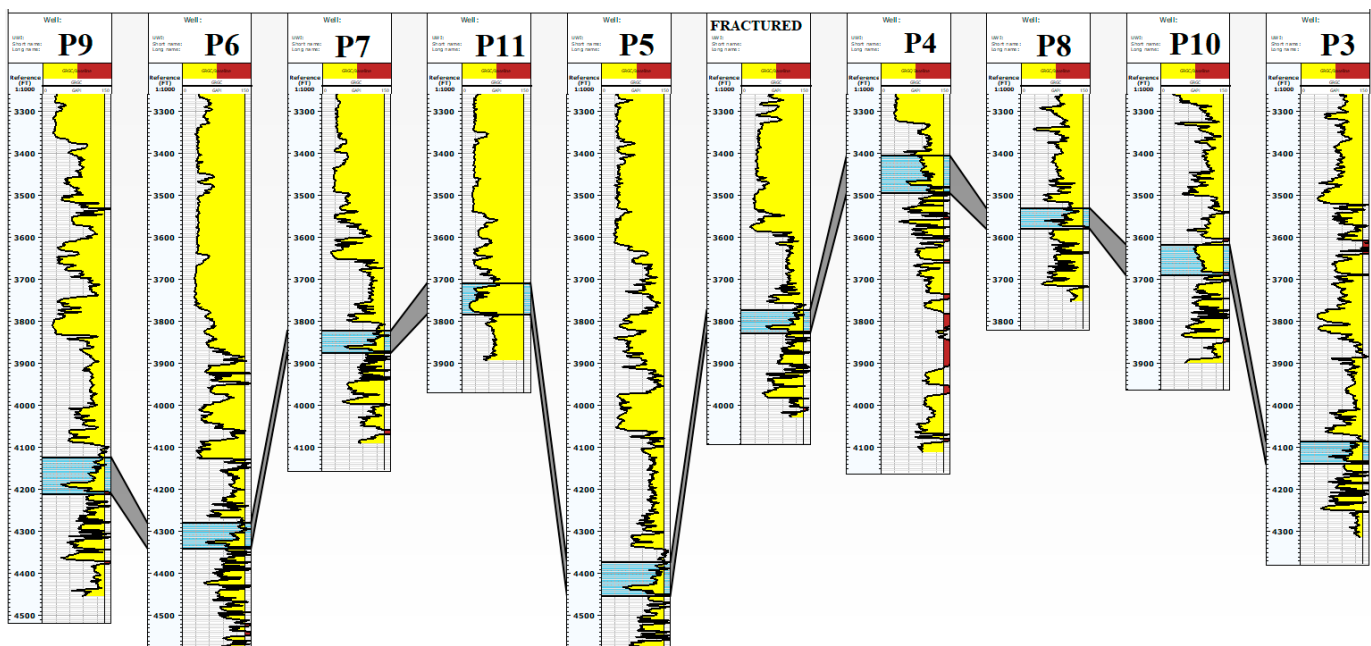


Figure 3. Lithostratigraphic correlation of the area of interest of the fractured well with wells P3 to P11, using gamma ray logs, oriented in the NS direction

Well: Fractured

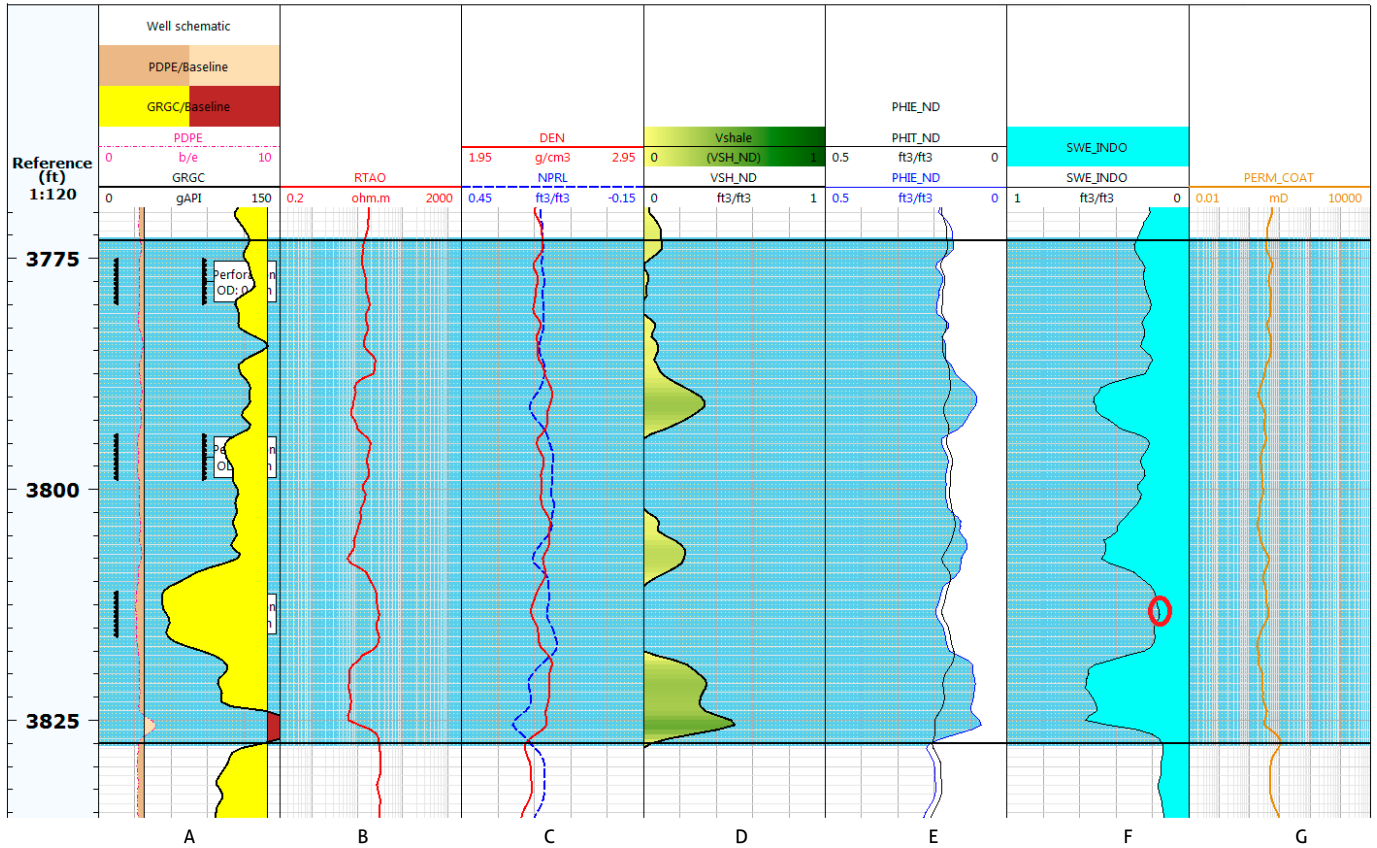


Figure 4. Petrophysical properties of the fractured well

a) gamma ray logs with drilled intervals; b) resistivity logs; c) density logs, in red, and neutron logs, in blue; d) volume of shale (Equation 1); e) total porosity (black, Equation 5) and effective porosity (blue, Equation 6); f) water saturation (Equation 7), where the red circle indicates the value of  $S_{wirr}$ ; g) permeability (Equation 8). Data processed in Techlog.

Table 1. Values obtained for the petrophysical properties of the wells under study, comparing the fractured well with wells P3 to P11

WellID	Gamma ray	Resistivity	Neutron	Density	Shale volume	Total porosity	Effective porosity	$S_{wirr}$	Permeability
	gAPI	Ohm <sup>2</sup> m	ft <sup>3</sup> /ft <sup>3</sup>	g/cm <sup>3</sup>	ft <sup>3</sup> /ft <sup>3</sup>	mD			
Fractured	130	20	0.17	2.37	0.2	0.17	0.16	0.16	5
P3	105	25	0.15	2.4	0.2	0.17	0.16	0.2	3
P4	90	40	0.2	2.25	0.18	0.2	0.17	0.08	45
P5	118	35	0.15	2.45	0.2	0.15	0.12	0.21	1
P6	120	20	0.15	2.45	0.2	0.15	0.12	0.21	1
P7	97	30	0.15	2.3	0.16	0.17	0.15	0.13	10
P8	120	20	0.18	2.4	0.2	0.2	0.14	0.16	8
P9	110	50	0.11	2.47	0.3	0.16	0.09	0.23	1
P10	85	40	0.21	2.22	0.03	0.21	0.2	0.1	80
P11	30	200	0.3	2.05	0.04	0.43	0.42	0.035	6000

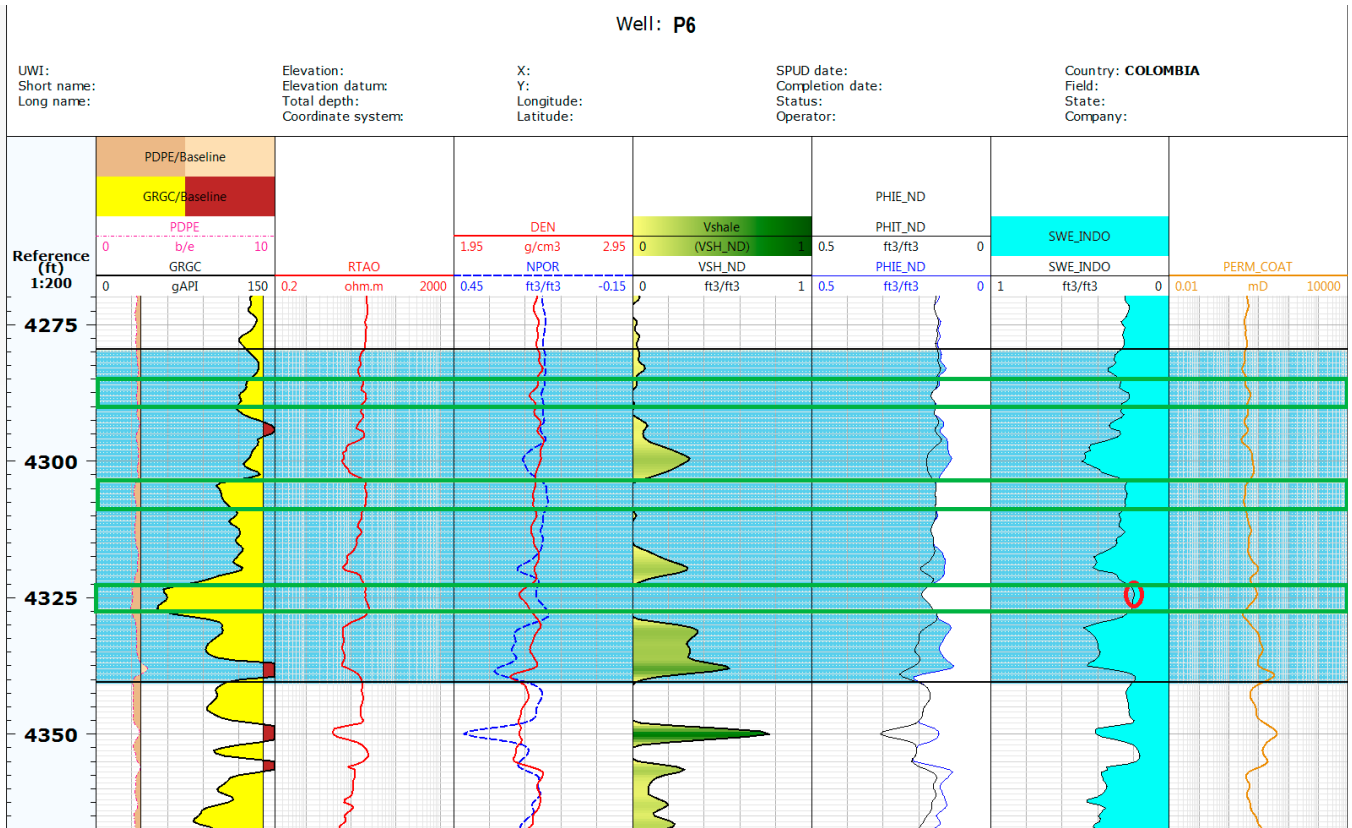


Figure 5. Petrophysical properties of well P6  
 a) Gamma ray logs with perforations intervals; b) resistivity logs; c) density logs, in red, and neutron logs, in blue; d) volume of shale (Equation 1); e) total porosity (black, Equation 5) and effective porosity (blue, Equation 6); f) water saturation (Equation 7), where the red circle indicates the value of  $S_{wirr}$ ; g) permeability (Equation 8). Data processed in Techlog.

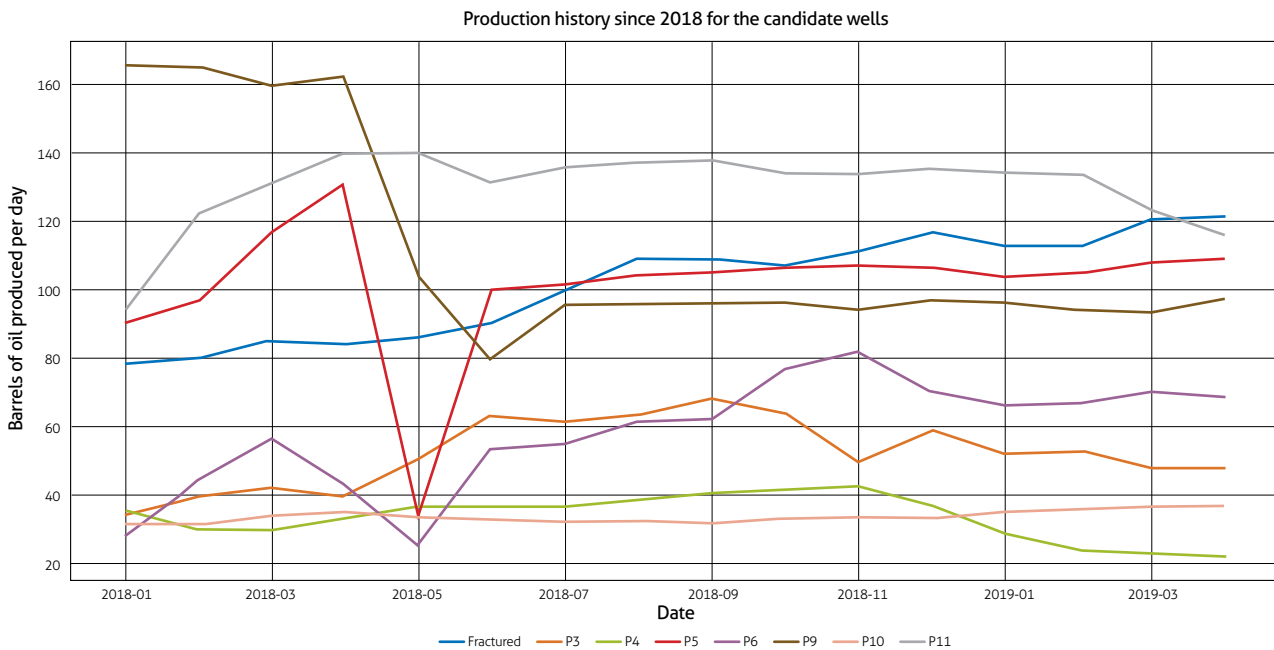


Figure 6. Production histories of the fractured well and wells P3, P4, P5, P6, P9, P10 and P11 in BOPD for 2018 and part of 2019

with a fracturing plan similar to that carried out for the fractured well but by adjusting the volumes of fluid and proppant according to the new depths of the intervals recommended in P6.

However, for the consideration of the second candidate, the following aspects were taken into account:

1. Wells P7 and P8 presented cementing problems; therefore, they were discarded by the operating company.
2. Of the remaining wells (P3, P4, P5, P6, P9, P10 and P11), an analysis of their production curves was performed (Figure 6) to determine their current state. With this information, wells that produce approximately 100 or more BOPD were discarded, that is, P5, P9 and P11. It was decided not to consider these wells because they already had high pro-

duction, so our next analysis focused on wells P3, P4, P6 and P10.

3. For economic reasons, it was decided to discard wells that had no perforations in the correlated area of interest to avoid the need for new perforations in the area for subsequent stimulation. Therefore, wells P3 and P6 were discarded.

4. Finally, among the remaining candidates, the petrophysical properties of P4 and P10 were compared (Figures 7 and 8, respectively) to determine the best well in which to perform hydraulic fracturing. The following was found:
  - From the gamma ray logs (Figure 8a) and the shale volume calculations (Figure 8d), well P10 has cleaner reservoir rock, that is, rock with less clay and more homogeneous delimited thickness (3605-3692.5'), unlike

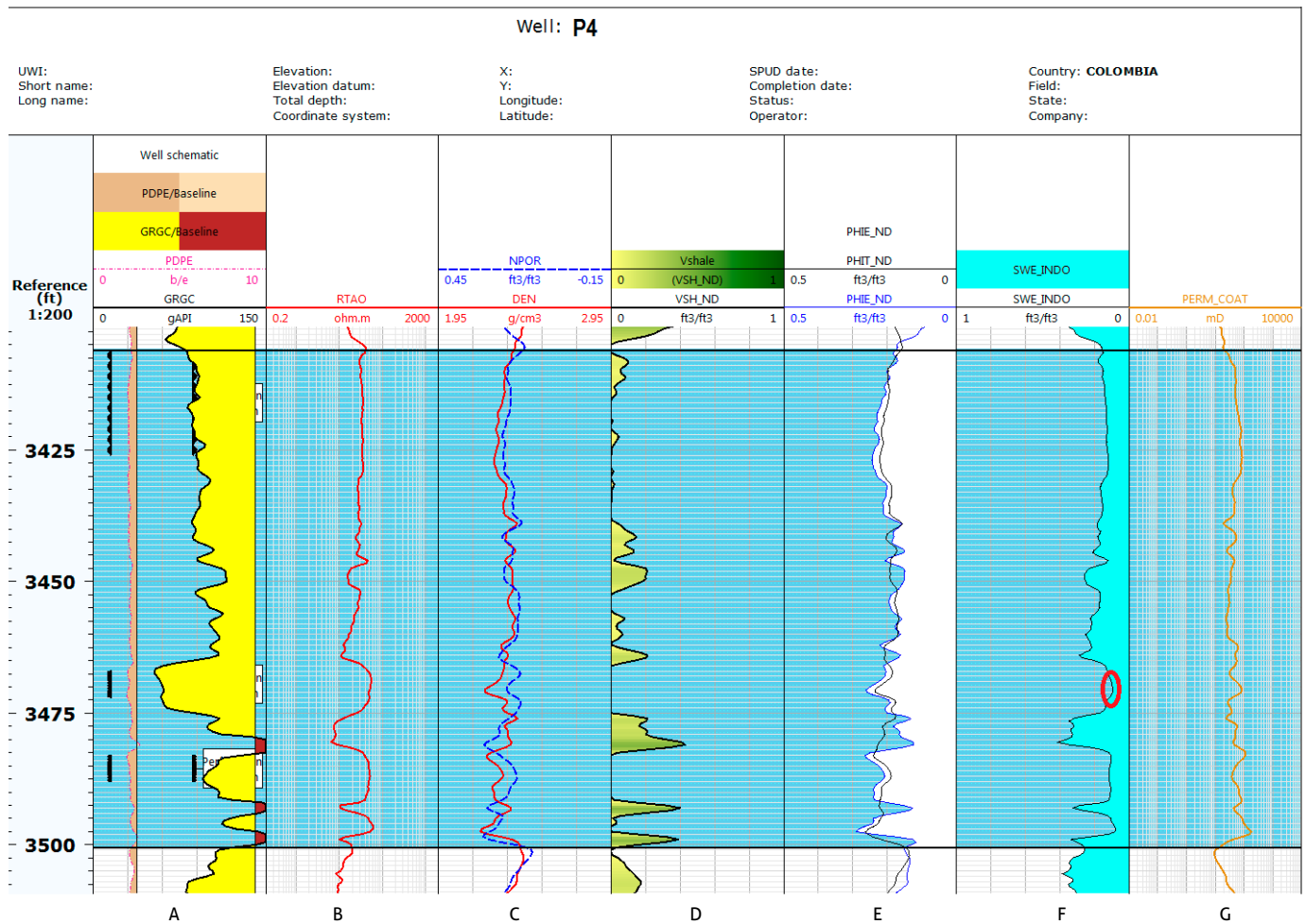


**Figure 7.** Petrophysical properties of well P4  
 a) gamma ray log with perforations intervals; b) resistivity logs; c) density logs, in red, and neutron logs, in blue; d) volume of shale (Equation 1); e) total porosity (black, Equation 5) and effective porosity (blue, Equation 6); f) water saturation (Equation 7), where the red circle indicates the value of  $S_{wirr}$ ; g) permeability (Equation 8). The green boxes show the recommended intervals for hydraulic fracturing. Data processed in Techlog.

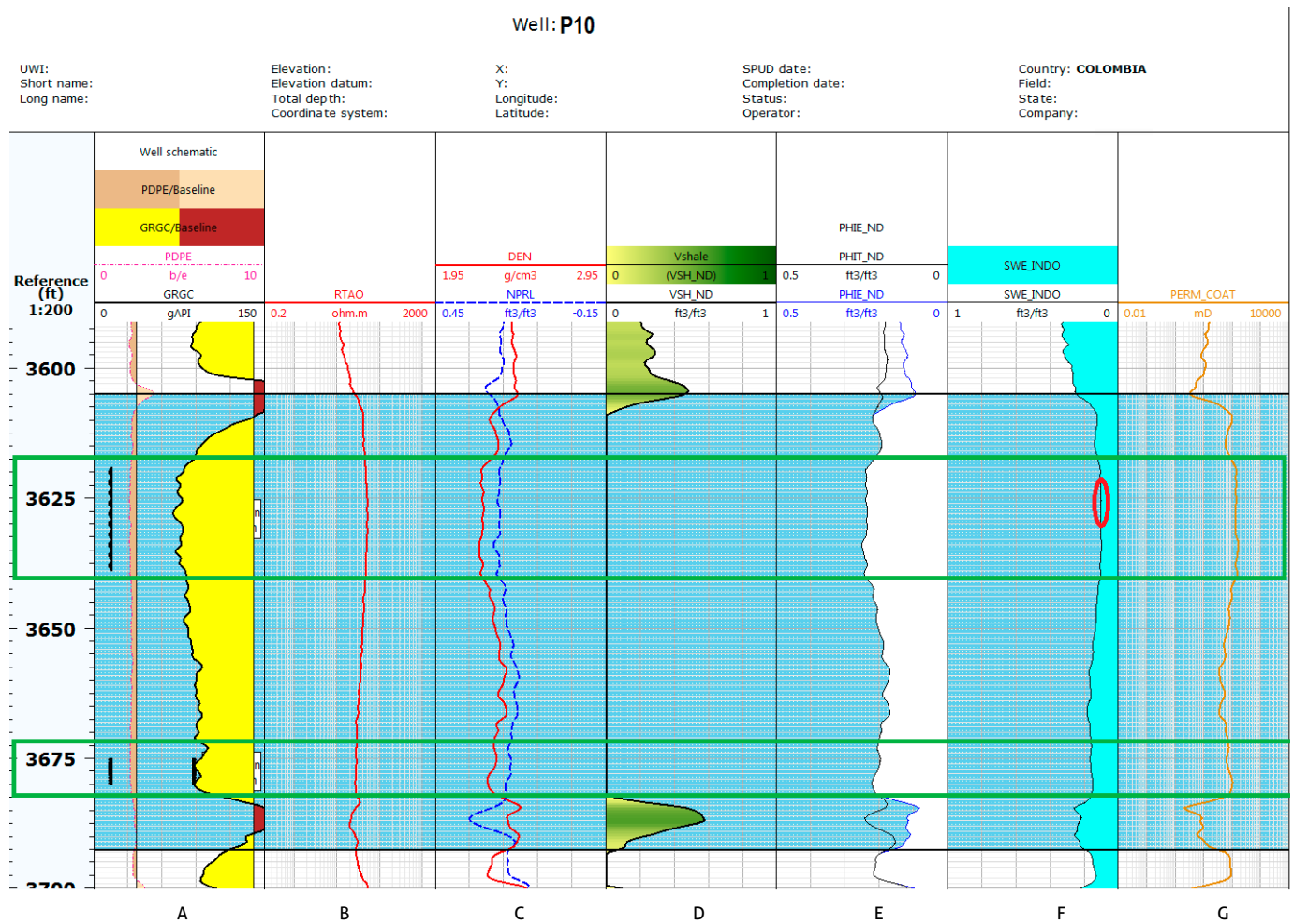


**Figure 8.** Petrophysical properties of well P10  
 a) Gamma ray logs with perforations intervals; b) resistivity logs; c) density logs, in red, and neutron logs, in blue; d) volume of shale (Equation 1); e) total porosity (black, Equation 5) and effective porosity (blue, Equation 6); f) water saturation (Equation 7), where the red circle indicates the value of  $S_{wir}$ ; g) permeability (Equation 8). Data processed in Techlog.

P4 (Figures 7a and 7d), which contains intercalations of clays in its reservoir in the indicated zone (3406-3500’).

- The effective porosity in the perforations (3619-3639’) is slightly higher in well P10 (0.23 ft<sup>3</sup>/ft<sup>3</sup>; Figure 8e) than in well P4 (3406-3426’, with 0.20 ft<sup>3</sup>/ft<sup>3</sup>; Figure 7e).
- The irreducible water saturation value is approximately the same in both wells (0.1 ft<sup>3</sup>/ft<sup>3</sup>). In addition, in the interval of interest of well P10 (3605-3692.5’; Figure 8f), less water saturation is observed in the boreholes than in well P4 (Figure 7f).
- The 20 ft of perforations in well P4 (3406-3426’) have permeability values between 50 and 100 mD (Figure

7g), while those in well P10 (3619-3639’) have values between 100 and 110 mD (Figure 8g).

- According to the resistivity logs and the water saturation curve, depths greater than 3500’ in well P4 have lower resistivity values (Figure 7b) and greater water saturation (Figure 7f) than in well P10 at depths greater than 3690’ (Figures 8b and 8f). Greater water saturation below the area of interest could represent problems due to *basic sediments and water* (BS&W), water coning and/or an increase in production in the future if stimulation is performed in well P4.

Therefore, as a final decision, it was determined that to replicate the successful work in the fractured well and improve the production of the new well, the optimal zone to execute new hydraulic fracturing is in well P10 in the perforations intervals in the Monserrate Formation (i.e., 3619-3639' and 3675-3680' in MD; Figure 8). At the time of this study, well P10 produces an amount of oil approximately equal to that of the fractured well prior to stimulation. Additionally, the values obtained for the petrophysical properties of well P10 are better than those of the fractured well (lower shale volume, greater porosity, greater permeability, and lower water saturation), and the intervals are at a lower depth. Given these findings, we could expect that stimulation in well P10 would produce similar or even better results than those obtained in the fractured well.

## 5. CONCLUSIONS

With the use of gamma ray and resistivity logs, it was possible to correlate the interval of interest of the fractured well (3775-3825') with the other wells under study based on the identification of repeated patterns in these logs.

Based on the petrophysical calculations, production histories and current conditions of each well under study, the optimal zone to perform new hydraulic fracturing was recommended based on technical criteria and updated information.

The first candidate (P6) presents log data and petrophysical properties most similar to those of the fractured well, according to which hydraulic fracturing in the intervals 4285-4290', 4303-4308' and 4322-4327' could be successful.

The optimal zone to perform new stimulation by hydraulic fracturing, considering the economic and historical aspects of production, corresponds to the intervals of 3619-3639' and 3675-3680' in MD for well P10.

A new hydraulic fracturing undertaking would increase productivity, that is, would enable the production of more barrels per dollar spent on the energy required to lift them.

The approach used in this study can be applied to more wells, even in other fields, which would allow the evaluation of different options to increase the production of oil wells through the use of hydraulic fracturing.

## ACKNOWLEDGMENTS

We thank the Department of Geosciences of the Universidad de los Andes, Colombia, and the operating company for authori-

zing the use of relevant information. Additionally, we acknowledge and thank the anonymous reviewers and the editorial team of *Boletín Geológico*, who helped to improve this manuscript.

## REFERENCES

- Atkinson, B. K. (ed.). (2015). *Fracture mechanics of rock*. Academic Press.
- Atlas, D. (1979). *Log interpretation charts*. Dresser Industries, Inc.
- Beck, A. E. (1981). *Physical principles of exploration methods*. Macmillan International Higher Education.
- Bendeck, J. (1992). *Perfiles Eléctricos, una herramienta para la evaluación de yacimientos*. Asociación Colombiana de Geólogos and Geofísicos del Petróleo.
- Coates, G. R., & Dumanoir, J. L. (1973, January). A new approach to improved log-derived permeability. *SPWLA 14th Annual Logging Symposium*. Society of Petrophysicists and Well-Log Analysts.
- Ekpoudom, O., Obe, A., Chike, I., & Onyekonwu, M. (2004). *A case study of permeability modeling and reservoir performance in the absence of core data*. Paper presented at the Nigeria Annual International Conference and Exhibition, Abuja, Nigeria, August 2004. <https://doi.org/10.2118/88964-MS>
- Glover, P. (2000). *Petrophysics MSc course notes*. University of Leeds.
- Hubbert, M. K., & Willis, D. G. (1957). Mechanics of hydraulic fracturing. *AIME, Petroleum Transactions*, 210, 153-168. <https://doi.org/10.2118/686-G>
- Kairuz, E., Ferreira, P., & Silva, O. S. (2000). *Provincia Petrolífera del Valle Superior del Magdalena, Colombia [paper in Spanish] Oil Province of the Upper Magdalena Valley, Colombia*. VII Simposio Bolivariano Exploración Petrolera en las Cuencas Subandinas, Caracas, Sep 10-13, 2000.
- Kamel, M. H., & Mabrouk, W. M. (2003). Estimation of shale volume using a combination of the three porosity logs. *Journal of Petroleum Science and Engineering*, 40(3-4), 145-157. [https://doi.org/10.1016/S0920-4105\(03\)00120-7](https://doi.org/10.1016/S0920-4105(03)00120-7)
- Katahara, K. (2008). What is shale to a petrophysicist? *The Leading Edge*, 27(6), 738-741. <https://doi.org/10.1190/1.2944158>
- Leveaux, J., & Poupon, A. (1971, July 1). Evaluation of water saturation in shaly formations. *The Log Analysts*, 12(04). <https://onepetro.org/petrophysics/article-abstract/171610/Evaluation-Of-Water-Saturation-In-Shaly-Formations>
- Pinas, M., & Acosta, E. R. (2019). Impact of tortuosity and cementation factor in water saturation calculations in heteroge-

- neous sands of the Tambaredjo Field, Guiana Basin, Suriname [preprint]. <https://doi.org/10.13140/RG.2.2.18518.70727>
- Poupon, A., & Gaymard, R. (1970, January). *The evaluation of clay content from logs*. SPWLA 11th Annual Logging Symposium. Society of Petrophysicists and Well-Log Analysts.
- Rutqvist, J., Tsang, C. F., & Stephansson, O. (2000). Uncertainty in the maximum principal stress estimated from hydraulic fracturing measurements due to the presence of the induced fracture. *International Journal of Rock Mechanics and Mining Sciences*, 37(1-2), 107-120. [https://doi.org/10.1016/S1365-1609\(99\)00097-0](https://doi.org/10.1016/S1365-1609(99)00097-0)
- Sánchez, C. (2019). *Determinación de una zona potencialmente óptima para ejecutar trabajos de fracturamiento hidráulico* [Undergraduate thesis]. Universidad de los Andes. <http://hdl.handle.net/1992/45728>
- Schlumberger. (2017). Techlog, versión 2017. [software]. Schlumberger. <https://www.software.slb.com/products/techlog>
- Simandoux, P. (1963). Mesures dielectriques en milieu poreux, application a mesure des saturations en eau: Etude du Comportement des Massifs Argileux. *Revue de l'institut Francais du Petrole, Supplementary Issue*, p. 193-215.
- Tenchov, G. G. (1998). Evaluation of electrical conductivity of shaly sands using the theory of mixtures. *Journal of Petroleum Science and Engineering*, 21(3-4), 263-271. <https://doi.org/10.1016/S0920-4105%2898%2900072-2>



This work is distributed under the Creative Commons Attribution 4.0 License.

Received: September 28, 2020

Revision received: February 9, 2022

Accepted: February 15, 2022

Published online: April 24, 2022

Research article

# Interpretation of Palaeozoic geofoms with the use of seismic attributes in a region of the Eastern Plains, Colombia

Interpretación de geofomas paleozoicas con el uso de atributos sísmicos en una localidad de los Llanos Orientales, Colombia

Laura Carolina Esquivel<sup>1</sup>, Fanny Villamizar<sup>2</sup>, Indira Molina<sup>3</sup>

<sup>1</sup> University of the Andes. Now at Servicio Geológico Colombiano, Bogotá, Colombia.

<sup>2</sup> Servicio Geológico Colombiano, Bogotá, Colombia.

<sup>3</sup> University of the Andes. Now at Servicio Geológico Colombiano, Bogotá, Colombia.

**Corresponding author:** Laura Carolina Esquivel, [lc.esquivel10@uniandes.edu.co](mailto:lc.esquivel10@uniandes.edu.co)

## ABSTRACT

This study focused on producing maps of Palaeozoic geofoms in the subsoil of a region of the Eastern Planes basin, Colombia. The results provide novel Palaeozoic information for the study area suggesting a possible shallow marine depositional environment in the Ordovician and a slightly deeper shallow marine environment in the Cambrian. This information was obtained from the analysis of both seism stratigraphic sequences and gamma ray well logs and from the seismic interpretation of possible geological structures at depth, using a seismic cube, four 2D seismic lines and four wells. The results were complemented with the application of the seismic attributes of coherence, variance, RMS amplitude and spectral decomposition to highlight geological characteristics such as structures and lithology. The information was integrated and analyzed to generate maps of geofoms corresponding to the Middle Ordovician, Lower Ordovician and Cambrian sequences.

**Keywords:** Eastern Plains basin, seismic, well logs, seismic attributes, Palaeozoic geofoms.

## RESUMEN

Este estudio se enfocó en producir mapas de geofomas paleozoicas en el subsuelo de una región de la cuenca de los Llanos Orientales de Colombia. Aportó resultados innovadores del Paleozoico para el área de estudio que sugieren un posible ambiente deposicional marino somero para el Ordovícico, y un ambiente marino somero ligeramente más profundo para el Cámbrico. Esto se obtuvo de los análisis tanto de secuencias sismoestratigráficas como de registro de pozo gamma ray, y de la interpretación sísmica de posibles estructuras geológicas en profundidad, la cual se realizó mediante el uso de un cubo sísmico, cuatro líneas sísmicas 2D y cuatro pozos. Estos resultados se complementaron con la aplicación de los atributos sísmicos de coherencia, varianza, amplitud RMS y descomposición espectral para resaltar características geológicas como estructuras y litología, con el fin

de integrar al análisis de la información y generar mapas de geoformas correspondientes a las secuencias Ordovícico medio, Ordovícico inferior y Cámbrico.

**Palabras clave:** cuenca de los Llanos Orientales, sísmica, registros de pozo, atributos sísmicos, geoformas paleozoicas.

## 1. INTRODUCTION

Seismic exploration is a geophysical method that consists in generating elastic waves that propagate and reflect in a medium to determine the shape, composition and distribution of different lithological units at various depths (Telford et al., 1990).

This method has become an indispensable tool for obtaining information from the subsoil. In the Eastern Plains of Colombia, the high density of information concerning the Cenozoic and Mesozoic area collected by the ANH [Agencia Nacional de Hidrocarburos] and the Universidad Nacional de Colombia is due to the hydrocarbon potential in the Eastern Plains of Colombia (Villamizar and Castillo, 2016).

Nevertheless, the Palaeozoic era has been little studied in Colombia (Suárez and Solano, 2012). Among the most relevant work is that of Martínez-González (2008), in which the characterization of different geological events of the sub-Andean basins in the Palaeozoic stands out. This project aims to contribute to these studies with different analyses of the geophysical information found (through 2D-3D seismic and well logs) in a region located southeast of the Eastern Plains basin (Figure 1). This was possible particularly because the seismic data used for this project were reprocessed to highlight elements of Palaeozoic formations in the deepest section; however, it is important to mention that the decrease in seismic resolution at greater depths made it difficult to interpret the different geological elements in detail.

This study was developed based on the interpretation of geological structures in a seismic cube, which was assessed by seismostratigraphic, electrofacial (Schlumberger, 1981) and sequential analyses of wells in the Palaeozoic section. Finally, the seismic attributes of coherence, spectral decomposition, variance and RMS amplitude were integrated into the seismic interpretation of structures (Brown, 1996), stratigraphies and lithologies (Chopra and Marfurt, 2007). As a result, the evaluation, integration and analysis allowed the generation of geoform maps with geological information on the sedimentation environments in the study area (Esquivel, 2020). Interpretations were performed for the Palaeozoic sequences

corresponding to the Middle Ordovician, Lower Ordovician and Cambrian periods.

## 2. GEOLOGICAL FRAMEWORK

The Eastern Plains basin a low relief region located to the east of the Eastern Cordillera. It is characterized as a foreland due to its geometry and is limited by the Guaicáramo fault system to the west and by the Guyana Shield to the east.

The formation of the Eastern Plains basin results from different tectonic and sedimentary processes throughout geological time. At the beginning of the Palaeozoic, in the Cambrian period, a divergent passive margin contributed to the formation of an epicontinental basin. Due to the normal faults gene-

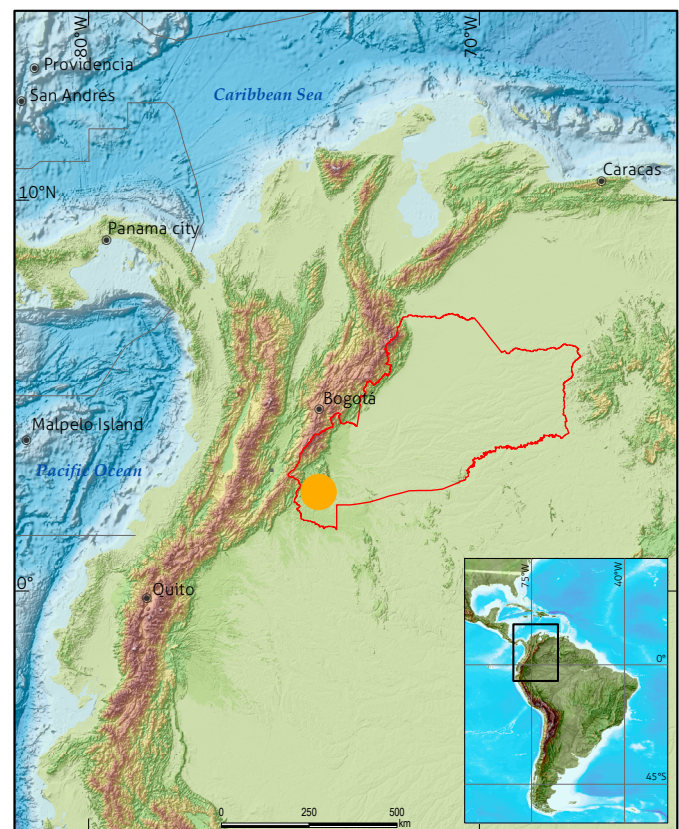


Figure 1. Location of the study area in the Eastern Plains basin in Colombia

rated by this event, a partial collapse occurred in which clastic and silicoclastic successions were deposited due to an increase in sea level (Cediel, 2019).

Then, at the beginning of the Ordovician, the *Caparonensis* orogeny was produced due to a retroarch accretion between Laurasia and Gondwana. During this event, high rates of subsidence, land accretions and fault inversions occurred in the previously filled partial collapse. These events caused extensive deposition of transgressive marine sequences, formed by intercalations of shales and sandstones (Cediel, 2019). During the Silurian, the process followed an extensional regime and continued a compressional regime in which the oceans began to close to form Pre-Pangea (Martínez-González, 2008).

At the end of the Devonian and the beginning of the Carboniferous, a marine transgression occurred with claystone, sandstone and limestone sediments. Subsequently, a compressional event occurred due to the *Hercynian* orogeny, which raised the sub-Andean basins and exposed them to erosive events. At the end of the Carboniferous, this same orogeny led to the assembly of Pangea due to the collision of Gondwana with Laurasia (Martínez-González, 2008).

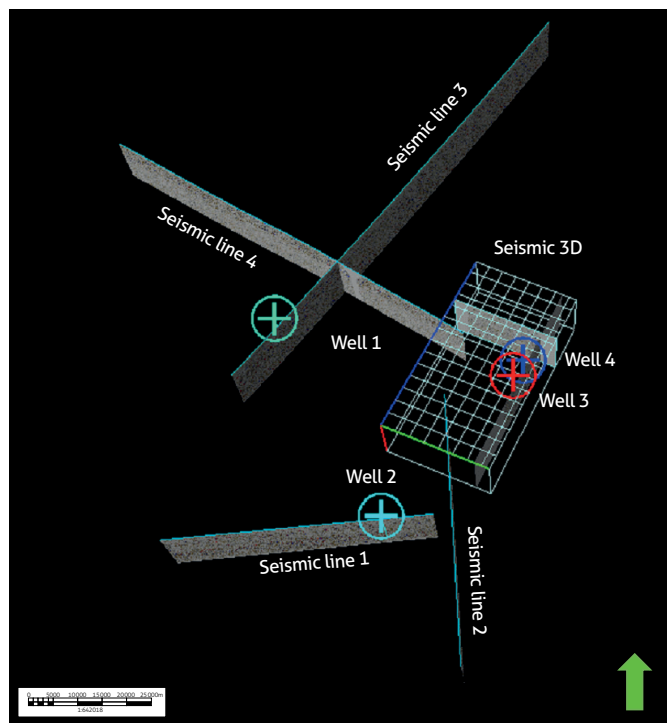


Figure 2. Distribution of 2D, 3D and well seismic information

### 3. DATA AND METHODS

The seismic and geophysical information used for this project was provided by the Colombian Geological Service (SGC) (Figure 2) and consisted of a) a 297 km<sup>2</sup> 3D seismic block with *prestack time migration* (PSTM) seismic processing; b) four seismic lines (35.5 km, 77 km, 60 km and 33 km); and c) four wells with a set of basic records.

The methodology used in the present study was based on the integration of available information. Initially, a bibliographic compilation was carried out on the geology of the study area, focused on stratigraphy (Annex 1) and structural events that affected the Eastern Plains region (Ecopetrol and Beicip, 1995; Lozano and Zamora, 2014; Sarmiento, 2011). Additionally, the information available in the well reports used was analysed.

Subsequently, the geophysical data interpretation software *PETREL*, version 2017, was used to analyse the data provided (Appendix 2). The seismic and well logs were loaded into this software and correlated with synthetic seismograms following the methodology described by Beltrán Jiménez (2015) (Appendix 2.1); the results correlate the seismic lines with the distribution of reported geological formations at depth in the wells with the seismic data. It is important to mention that 2D seismic lines and wells 1 and 2 were used only as control formations near the study area. The methods for analysing this information consisted of the following:

- » Sequence stratigraphy, according to the methodology described by Stuart et al. (2014): Discontinuities and stratigraphic cycles were defined based on the fall and rise of the eustatic curve.
- » Seismo-stratigraphy or stratigraphy, according to the methodology proposed by Vail et al. (1977) and Mitchum et al. (1977): Seismic sequence limits and unconformities were identified.
- » Seismofacies analysis, according to the methodology described by Sangree and Widmier (1977), allowed the generation of AB/C maps.

Finally, the seismic attributes of coherence, spectral decomposition, RMS amplitude and variance were applied to the top of each sequence corresponding to the Palaeozoic (Neidell and Tanner, 1971). The results of these attributes were integrated with the information previously analysed to obtain the distribution of geofoms in the study area.

## 4. RESULTS

### 4.1. Sequence stratigraphy

For the sequential analysis, the GR (gamma ray) and resistive logs were used only from well 3 because it was within the seismic block, and well 4 did not provide information associated with the Palaeozoic. Three demarcated surfaces of maximum flooding (SMF) were identified from the GR log data from well 3; thus, we obtained the information illustrated in Figure 3, which was constructed based on the interpreted data (without including the information found in the Guayabo formation,

which was not taken into account for this study). It is important to mention that sequence B was divided into inferior and superior due to a slight change in treatment from high to low transgressive levels. However, because the interval of interest was in the Palaeozoic, the interpretation corresponding to that marker was performed (Figure 4).

The marker corresponding to the top of the Palaeozoic, well C sequence, has a limit close to 443 Ma and is biostratigraphically dated as belonging to the Ordovician (according to reports from well 3). Under this surface, an event is identified that shows a decrease in the A/S (deposition/sediment) ratio;

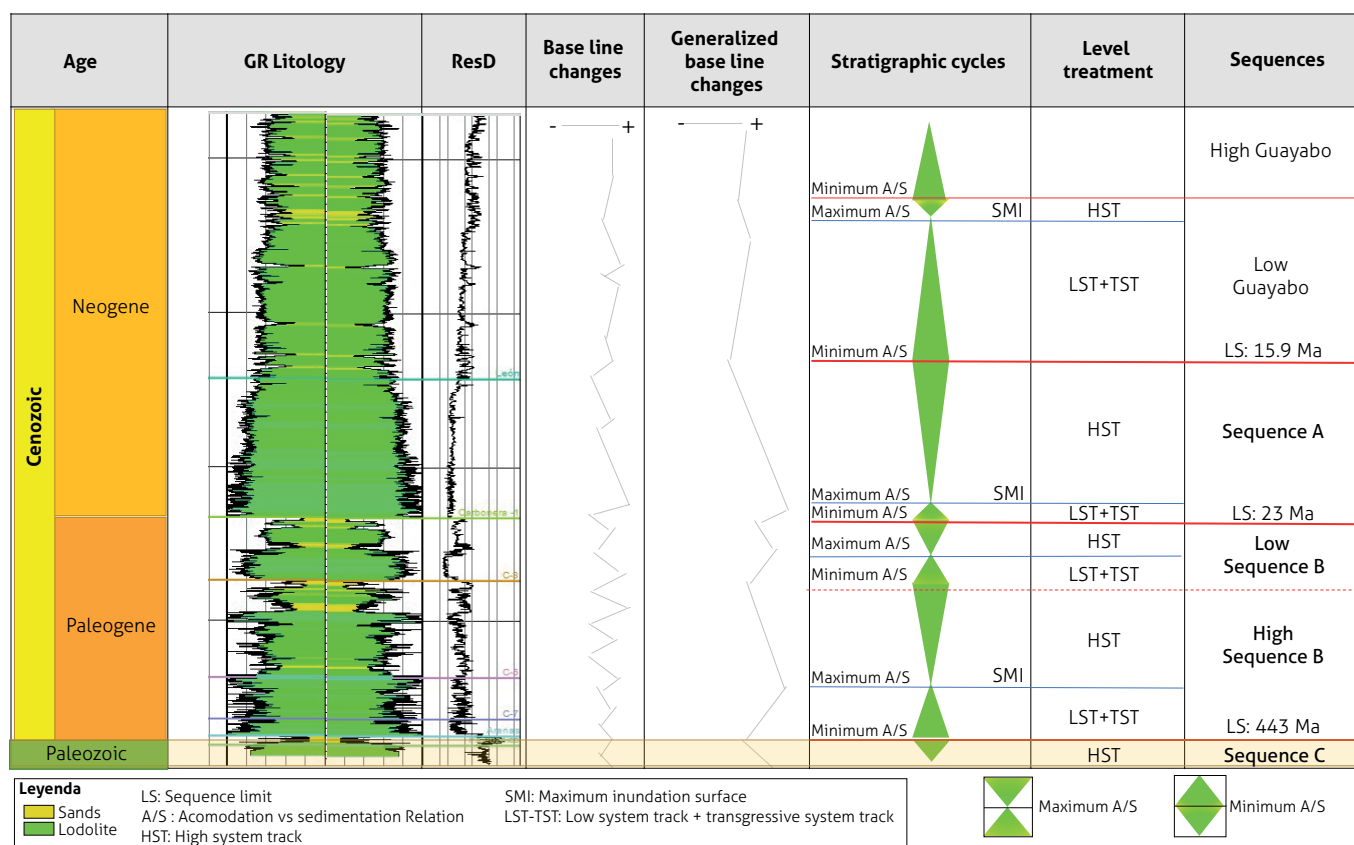


Figure 3. Stratigraphic analysis based on base-level changes for well 3

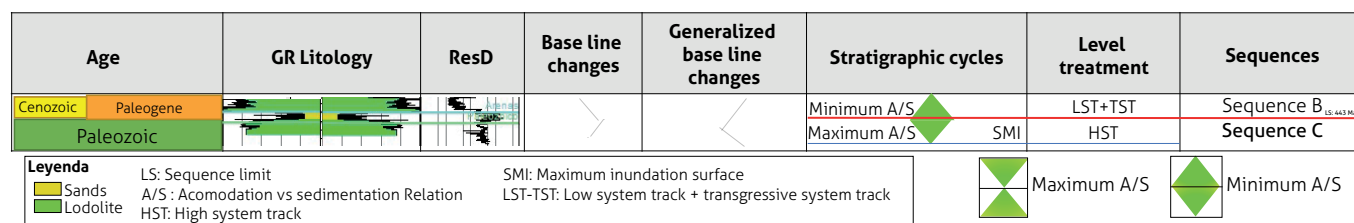


Figure 4. Stratigraphic analysis based on base level changes in the Palaeozoic for well 3

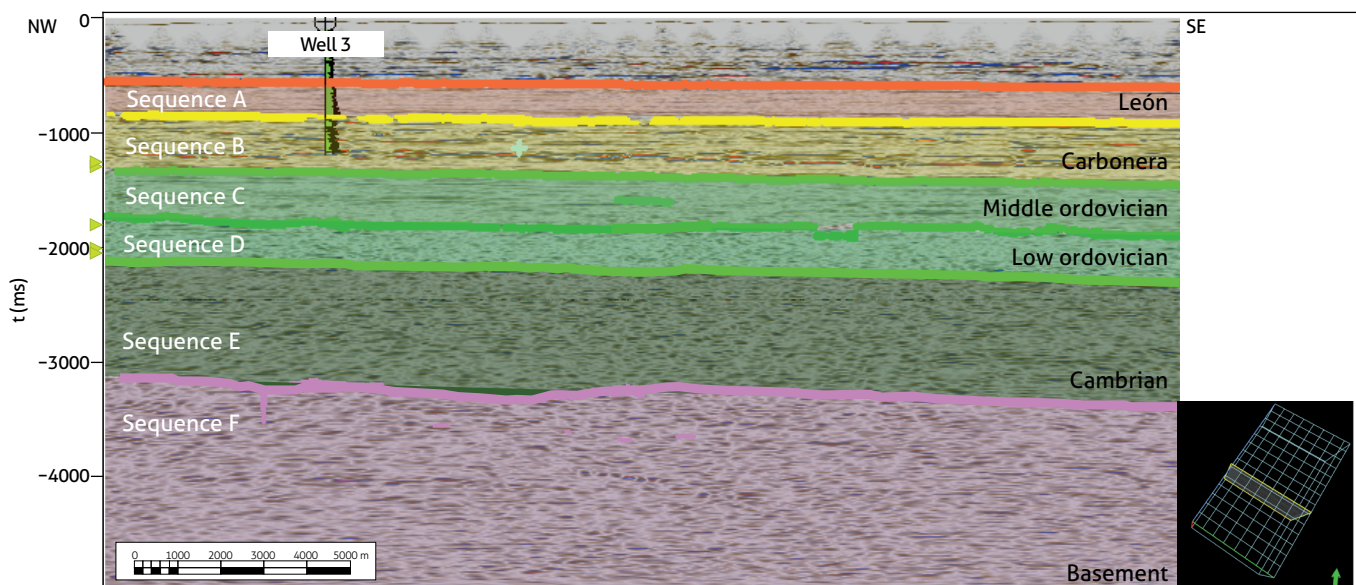


Figure 5. Sequences established for the study area (*Inline: 650*)

the event is limited towards the base, with a surface of maximum flooding, and towards the top, with a surface of unconformity. Figure 4 shows prograding patterns corresponding to a high-level treatment (HST) that according to the electrofacial analysis, is associated mainly with a shallow marine environment. On this marker, an event corresponding to a low-level treatment (LST) is recorded; the event shows retrograde patterns and an increase in the A/S ratio, with the top limited by a surface of maximum flooding, corresponding to a treatment transgressive level (TST).

#### 4.2. Seismo-stratigraphy

Six horizons corresponding to six seismic sequences were identified for the study area, as shown in Figure 5. Of these six sequences, for the Palaeozoic, three seismic sequences corresponding to the Middle Ordovician, Lower Ordovician, and Cambrian were found along with the basement (sequences C, D, E and F,

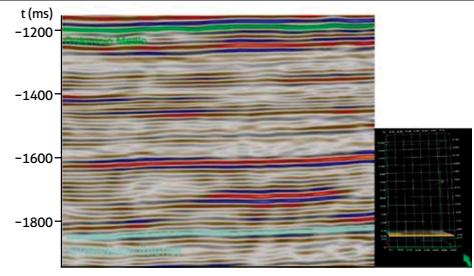
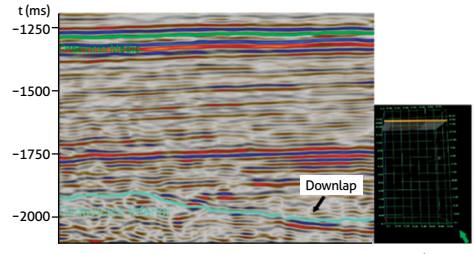
respectively). For the age correlations in the seismic data, the palynological data from the final reports of well 3 (Appendix 3.2.), which were drilled up to the top of sequence C, were used; the lower sequences were defined based on interpretation.

The interpretations of seismic sequences C, D, E and F are shown, organized from youngest to oldest. Different behaviours were found in the reflectors to the north and south of the seismic block; for this reason, detailed descriptions are provided for sequences C, D and E.

##### 4.2.1. Seismic sequence C

Seismic sequence C, presented in Table 1, corresponds to Palaeozoic formations whose base horizon is 470 Ma and whose top is 443 Ma. That is, it corresponds to Medium to Late Ordovician units according to the biostratigraphic dating of well 3. In addition, the thicknesses are preserved throughout the study area.

**Table 1.** Results of the seismic facies analysis for sequence C

Sequence	Seismofacies	Internal configuration	Example
Sequence C	CC/ P to subparallel	The reflectors are parallel, continuous and have moderately high amplitudes and frequencies.	 <p>Seismic facies corresponding to the southern part of the study area (Inline: 72481).</p>
	CD/W	The reflectors are wavy and interrupted with moderate amplitudes and high frequencies.	 <p>Seismic facies corresponding to the northern part of the study area (Inline: 1019251).</p>

C: concordant; D: *downlap*; W: wavy

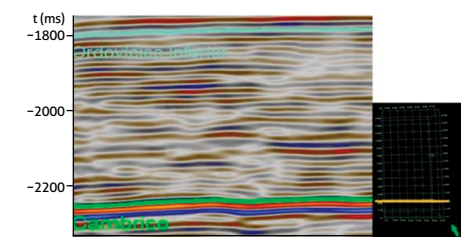
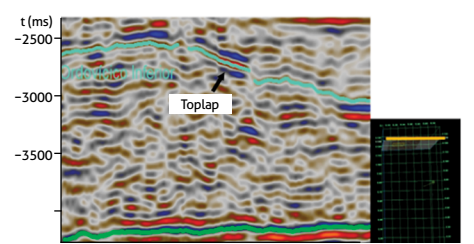
#### 4.2.2. Seismic sequence D

Seismic sequence D, presented in Table 2, was associated with Palaeozoic formations whose base horizon is at 488 Ma and its top at 471 Ma, that is, with Early Ordovician units. The reflectors of this sequence are characterized by preserving thicknesses throughout the seismic block.

#### 4.2.3. Seismic sequence E

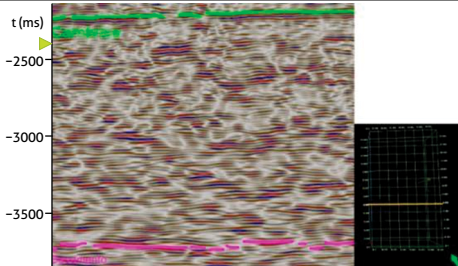
Seismic sequence E, presented in Table 3, was related to Palaeozoic formations whose base horizon is at 542 Ma and top is at 488.3 Ma; that is, to Cambrian units. It presents reflectors with subparallel, wavy, interrupted, contorted and chaotic configurations.

**Table 2.** Results of the seismic facies analysis for sequence D

Sequence	Seismofacies	Internal configuration	Example
Sequence D	CC/P to subparallel	The reflectors are continuous and have moderately strong amplitudes and high frequencies.	 <p>Seismic facies corresponding to the southwestern part of the study area (Inline: 148736).</p>
	Top-C/W	The reflectors have moderately high amplitudes and frequencies, with chaotic and contorted undulations.	 <p>Seismic facies corresponding to the northwestern part of the study area (Inline: 979991).</p>

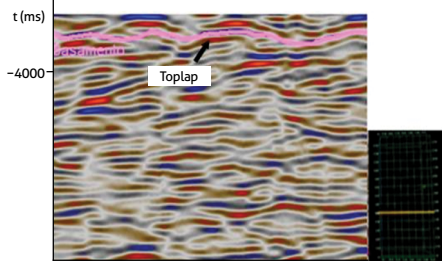
C: concordant; D: *downlap*; W: wavy; Top: *toplap*.

Table 3. Results of the seismic facies analysis for sequence E

Sequence	Seismofacies	Internal configuration	Example
Sequence E	CC/W	The reflectors are presented in a subparallel, contorted and chaotic form with moderately low amplitudes and medium frequencies.	 <p>Seismic facies corresponding to the centre of the study area (Inline: 449226).</p>

C: concordant; W: wavy.

Table 4. Results of the seismic facies analysis for sequence F

Sequence	Seismofacies	Internal configuration	Example
Sequence F	TC/chaotic	The reflectors are presented in a subparallel, chaotic and noncoherent way.	 <p>Seismic facies corresponding to the centre of the study area (Inline: -520951).</p>

#### 4.2.4. Sequence F

Sequence F, presented in Table 4, was related to formations whose top horizon is at 542 Ma and base age is < 542 Ma, i.e., Precambrian units associated with the basement. This sequence presents reflectors with low amplitudes and a chaotic configuration, without continuity and with little coherence. Their endings in the lower part are concordant, and in the upper part, they can be interpreted as truncations.

#### 4.3. Interpretation of faults

The interpretation of faults was performed for the entire seismic block. Figure 6 shows the fault corresponding to *Inline* 650 with simple amplitude processing (ABS), which consists of the calculation of the absolute value of the trace and is used to highlight structural events.

Figure 6 also shows a system of inverse faults, predominant in the Palaeozoic, with some reaching Cenozoic formations. The faults present have dips in the north-western and south-eastern directions and extend to Precambrian ages. For sequence C, these reverse faults predominate in the northern zone of the seismic cube, while in sequences D and E, they are identified towards the central and southern zones of the seismic cube (Annex 3.1.).

#### 4.4. Seismic attributes

The seismic attributes were applied with the objective of knowing the distribution of the stratigraphic and structural elements for the study area (Chen and Sidney, 1997; Tanner, 2001). In general, they allowed the identification of lithologies, channels and faults (Table 5).

These attributes were calculated on the interpreted seismic horizons, which correspond to the caps of seismic sequences C, D and E and can be visualized as maps. The results are shown in Figures 7, 8 and 9.

The RMS coherence and amplitude attributes for this study allowed us to identify stratigraphic elements, lithologies and channels. On the other hand, the attributes of spectral decomposition and variance facilitated the interpretation of some channels, sinuosity and faults only for sequence C, since for deeper sequences, structural elements were not clearly recognized. In this way, a difference in behaviour was recorded between the north-eastern and southwestern zones of the seismic block for sequences C and D; therefore, a distinction was made for these sequences in these zones. The results of these interpretations are presented in Table 5.

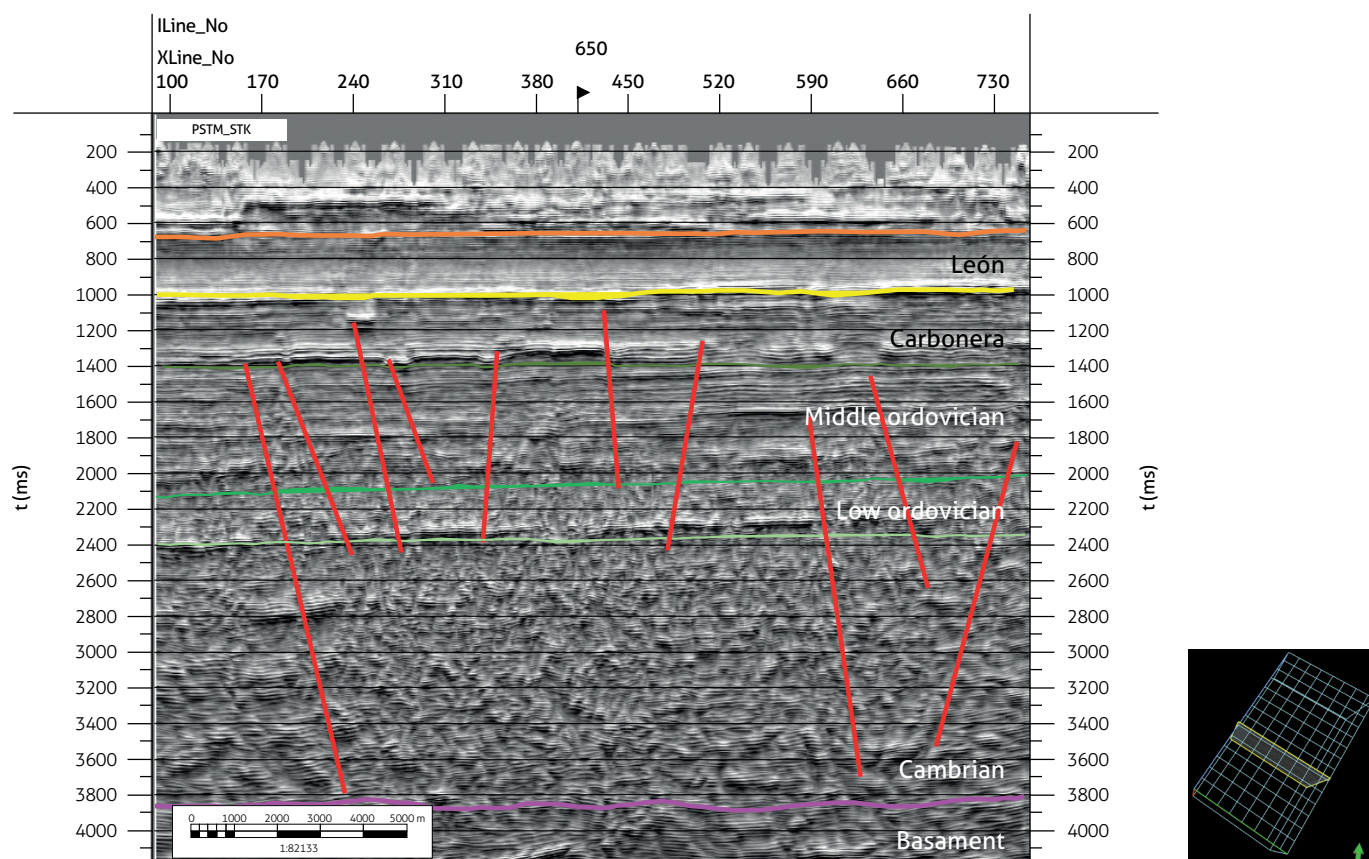


Figure 6. Interpretation of faults (red lines) along Inline 650 of the seismic block

Sequence C

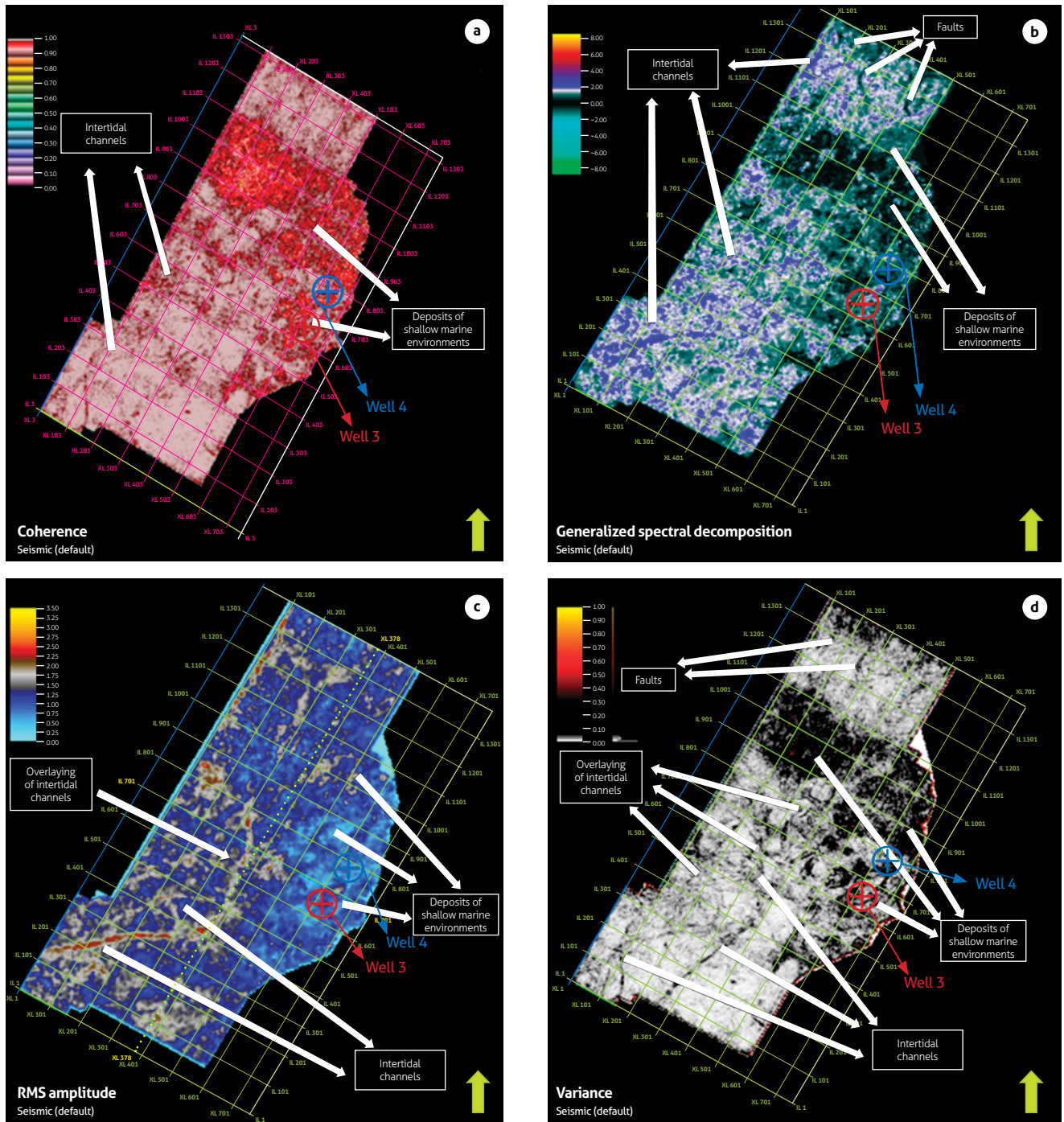


Figure 7. Attributes of a) coherence, b) spectral decomposition, c) RMS amplitude and d) variance for the top of sequence C (Middle Ordovician horizon)

In the lower part of the figure, the wells in the seismic cube are shown. Well 3 provided the biostratigraphic data correspon-

ding to the Palaeozoic, with reference to the seismostratigraphic units of well 1 with Line 1 (left) and well 3 with *Inline 650* (right).

Sequence D

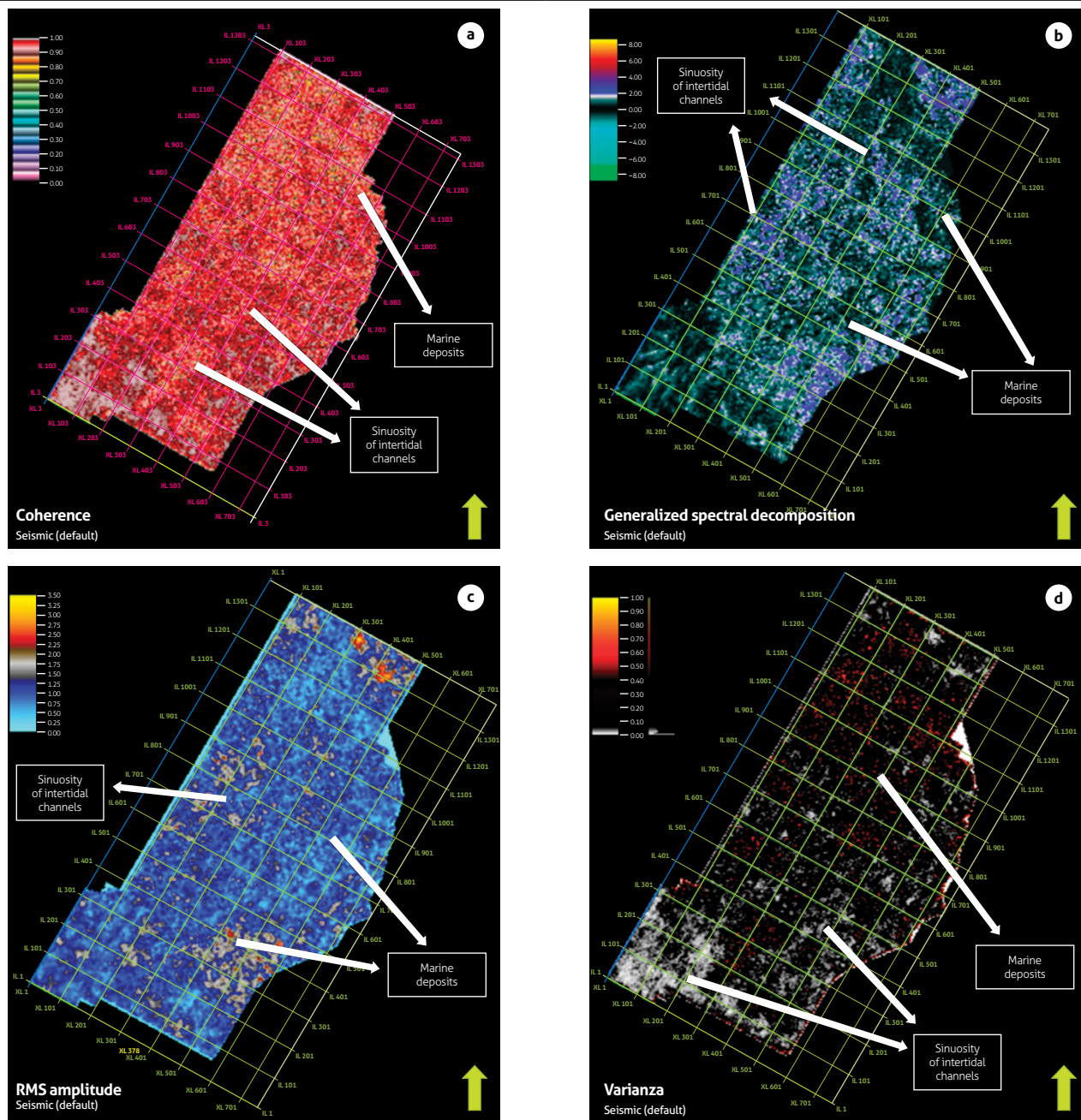


Figure 8. Attributes of a) coherence, b) spectral decomposition, c) RMS amplitude and d) variance applied to the top of sequence D (Lower Ordovician horizon).

Sequence E

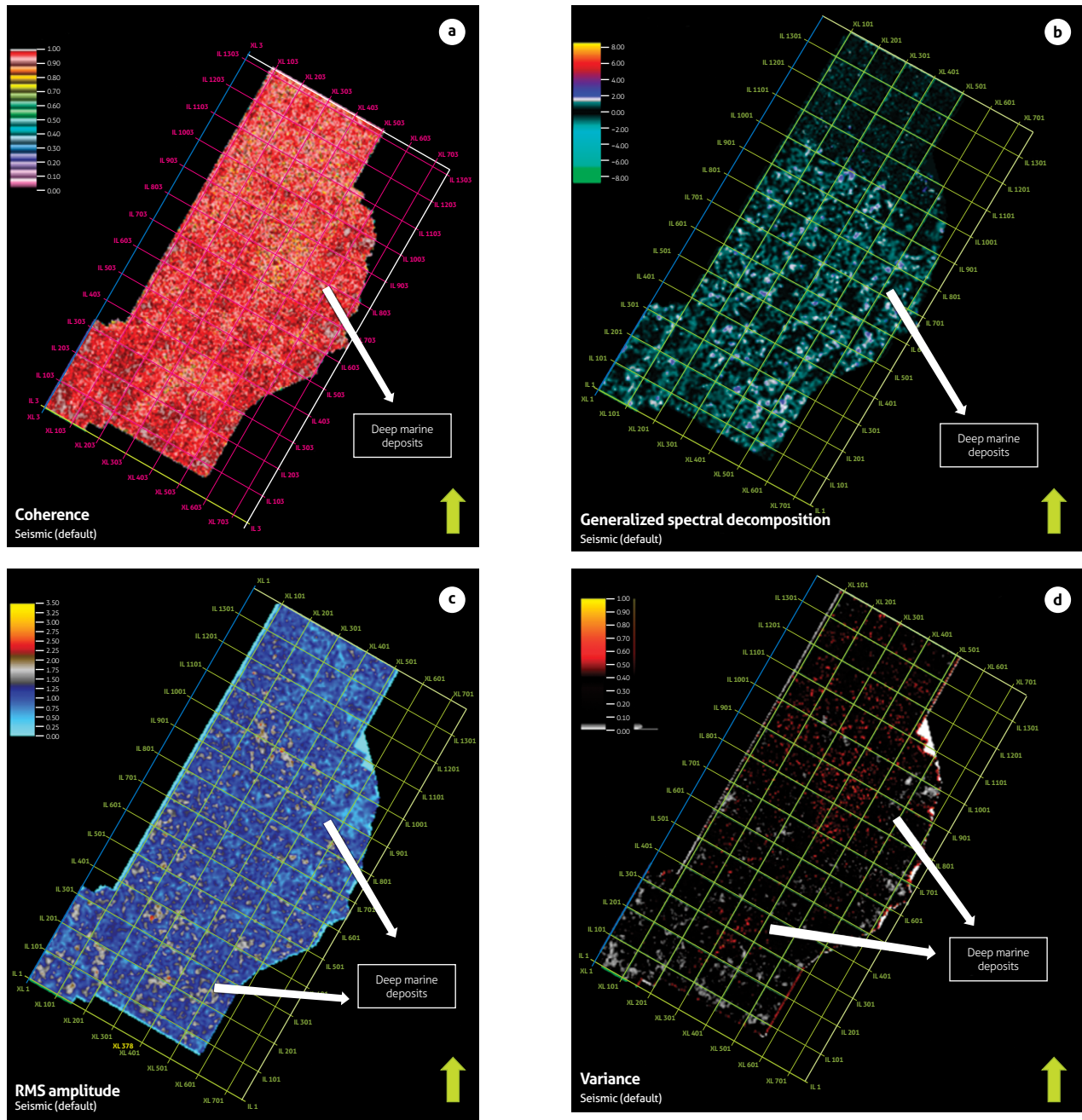


Figure 9. Attributes of a) coherence, b) spectral decomposition, c) RMS amplitude and d) variance applied to the top of the sequence E (lower Ordovician horizon).

Table 5. Results and interpretation of the seismic attributes applied

Sequence	Seismic attribute	Coherence	Spectral decomposition	Amplitude RMS	Variance	Interpretation
Sequence C	NW	High similarity.	Low frequencies with the presence of segments with moderate to high frequencies.	Low energy, porosities and amplitudes.	Low correlations with segments of moderate correlations.	Deposits of clayey and muddy lithologies. Failures.
	SE	Moderate to low wavy morphologies.	High frequencies in the wave morphology.	High energies, porosities and amplitudes in the wave morphology.	Low correlations with the presence of high correlations that demarcate the wave bodies.	Sedimentation of muddy lithologies with sand intercalations. Channels.
Sequence D	NW	High similarity.	Low frequencies with the presence of segments with moderate frequencies.	Low energies, porosities and amplitudes.	High correlations.	Deposits of clayey and muddy lithologies.
	SE	Moderate values of similarity.	Moderate to low frequencies for wavy patterns.	Moderate to low energies, porosities and amplitudes.	Moderate to high correlations.	Sinuosity of clayey and muddy lithologies.
Sequence E		High similarities.	Low frequencies.	Low energy, porosities and amplitudes.	High correlations.	Deposits of clayey and muddy lithologies.

## 5. DISCUSSION

Inverse faults in the north-eastern to southwestern direction predominate in the northern zone of the seismic block for sequence C and throughout the block for sequences D and E. These structural elements are related to the events reported in the literature, which indicate a *rifting* at the end of the Proterozoic and early Cambrian, which produced a partial collapse with normal faults that were reactivated in the Palaeozoic due to compressive events (Cediel, 2019) that generated a failure inversion. These were extended to more superficial sequences because they are areas of structural weakness.

For sequence C, which is associated with the Middle Ordovician according to palynological data, the stratigraphy of sequences showed a drop in sea level due to the presence of muddy lithologies with sands. On the other hand, the analysis of seismic facies determined different behaviours in the reflectors in the north-eastern and southwestern areas could be related to the locations of the faults found in the seismic block. Finally, the seismic attributes provided information on the distribution of lithologies, where muddy and sandy sediments associated with the intertidal channels were identified. These characteristics would seem typical of a shallow marine sedimentation environment (Serra, 1984).

For sequence D, which was interpreted in this project as Lower Ordovician based on the analysis of seismic facies, different behaviours were recorded in the north-eastern and southwestern areas of the seismic block, which are associated with faults in these areas. The seismic attributes of this sequence indicated mostly muddy lithological distributions with small sand lenses towards the centre of the block associated with apparent sinuosity of intertidal channels in a shallow marine environment. Lithologies were recognized from the characteristics provided by the seismic attributes mentioned in Table 5.

For sequence E, which was interpreted in this project as Cambrian, the analysis of seismic facies recognized a similar behaviour for the entire seismic block, which may be due to the decreased presence of faults compared to more superficial sequences or the decrease in the vertical resolution at depth, which could prevent the clear visualization of elements (Sheriff, 1997). On the other hand, the seismic attributes indicate high lithological similarities associated with sludge. This interpretation and the drop in sea level towards the Middle Ordovician corresponding to sequence C indicate for sequence E a shallow marine sedimentation environment that is slightly deep (Serra, 1984).

## 6. CONCLUSIONS

The analysis of sequential stratigraphy based on information from wells and 2D and 3D seismic data facilitated an understanding of the stratigraphic and structural elements of the study area for the Palaeozoic interval. Therefore, it was possible to interpret a shallow marine depositional environment that was somewhat deep in the Cambrian and a shallower marine environment in the Lower Ordovician. These results provide innovative geological information for this period in the study area.

The analysis of seismic facies for seismostratigraphic sequences C, D, E and F showed differences in behaviours between the northeastern and southwestern zones of sequences C and D.

The seismic attributes applied to the 3D seismic information (coherence, RMS amplitude, spectral decomposition and variance) turned out to be a very useful tool to find the distribution of lithologies and faults and associate them with geological events. In the Cambrian, mudstones and claystones from slightly deep and shallow marine environments predominate;

in the Lower to Middle Ordovician, there was a transition in which intertidal channels of muddy and clayey lithologies were presented with fine sandy bodies related to shallower marine environments towards the southwest.

Based on these attributes, maps of geofoms were obtained (Appendix 3.3.) This facilitated the understanding of the distribution of lithological deposits in the study area. However, the interpretation of the attributes was not as detailed for seismic-stratigraphic sequences D and E as it was for the other sequences because the seismic resolution at these depths did not facilitate the recognition of all structural and stratigraphic elements.

Further geophysical studies, such as reach greater depths, provide more direct information, achieve greater analytical detail, and reduce the uncertainty about the composition of seism-stratigraphic sequences D and E.

This study provides innovative geophysical information in the study area, which has some potential for hydrocarbon exploration; since the study is focused on the Palaeozoic era and was conducted within a historically hydrocarbon-rich basin, geofoms were found that had not been identified.

## 7. SUPPLEMENTARY DATA

Supplementary data for this article can be found online at <https://doi.org/10.32685/0120-1425/bol.geol.49.1.2022.557>

## ACKNOWLEDGEMENTS

We thank the Servicio Geológico Colombiano for allowing the use of information and its technical contributions for the development of this thesis project. Additionally, we thank the peer reviewers chosen by the *Boletín Geológico* for enhancing the document and the research with their suggestions.

## REFERENCES

- Agencia Nacional de Hidrocarburos (ANH), & Universidad Nacional de Colombia. (2010). *Plan de cubrimiento sísmico*. Vol. 1 and 2. <https://www.anh.gov.co/Informacion-Geologica-y-Geofisica/Metodos-de-Visualizacion/Paginas/PLAN-DE-CUBRIMIENTO-S%C3%8DSMICO.aspx>
- Beltrán Jiménez, V. F. (2015). *Metodologías para la elaboración de un sismograma sintético y estimación de las propiedades petrofísicas del pozo U* [Undergraduate thesis]. Instituto Politécnico Nacional, México D. F. <https://tesis.ipn.mx/bits-tream/handle/123456789/14962/Metodolog%C3%adas%20para%20la%20elaboraci%C3%B3n%20de%20un%20sismograma%20sint%C3%A9tico%20y%20estimaci%C3%B3n%20de%20las%20propiedades%20petrof%C3%adsicas%20del%20pozo%20U.pdf?sequence=1&isAllowed=y>
- Brown, A. (1996). Seismic attributes and their classification. *The Leading Edge*, 15(10), 1090.
- Cabañas, W. M. (1996). Interpretación geológica de sismogramas sintéticos. Un ejemplo aplicado al sondeo río Segura G-1. *Geogaceta*, 20(1), 153-156.
- Cediel, F. (2019). Phanerozoic orogens of northwestern South America: Cordilleran-type orogens. Taphrogenic tectonics. The Maracaibo orogenic float. The Chocó-Panamá indenter. En F. Cediel & R. P. Shaw (eds.), *Geology and tectonics of northwestern South America* (pp. 3-95). Springer. [https://doi.org/10.1007/978-3-319-76132-9\\_1](https://doi.org/10.1007/978-3-319-76132-9_1)
- Chen, Q., & Sidney, S. (1997). Seismic attribute technology for reservoir forecasting and monitoring. *The Leading Edge*, 16(5), 445-448.
- Chopra, S., & Marfurt, K. J. (2007). *Seismic attribute for prospect identification and reservoir characterization*. SEG Library.
- Ecopetrol y Beicip. (1995). *Estudio geológico regional. Cuenca de los Eastern Plains*.
- Esquivel Arenales, L. C. (2020). *Interpretación de geoformas palaeozoicas en una localidad de los Eastern Plains en Colombia aplicando atributos sísmicos* [Undergraduate thesis]. Universidad de los Andes. <https://repositorio.uniandes.edu.co/handle/1992/49259>
- Schlumberger Oilfield Glossary. (2020). Recuperado en abril de 2020. <https://glossary.oilfield.slb.com>
- Hubach, E. (1957). Contribución a las unidades estratigráficas de Colombia. Informe 1212. Servicio Geológico Nacional. Bogotá.
- Lozano, E., & Zamora, N (2014). Compilación de la cuenca de los Eastern Plains. Anexo 1. Servicio Geológico Colombiano.
- Martínez-González, J. A. (2008). *Síntesis estructural del Palaeozoico en las cuencas subandinas*. Asociación Colombiana de Geólogos and Geofísicos del Petróleo (ACGGP).
- Mitchum, R., Vail, P., & Thompson, S. (1977). *The depositional sequence as a basic unit for stratigraphic analysis: Memoir 26 Seismic Stratigraphy – Applications to hydrocarbon exploration*. America Association of Petroleum Geologists Bulletin, 1, 53-62.

- Neidell, N., & Tanner, M. (1971). Semblance and other coherency measures for multichannel data. *Geophysics*, 36(3), 482-497. <https://doi.org/10.1190/1.1440186>
- Parra, M., Mora, A., Jaramillo, C., Torres, V., Zeilinger, G., & Strecker, M. R. (2010). Tectonic controls on Cenozoic foreland basin development in the north-eastern Andes, Colombia. *Basin Research*, 22(6), 874-903. <https://doi.org/10.1111/j.1365-2117.2009.00459.x>
- Sangree, J., & Widmier, J. (1977). Seismic stratigraphy and global changes of sea level: Part 9. Seismic interpretation of clastic depositional facies: Section 2. Application of seismic reflection configuration to stratigraphic interpretation. In *Seismic Stratigraphy, Applications to hydrocarbon Exploration*. Memoir 26. American Association of Petroleum Geologists Bulletin. <https://archives.datapages.com/data/specpubs/seismic1/data/a165/a165/0001/0150/0165.htm>
- Sarmiento, L. F. (2011). *Llanos Basins*. (Vol. 9). Universidad EAFIT.
- Sheriff, R. E. (1997). Seismic resolution a key element.
- Schlumberger Limited. (1981). *Principios/aplicaciones de la interpretación de registros de pozo Schlumberger*. Schlumberger Educational Services.
- Serra, O. (1984). *Análisis de ambientes sedimentarios mediante perfiles de pozo*. Schlumberger.
- Stuart, J., Mountney, N., McCaffrey, W., Lang, S., & Collinson, J. (2014). Prediction of channel connectivity and fluvial style in the flood-basin successions of the Upper Permian Rangal coal measures (Queensland). *AAPG Bulletin*, 98(2), 191-212. <https://doi.org/10.1306/06171312088>
- Suárez, H., & Solano Y. (2012). El Palaeozoico en los Eastern Plains de Colombia: una ventana en la búsqueda de fuentes de Hidrocarburos. *Revista GEO Petróleo*, 14, 8-11.
- Tanner, M. T. (2001). Seismic attributes. *CSEG Recorder*, 26(07), 48-56.
- Telford, W. M., Telford, W. M., Geldart, L. P., Sheriff, R. E., & Sheriff, R. E. (1990). *Applied geophysics*. Cambridge University press.
- Vail, P. R., Mitchum Jr, R. M., & Thompson III, S. (1977). Seismic stratigraphy and global changes of sea level: Part 3. Relative changes of sea level from Coastal Onlap: section 2. In *Seismic Stratigraphy — Applications to Hydrocarbon Exploration*, Vol. 26 American Association of Petroleum Geologists. <https://doi.org/10.1306/M26490>
- Villamizar, F. J., & Castillo, L. A. (2016). Análisis sismoestratigráfico y secuencial del sector suroeste de la cuenca de los Eastern Plains (Colombia). *Boletín de Geología*, 38(3), 55-69. <http://dx.doi.org/10.18273/revbol.v38n3-2016004>



This work is distributed under the Creative Commons Attribution 4.0 License.

Received: October 29, 2021

Revisión received: May 16, 2022

Accepted: May 30, 2022

Published online: June 30, 2022

# Gravity Studies at the Cerro Machín volcano, Colombia

## Estudios gravimétricos en el volcán Cerro Machín, Colombia

Nicolás Felipe Pedraza<sup>1</sup>, Juan Diego Velásquez<sup>1</sup>, Indira Molina<sup>2</sup>, Andrés Pedraza<sup>1</sup>

<sup>1</sup> Universidad de los Andes, Bogotá, Colombia.

<sup>2</sup> Universidad de los Andes. Now at Servicio Geológico Colombiano, Bogotá, Colombia.

**Corresponding author:** Nicolás Felipe Pedraza, [nf.pedraza@uniandes.edu.co](mailto:nf.pedraza@uniandes.edu.co)

### ABSTRACT

A gravimetric study was performed at the Cerro Machín volcano (4° 29' N, 75° 22' W), Tolima Department, Colombia, to obtain a density distribution of the volcanic edifice and its basement. This study was divided into three main sections. The first section consisted of gravimetric measurements on the volcano, which were performed with a Scintrex Autograv CG-5 gravimeter. In the second section, a complete Bouguer anomaly was obtained by applying gravimetric corrections to the field data, such as instrumental drift, latitude, free-air, Bouguer, and topographic corrections. For the third section, we used the GM-SYS extension of Oasis Montaj to obtain a forward model of the subsurface density distribution that allowed us to explain the source of the gravimetric anomaly. As the main results for this study, we determined that the field-obtained Bouguer anomaly ranged between -87 mGal and -29 mGal in the study area. The Oasis Montaj density model allowed us to infer an elongated dacitic complex at the top of the distribution with a mean density of 2300 kg/m<sup>3</sup>, with the presence of a volcanic conduit of 2400 kg/m<sup>3</sup> at the base. The seismicity in the area suggests that the gravimetric anomaly caused by the dome and its surrounding materials may be related to a large weakened zone at the interface between the volcanic edifice and the metamorphic basement, provoked by fault activity, interaction with the hydrothermal system and the ascent of hot, fluid material to the surface. This study suggests one interpretation of the Machín dome volcanic complex and encourages further gravimetric studies and modeling over a wider area.

**Keywords:** Gravimetry, Gravimetric corrections, Bouguer anomaly, Oasis Montaj, Forward modeling, Geological modeling.

### RESUMEN

Un estudio gravimétrico fue hecho en el volcán Cerro Machín (4° 29' N, 75° 22' W), en el departamento de Tolima, Colombia, para obtener una distribución de densidades del edificio volcánico y su basamento. El estudio fue dividido en tres partes: la primera consistió en la toma de datos gravimétricos en el volcán con un gravímetro *Scintrex Autograv* CG-5. En la segunda se obtuvo la anomalía completa de Bouguer del área de estudio tras aplicar las correcciones gravimétricas a los datos de campo, como la corrección de deriva instrumental, latitud, aire libre, Bouguer simple y topográfica. En la tercera se utilizó la extensión GM-SYS de *Oasis Montaj* para obtener un modelo de distribución geológica que permita explicar el origen de la anomalía gravimétrica, utilizando

el método de modelamiento directo. Como resultado principal se obtuvo que la anomalía de Bouguer en campo oscila entre  $-87 \text{ mGal}$  y  $-29 \text{ mGal}$  en la zona de estudio. El modelo de densidad *Oasis Montaj* permite inferir un complejo dacítico alargado en la parte superior de la distribución con una densidad media de  $2300 \text{ kg/m}^3$ , y la presencia de un conducto volcánico de  $2400 \text{ kg/m}^3$  en su base. La sismicidad en la zona mostró que la anomalía gravimétrica causada por el domo y sus materiales circundantes puede estar relacionada con una gran zona de debilidad en la interfaz entre el edificio volcánico y el basamento metamórfico, a causa de la actividad de las fallas, la interacción con el sistema hidrotermal y el ascenso de material caliente y fluido a la superficie. Este trabajo motiva a realizar futuros estudios y modelamientos gravimétricos en un área más grande.

**Palabras clave:** Gravimetría, correcciones gravimétricas, anomalía de Bouguer, Oasis Montaj, modelamiento directo, modelamiento geológico.

## 1. INTRODUCTION

Geophysical methods have been a useful tool for monitoring the activity of different volcanoes worldwide. Vulcanologists who use these methods have pursued three main objectives: i) characterization of magma movement through the crust and its location within a magmatic chamber, ii) observation of the hydrothermal activity associated with a volcano, and iii) monitoring of the stability of the volcanic edifice (Wynn et al., 2006). Gravimetry has been essential for the study of changes in the stress tensor and the temperature gradient at the subsurface due to intrusions of magmatic bodies. This results in density variations and surface deformations where the body intrudes, which can be detected by fluctuations in the vertical vector of gravitational attraction (e.g., Vajda, 2016). The monitoring of such dynamics is especially relevant since it has been demonstrated that these deformations on the volcanic edifice are precursors of volcanic eruptions. Thus, their monitoring is fundamental in the evaluation of volcanic hazards (e.g., Vajda, 2016).

Our main objective in this contribution is to present a gravimetric study of the Cerro Machin volcano and to obtain (using data acquired from fieldwork between March 16th and March 19th, 2020) a representative model of the density distribution from its crater area at depth. Based on the total Bouguer anomaly obtained from the field data, this model was evaluated and compared with the geology and seismicity of the area, aiming to contribute to the general characterization of the processes associated with the activity of the Cerro Machin volcano.

## 2. TECTONIC-STRUCTURAL SETTING

The Cerro Machin volcano (2750 m MSL) is located on the eastern flank of the Colombian Central Cordillera, 17 km to

the northwest of the city of Ibagué (Murcia et al., 2008). According to the stratigraphic record, it has produced at least six major dacitic eruptions, the last one dated at 900-year B.P. (Laeger et al., 2013). This volcano is part of the Northern Volcanic Zone (NVZ) of the Andean Volcanic Belt, which stretches up to Ecuador. This belt is the result of the subduction of the Nazca Plate beneath the South American Plate (Laeger et al., 2013). The volcanic arc in Colombia runs parallel to the Colombia-Ecuador Trench, located 300 km west of the arc (Rueda, 2005). The arc subdivisions are usually named considering the proximity of the volcanoes to each other (Monsalve and Pulgarín, 1993). Nonetheless, other authors have established the existence of a sole segment (named the Cauca segment), which includes the totality of the Colombian volcanic arc (Rueda, 2005). This segment is subdivided into three subsegments: North, Central, and South. The Cerro Machín volcano is located in the southernmost area of the northern subsegment, along with other volcanoes such as Nevado del Ruiz, Cerro Bravo, Nevado del Tolima, and Nevado del Quindío. This subsegment extends for 90 km from the SW to the NE (Hall and Wood, 1985) and is defined by two main fault systems in the region: the Cauca-Patía (east of the Colombian West Cordillera) fault, the Romeral-Dolores fault (west of the Colombian Central Cordillera) and the secondary faults associated with both main faults (Rueda, 2005).

Cerro Machin is located at the intersection of two faults: the Cajamarca fault, with a  $N 20^\circ E$  strike and vertical dip, and the Machin fault, with a  $N 42^\circ W$  strike and normal movement with a dextral component (Rueda, 2005). Both faults have shown activity during the Holocene since their movements affect only volcanic deposits and paleosols associated with the activity of the volcano during this period (Rueda, 2005). The formation of Cerro Machin could be attributed to the existence

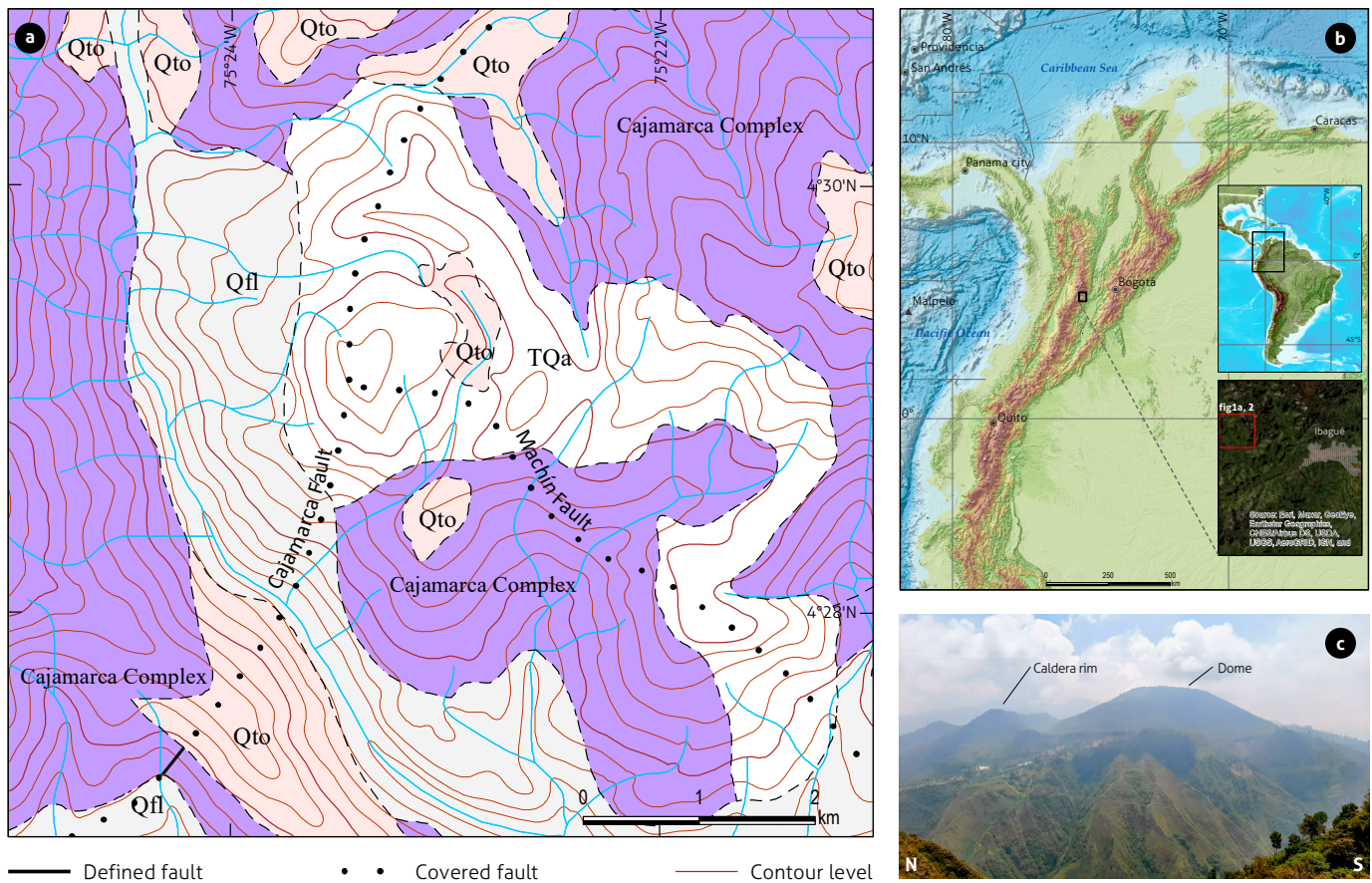


**Figure 1.** a) Geological map of the study area extracted from Geology Map 244 of the Servicio Geológico Colombiano (Mosquera et al., 1982), Machin fault from Méndez Fajury et al. (1996). b) Global and regional location of the Cerro Machin volcano in Colombia. c) N-S Panoramic view of the Cerro Machin volcano

of a pull-apart structure (with undefined dimensions) generated by the lateral movement of the previously mentioned faults of the region. This rifting structure could have facilitated the ascent of magmatic material that led to the formation of the volcano (Rueda, 2005).

### 2.1. Geological setting

The volcano formed on top a set of metamorphic rocks known as the Cajamarca Complex (Figure 1), which is the central core of the Colombian Central Cordillera (Piedrahita et al., 2018). These rocks are characterized by low-pressure regional metamorphism with a predominance of green schist, quartz-sericitic phyllites and quartzites generated from mafic lava flows, pyroclastic material, and sedimentary rocks of different compositions and grain sizes. These rocks were deposited in the Triassic during rifting between North and South America and subsequently underwent different anatexis events due to the

continental arc magmatism that occurred in the region during the Jurassic (Laeger et al., 2013).

The actual volcanic edifice is formed by a dacitic dome and various pyroclastic flow deposits resulting from the last and previous eruptive activities of the volcano (Laeger et al., 2013). These deposits are grouped in a unit called “Anillo”, which is divided into five lithofacies types generated from different pyroclastic flow density currents of high turbulence and low density currents whose formation could involve water (Piedrahita et al., 2018). Furthermore, this and other differentiated units from previous recognizable eruptions have been grouped into a single stratigraphic unit named the Machin Formation, divided into five subunits, each associated with eruptive volcanic activity (Rueda, 2005). Their composition consists mainly of tephra and pumice, as well as pyroclasts and distal deposits related to the lahars formed during the eruptive events (Méndez, 2002).

### 3. METHODS

The study was divided into three sections:

#### 3.1 Data collection campaign at the Cerro Machin volcano

Gravimetric and GPS data were obtained during a field campaign conducted from March 16<sup>th</sup> to March 20<sup>th</sup>, 2020. Forty measurements were taken, mostly inside the crater of the volcano around the Machin dome (Figure 2), with two measurements made on the two summits of the dome, using a Scintrex Autograv CG-5 gravimeter. For the base station of the gravity survey, the absolute gravity value ( $g_A$ ) and its coordinates were provided by the Servicio Geológico Colombiano (SGC) ( $g_A$ : 977480.179 mGal; latitude: 4.48537; longitude: -75.38008; height: 2526.2 m). It was used to calculate the absolute gravity at each station.

#### 3.2 Data processing and Bouguer correction

For the processing of the data obtained during the campaign, we prepared an Excel spreadsheet. Here, the appropriate gravimetric correction equations were applied to the data as follows:

$$\Delta g_D = \frac{L2B_1 - L1B_1}{t2B_1 - t1B_1} * \Delta t \text{ (mGal)} \quad (1)$$

$$\Delta g_{lat} = 0.000812 * \sin(2\lambda) * l \text{ (mGal)} \quad (2)$$

$$\Delta g_{FA} = 0.3086 * h \text{ (mGal)} \quad (3)$$

$$\Delta g_{BP} = 2\pi G\rho h \text{ (mGal)} \quad (4)$$

where  $L1B_1$  and  $L2B_1$  are the gravity measurements taken at the base station at the beginning and at the end of the day, respectively;  $t1B_1$  and  $t2B_1$  are the times at which these measurements were performed, respectively;  $\Delta t$  is the difference between the time at which a measurement was taken at the station and at the base on a given day;  $\lambda$  is the latitude coordinate of the measurement station;  $l$  is the linear distance between the measurement station and the base;  $h$  is the height of the measurement station relative to the datum;  $G$  is the gravitational constant ( $6.672 * 10^{-11} \text{ N m}^2/\text{kg}^2$ ); and  $\rho$  is the plate density (in  $\text{kg}/\text{m}^3$ ).

To calculate the instrumental drift correction ( $\Delta g_D$ ), we applied Equation 1. Using the data collected at the base at the beginning and at the end of each day, we obtained a drift rate, which was then multiplied by the time interval between the

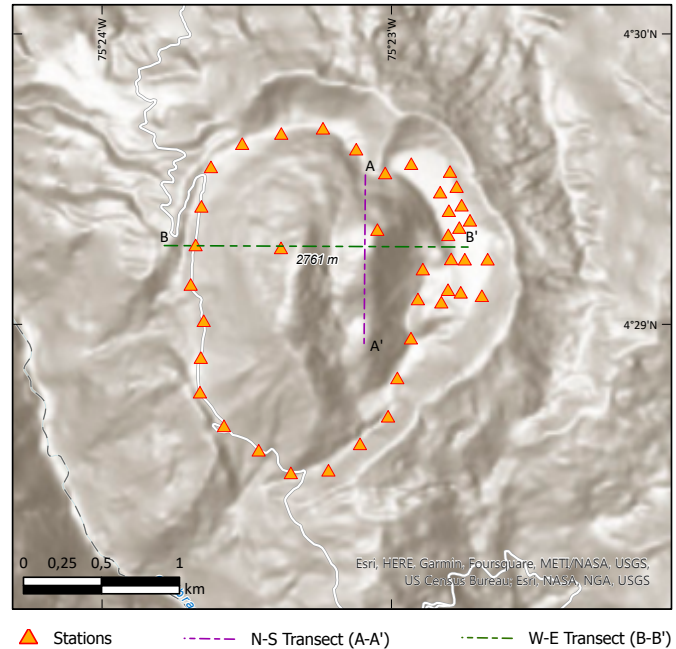


Figure 2. Map showing the contour level map showing the measurement stations throughout the volcano crater and the transects used on the 2D density models on Oasis

initial and final daily measurements at the base. Subsequently, we either added this value, if the measurement at a station was lower than that at the base, or subtracted this value, if the measurement at a station was larger than that at the base, from the relative gravity data obtained. This value was then added to the absolute gravity at the base (provided by the Servicio Geológico Colombiano) and repeated to tie each station by adding the value of the relative gravity measured at each station with the value obtained at the base. This total variation in gravity was finally added to the absolute gravity at the base to obtain the measured gravity at each station.

The latitude correction ( $\Delta g_{lat}$ ) was calculated using Equation 2, for which we considered the latitude coordinate of every station and its distance to the base. The free air correction ( $\Delta g_{FA}$ ) was obtained using Equation 3, taking the difference in height between the station and the sea level, considered as the reference. We then applied Equation 4 to calculate the Bouguer plate correction ( $\Delta g_{BP}$ ), for which we needed the difference in height between the station and the reference level, as well as the existing mass between both points; thus, an optimal density for this mass was obtained. An average crustal density of  $2670 \text{ kg}/\text{m}^3$  (Hinze, 2003) was implemented. Finally, for each point, we calculated the free air correction to obtain the simple Bouguer anomaly, which can be expressed by the following equation:

$$\Delta_B = g_s + 0.3086h - 2\pi G\rho h \text{ (mGal)} \quad (5)$$

where  $g_s$  is the relative gravity at the station in relation to the reference point,  $h$  is the height of the measurement station (in meters), and  $\rho$  is the density used for the calculation of the Bouguer plate correction (in  $\text{kg/m}^3$ ).

Finally, a topographic correction ( $\Delta g_T$ ) was applied to the data collected at all stations. This correction considers the irregularities of the surface in the vicinity of the stations. These irregularities may exert an upward pull on the gravimeter for an excess of mass or a downward pull for a lack of mass in the area, which may affect the gravimetric measurements. The topographic correction at each measurement point was calculated by using a computational method in MATLAB provided by Palacios (2017). This implementation required the use of a digital elevation model (DEM) extracted from the Copernicus DEM (OpenTopography, 2021), which was used as an input for the calculation. Another script from Palacios (2017) transformed the topography provided by the DEM into polyhedra of different sizes and two distinct shapes (squared and triangular prisms) and divided the area covered by the DEM into six concentric, square-shaped sections centered on the base station. Over 5 million polyhedra were created with this method. Thus, the correction values for each station depended on the polyhedra where they were located.

All aforementioned calculated values were combined to obtain the total Bouguer anomaly for each station using the following equation:

$$\Delta_B = (g_A \pm g_0 \pm \Delta g_D) + (\Delta g_{lat} \pm \Delta g_{FA} \pm \Delta g_{BP} + \Delta g_T) - g_{th} \text{ (mGal)} \quad (6)$$

where  $g_A$  is the absolute gravity,  $g_0$  is the gravity value obtained with the gravimeter, and  $g_{th}$  is the theoretical gravity for each location, which was obtained using the International Gravitational Formula (Dentith and Mudge, 2014):

$$g_{th}(\lambda) = \frac{9.7803253359 * 1 + 0.00193185241 \sin^2 \lambda}{\sqrt{1 - 0.00669437999014 \sin^2 \lambda}} \quad (7)$$

where  $\lambda$  is the latitude coordinate of the station.

### 3.3 Generation of the 2D forward models using Oasis Montaj

The processing of the gravity and topographic data (gridding and imaging) and the forward modeling of the gravity data

were carried out using Oasis Montaj software and its GM-SYS extension. To do so, the process consisted of i) the interpolation and generation of the topographic and total Bouguer anomaly maps and ii) the forward modeling of a test configuration of the density distribution of the volcano at depth using GM-SYS.

The forward modeling was carried out with the GM-SYS extension of Oasis Montaj. This modeling type involves the generation of a hypothetical density model where the physical parameters (such as the density and geometry of the model) are adjusted by the interpreter until a match is obtained between the computed response of the model and the observed data. This is an iterative process that requires the model and both the observed and computed responses to be displayed graphically so that the results can be assessed by the interpreter (Dentith and Mudge, 2014, p. 74). GM-SYS is a modeling program that allows an interactive manipulation of the geological model and real-time calculation of the gravity response. The methods used in this program to calculate the gravity and magnetic model responses are based on the methods developed by Talwani et al. (1959) and Talwani and Heirtzler (1964) and make use of the algorithms described in Won and Bevis (1987) (NGA, 2004).

GM-SYS uses a two-dimensional, flat-Earth model for gravity and magnetic calculations; that is, each structural unit or block extends to plus and minus infinity in the direction perpendicular to the profile. The Earth is assumed to have topography but no curvature. The models also extend by default plus and minus  $3 \times 10^4$  kilometers along the profile to eliminate edge effects (NGA, 2004).

## 4. RESULTS

### 4.1 Field-obtained Bouguer anomaly

Figure 3 shows the results after the application of the gravimetric corrections to the field-obtained data (see Table 1 in Supporting Information). The resulting Excel spreadsheet was imported into Oasis Montaj, which was used to generate the Bouguer anomaly map (Figure 3a) of our study area. The locations of the recorded earthquakes in the study area (León, 2019) were included in the Bouguer anomaly map, as one of the main objectives of our work was to identify the possible origins of the observed anomaly. The transects where the 2D depth profiles were obtained are also included in Figure 3b.

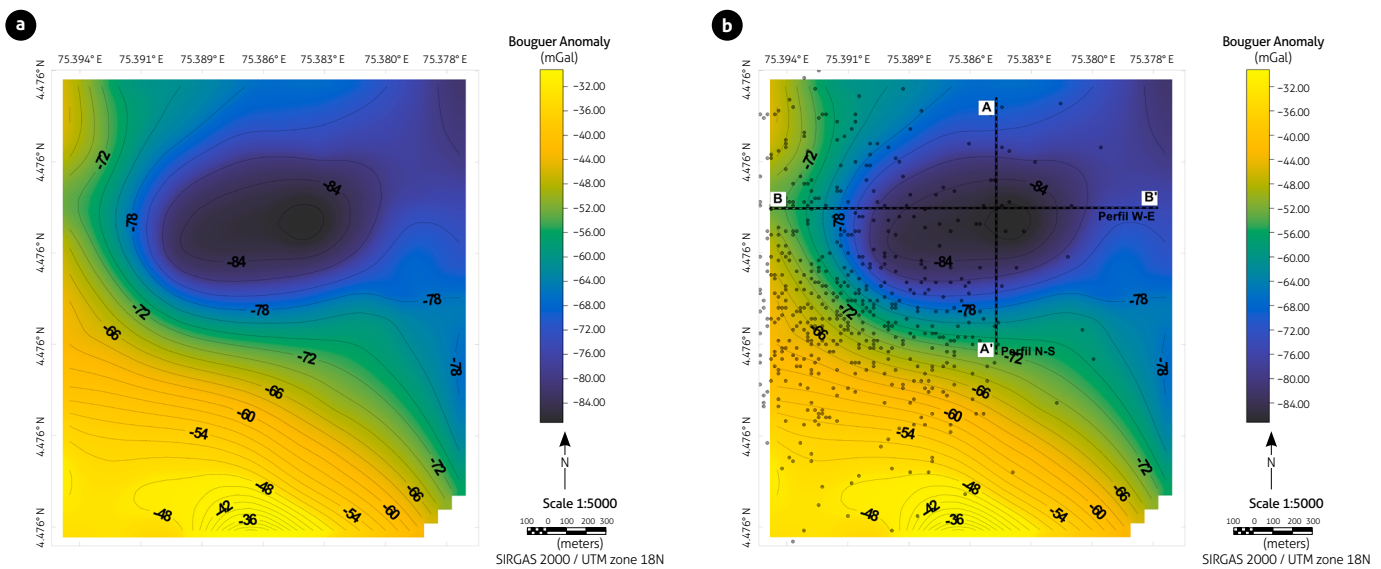


**Figure 3.** a) Bouguer map calculated using Equation 6 in the study area. b) Bouguer anomaly map, overlapped with the earthquakes shown by black dots, and the N-S and W-E transects for the depth models shown in Sections 3.3 and 4.2

The field-obtained anomaly showed a range of values ranging between approximately  $-87$  and  $-29$   $mGal$  (see values in the Supplementary Data). The lowest anomaly values were found in the area above the topographic highs of the dome (Figure 2). Figure 3b also shows that the earthquakes were mostly located southwest of the volcano. The locations of the earthquakes, all of which were associated with activity below the Machin dome, support the idea of the existence of an anomaly in this area. In addition, the data processing designated a region where the anomaly was less negative ( $-29$   $mGal$ ) over the entire study area. This measurement was located at the southernmost station at a low elevation near a hot spring at 2412 meters.

#### 4.2 Oasis Montaj 2D forward modeling

To better understand the way the density distribution of the geological bodies affected the observed gravity, N-S and W-E depth profiles, shown in Figure 2, were analyzed. The resulting models suggest the following distribution: a dacitic dome complex at the top and a weakened section below (simplified as a single unit that comprises a complex system of dikes and volcanic conduits) embedded over the edifice, which comprises volcanoclastic sequences from the previous eruptive activity, whose density increases with depth.

For this distribution, we assumed the volcanic edifice to be surrounded by host rock with an average crustal density of  $2670$   $kg/m^3$ , which is represented by the green layers in Figure 4. Within the study area, we set 3 layers named volcanoclastic sequences that sit over the metamorphic basement, cut by the dacitic complex that connects with deeper magmatic chambers. The density of the fragmented part of the dome, which we set up between the topographic relief and a depth of  $0$  km, is  $2300$   $kg/m^3$ , while volcanoclastic sequence layers vary between  $2500$   $kg/m^3$  (uppermost volcanoclastic sequence layer) and  $2670$   $kg/m^3$  (deeper volcanoclastic sequence layer). Ultimately, the metamorphic complex density was established at  $2900$   $kg/m^3$ , close to the dacitic complex in the northwestern regions of the volcano and tilting downward toward the southeast. It is important to note the presence, below the fragmented dome complex, of a weakened section, modeled as a simplified unit that includes a complex system of dikes and volcanic conduits, with a density of  $2400$   $kg/m^3$ . This distribution allowed us to obtain the best adjustment to the observed anomaly. We associate this fragmentation with the activity of the faults in the area (especially the Cajamarca fault, trending NE-SW) and with the presence of the hydrothermal system of the volcano that may include the infiltration of meteoric waters, the ascent of waters stored in the metamorphic complex or from the magmatic reservoir of the volcano, which is much deeper and outside the study area.

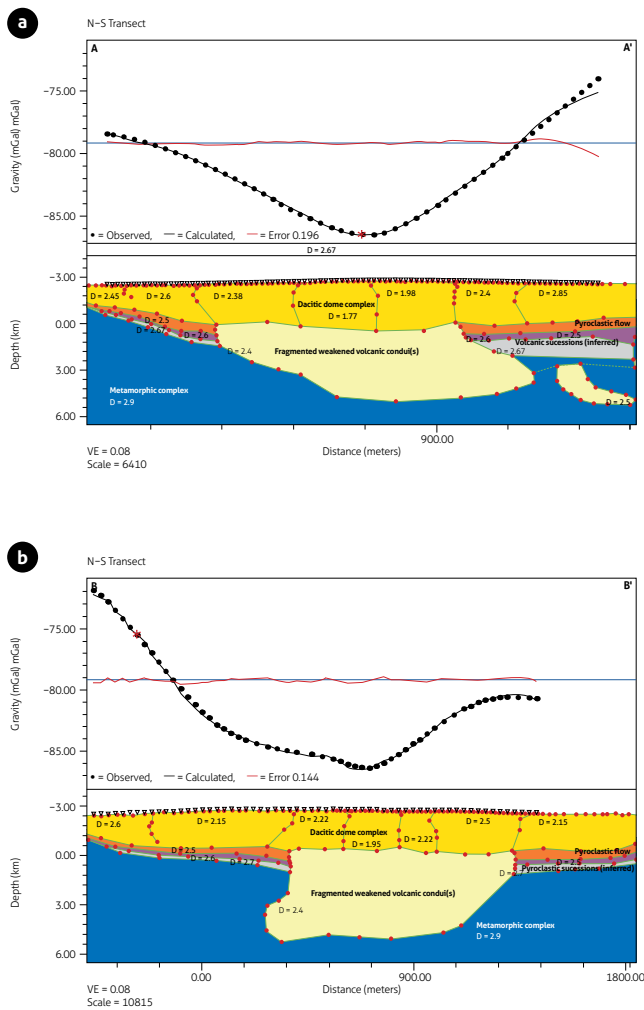


**Figure 4.** Tested 2D models for a density configuration of a) the N-S transect and b) the W-E transect. See Figure 4b for profile location over the Bouguer Anomaly. Red dots: Block model editing vertices.

## 5. DISCUSSION

### 5.1 Geological interpretation of the Bouguer anomaly

Based on the analysis of the Bouguer anomaly and the 2D forward models, we determined that the dome sector is less dense than its surrounding subsoil. This can be explained by alterations caused by the hydrothermal system associated with the Cerro Machin volcano and the interactions between its different parts. Piedrahita et al. (2018) suggested the presence of aquifers in the Cajamarca Complex, which, given the levels of shearing and fracturing of these rocks, would allow the movement and storage of confined water. Likewise, Cerpa (2018)

stated that the hydrothermal system of the Cerro Machin volcano is characterized by the interaction of meteoric water that infiltrates from the surface to the basement, as well as by endogenous waters coming from a deep magmatic reservoir. The transport of these waters is favored by the permeability of the existing rocks (especially recent lava flows) and the fractures associated with the activity of the Cajamarca fault, which suggests the presence of different “mixing zones” between all these types of water. One of these zones stands out, located just below the area of the Cajamarca fault (see Figure 33 of Cerpa, 2018). This suggests that fracturing and infiltration of hydrothermal fluids in the lower part of the Machin dome considerably affected its density, which is reflected in the observed Bouguer anomaly.

Last, the higher values of the Bouguer anomaly in the southern part of the study area (Figure 3b) can also be explained by the hydrothermal processes associated with the volcano. This point is close to two thermal springs, named “Piscinas” and “Estatuas” by Inguaggiato et al. (2016). The first of these sources is characterized by relatively high concentrations of chlorides and silica, while the second is mainly distinguished by the presence of large amorphous silica concretions along a zone of structural discontinuity through which hydrothermal fluids ascend (Inguaggiato et al., 2016). Based on the presence of these concretions, we infer that due to the large accumulation of silica precipitated from the infiltrated fluids and considering that this new material fills the spaces left by the original porosity of the deposited rocks, there might have been a slight increase in the average density of the subsoil in this sector. The effects of these concretions, nonetheless, should be further investigated due to the lack of evidence or studies regarding this matter both in the study area and in other similar tectonic environments.

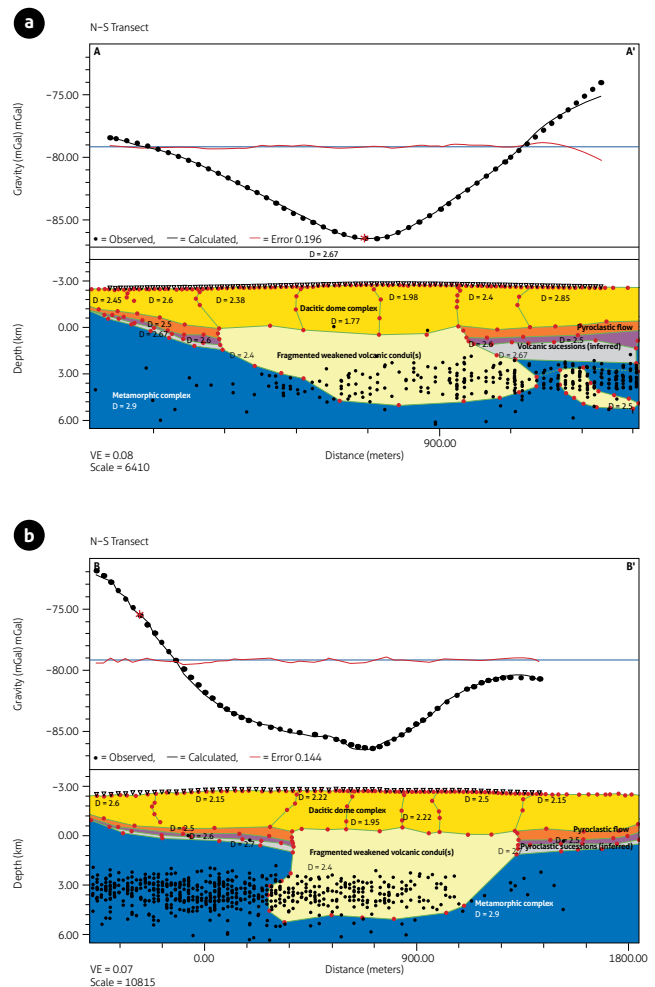
### 5.2 Geological interpretation of the Oasis Montaj models

Figure 5a and 5b show that the earthquakes located within our study area overlapped with those over the Oasis Montaj models. The earthquake locations were provided by the Servicio Geológico Colombiano and correspond to the period from 2004 to 2019. The obtained densities for all modeled units coincide with what has been reported in the literature for similar types of volcanoes (dacitic to andesitic stratovolcanoes with domes) outside Colombia and the Cerro Machin. For example, Kueppers et al. (2005) made density measurements for sev-

eral dry rock samples from the deposits that were generated during the 1990-1995 eruptive cycle of Mount Unzen in Japan. The authors found a bimodal density distribution with peaks of  $2000 \pm 100 \text{ kg/m}^3$  and  $2300 \pm 100 \text{ kg/m}^3$  and reported that the density values could vary between 1400 and  $2400 \text{ kg/m}^3$ . Similarly, Hoblitt and Harmon (1993) found a bimodal density distribution for the dacitic rocks from the 1980 eruption of Mount St. Helens, with peaks of 1600 and  $2300 \text{ kg/m}^3$ . Furthermore, Acosta (2019) calculated the bulk density for several rock samples associated with the activity of three volcanoes in Colombia (Azufra, Doña Juana and Cerro Machin). For the Cerro Machin samples, the author found bulk density values between 2000 and  $2300 \text{ kg/m}^3$ .

The above studies show that the chosen range of density values is plausible with the common geology that is associated with the activity of dacitic volcanoes similar to Cerro Machin. It also opens the opportunity for future investigations and modeling regarding the density of rock samples within the study area to obtain more complete data and more detailed constraints for the models. This is important considering the following: 1) the nonunique solution principle, which indicates that different geological distributions can be the best fit for a set of gravimetric data, and 2) even though there is a coincidence between what is reported here and what was reported in previous studies, there are some other studies where much lower densities were found for the volcanoclastic sequences. For example, Rueda et al. (2013) reported density values that ranged from 920 to  $960 \text{ kg/m}^3$  for the volcanoclastic products of a 31 ka Plinian-sub-Plinian eruption at Tlaloc Volcano in Mexico. Similarly, Arce et al. (2005) reported samples from a volcanoclastic deposit associated with a 12.1 ka Plinian-sub-Plinian eruption of Volcán Nevado de Toluca (Mexico), whose density variation was established from 700 to  $820 \text{ kg/m}^3$ .

These results coincide with the model proposed by Londoño (2011). By performing seismic P-wave velocity tomography to obtain the internal structure of Cerro Machin down to a depth of 4 to 5 km, this author determined that the dacitic dome reached a depth up to 3 km (from topographic relief), which explained why the seismicity was generally located at these depths. Furthermore, Londoño found that although the inner parts of the dome were compact enough to avoid fracturing and thus the circulation of fluid material to the shallowest parts of the system, two zones extending E and SW of the dome featured lower P-wave velocities. This behavior was associated with the genesis of weakening zones in the deepest part of the



**Figure 5.** Tested 2D profiles, including the seismicity provided by the Servicio Geológico Colombiano. a) Model for the N-S transect and b) model for the W-E transect  
Black dots: Projection of the location of seismic events recorded by the Servicio Geológico Colombiano during 2004-2019. Red dots: Block model editing vertices.

dome, which were produced by the hot, fluid material coming from the magmatic reservoir attempting to reach the surface. This would explain the fracturing in these sectors and, therefore, the general seismic environment.

Taking these results into account, we built a general 2D W-E geological schematic model (Figure 6). For this, we extrapolated the density distribution that we obtained with the gravity forward models. The depth in which this extrapolation reaches was decided based on the resolution depth that we calculated using the equation given by Musset and Khan (2000) for obtaining the depth of an anomalous irregular body. This

equation relates the maximum gravity anomaly and the maximum slope of the gravimetric profile; therefore, we used the one that we obtained when modeling the W-E forward model for our calculation. Taking this into account, we obtained a depth of approximately 6.2 km, which is the limit that we defined for our forward models. The schematic model reaches 10 km, which we inferred based on the seismic and geological data available for the Cerro Machin volcano, indicating that there may be a magmatic reservoir outside our study area at the selected depth (León, 2019; Londoño, 2011).

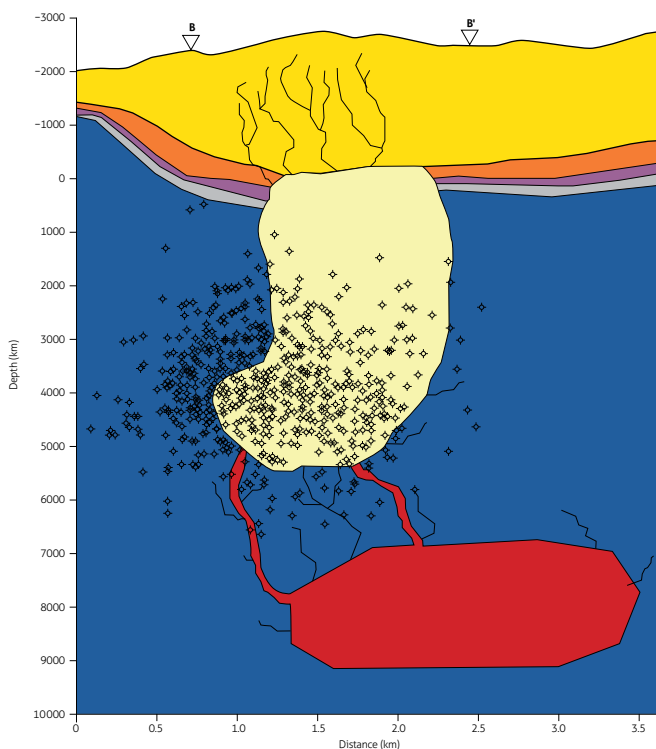
A dacitic dome complex occupies the uppermost part of our model. This dome is located over a series of layers associated with the volcanoclastic sequences that were formed during the reported volcanic activity of the Cerro Machin volcano and whose density may have been diminished due to weathering produced by infiltration of meteoric waters. At a depth of 3 km

from the surface, we infer a transition to a more compact, less fragmented, slightly denser zone of the dacitic complex, just above the Cajamarca metamorphic complex, where the seismic activity associated with the volcanic activity is located. This transition corresponds to altered materials affected by the different geological processes described in this study. Thus, we associate the existence of this sector with the existence of a weakened zone provoked by the general fault activity associated with the Cajamarca fault, the interaction with the hydrothermal system of the volcano and the ascent of hot fluid material that may have risen to the surface through less compact material (as Londoño, 2011). This ascent would have been through a system of dikes and fractures that connects this sector with a magmatic reservoir located to the SE of our study area and at a much deeper depth (Londoño, 2011). The contrast between the volcanoclastic sequences and this weakened zone is what we infer to be the origin of the gravity anomaly.

This general test configuration model offers valuable results as a starting point for future investigation projects in the area. The obtained results may have been slightly affected by the limited quantity of acquired data, which negatively impacts the resolution of the models explicitly defining the origin, spatial distribution and magnitude of the gravimetric anomaly related to the Cerro Machin volcano. We suggest, for future research, to focus on improving the data resolution of the study area, minimizing the distance between stations/points. Further measurements, such as seismic tomography and rock sampling, would provide precise density value information over the study area.

## 6. CONCLUSIONS

Based on observed gravity data acquired between March 16<sup>th</sup> and March 19<sup>th</sup>, 2020, we studied the local gravimetric anomalies in the Cerro Machin volcano. The minimum observations ranged from  $-87 \text{ mGal}$  in the Machin dome area and reached up to  $-29 \text{ mGal}$  in a measurement zone near hydrothermal sources in the southern area. These results allowed us to obtain a geological configuration with volcanoclastic sequences whose density values varied between  $2500 \text{ kg/m}^3$  and  $2600 \text{ kg/m}^3$  and a dacitic complex with an average density of  $2300 \text{ kg/m}^3$  over a less altered volcanic conduit with a suggested density of  $2400 \text{ kg/m}^3$  between the Machin dome and the metamorphic basement (Cajamarca Complex). These density values coincide with what has been reported for similar vol-



### Legend

- ◆ Earthquakes
- Dacitic complex
- Weakened volcanic conduit
- Pyroclastic flow
- Pyroclastic successions (Inferred)
- Metamorphic complex
- Magmatic reservoir

**Figure 6.** Final proposed test model of the geological distribution based on the GM-SYS modeling results. The red dashed line represents the vertical limits of the study. Seismic hypocenters were furnished by the Servicio Geológico Colombiano (Manizales).

canoes in other parts of the world and for Cerro Machin. We interpret our results with a general weakening of the dacitic dome complex due to weathering caused by infiltration of meteoric waters in the uppermost section, the ascent of hot fluid material, as well as the activity of the faults located in the study area (particularly the Cajamarca fault), and the hydrothermal system associated with the Cerro Machin volcano. All these factors contributed to the generation of a weakened zone in the deepest part of the Machin dome at the interface between the volcanic edifice and the metamorphic basement. Through a system of dikes and fractures, this weakened zone may be connected to another reservoir (the Cerro Machin magmatic reservoir) located to the SE of our study area and at deeper depths (Londoño, 2019).

For future studies, we would like to extend our study area beyond the Machin dome zone and have a broader record of the gravimetric anomaly in the influence zone of the Cerro Machin volcano and a better understanding of the associated geology. This study allowed us to obtain an initial model providing a first glimpse at the geological distribution associated with this volcanic system. This represents a starting point for further understanding this volcano and its associated processes.

## 7. ACKNOWLEDGMENT

This work was supported by the FAPA project (Fondo de Apoyo para Profesores Asistentes) No. INV-2019-63-1702 from the Universidad de los Andes, Colombia.

## 8. SUPPLEMENTARY DATA

Supplementary data for this article can be found online at <https://doi.org/10.32685/0120-1425/bol.geol.49.1.2022.619>

## REFERENCES

- Acosta Agudelo, L. (2019). *Contrastes texturales en fragmentos juveniles de depósitos de flujos piroclásticos de erupciones vulcanianas en los andes del norte: casos de estudio Cerro Machín, Doña Juana y Azufral, Colombia* [Undergraduate thesis]. Universidad de los Andes. <https://repositorio.uniandes.edu.co/handle/1992/45549>
- Arce, J. L., Cervantes, K. E., Macías, J. L., & Mora, J. C. (2005). The 12.1 ka Middle Toluca Pumice: A dacitic Plinian-subplinian eruption of Nevado de Toluca in Central Mexico. *Journal of Volcanology and Geothermal Research*, 147(1-2), 125-143. <https://doi.org/10.1016/j.jvolgeores.2005.03.010>
- Cerpa, A. C. (2018). *Caracterización del potencial geotérmico a partir de análisis geoquímicos de fuentes termales, en el volcán Cerro Machín, Colombia* [Undergraduate thesis]. Universidad EIA.
- Dentith, M., & Mudge, S. T. (2014). *Geophysics for the Mineral Exploration Geoscientist*. Cambridge University Press.
- Hall, M. L., & Wood, C. A. (1985). Volcano-tectonic segmentation of the northern Andes. *Geology*, 13(3), 203-207. [https://doi.org/10.1130/0091-7613\(1985\)13<203:VSOT-NA>2.0.CO;2](https://doi.org/10.1130/0091-7613(1985)13<203:VSOT-NA>2.0.CO;2)
- Hinze, W. J. (2003). Bouguer reduction density, why 2.67? *Geophysics*, 68(5), 1559-1560. <https://doi.org/10.1190/1.1620629>
- Hoblitt, R. P., & Harmon, R. S. (1993). Bimodal Density Distribution of Cryptodome Dacite from the 1980 Eruption of Mount St. Helens, Washington. *Bulletin of Volcanology*, 55, 421-437. <https://doi.org/10.1007/BF00302002>
- Inguaggiato, S., Londoño, J. M., Chacón, Z., Liotta, M., Gil, E., & Alzate, D. (2016). The hydrothermal system of Cerro Machín volcano (Colombia): New magmatic signals observed during 2011–2013. *Chemical Geology*, 469, 60-68. <http://dx.doi.org/10.1016/j.chemgeo.2016.12.020>
- Kueppers, U., Scheu, B., Spieler, O., & Dingwell, D. B. (2005). Field-based density measurements as tool to identify pre-eruption dome structure: set-up and first results from Unzen volcano, Japan. *Journal of Volcanology and Geothermal Research*, 141(1-2), 65-75. <https://doi.org/10.1016/j.jvolgeores.2004.09.005>
- Laeger, K., Halama, R., Hansteen, T., Savov, I. P., Murcia, H. F., Cortés, G. P., & Garbe-Schönberg, D. (2013). Crystallization conditions and petrogenesis of the lava dome from the ~900 years BP eruption of Cerro Machín Volcano, Colombia. *Journal of South American Earth Sciences*, 48, 193-208. <https://doi.org/10.1016/j.jsames.2013.09.009>
- León, A. (2019). Estudio de Coda Q para sismos volcano-tectónicos en el volcán Cerro Machín (Colombia) [Bachelor thesis]. Universidad de los Andes.
- Londoño, J. M. (2011). 3D seismic tomography of Cerro Machín Volcano, Colombia. In *XIV Latinamerican Congress of Geology*. Medellín, Colombia.
- Londoño, J. M., & Kumagai, H. (2018). 4D seismic tomography of Nevado del Ruiz Volcano, Colombia, 2000–2016. *Jour-*

- nal of Volcanology and Geothermal Research*, 358, 105-123. <https://doi.org/10.1016/j.jvolgeores.2018.02.015>
- Méndez Fajury, R. A., Cepeda Vanegas, H., Monsalve Bustamante, M. L., Murcia Leal, L. A., & Núñez Tello, A. (1996). Volcán Cerro Machín, departamento del Tolima, Colombia: Pasado, presente y futuro. Instituto Nacional de Investigaciones Geológicas Mineras (Ingeominas). <https://miig.sgc.gov.co/Paginas/Resultados.aspx?k=110020101010002305000000000>
- Méndez, R. A. (2002). Formación Machín (Qm), cordillera Central, departamento del Tolima. In *Catálogo de las Unidades Litoestratigráficas de Colombia*. Instituto Colombiano de Geología y Minería (Ingeominas).
- Monsalve, M. L., & Pulgarín, B. (1993). Mapa preliminar de amenaza volcánica potencial del volcán Puracé: Memoria explicativa. *Revista Ingeominas*, 2, 3-27.
- Mosquera, D., Núñez, A., & Vesga-Ordóñez, C. J. (1982). Geología de la Plancha 244 Ibagué. Instituto Colombiano de Geología y Minería (Ingeominas). <https://miig.sgc.gov.co/Paginas/Resultados.aspx?k=130100101010024375000000000>
- Musset, A. E., & Khan, M. A. (2000). *Looking Into the Earth: An Introduction to Geological Geophysics*. Cambridge University Press.
- Northwest Geophysical Associates, Inc. (2004). Modeling Concepts. In *GM-SYS Gravity/Magnetic Modeling Software: Vol. 4.9*.
- OpenTopography. (2021). Copernicus GLO-90 Digital Surface Model. <https://doi.org/10.5069/G9028PQB>
- Palacios, N. (2017). *A Matlab code to compute gravity measurements' terrain corrections in Puracé (Cauca), Colombia* [Bachelor thesis]. Universidad de los Andes, Bogotá, Colombia.
- Piedrahita, D. A., Aguilar-Casallas, C., Arango-Palacio, E., Murcia, H., & Gómez-Arango, J. (2018). Estratigrafía del cráter y morfología del volcán Cerro Machín, Colombia. *Boletín de Geología*, 40(3), 29-48. <http://dx.doi.org/10.18273/revbol.v40n3-2018002>
- Rueda, H. (2005). Erupciones plinianas del Holoceno en el volcán Cerro Machín, Colombia: Estratigrafía, Petrografía y Dinámica Eruptiva [Master Thesis]. Universidad Nacional Autónoma de México.
- Rueda, H., Macías, J. L., Arce, J. L., Gardner, J. E., & Layer, P. W. (2013). The ~ 31 ka rhyolitic Plinian to sub-Plinian eruption of Tlaloc Volcano, Sierra Nevada, central Mexico. *Journal of Volcanology and Geothermal Research*, 252, 73-91. <https://doi.org/10.1016/j.jvolgeores.2012.12.001>
- Vajda, P. (2016). Recent Developments and Trends in Volcano Gravimetry. In K. Nemeth, *Updates in Volcanology – From Volcano Modelling to Volcano Geology*. IntechOpen. <http://dx.doi.org/10.5772/63420>
- Wynn, J., Dzurisin, D., Finn, C. A., Kauahikaua, J. P., & LaHusen, R. G. (2006). Applications of Geophysical Methods to Volcano Monitoring. 19th Symposium on the Application of Geophysics to Engineering and Environmental Problems. Seattle, United States.



Panorámica del suroeste antioqueño desde el municipio de Jamésis  
Fotografía de Paola Andrea Palacio B.



This work is distributed under the Creative Commons Attribution 4.0 License.

Received: October 29, 2021

Revisión received: May 30, 2022

Accepted: May 31, 2022

Published online: June 30, 2022

## Case study article

# Hydrogeological potential in soft formations and hard rocks: A case study in the Cauca River Canyon, Antioquia, Colombia

Potencial hidrogeológico en formaciones blandas y rocas duras: Un estudio de caso en el cañón del río Cauca, Antioquia, Colombia

Paola Andrea Palacio<sup>1</sup>, Rodrigo Alonso Díaz<sup>1</sup>, María Alejandra Vela<sup>1</sup>, Juliana Ossa<sup>1</sup>

**1.** Group of Engineering and Environmental Management (GIGA), School of Engineering, Universidad de Antioquia, Medellín, Colombia.

**Corresponding author:** Paola Andrea Palacio, papabu2@yahoo.es

## ABSTRACT

From the end of 2020 until July 2021, the first phase of a study that evaluated the hydrogeological potential in tropical dry forest (TDF) areas took place in the bosque seco tropical (BS-T), which was associated with the Cauca River Canyon in the jurisdiction of Corantioquia. Based on the litho-structural evaluation of the area, hypotheses were established by which conditions of greater or lesser aquifer potential were assigned according to the different types of geological materials present. The first step to confirm these hypotheses was an inventory of groundwater points. The results indicated the existence of more than 1172 points, including springs, hand-dug wells, galleries and wells.

Relating the occurrence of these water points with the lithological units, approximately 560 points in Quaternary deposits and rocks of the Amagá Formation and the Urrao Member of the Penderisco Formation were found; 146 were located in volcano-sedimentary deposits of the Combia Formation, and more than 466 were associated with hard rocks. It is thus concluded that in the study area, the igneous and metamorphic rocks, intensely affected by tectonic effects, have gained permeability conditions, which was evidenced by field observations, which confer aquifer conditions. This finding provides new research perspectives toward fractured environments and presents groundwater as a main and alternative source to meet the needs of the population, in addition to playing a fundamental role in terms of the ecosystem sustainability of the tropical dry forest.

**Keywords:** hydrogeology in Antioquia, groundwater, inventory of groundwater points, hydrogeological potential, tropical dry forest.

## RESUMEN

Desde finales del año 2020 hasta julio de 2021 tuvo lugar la primera fase de un estudio que evaluó el potencial hidrogeológico en zonas de bosque seco tropical -Bs-T- asociadas al cañón del río Cauca en jurisdicción de Corantioquia. Con base en la evaluación lito-estructural de la zona, se establecieron hipótesis mediante las cuales se asignaron condiciones de mayor o menor potencial acuífero, según los distintos tipos de materiales geológicos presentes. El primer paso para confrontar estas hipótesis con la realidad

fue el inventario de puntos de agua subterránea; los resultados, al año 2021, señalan la existencia de más de 1172 puntos, entre ellos: manantiales, aljibes, galerías y pozos.

Relacionando la ocurrencia de estos puntos de agua con las unidades litológicas, se encontraron cerca de 560 puntos en depósitos del Cuaternario, y en rocas de la Formación Amagá y el Miembro Urrao de la Formación Penderisco; 146 se ubican en depósitos vulcano-sedimentarios de la Formación Combia y más de 466 se asocian con rocas duras. Se concluye así, que en la zona de estudio las rocas ígneas y metamórficas, intensamente afectadas por efectos tectónicos, han ganado condiciones de permeabilidad, la cual fue evidenciada mediante observaciones en campo, que les confieren la condición de acuíferos. Este hallazgo brinda nuevas perspectivas de investigación hacia medios fracturados y presenta el agua subterránea como una fuente principal y alternativa para satisfacer las necesidades de la población, además de cobrar un rol fundamental en términos de la sostenibilidad ecosistémica del bosque seco tropical.

**Palabras clave:** hidrogeología en Antioquia, aguas subterráneas, inventario de puntos de agua subterránea, potencial hidrogeológico, bosque seco tropical.

## 1. INTRODUCTION

In the regions associated with the Cauca River Canyon, in the department of Antioquia, groundwater has an important role as a main or secondary source of supply in the demands of consumption, economic and recreational activities, and their satisfaction. With the objective of deepening their knowledge and having the tools to protect the tropical dry forest ecosystem in the jurisdiction of Corantioquia, at the end of 2020, an exploration was launched into the hydrogeological potential of geological formations located in the area of direct and indirect influence of the tropical dry forest (bosque seco tropical or BS-T) associated with the Cauca River Canyon.

During the first months of development of the project, the collection of available secondary information was carried out, which could serve the initial purposes of groundwater exploration. The starting point was the recognition and determination of the area of influence, followed by the development of a sociodemographic evaluation that would allow the first approach to the fieldwork.

The geological conditions, determined both by the type of rocks and by the tecto-structural affectation on them, provided guidelines to identify and characterize the different types of hydrogeological units. For this, an assembly of the geological cartography at a scale of 1:100 000 and 1:400 000 of the Servicio Geológico Colombiano (SGC) was verified in the field.

Based on the porosity and permeability conditions of the geological units present in the study area, the following categories were classified: aquifer, aquitard or aquifuge, and they were assigned a hydrogeological potential: very high, high, me-

dium, low or null. The areas obtained for each category were subsequently refined from the results of the inventory of water points, with which the information that fed all the elements of the conceptual hydrogeological model was gathered, laying the foundations that allowed the involvement of communities in the construction of knowledge and preparation for the subsequent definition and application of management measures.

## 2. REFERENCE FRAMEWORK

The study area was delimited, considering the hydrographic subzones of the Cauca River basin which is a part of the BS-T ecosystem under the jurisdiction of the Regional Autonomous Corporation of the Center of Antioquia (Corantioquia). It has an area of approximately 10 662 km<sup>2</sup> and runs through the municipalities associated with the Cauca River basin from Caramanta to Valdivia, with elevations ranging between 171 and 3609 meters above sea level (masl).

This ecosystem corresponds to a forest biome that develops at low altitudes from 0 to 1000 masl in intertropical areas with temperatures above 24 °C and annual rainfall between 700 and 2000 mm (IAVH, 1998). It is characterized by climate variability of one or two periods of very marked drought per year (rainfall less than 100 mm) of at least 5 to 6 months (Bullock et al., cited in Pizano and García, 2014). In the BS-T, the evapotranspiration process consumes most of the water, so the recharge and rate of change in the phreatic levels play an important role in the sustainability of vegetation because it becomes the only alternative to be used by plants in the processes of nutrient absorption and transpiration (Le Maitre et al., 1999).

In Colombia, this biome exists in at least six biogeographic regions: the Patía River Valley, the southern Cauca Valley, the Cauca River Valley, the upper and middle Magdalena River Valley, the departments of Santander and Norte de Santander and in the region of the Caribbean coast and Orinoquía (Figure 1). In the study of the tropical dry forest (TDF) ecosystem conducted by the Alexander von Humboldt Institute for Biological Resources Research (Pizano and García, 2014) and based on studies available since 1997 (IAVH, 1998; IAVH, 1997; Cabrera and Galindo, 2006), a loss close to 92% of the 9 million hectares covered by this ecosystem is evidenced in the map presented by Etter et al. (2008). In addition, it is mentioned that those territories that have been deforested and were BS-Ts currently present desertification scenarios; consequently, they are no longer productive for the development of agriculture or livestock, that is, they are unsustainable (Benítez et al., 2014). The state of this ecosystem in Colombia urgently needs measures to conserve the remnants that survive.

The Cauca River Basin is one of the most populated regions in Antioquia. Anthropogenic pressure on the territory has affected the natural balance of the ecosystem to the point that there is a scarcity of water for humans and other life forms in the region, including the BS-T, characteristic of the low-lying areas in the vicinity of the Cauca River Canyon. Thus, a project was proposed to deepen knowledge of the hydrogeological systems in the region, the opportunities offered by groundwater as the main or secondary sources of water and its relationship and impact on the sustainability of the BS-T ecosystem.

In the Earth's crust, the nature of various geological units allows some features to conserve intergranular porosity or primary porosity, while others do not. However, porosity can be acquired thanks to subsequent events, such as dynamic effects or by the action of weathering, which results in secondary porosity.

Considering that a hydrogeological unit is a geological formation, part of it has similar hydraulic characteristics, which are related to the capacity to store water (porosity) and the possibility of flow between the pores (permeability or coefficient of hydraulic conductivity). Hydrogeological units are classified as aquifers, aquitards, aquicludes or aquifuges. An aquifer can store and transmit enough water in acceptable quantity conditions, and its extraction can be economically viable; an aquitard stores and transmits water very slowly, so its exploitation demands more energy than the previous one; an aquiclude stores but does not allow the transit of water between the pores;

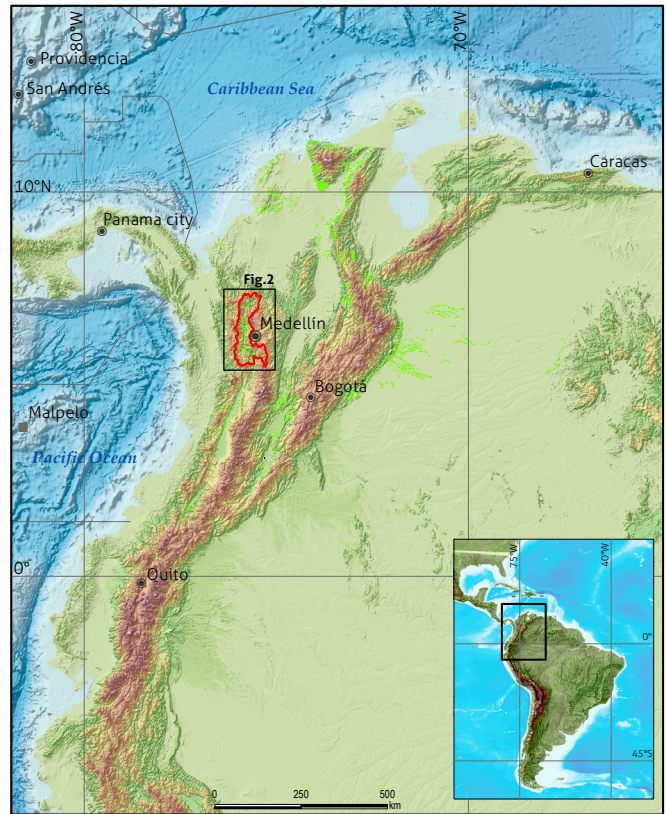


Figure 1. Distribution of the tropical dry forest in Colombia at a scale of 1:100 000

See legend in this [kmz file](#) (see in Google Earth). Source: Modified from Instituto de Investigación de Recursos Biológicos Alexander von Humboldt (2014).

and finally, an aquifuge does not store or let groundwater flow (Custodio and Llamas, 1996).

Those materials that make up units with hydrogeological potential, in order of importance, are the following: unconsolidated deposits of gravel and sand, karst formations, conglomerate sedimentary rocks or sandstone with low amounts of finer material, volcanic rock, and other rocks according to origin and evolution. Igneous rocks that have acquired secondary porosity and permeability, especially when their thicknesses are considerable in the case of deposits and sedimentary rocks. In contrast, they are not aquifers: clay and silt deposits, siltstone or claystone sedimentary rocks and igneous or metamorphic rocks without alteration.

Before 2021, several studies were conducted to understand hydrogeological systems in different regions of Antioquia, mostly focusing on hydrogeological units associated with sedimentary rocks and recent deposits. Two of these hydrogeological systems are located within the study area: the first is in the

western subregion, with an extension of 103 km<sup>2</sup>, which includes the municipalities of Santa Fe de Antioquia, San Jerónimo, Sopetrán and Olaya; the second system integrates the municipalities of La Pintada and Valparaíso associated with the Cauca River with an area of 184 km<sup>2</sup>.

Table 1 shows the studies that were consulted, and Figure 2 shows the location of the hydrogeological systems that present progress in their knowledge.

The study area included approximately 40 geological units with formation ages between the Proterozoic and Cenozoic eras, including 7 metamorphic units, 24 igneous types and 9 sedimentary types.

Figure 3 shows the geological map of the area studied, which corresponds to an adaptation by Betancur Vargas (2021), modified from González (2001), and geological maps at scale 1:100 000 and 1:400 000 (Servicio Geológico Colombiano).

In any hydrogeological exploration project, one of the first activities developed is the inventory of groundwater points. Where a water point is a natural place, civil works allow direct or indirect access to the aquifer. In this sense, the previous definition includes all existing boreholes, whether or not exploited, abandoned or even destroyed, and the sources or springs that in principle should be considered natural spillways of the aquifers (Custodio and Llamas, 1996). The following were the objectives of this study: springs, filtering galleries, hand-dug wells, wells and piezometers.

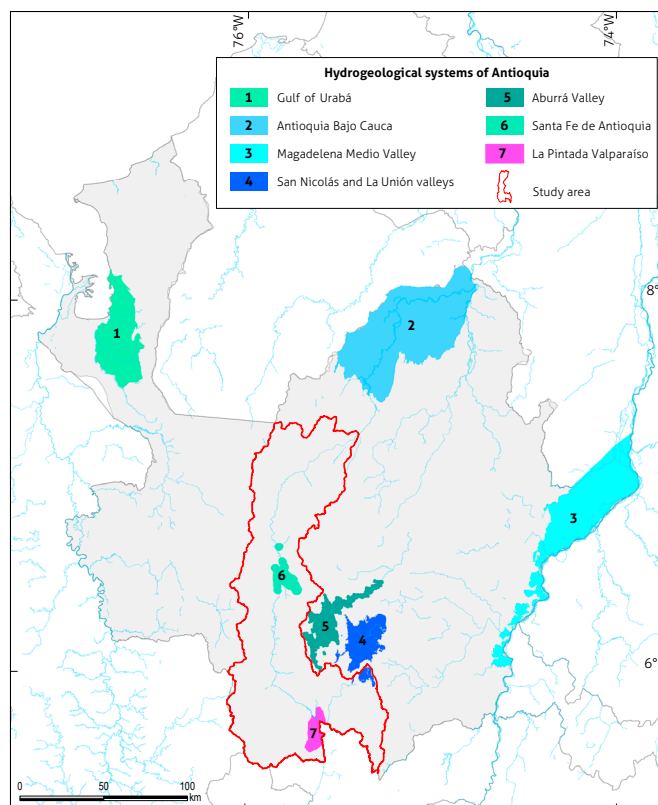
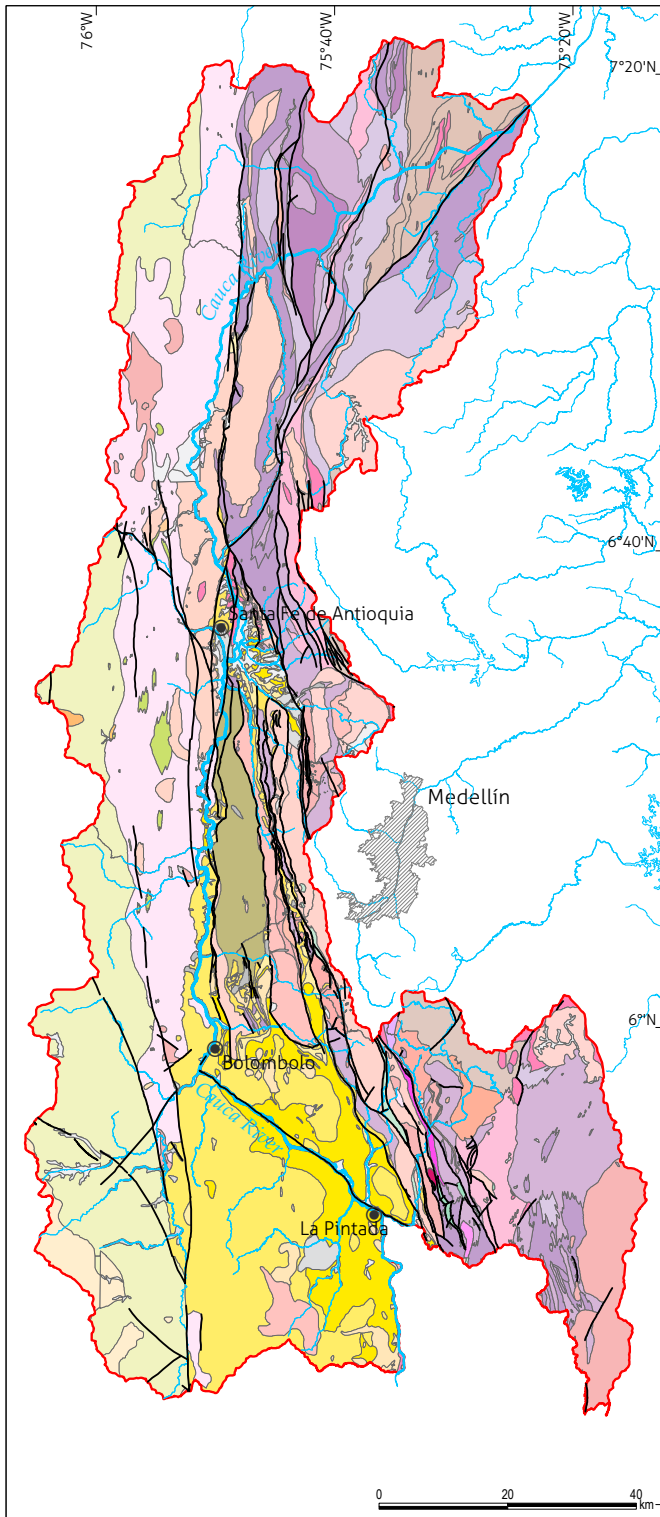


Figure 2. Location of the hydrogeological systems of Antioquia that present progress in their knowledge. See legend in this [kmz file](#) (see in Google Earth). Source: Modified from the Public Companies Foundation of Medellín, Government of Antioquia (2018).

Table 1. Hydrogeological studies consulted as secondary information

Aquifer System	Studies consulted	Author
Gulf of Urabá	Plan de manejo ambiental de acuífero sistema hidrogeológico Golfo de Urabá	Universidad de Antioquia and Corpourabá (2016)
	Análisis de calidad y cantidad	Corpourabá (2016)
Magdalena Medio Valley	Estudio regional del agua	Corantioquia and GOTTA Ingeniería (2016)
	Formulación del plan de manejo ambiental del acuífero del Magdalena Medio	Corantioquia and GOTTA Ingeniería (2017)
Aburrá Valley	Plan de manejo ambiental del sistema acuífero de la cuenca del río Aburrá	AMVA and Universidad de Antioquia (2018)
	RedRío, componente aguas subterráneas. Convenio 1050	AMVA and Universidad de Antioquia (2018)
Santa Fe de Antioquia	Estudio regional del agua	Corantioquia and SHI (2016)
	Formulación del plan de manejo ambiental del sistema acuífero del Occidente Antioqueño	Corantioquia and GOTTA Ingeniería (2017)
Antioquia Bajo Cauca	Plan de manejo ambiental del sistema de acuífero del Bajo Cauca antioqueño	Corantioquia and Universidad de Antioquia (2014)
	Estudio regional del agua	Corantioquia and GOTTA Ingeniería (2016)
San Nicolás and La Unión valleys	Investigación de aguas subterráneas región valles de San Nicolás. FASE II	Corantioquia and Universidad Nacional de Colombia (2001)
	POMCA Río Negro	POMCAS Oriente Antioqueño Consortium (2017)
	ICA Aguas subterráneas	Cornare (2016)
La Pintada - Valparaíso	Evaluación hidrogeológica en los municipios de La Pintada y Valparaíso Jurisdicción de la Dirección Territorial Cartama de Corantioquia	Corantioquia and SHI (2014)
	Estudio regional del agua	Corantioquia and Gotta Ingeniería (2016)



**Figure 3.** Geological map of the study area  
See legend in this kmz file (see in Google Earth). Source: Betancur (2021), modified from González (2001)

### 3. METHODS

In Colombia, the information collected in the inventory of water points is recorded following the parameters defined by the National Single Form of Groundwater (FUNIAS), proposed by the Institute of Hydrology, Meteorology and Environmental Studies (Ideam). This document contains a series of sections of various types, such as administrative location (municipality, village, neighborhood), technical (nature of the work, mode of drilling, diameter, materials, depth, etc.), hydrological (piezometric levels at different times, chemical quality), and uses. This activity can be carried out directly by touring the study area or indirectly by going to people or public and private entities that by their work can indicate the existence of water points and provide the information required for the inventory.

In the first instance, a review of secondary information was carried out to locate previously identified water points, such as records of groundwater concessions by the Environmental Corporation, information from existing FUNIAS, and the Water Resource Information System (Sistema de Información del Recurso Hídrico), Environmental Impact Studies (EIA), Aquifer Environmental Management Plans (PMAA), Watershed Management Plans (POMCA), Water Resources Management Plans (PORH), and a review of the databases provided by the corporation.

The collection and collection of primary information was carried out through field trips by professionals in hydrogeology, supported by a social, communication and relationship component, which was aimed at identifying the key actors, direct users and users of indirect resources of the underground water resource, as well as the organizations or entities that are part of the exercise of socialization and appropriation of the knowledge generated by the project in the territory.

For both primary and secondary information, the coding of the inventory of water points defined by Ideam was implemented, according to the FUNIAS; this structure allows, in a methodical way, the assignment of a unique code to each water point. This represents the possibility of ordering and unifying the registration information of the points from different sources, allowing a database with a common language between entities, which became a management tool for authorities and environmental entities in the administration. of water resources.

Figure 4 shows the methodological scheme that was used for the inventory of groundwater points.

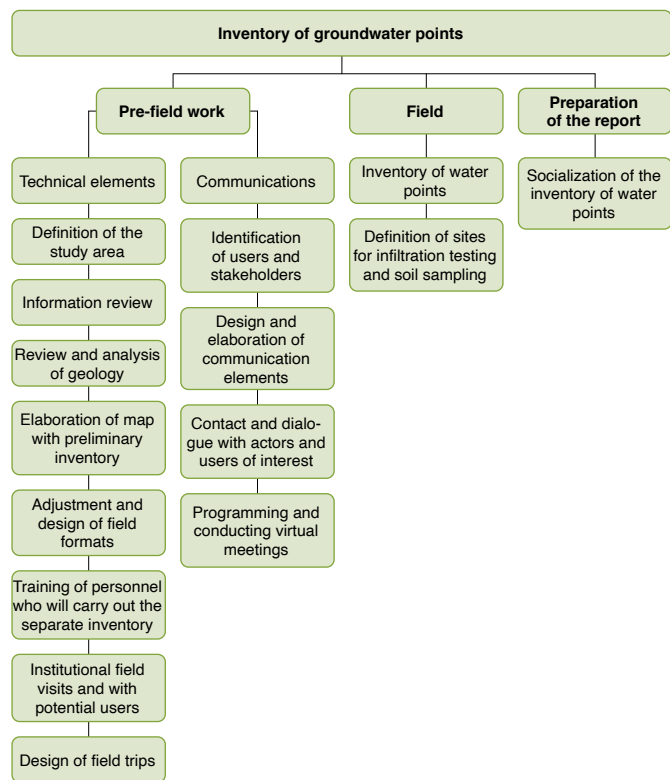


Figure 4. Methodological scheme of the groundwater inventory

For the characterization of the hydrogeological units, a geological-structural evaluation was carried out that focused on determining the relevant porosity and permeability conditions that promoted the storage and flow of groundwater. The deposits and clastic sedimentary rocks, given their primary porosity, were evaluated and verified in the field as potential aquifers. Likewise, the condition of the hydrogeological unit was determined for the hard rocks that have been or have not been affected structurally or by weathering with the help of professionals with experience in hydrogeology.

The fault systems with direct interference in the study area are the San Jerónimo System, the Espiritu Santo Fault and the Romeral System. The large fractures have, in general, a clear morphological expression and present fractured, sheared rocks with alteration and brecciation, while the smaller ones present only some of these characteristics and are preferentially marked by visible alignments in the aerial photographs.

Prior to the inventory and applying the Analytic Hierarchy Process (AHP) methodology based on the work of Saaty (2008), ten professionals in geology and hydrogeology, knowledgeable in the area of study, were consulted about the

Table 2. Rating scale of hydrogeological conditions based on porosity and permeability

Unit type	Qualification of hydrogeological potential
Aquifer	Very high
	High
	Medium
Aquitard	Low
Aquifuge	Null

hydrogeological potential of the geological units in question (see annex 2). For this exercise, different levels of importance were considered, according to the porosity and permeability characteristics of each unit and the categories: aquifer, aquitard or aquifuge. This was done to assign hydrogeological potential based on the qualitative weighting matrix of Table 2. Analytical and hierarchical processes, such as Saaty, with a sufficiently large survey size and expert and independent evaluators, allow assigning weights and guarantee a reasonable reduction of the so-called “decision bias” (Universidad de Antioquia and Corpourabá, 2016).

According to the responses obtained, the initial mapping of hydrogeological potential was proposed (Figure 5, upper left: a), which was key for the planning of the field work, aimed at the development of the inventory of water points, one of the most suitable tools for the construction of preliminary knowledge of the hydrogeological conditions of the area. As a result of the matrix, the areas of potential were identified; then, the geology in the field and superposition of the inventoried water points corroborated or corrected the different lithological units of the study area.

#### 4. RESULTS

In the first stage of the project, 1172 water points were identified, distributed in 751 springs, 394 hand-dug wells, 13 piezometers, 12 wells and 2 filter galleries. The initial approach to the hydrogeological potential was corroborated by field reconnaissance work and the superposition of the inventoried water points, making it possible to confirm or redefine the hydrogeological character of the lithological units, which allowed us to complete the categorization exercise of the units from their benefits or limitations and as storage and facilitators of groundwater flow.

The results of the process of evaluating the hydrogeological potential of sites and subsequent additions to the inventory can

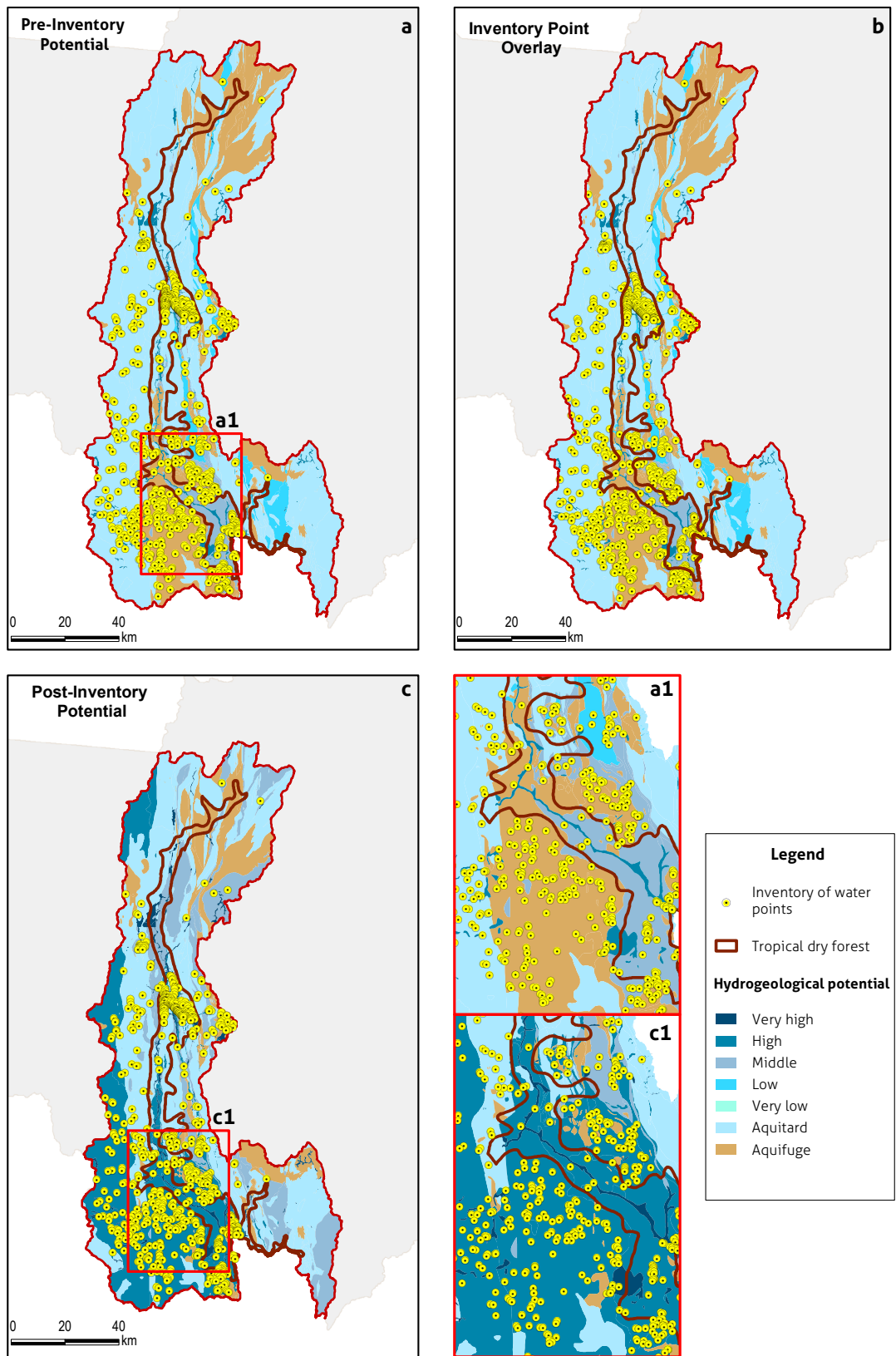


Figure 5. Representation of the superposition of water points and hydrogeological potential adjustment  
 See legend in this [kmz file](#) (see in Google Earth). Source: Adapted from Corantioquia and Universidad de Antioquia (2021).

be visualized in Figure 5. Table 3 shows the results for some of the geological units of interest, according to the type of rock. In Table S1, detailed information regarding the total number of points inventoried is shown.

According to the results of synthesis and geological verification in the field, in the area of direct and indirect influence of the BS-T associated with the Cauca River in Corantioquia, 33% of deposits and sedimentary rocks are soft geological formations and 67% are hard rocks (igneous and metamorphic). Ninety-six percent of the soft rocks have a high or very high hydrogeological potential, and in the case of igneous and metamorphic rocks, which are mostly structurally affected, 24% have a medium hydrogeological potential, and 1.5% have a high hydrogeological potential. This distribution can be visualized in Figure 6.

As a result of this exercise, it was found that the quaternary deposits are the geological units with the highest concentration of water points, with the alluvial deposits and terraces having the greatest amount, a total of 358. The Amagá Formation, Upper Member, Combia Formation and Urrao Member of the Pendersco Formation are geological units that follow in importance, taking into account the number of water points associated with them. In the first unit, 109 water points were recorded, 146 points were identified in the Combia Formation, and 93 were found in the Urrao Member.

The aquifer potential is also evidenced in units such as the quartz-meritic schists of the Cajamarca Complex (62 water points inventoried); the Sabanalarga Batholith (13 points); Buriticá Andesite (21 points); Sheep Tonalite (17 points) and Pueblito Diorite (10 points).

Table 3. Evaluation of the hydrogeological potential in geological units of interest

Type	Unity	Subunit	Structures	Porosity	Preliminary potential to the inventory	Inventory points	Post-inventory potential
Metamorphic rocks	Intrusive Neysics Synthectonics (Pzin)	Intrusive neis of Abejorral	Dynamic effects of variable intensity, marked by fracturing.	Secondary	Low	4	Medium
Plutonic igneous rocks	Stock of Amagá		It is a solid rock, granular to porphyritic, with medium to coarse grain. The texture is granular hypidiomorphic.	NA	Very Low	25	Low
	Combia training	Combia Formation - Volcanic Member	The fine pyroclastic levels of ash tuffs occupy topographically elevated areas. They present jointing.	Primary and secondary	Low	241	High
Sedimentary rocks		Combia Formation - Sedimentary Member	The sedimentary layers are jointed with a horizontal, vertical or inclined attitude.	Primary	High		High
Deposits	Quaternary deposits	Alluvial deposits		Primary	High	363	Very high

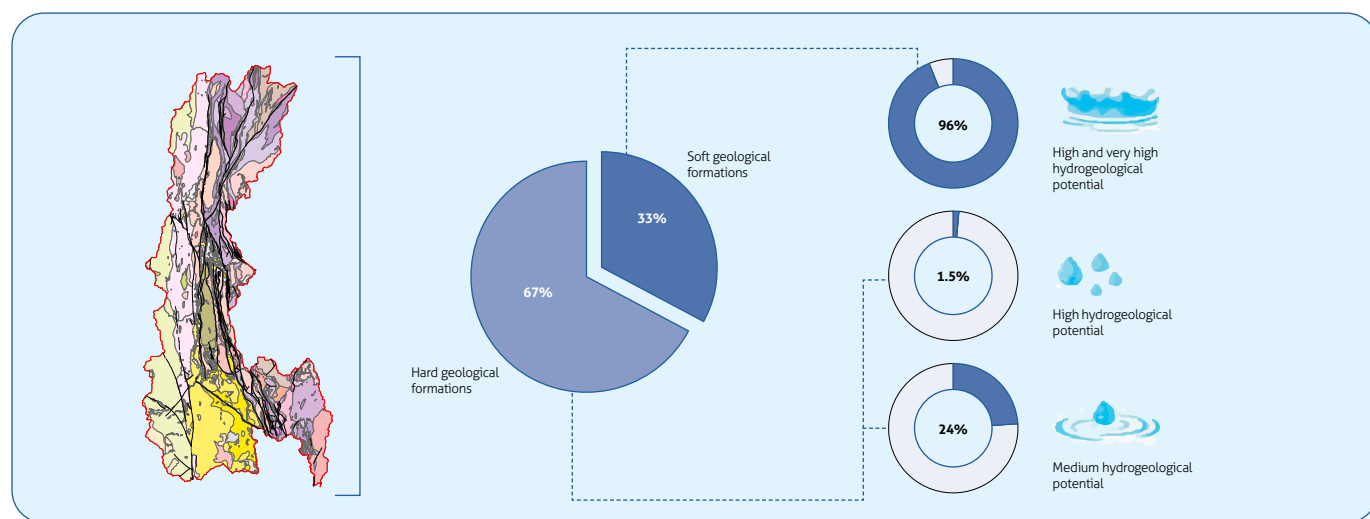


Figure 6. Synthesis of the hydrogeological potential in the study area

## 5. DISCUSSION

Of the 1172 groundwater points, 947 were identified in the collection of secondary information; although they represent a vast volume in the study area, it is necessary to complete missing data, such as water uses, volumes captured, properties; hydraulics, and subsoil records, with the objective that the information is useful to the inventory. The data obtained in the field work supplemented the primary information of the water point registry, added to the collection of secondary information and promoted dialog with the experts, providing the basis for an approximation to the hydrogeological potential of the study area.

From what was found in the field work, it was possible to corroborate the importance of deepening the study of groundwater and hydrogeological systems in the subregions that made up the study area, considering each area's sociodemographic, economic and ecosystem characteristics, which affect the dynamics of the BS-T.

## 6. CONCLUSIONS

The inventory of water points is a fundamental tool in the classification and redefinition of hydrogeological units; from it, primary information is obtained that allows feeding most of the components of the conceptual hydrogeological model. The fieldwork of the inventory corroborates the importance of building knowledge from the implementation of participation, education and communication strategies that are supported in the dialog of knowledge and in the construction of citizen science.

The 1172 water points documented in the BS-T associated with the Cauca River Basin in Antioquia confirms the hydrogeological potential that exists in the region.

In Antioquia, the hydrogeological potential of igneous and metamorphic rocks that have acquired porosity and secondary permeability after being subjected to intense tectonic effects over time is significant, because 24% have a medium hydrogeological potential and 1.5% a high potential. In terms of groundwater availability, this is relevant data, since hard geological formations occupy a 67% study area.

This information serves as a reference point to deepen the knowledge of fractured environments and highlights the possibility of having alternative and complementary sources of water to satisfy human needs. In addition, it plays a fundamental role in terms of the sustainability of the tropical dry forest ecosystem.

## 7. ACKNOWLEDGMENTS

We thank Corantioquia for financing exploration of the hydrogeological potential in the Cauca River Canyon in its the jurisdiction, making it was possible to carry out this research.

Thanks also to Teresita Betancur Vargas, geologist and project advisor; the engineers Cristina Martínez, Alba Nury Gallego, Breiner Dan Bastidas and Andrés Felipe Zapata; to the communicators Deisy Rivera and Lilibian Monsalve; the technician Ángela Díaz; members of the GIGA Research Group of the Faculty of Engineering of the Universidad de Antioquia; and those who contributed their knowledge and work in the formulation and reality of the project.

We also appreciate those people who opened their doors to allow us to collect data about their use of groundwater and shared their perceptions and knowledge with us.

## 8. SUPPLEMENTARY DATA

Supplementary data for this article can be found online at <https://doi.org/10.32685/0120-1425/bol.geol.49.1.2022.620>

### Available data

Table S1. Synthesis of information from the inventory of 1172 groundwater points in the study area

### Data in kmz files

Figure 1. Distribution of the tropical dry forest in Colombia at a scale of 1:100 000

Figure 2. Location of the hydrogeological systems of Antioquia that present progress in their knowledge

Figure 3. Geological map of the study area

Figure 5. Representation of the superposition of water points and hydrogeological potential adjustment

## REFERENCES

- AMVA & Universidad de Antioquia. (2018). Plan de Manejo Ambiental del Sistema Acuífero de la Cuenca del Río Aburrá.
- AMVA & Universidad de Antioquia. (2018). Red Río, componente aguas subterráneas Convenio 1050.
- Betancur-Vargas, T. (2021). *Potencial & perspectivas de exploración hidrogeológica en Antioquia según criterios litoestructurales*

- [Memory]. XVIII Congreso Colombiano de Geología, 2021. <https://sociedadcolombianadegeologia.org/potencial-y-perspectivas-de-exploracion-hidrogeologica-en-antioquia-segun-criterios-litoestructurales/>
- Betancur-Vargas, T., Martínez-Uribe, C., García-Aristizábal, E. F., & Escobar-Martínez, J. F. (2017). Identification and characterization of regional water flows contributing to the recharge of an unconfined aquifer. *Revista Facultad de Ingeniería*, (85), 70-85. <https://doi.org/10.17533/udea.redin.n85a07>
- Bullock, S. H., Mooney, H. A., & Medina, E. (eds). (1995). *Seasonally Dry Tropical Forests*. Cambridge University Press. <https://doi.org/10.1017/CBO9780511753398>
- Cabrera-Montenegro, E., & Galindo-García, G. A. (2006). *Aproximación metodológica para la delimitación de los ecosistemas de enclaves secos. Caso piloto: Cañones del río Dagua & del río Tuluá*. Instituto de Investigación de Recursos Biológicos Alexander von Humboldt.
- Consortio POMCAS Oriente Antioqueño. (2017). *POMCA Río Negro*.
- Corantioquia & Gotta Ingeniería. (2016). *Estudio regional del Agua (Bajo Cauca Antioqueño)*.
- Corantioquia & Gotta Ingeniería. (2016). *Estudio regional del Agua (La Pintada - Valparaíso)*.
- Corantioquia & Gotta Ingeniería. (2016). *Estudio regional del Agua (Valle Medio del Magdalena)*.
- Corantioquia & Gotta Ingeniería. (2017). *Formulación del Plan de Manejo Ambiental del Acuífero del Magdalena Medio*.
- Corantioquia & Gotta Ingeniería. (2017). *Formulación del Plan de Manejo Ambiental del Sistema Acuífero del Occidente Antioqueño*.
- Corantioquia & Servicios Hidrogeológicos Integrales. (2014). *Evaluación Hidrogeológica en los Municipios de La Pintada & Valparaíso Jurisdicción de la Dirección Territorial Cartama de Corantioquia*.
- Corantioquia & Servicios Hidrogeológicos Integrales. (2016). *Estudio Regional del Agua (Santa Fe de Antioquia)*.
- Corantioquia & Universidad de Antioquia. (2014). *Plan de Manejo Ambiental del Sistema de Acuífero del Bajo Cauca Antioqueño*.
- Corantioquia & Universidad de Antioquia. (2021). *Aunar esfuerzos para la exploración del potencial hidrogeológico en zonas de bosque seco en el cañón del río Cauca en la jurisdicción de Corantioquia, Medellín*.
- Corantioquia & Universidad Nacional de Colombia. (2001). *Investigación de Aguas Subterráneas Región Valles de San Nicolás, Fase II*.
- Cornare. (2016). *ICA Aguas Subterráneas de los Valles de San Nicolás & La Unión*.
- Corpourabá. (2016). *Análisis de calidad & cantidad del recurso hídrico del Golfo de Urabá*.
- Custodio, E., & Llamas, M. R. (1996). *Hidrología subterránea*, (vol. 2.). Ediciones Omega S. A.
- Etter, A. C., McAlpine, C., & Possingham, H. (2008). A historical analysis of the spatial and temporal drivers of landscape change in Colombia since 1500. *Annals of the American Association of Geographers*, 98(1), 2-23. <https://www.jstor.org/stable/25515096>
- Fundación Empresas Públicas de Medellín & Gobernación de Antioquia. (2018). *Antioquia, un territorio para proteger*. Fundación EPM.
- González, H. (2001). Mapa geológico del departamento de Antioquia. Memoria explicativa. Ingeominas. <https://miig.sgc.gov.co/Paginas/Resultados.aspx?k=BusquedaPredefinida=-DGBMapGeolDepart>
- Instituto de Investigación de Recursos Biológicos Alexander von Humboldt. (1998). *El Bosque Seco Tropical (Bs-T) en Colombia*. <https://media.utp.edu.co/ciebreg/archivos/bosque-seco-tropical/el-bosque-seco-tropical-en-colombia.pdf>
- Instituto de Investigación de Recursos Biológicos Alexander von Humboldt. (1997). Informe Nacional Sobre el Estado de la Biodiversidad. PNUMA, Ministerio de Medio Ambiente, Bogotá, Colombia.
- Instituto de Investigación de Recursos Biológicos Alexander von Humboldt. (2014). Mapa actual real de bosque seco tropical en Colombia a escala 1:100 000. <http://www.humboldt.org.co/images/documentos/pdf/investigacion/mxd-bst.jpg>
- Le Maitre, D. C., Scott, D. F., & Colvin, C. (1999). Review of information on interactions between vegetation and groundwater. <https://researchspace.csir.co.za/dspace/handle/10204/524>
- Pizano, C., & García, H. (eds.) (2014). *El bosque seco tropical en Colombia*. Instituto de Investigación de Recursos Biológicos Alexander von Humboldt. <http://repository.humboldt.org.co/handle/20.500.11761/9333>
- Saaty, T. L. (2008). Decision making with the analytic hierarchy process. *International Journal of Services Sciences*, 1(1), 83. <https://doi.org/10.1504/IJSSCI.2008.017590>
- Universidad de Antioquia & Corpouraba. (2016). *Plan de Manejo Ambiental de Acuífero Sistema Hidrogeológico Golfo de Urabá*. Convenio de cooperación número 21302406-005-2015. Informe final. <http://repositorio.corpouraba.gov.co:8082/xmlui/handle/123456789/87>



Case study article

# Region-scale estimation of potential groundwater recharge in soft and hard rock formations through a distributed water balance in the area of influence of the tropical dry forest in the Cauca River canyon, Antioquia, Colombia

Estimaciones regionales de recarga potencial de aguas subterráneas en formaciones blandas y rocas duras, mediante un balance hídrico distribuido en zona de influencia del bosque seco tropical en el cañón del río Cauca, Antioquia, Colombia

Breiner Dan Bastidas<sup>1</sup>, Juliana Ossa<sup>1</sup>, Cristina Martínez<sup>1</sup>, María Alejandra Vela<sup>1</sup>, Teresita Betancur<sup>1</sup>, Arbei Osorio<sup>1, 2</sup>

<sup>1</sup> Faculty of Engineering, Universidad de Antioquia (University of Antioquia), Medellín, Colombia.

<sup>2</sup> Corporación Autónoma Regional del Centro de Antioquia (Regional Autonomous Corporation of Antioquia) (Corantioquia), Medellín, Colombia.

**Corresponding author:** Breiner Dan Bastidas, breiner.bastidas@udea.edu.co

## ABSTRACT

Groundwater potential recharge is commonly estimated by water balances per hydrogeological unit. Most studies in Antioquia (Colombia) examine recharge in alluvial deposits or sedimentary rock units. The evaluation of the hydrogeological potential in the area of influence of the tropical dry forest in the Cauca River canyon, in the jurisdiction of Corantioquia, began in 2020, including regional estimates of potential recharge by precipitation. Recharge was estimated through a distributed soil water balance model at a daily time step, which efficiently incorporated the spatiotemporal variability of the meteorological conditions of the region as well as the spatial variability of the surface properties, such as soils, land cover and topography.

Between 2013 and 2020, annual recharge rates were estimated to vary spatially between 5 mm/year and 2000 mm/year, which represents between 0.4% and 45% of the annual precipitation, with a spatial and multiyear average of 342 mm/year (17% of precipitation). The aquifers of the Penderisco Formation are characterized by an average annual potential recharge of between 284 mm (to the northwest) and 756 mm (to the southwest), the aquifers of the Combia Formation show average annual recharge rates of 456 mm, and the unconfined aquifer of Western Antioquia and others associated with Quaternary deposits record average annual

recharge rates of 36 mm. The recharge behavior in the area favors regional flows between hydrogeological units and confirms the considerable hydrogeological potential of various units of fractured hard rocks.

**Keywords:** potential recharge, distributed water balance, soft formations and fractured media, regional estimates, tropical dry forest, regional flows.

## RESUMEN

La recarga potencial de aguas subterráneas se estima comúnmente mediante balances hídricos por unidad hidrogeológica. La mayoría de los estudios en Antioquia (Colombia) se refieren a la recarga en depósitos aluviales o unidades de rocas sedimentarias. En 2020 se inició la evaluación del potencial hidrogeológico en zona de influencia del bosque seco tropical en el cañón del río Cauca, en jurisdicción de Corantioquia, incluyendo estimaciones regionales de recarga potencial por precipitación. La estimación de la recarga se realizó a través de un modelo distribuido de balance de humedad en el suelo a escala diaria, en el que se incorporó de manera eficiente la variabilidad espaciotemporal de las condiciones meteorológicas de la región, así como la variabilidad espacial de las propiedades de superficie, como suelos, coberturas terrestres y topografía.

Entre 2013 y 2020 se estimaron tasas de recarga anual que varían espacialmente entre 5 mm/año y 2000 mm/año, lo que representa entre 0,4 % y 45 % de la precipitación, con promedio espacial y multianual de 342 mm/año (17 % de la precipitación). Los acuíferos de la Formación Penderisco se caracterizan por recarga potencial media anual entre 284 mm (al noroeste) y 756 mm (al suroeste); los acuíferos de la Formación Combia presentan tasas de recarga media anual de 456 mm; el Acuífero Libre del Occidente Antioqueño y otros asociados a depósitos cuaternarios registran tasas de recarga media anual de 36 mm. El comportamiento evidenciado de recarga en la zona favorece la condición de flujos regionales entre unidades hidrogeológicas y ratifica el potencial hidrogeológico significativo de diversas unidades de rocas duras fracturadas.

**Palabras clave:** recarga potencial, balance hídrico distribuido, formaciones blandas y medios fracturados, estimaciones regionales, bosque seco tropical, flujos regionales.

## 1. INTRODUCTION

Groundwater accounts for more than 96% of the planet's fresh water (Lamichhane and Shakya, 2019). Its movement through the soil is conditioned by the climatic, geological and hydrological characteristics present during the recharge, transit and discharge processes (De Vries and Simmers, 2002; Harlow and Hagedorn, 2018; Mussa et al., 2021). According to Hussin et al. (2020), groundwater extraction worldwide occurs at an approximate rate of 986 km<sup>3</sup>/year, and its overexploitation has been causing problems in several regions, especially in arid and semiarid areas.

Groundwater recharge is a part of the hydrological cycle that has a significant contribution to the water balance at the local, regional and global scales (Fauzia et al., 2021). Those areas where the soil allows the infiltration and percolation of water through its layers until reaching the vadose zone or continuing to flow to an aquifer are identified as *potential recharge zones* (Ahmed et al., 2021). Understanding the recharge and discharge balance of the aquifers forms the basis of groundwater resource management (Moeck et al., 2020).

Measuring natural recharge directly and accurately is challenging because the processes vary spatiotemporally according to climate, soil and geology, surface topography, hydrology and vegetation (Barua et al., 2021; Harlow and Hagedorn, 2018; Hussin et al., 2020). To accommodate the specific site conditions, different methods involving different spatial and temporal scales, ranges and reliabilities are used to estimate groundwater recharge. The uncertainties in each approach to estimate the recharge underscore the need to apply multiple techniques to improve the reliability of the calculated estimates (Scanlon et al., 2002).

Among the methods cited in the specialized literature to evaluate recharge are the application of Darcy's law, the measurement of infiltration through lysimeters installed in the unsaturated zone, the measurement and modeling of soil moisture content, estimates of heat flow, basin-scale water balances, remote sensing, numerical models, the water-table fluctuation (WTF) method and balancing chlorides and/or radioisotope concentrations (Barua et al., 2021). Most of these techniques are reliable at the level of experimental plots or in studies that cover local areas.

Dos Santos et al. (2021) estimated two types of recharge for the Cerrado basin in Brazil and determined the potential recharge through distributed modeling and the effective recharge with numerical modeling, the WTF method and base flow separation. Oliveira et al. (2015) evaluated the influence of land cover on the water balance of an undisturbed area in the Cerrado. Wang et al. (2021) applied the concept of *stable base flow* to estimate groundwater recharge in ten hydrogeological regions in Taiwan under historical conditions and climatic scenarios. Peijun et al. (2021) used tracers (isotopes of water, chlorides and nitrates) to estimate the recharge rates with methods that consider the differences in deep and shallow rooted vegetation as well as in the unsaturated and saturated zones.

When covering areas of regional extension, in which geological, physiographic and hydroclimatological variations can be recorded and, consequently, different ecosystems evolve, the recharge distribution includes direct recharge, which is generated by rainfall (also called diffuse recharge) that reaches aquifers or generates deep percolation that, over time, takes part in regional flows. In this sense, it is notable that the study of classical hydrogeology has focused on the knowledge of hydrogeological units associated with primary porosity; however, the need for hydrogeological exploration in rocks that have acquired secondary porosity, which function as reservoirs, recharge and transit zones in regional aquifer systems and serve as water resources to the population, is becoming increasingly evident (Koïta et al., 2018).

Much of the water available in ecosystems such as the tropical dry forest (TDF) is found in lowlands, between 0 m and 1000 m of altitude, in tropical areas with temperatures above 24 °C and annual precipitation between 700 mm and 2000 mm; these areas experience one or two periods of marked drought per year—with less than 100 mm of precipitation—of at least five to six months (Mooney et al., 1995, cited by Pizano and García, 2014). Under these conditions, direct recharge is usually low. Thus, the sustainability of this ecosystem is generally dependent on groundwater contributions from adjacent hydrogeological units that have received direct recharge, which is then transported laterally through regional flows, depending on the structural patterns in the zone. In this article, *sustainability* refers to the water available to biological processes of the TDF ecosystem vegetation. Given these conditions, it is essential to further explore the estimation and calculation of recharge at the regional scale, where direct recharge flows in some areas can subsequently become indirect recharge flows for other areas that are geologically, geomorphologically and hydraulically connected.

Some studies have used numerical models of groundwater flow and have dynamically linked them with hydrological models to estimate recharge variations in different climatic and land cover conditions (Aguilera and Murillo, 2009; Herrera-Pantoja and Hiscock, 2008; Jabloun and Sahli, 2012). The soil water balance model has been widely used to evaluate recharge by precipitation and is generally combined with other techniques, such as geographic information systems (GIS) and numerical flow models (Melo et al., 2015; Vela Mayorga, 2001; Westenbroek et al., 2010). It should be noted, however, that the water balance method usually provides results for direct potential recharge and not actual recharge since it does not incorporate enough information from the saturated zone.

Thus, soil water balance models are currently the most useful (Xie et al., 2017) since they help to efficiently estimate the direct potential recharge associated with precipitation and its response to surface changes (land cover, land use, precipitation, evapotranspiration), which makes these methods valuable tools for the comprehensive management of water resources and projection of these resources over time (Ehlers et al., 2016; Harlow and Hagedorn, 2018; Mair et al., 2013; Westenbroek et al., 2010). Soil water balance models can be subdivided into *mathematical reservoir-type approximations* and *coupled mathematical models* (Xie et al., 2017). The former simplifies the medium into vertical cells where water is stored or discharged by inflow (precipitation), outflow (evapotranspiration) and excess storage capacity (recharge), while the coupled models represent the evapotranspiration process as a submodel (greater refinement) and transit the infiltration through the unsaturated zone as a response to the Richard equation for flow in the vadose zone (Ruiz et al., 2010; Turkeltaub et al., 2015).

Soil water balance (SWB) (Westenbroek et al., 2010) is a distributed model implemented and widely used by the United States Geological Survey (USGS) for different hydrological environments of the United States and also used in some areas of Korea and recently in regions of Colombia (Bastidas, 2019; Engott et al., 2017; Harlow and Hagedorn, 2018; Johnson et al., 2018; Bradbury et al., 2017; Mair et al., 2013; Oviedo, 2020; Patiño, 2021; Westenbroek et al., 2010, 2018). The most notable advantage of this model is its ability to evaluate and spatially incorporate the regional factors involved in the direct recharge process (Harlow and Hagedorn, 2018), in addition to allowing the simulation of this hydrological flow over long and continuous periods of time, such as several years and even decades, all at a detailed time step, such as the daily scale. Several authors have shown that direct

recharge estimates, calculated at a monthly scale, differ significantly from those presented on a daily scale; the latter is the most recommended (Harlow and Hagedorn, 2018; Jasechko and Taylor, 2015; Scanlon et al., 2002).

The purpose of this work was to contribute to constructing a conceptual hydrogeological model in a complex geological, physiographic and hydroclimatological zone to estimate the direct potential recharge over the area and zone of influence of the TDF in the department of Antioquia. The results help identify the factors that contribute to the regional dynamics of groundwater flow and that can affect the sustainability of one of the most vulnerable ecosystems in Colombia. The SWB model described is the most relevant for achieving the defined objective since it can evaluate the impact of the variability of the different physical factors on the spatial distribution and magnitude of the recharge. The information necessary to characterize the water balance and, consequently, estimate the recharge is described in this article, as are the methods used for information collection, model execution, processing and analysis.

## 2. REFERENCE FRAMEWORK

The study area (Figure 1) is demarcated in the department of Antioquia (Colombia, South America) by a polygon that brings together several hydrographic subzones of the Cauca River basin and that are directly or indirectly associated with the TDF ecosystem. Among the main tributaries along with the Cauca River are the Aurrá, San Juan, Piedras, Poblano, Amagá and El Buey rivers (see Figure 3d).

The study area has been defined at the scale of basins afferent to the Cauca River canyon based on the hypothesis that the dynamics of the water supply of the TDF ecosystem depend not only on the underground water availability throughout the ecosystem but also on lateral contributions of groundwater due to conditions such as climatology, topography and hydrogeological units. As explained in the introduction, these contributions can come from the upper watersheds, as observed by Vélez and Rhenals (2008) in the aquifers of western Antioquia, which are part of the study area of this research.

The study area elevation ranges from 171 meters above sea level (masl) to 3609 masl, with an approximate area of 10 662 km<sup>2</sup>. According to the precipitation and temperature data recorded in the *Statistical Yearbook of Antioquia* (Gobernación de Antioquia, 2018), the municipalities with the highest precipitation are within the upper slopes of the mountain ran-

ges and record average values above 2000 mm/year; near the Cauca River (bottom of the canyon), precipitation tends to be less than 1000 mm/year. The maximum temperatures fluctuate between 27 °C and 29 °C at the bottom of the Cauca River canyon, while the lowest (<15 °C) occurs in the higher-elevation municipalities. Therefore, it is deduced that the spatial behavior of precipitation and temperatures in the study area is strongly marked by the topographic gradient. The regions with average temperatures above 24 °C are located at elevations below 1000 masl and where precipitation is less than 2000 mm/year (Murphy and Lugo, 1986), showing typical conditions of the TDF ecosystems. Specifically, the TDF is present in the territory of municipalities along the Cauca River and is connected, along the eastern slopes of the Western Cordillera and the Central Cordillera, with other related ecosystems.

Originally, there were 150 400 ha of TDF associated with the Cauca River in Antioquia, from the southern border with the department of Caldas to the north in the municipality of Valdivia. According to the current cover map (Pizano and García, 2014), only 44 485 ha, 30% of the original cover, remains; of this total, 17% is TDF and 13% is successional vegetation.

In this territory, anthropogenic intervention has increased with the development of road infrastructure projects; in addition, there is considerable pressure on the extraction of metallic minerals (copper and gold), which has triggered opposition by the people to some projects. The economic dynamics of the region are fundamentally related to the activities that occur in the northern, western and southwestern subregions of Antioquia, especially livestock and agriculture in the north and west; the dairy and meat industry in the north; tourism, mining and logging in the west; and coffee and mining in the southwest.

The geological characteristics of the study area provide important elements for determining potential hydrogeological conditions, including recharge.

Through exercises of superposition, comparison and adjustments to define units and employ standardized nomenclature, the *geological map of Antioquia* was modified (González, 2001) from the official cartography, at a scale of 1:100 000, available in the geoportal of the SGC (Calle and González, 1980, 1982; Hall et al., 1970a, 1970b; Mejía, 1984a, 1984b; Servicio Geológico Colombiano, 1979, 1996). As a result of this process, Betancur (2021) assembled a synthesized geological map for the study area, as shown in Figure 1. With hydrogeological criteria, the description of the geology focused on determining the conditions of porosity and permeability that are

key in facilitating the storage and flow of groundwater. Both for deposits and clastic sedimentary rocks, as well as for hard rocks, the condition of the hydrogeological unit and its potential as an aquifer was determined.

The oldest units date from the Proterozoic and Paleozoic, which correspond to metamorphic rocks: migmatites (PeAmm); feldspathic and aluminum quartz gneisses (Pzmf, Pznl); rocks of the Cajamarca Complex, such as quartz-sericite schist (Pzes), chlorite-actinolite schists (Pzev) and intercalated schists (Pzes + Pzev); and amphibolites are also recorded (Pza). Along the western flank of the Central Cordillera is a tectonically elongated belt of medium-pressure metamorphites called the Arquía Complex (Kica), which, due to its tectostrucutural involvement, has developed secondary permeability. Both flanks of the Central Cordillera are characterized by the presence of variable-sized bodies, elongated in the regional tectonic direction, of syntectonic intrusives of gneissic structure; their ages are Paleozoic, and they are found in Abejorral and

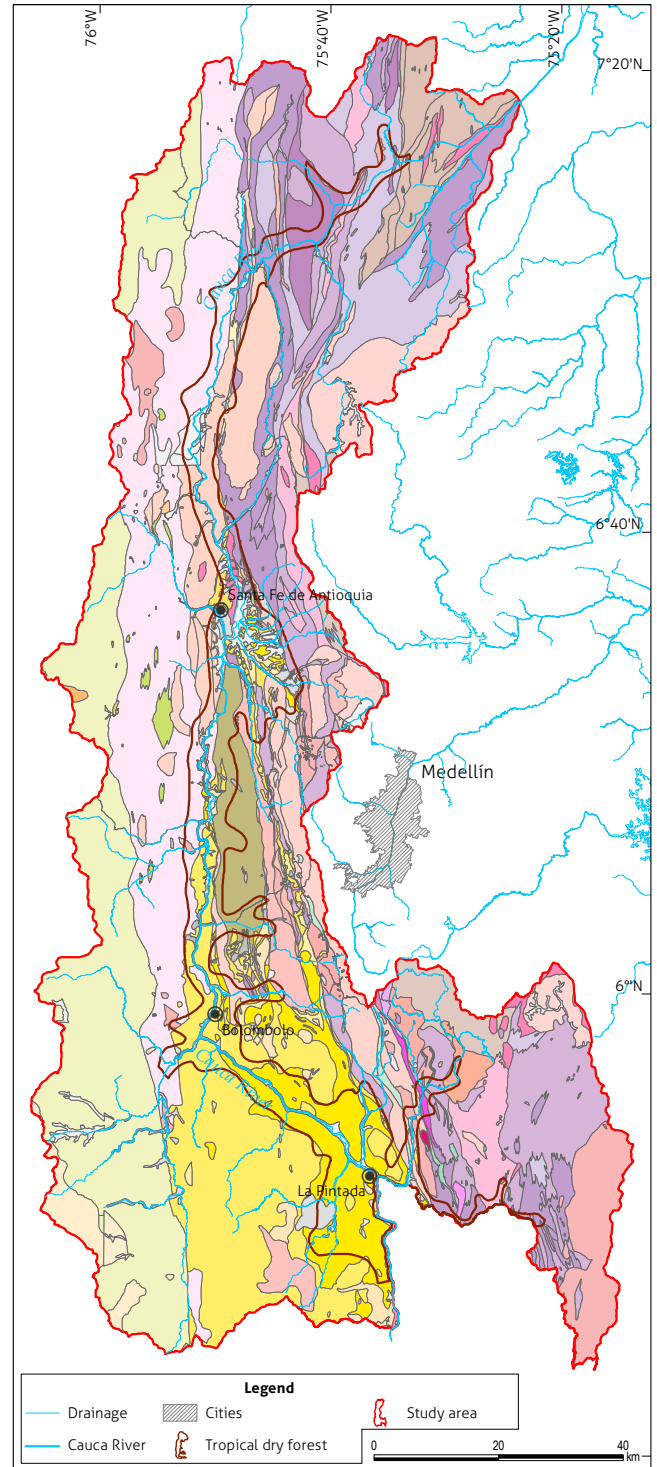
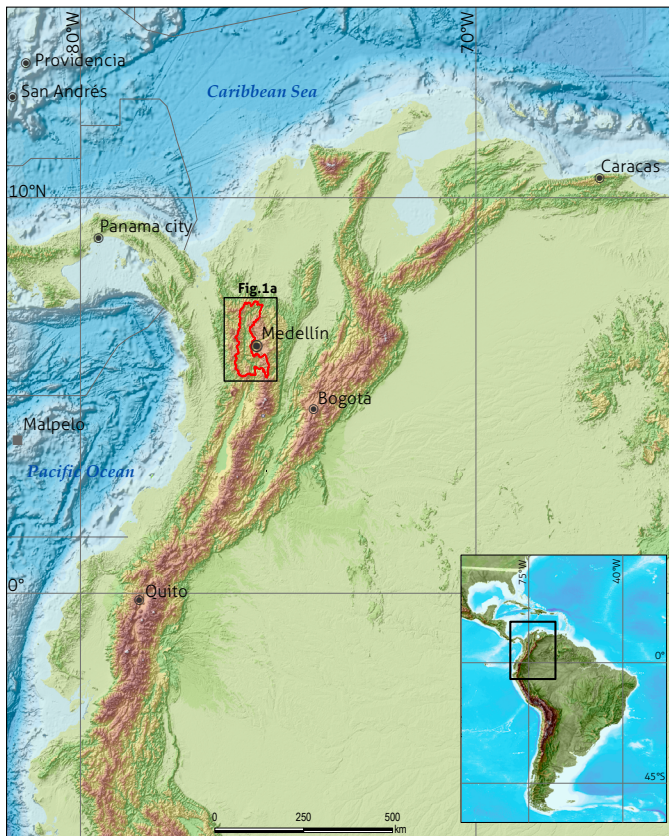


**Figure 1.** Delimitation of the study area and geological units present. Description of the complete geological legend available in the supplementary data. See legend in this [kmz file](#) (see in Google Earth). Source: modified from González (2001).

Alto de Minas (Pnim), Pantanillo (Pnip) and Río Verde (Pniv) (González, 2001).

Igneous activity in the Central Cordillera extended until the Triassic with the intrusion of adamellite stocks on the western flank of this mountain range (Honda Stock [TraH], Quebrada Liborina stock [TradL] and Buey stock [Trab]) and continued more intensely during the Jurassic with the intrusion of the Segovia and Sonsón batholiths (Jts), continuing until the end of the Cretaceous with the formation of the Antioquia Batholith (Ksta). A significant number of manifestations of igneous units complete the lithology of hard rocks (González, 2001).

Cretaceous sedimentary rocks are found in both the Central and Western Cordillera. According to their geographical or tectonic position and age, the following units were defined: San Pablo Formation, La Soledad Formation, Abejorral Formation (Kisa), Quebradagrande Group (Kisqg) and Cañasgordas Group (Urrao Member: Ksu; Cañasgordas Member: Ksn).

Belonging to the Cenozoic, the main soft formations (deposits, clastic sedimentary rocks and volcanoclastic rocks) are found in the Cauca River Valley in Antioquia. The accumulation of these materials was influenced by tectonism and subsequent magmatic activity; the Amagá Formation (lower member: Pgai; middle member: Pgam; and upper member: Ngas) and the Combia Formation (Ngc) stand out for their magnitude (González, 2001).

Quaternary deposits are mainly alluvial (Qal, Qat and Qt) and extend toward the flat areas of the department. Flow and colluvial deposits (Qcl), due to their extension, are not always represented on the map, although they may be locally important (González, 2001).

The crustal structure in the department of Antioquia is the result of the processes that were generated by the joining of the Nazca, Caribbean and South American plates. The Neogene and Quaternary deformations frequently overlap. Several fault zones with Quaternary displacement are located along the old shear zones that constitute subduction zones (González, 2001).

### 3. MATERIALS AND METHODS

#### 3.1. Distributed soil water balance (SWB) model

The principle of soil water balance is based on applying the law of conservation of mass, which takes the first soil strata (soil-plant system) as the control volume and schematizes all the natural flows involved in the generation of recharge, as shown in Figure 2. For this research, the distributed SWB model was

used (Westenbroek et al., 2010), which is deterministic, distributed and quasi-three-dimensional and operates on a daily scale; its spatial variability is given by a gridded arrangement in which various physical variables that influence the recharge process are configured, such as soil properties, land cover, topography (flow directions) and weather conditions (mainly precipitation and temperature).

The use of a distributed model to solve the water balance is pertinent given the considerable extent of the study area and the wide spatial variability presented by the physical variables that influence the recharge process. A distributed model allows the optimal incorporation and continuity of this variability to evaluate its impact on the spatial distribution of the magnitude of the recharge.

In the SWB model, the direct potential recharge is estimated as the remainder of the water balance in the defined control volume, where the vadose zone is conceptualized as a set of reservoirs in horizontal grid cells with variable thickness, depending on the depth of the roots. To solve the balance equation, a modified version of the Thornthwaite and Mather method is used to determine soil moisture and actual evapotranspiration at each time step and in each cell of the model domain (Bastidas, 2019). The soil water balance equation applied in the gridded cell SWB model is as follows:

$$DPR = Inflow - Outflow - Storage\ variation \quad (1)$$

$$DPR = (P + IF) - (Inp + ETa + DR) - \Delta H \quad (2)$$

where DPR: direct potential recharge; P: precipitation; IF: inflow from other cells; Inp: interception in the foliage; ETa: actual evapotranspiration; DR: direct surface runoff;  $\Delta H$ : variation in soil moisture.

#### 3.2. Information available and acquired

The information necessary to apply the distributed SWB model and thus obtain regional estimates of direct potential recharge is categorized into three large groups: soil and cover information, hydrometeorological data and geomorphological data. For the analysis of the water balance, it is assumed that the soil, cover and geomorphological data associated with the topography and the drainage network do not vary in time but do vary in space; therefore, they are called *static data* (invariant in time). While the hydrometeorological data vary in both space and time and are called *dynamic data*.

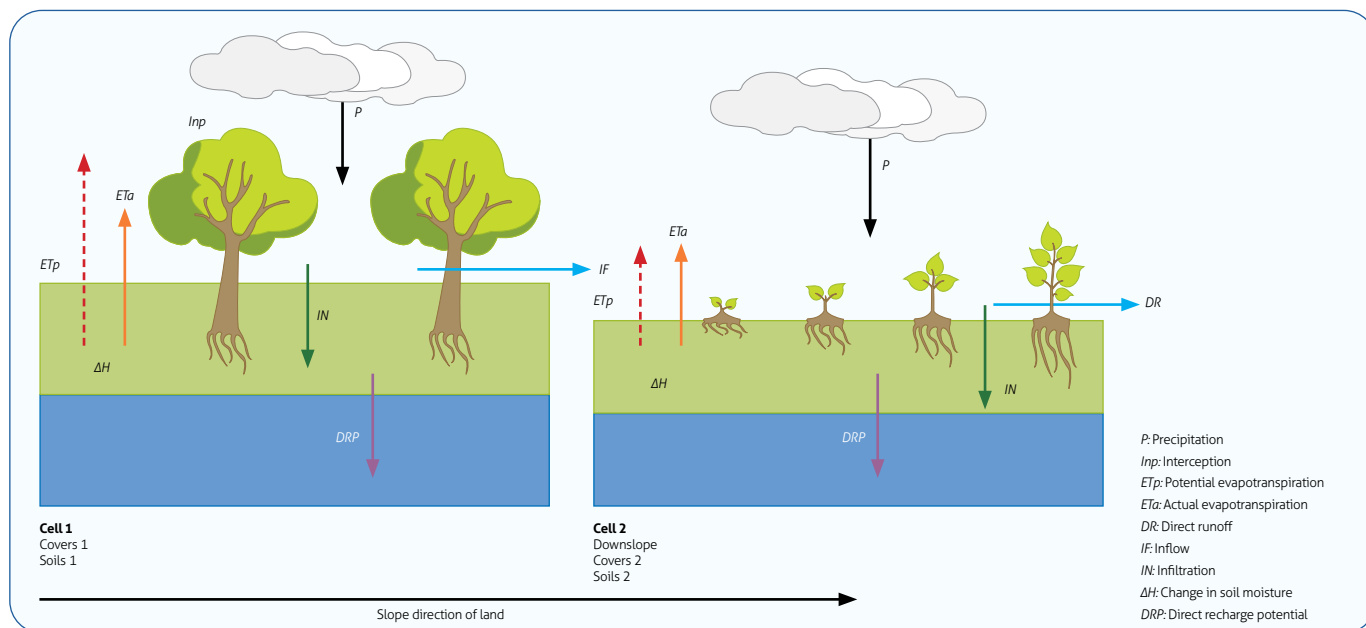


**Figure 2.** Diagram representing the soil-plant control volume cell by cell in the SWB model domain and the elements of the soil moisture balance involved in the estimation of the direct potential recharge. Source: Bastidas (2019).

Hydrometeorological data are an input for the application of the water balance, since precipitation is the main input to the control volume where the soil moisture balance is defined, and other hydrometeorological variables, such as temperature, solar brightness and relative humidity, are useful for the estimation of evapotranspiration. Based on this information, a clear and detailed hydroclimatological context for the region is constructed, which helps to better define the application scenarios of the water balance.

The hydrometeorological information consists of the daily records of the monitoring stations of the Institute of Hydrology, Meteorology and Environmental Studies (Ideam) (142 stations within and near the study area) and the Piragua monitoring network of Corantioquia (58 stations within and near the study area).

In total, information was obtained from 137 pluviometric and pluviographic stations and 35 weather and 28 limnigraphic and limnimetric stations. Of these 200 stations, 191 series of total daily precipitation were obtained, 23 of daily maximum temperature, 23 of daily minimum temperature, 24 of daily average flow and one of daily relative humidity. With this information from the hydrometeorological stations, whose locations are shown in Figure 3a, it was possible to obtain an adequate hydrometeorological context of the region and suffi-

cient information for the application of the distributed water balance model.

The geomorphological data correspond to a digital elevation model (DEM) and a detailed surface drainage network. The DEM is obtained from the Advanced Spaceborne Thermal Emission and Reflection Radiometer (ASTER) satellite mission, which can be downloaded for free on the website <http://asterweb.jpl.nasa.gov>, and has a spatial resolution of 30 m  $\times$  30 m pixel size. This DEM is shown in Figure 3d, adequately representing the relief of the study area, and elevations ranging from 167 masl can be seen at the bottom of the canyon and toward the north, up to 3609 masl in the headwaters of the main tributary basins. The DEM was obtained from the Advanced Land Observation Satellite (ALOS), which collects terrestrial images through its Phased Array Type L-band Synthetic Aperture Radar (PALSAR) sensor (ASF DAAC, 2015), with a spatial resolution of 12.5 m  $\times$  12.5 m pixels, and was also initially considered for the study area; however, given its regional extension, it was considered pertinent to work at a coarser resolution to reduce the computational times of the model, so the ASTER DEM was selected.

Regarding the drainage network, information from two main sources was used: the double and single drainage network of the Agustín Codazzi Geographic Institute (IGAC) at a scale of 1:100 000 and the single and double drainage network

of Corantioquia at a scale of 1:25 000. Figure 3 shows the cartographic generalities of the drainage network in the study area.

The soil information was obtained from *the General study of soils and land zoning of the department of Antioquia*, conducted by the Agustín Codazzi Geographical Institute (IGAC and Gobernación de Antioquia, 2007) at a scale of 1:100 000, which describes the soil mapping units of the entire department, and includes planning and management information for the watersheds (POMCA) of the Amagá River-Sinifaná Creek and the Aurrá River at a scale of 1:25 000 (Corantioquia et al., 2018a; Corantioquia et al., 2018b). For each mapping unit, various soil profiles surveyed in the field are presented in the framework of these studies; within the description of the profiles is the granulometry of these profiles at different depths and their textural classification.

In the study area, 41 soil mapping units are identified, which, in turn, are subdivided into 202 units differentiated by geomorphological phases (slope and erosion). In the study area and its surroundings, 157 soil profiles obtained from the IGAC study (2007) and 60 soil profiles obtained from the aforementioned POMCAs (21 from the Aurrá River POMCA and 39 from the Amagá River-Sinifaná Creek POMCA) were identified. From these profiles, it is possible to directly characterize 94 of the soil mapping units differentiated by geomorphological phases. Although there is a considerable number of profiles, these are distributed in such a way that they are not sufficient to adequately characterize the properties of the soil mapping units in the study area; as a result, there are various areas of spatial information gaps, mainly in the northern area. Therefore, in the framework of this research, soil samples were taken at 30 points in the field for particle-size analysis in the laboratory to refine and complete this information. The locations of the 217 profiles obtained from the baseline studies and the 30 soil samples are presented in Figure 3c.

Regarding land cover, three main sources of documentary information related to land cover in the study area were used: 1) *National land cover map of Colombia according to the Corine Land Cover methodology* (Ideam, 2010), 2) *POMCA - Planning and management plan of the hydrographic basin of the Amagá River and Sinifaná Creek* (Corantioquia et al., 2018b), 3) *POMCA - Aurrá River Watershed Management and Landuse Plan* (Corantioquia et al., 2018a). Given the regional scale and the extension of the study area, the land cover is based on the national cover map, interpreted at level 3, which refers to the level of detail in the cartographic definition for each land cover unit.

According to the *Corine Land Cover* methodology adopted by Colombia, the level ranges from 1 (general) to 6 (maximum detail). This map and its legend are shown in Figure 3b.

### 3.3. Data treatment and processing

Specific treatments were performed on the hydrometeorological, geomorphological, soil and cover data with the objective of preparing the information to be used within the distributed SWB model.

The hydrometeorological data were processed to obtain the average annual cycle of the main variables involved in recharge: precipitation and temperature (as an indicator variable for the estimation of evapotranspiration). The basic quality analysis of the records was performed, defining record length, coincident periods between stations and percentage of missing data. Subsequently, the graphical and statistical correlation of precipitation with the macroclimatic phenomenon El Niño-Southern Oscillation (ENSO), the main modulator of the interannual variability of the climate in Colombia, was analyzed (Poveda, 2004; Poveda et al., 2002; Poveda and Álvarez, 2012). Based on the quality analysis of the records and the correlation with ENSO, the simulation period of the water balance was defined, which captures contrasting hydrological years (dry, wet and normal years).

Subsequently, the reconstruction of missing data in the daily records of precipitation and maximum and minimum temperatures for the simulation period was performed. The data were reconstructed through the mean ratio method (Unesco and Rostlac, 1982) and inverse distance weighted (IDW) interpolation (Echavarría, 2013).

For the simulation period, a series of daily maps of precipitation, maximum temperature and minimum temperature were generated in the study area with the objective of capturing and incorporating the spatiotemporal variability of these variables in the SWB model. To this end, recurring daily interpolations of the aforementioned variables were performed based on the implementation of the deterministic technique of thin plate spline interpolation (TPS) (Nychka et al., 2015) incorporated into a recurring code programmed in R (Bastidas Osejo and Betancur, 2019). The TPS is part of the family of polyharmonic splines, is widely used for the spatial smoothing of dispersed data and is considered a good deterministic approach to the universal kriging geostatistical procedure for various applications (Donato and Belongie, 2002; Moreles and Mejía, 2010).

The interpolations were performed for a cell size of 100 m × 100 m, and with the use of control points in areas where the

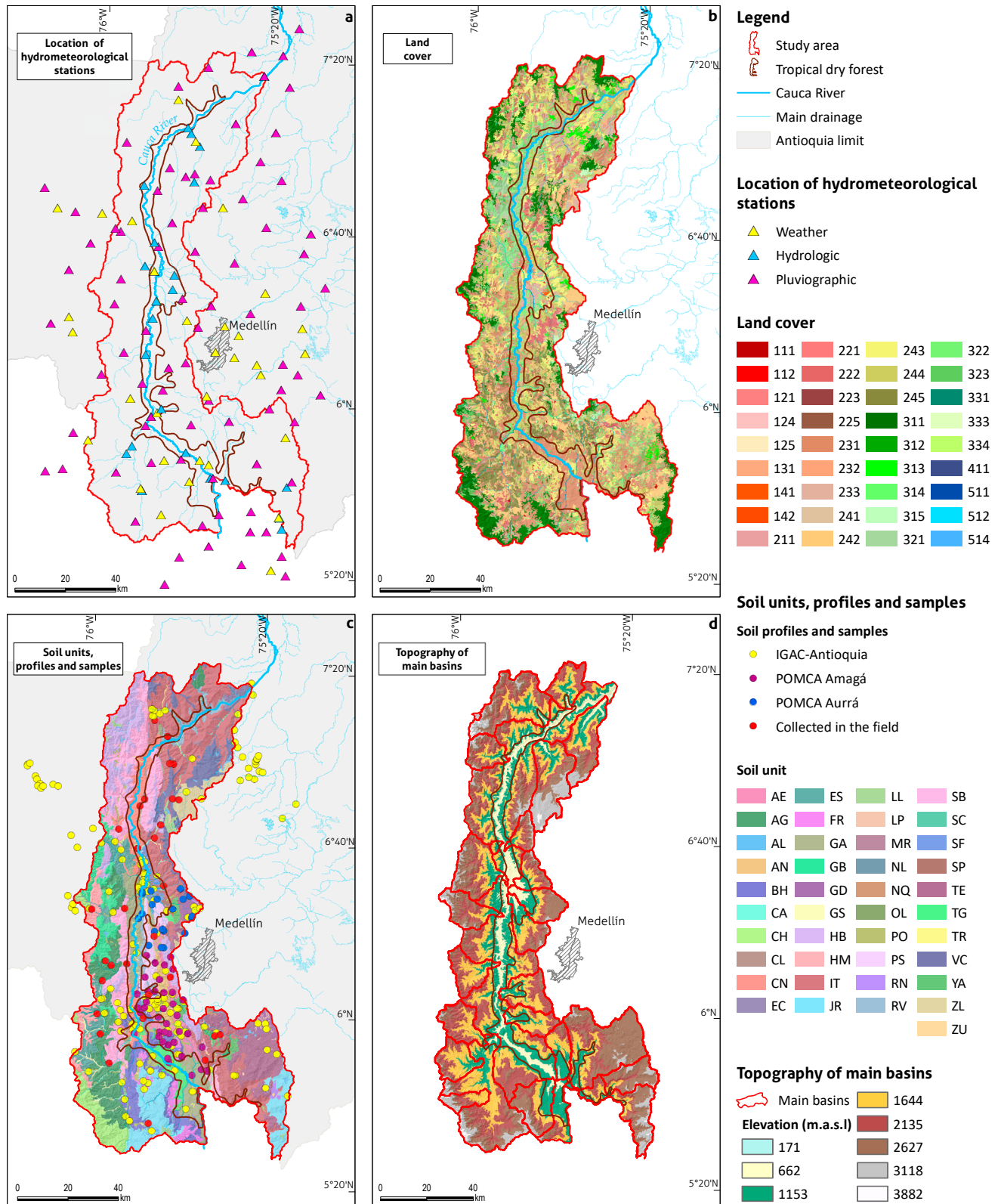


**Figure 3.** Graphic summary of the spatial information used for the implementation of the SWB model in the study area. Details of the stations used, description of the soil legend and description of the land cover are available in the supplementary data. See legend in this [kmz file](#) (see in Google Earth).

monitoring density was not sufficient; these were taken from the maps of the multiyear averages of the hydrometeorological variables generated in the framework of this research.

The geomorphological information was incorporated into the SWB model from the surface flow direction map (required in ArcGIS D8 format). The procedure for obtaining this information was described by O'Callaghan and Mark (1984) and Universidad Nacional de Colombia (2011) and is programmed in the *MapWindow software* with the *Watershed Delineation* tool. From the surface flow direction map, it is possible to outline the main hydrographic basins in the study area, which are shown in Figure 3d and generally correspond to hydrographic subzones defined by Ideam.

With the information of the 247 profiles and soil samples obtained in the study area, the soil properties required to run the SWB model were characterized: spatial distribution of soil textures (NRCS-USDA classification), spatial distribution of soils classified by hydrological group (according to the NRCS) and spatial distribution of the field capacity of the soils. These properties were particularly defined for each soil profile and sample in the study area, based on the reported particle-size composition (percentages of sands, silts and clays), with the use of the universally accepted textural triangle of the United States Department of Agriculture (USDA) (NRCS-USDA, 2018) and pedotransfer functions (Saxton and Rawls, 2006). The spatial distribution was determined from a geospatial analysis by soil mapping unit as follows: for each unit, a qualitative spatialization was carried out using the Thiessen (also known as Voronoi) polygons geometric technique (De Berg et al., 2008), with a subsequent adjustment to the limits of influence of each profile with geomorphological criteria (watershed divide, slope changes, drainage network, etc.). Finally, the mapping units differentiated by profile or area of influence were assembled in a single map following the methodology presented by Bastidas (2019).

The texture map obtained and used within the SWB model is shown in Figure 4a, in which a diversity of soil textures is observed, with a notable predominance of three types: sandy loam (29%), clay (20%) and clay loam (19%). These soil textures exhibit a defined spatial pattern, where the coarsest (loamy sand, sandy loam and loam) occur mainly in the upper part of the hydrographic basins associated with the Cauca River canyon. Among them are the upper part of the basins of the Arma River to the southeast, that of the San Juan River to the southwest, that of the Aurrá River between Sopetrán and San Jerónimo, that of the Tonusco River in Santa Fe de An-

tioquia and that of the Peque Creek and the Ituango River to the northwest. While the finest textures (clays and clay loams) are mainly present in the lower and middle parts of the basins, clayey textures are notably observed toward the bottom of the Cauca River canyon between Sabanalarga and Toledo and between clays and clay loams between Fredonia and Ebéjico.

The field capacity (FC) is the hydraulic property of the soil of greatest interest in the SWB model since it configures the maximum moisture capacity in the soil, which represents the threshold that must be exceeded for recharge processes to be generated. The FC was estimated from the textural data collected from the soils and with the application of the pedotransfer function of Saxton and Rawls (2006). Figure 4b shows the spatial distribution of the FC in the study area. It can be seen that the FC varies spatially between 16.7% and 48%, where the highest FC is recorded in the middle and lower parts of the basins, where there are finer textures, while the lowest FC occurs in the upper parts of the hydrographic basins, where coarser textures predominate.

### 3.4. Model settings

The SWB model version 1.0 estimates the surface runoff of grid cells using the *curve number* (CN) method (Cronshey et al., 1986); the estimated runoff in each cell runs downhill following the directions of surface flow (in D8 format), then becomes inflow to adjacent downslope cells and thus applies the algorithm described by O'Callaghan and Mark (1984) and the Universidad Nacional de Colombia (2011). The ability to route inflow in the model is considered an improvement in terms of traditional methods of estimating recharge by water balance (Harlow and Hagedorn, 2018). The model assumes that all the precipitation entering the model domain in one day is distributed in the different compartments and flows on the same day, including the total outflow of the runoff.

This model has five programmed methods to estimate potential evapotranspiration (ET<sub>p</sub>): Thornthwaite and Mather (1957); Turc (1961); Hargreaves and Samani (1985); Jensen-Haise (1963) and Blaney-Criddle (cited by Dockter and Palmer, 1994); for this research, the method of Hargreaves and Samani (1985) was used, mainly because it is the only one that allows the incorporation of the spatial variability of the ET<sub>p</sub> in the model and because of the amount of information required (daily maps of maximum and minimum temperature).

Part of the precipitated water can be intercepted by the plants before contacting the soil surface; this amount is called

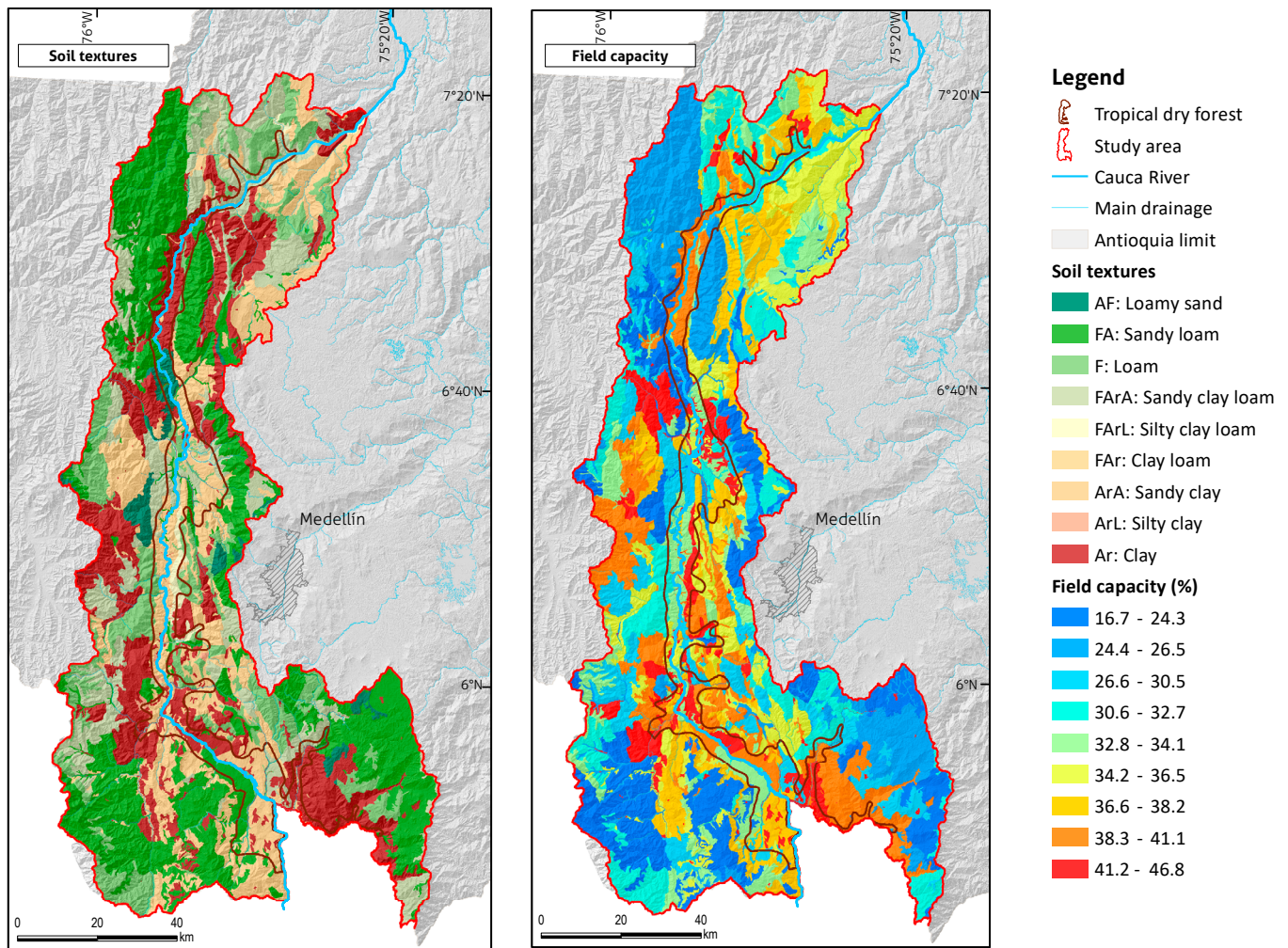


Figure 4. Spatial distribution of soil textures and field capacity in the study area. See legend in this [kmz file](#) (see in Google Earth).

interception by foliage, and within the SWB model, it is estimated in a simple manner from a reservoir approach (Westenbroek et al., 2010), based on thresholds that must be exceeded by precipitation, which depend on the type of land cover and hydrological conditions.

The joint occurrence of a specific type of soil and a specific type of cover defines various parameters of the SWB model, such as the CN for the three antecedent moisture conditions (normal CNII, dry CNI, wet CNIII) and the assumed percentage of impervious surface, maximum recharge rate ( $R_{max}$ ) and rooting depth (RD). These factors determine the vadose zone thickness (VZT), where evapotranspiration occurs, and represent the soil-plant control volume for the model (Dripps and Bradbury, 2007; Mair et al., 2013; Westenbroek et al., 2010).

From the cross between the type of soil and the type of cover, the aforementioned parameters are obtained, and the reference values for each cross are obtained from Thornthwaite and Mather (1957); Mockus (1965); Cronshey et al. (1986); Dripps and Bradbury (2007); Westenbroek et al. (2010). The values assigned to the parameters of curve number CN,  $R_{max}$  and RD, among others, are presented in the supplementary data.

The SWB model is configured to continuously simulate several years at a daily time step. To define the simulation period, two main criteria have been taken into account: a) availability of information to construct the input variables of the SWB model, mainly hydrometeorological information, and b) a continuous period that allows the capture of the seasonal and interannual variability of the hydrometeorological vari-

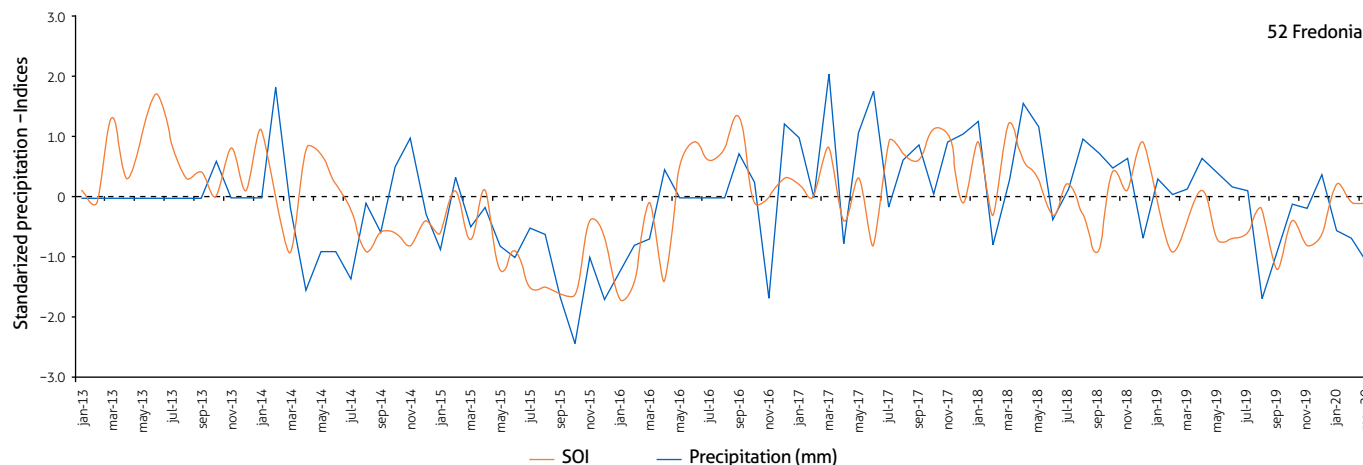


**Figure 5.** Standardized monthly precipitation at one of the stations in the study area (Station 52, Fredonia of Piragua) and its graphic temporal correlation with the occurrence of the ENSO phenomenon from the monthly series of the Southern Oscillation Index (SOI) Positive values indicate the occurrence of the La Niña cold phase, and negative values indicate the occurrence of the El Niño warm phase.

ables; thus, a dry, normal and wet year is captured. In the study area, an important relationship has been found between the macroclimatic phenomenon ENSO and the hydrometeorological variables, mainly precipitation, as illustrated in Figure 5. Therefore, the selected simulation period is also related to the occurrence of the cold and warm phases of ENSO.

The specific simulation period selected corresponds to 2012-2020, where the SWB model is started in 2012, so that it loses sensitivity to the initial soil moisture condition (a factor of high uncertainty in the simulations) (Westenbroek et al., 2010). That is, this same year is used for the internal calculations of the model, but no results of the estimated flows in that year are exported, nor are they analyzed.

The year 2014 is characterized as normal (neutral phase of the ENSO); 2015, a dry year (very strong El Niño), and 2018, a wet year (weak La Niña). Since the simulation scale of the

SWB model is daily, for the aforementioned period, the daily maps of maximum and minimum temperature and precipitation in the study area are generated, for which the previously mentioned methodology is followed, and 9864 maps are obtained, 3288 for each variable, which are stored in simple ASCII format, for a total storage volume of 323 GB.

Finally, Table 1 summarizes the SWB model applied to characterize the water balance in the study area.

#### 4. RESULTS

With all the inputs prepared for the study area, the SWB distributed model was executed in an approximate computation time of 72 hours (3 days) and the resulting file writing (monthly and annual potential recharge maps, actual evapotranspiration, potential evapotranspiration, interception by foliage, surface ru-

**Table 1.** General data of the specific SWB model settings to be applied to the study area

Coordinate system	Magna Colombia Bogotá Zone (3116)	Model operating units	inches (") and degrees Fahrenheit (°F)
Spatial domain of the model	Xmin: 774679	Model domain units	meters
	Ymin: 1094226	Number of rows	2149
	Xmax: 873479	Number of columns	988
	Ymax: 1309126	Cell size	100 m
Wet season	April-May and September-November	Precipitation (point or spatially distributed)	Distributed
Temperature (point or spatially distributed)	Distributed	Initial abstraction parameter	0.05
Evapotranspiration method	Hargreaves and Samani, (1985) (distributed)	Water storage capacity in the soil	Rooting depth by field capacity
Runoff method	Curve number	Time step	Daily
Initial soil moisture	At field capacity (100% FC)	Time scale of outputs	Monthly and yearly
Simulation period	January 2012 to December 2020	Output variables	Direct potential recharge, actual evapotranspiration, soil moisture, direct runoff, interception
Warm period	January 2012 to December 2012		

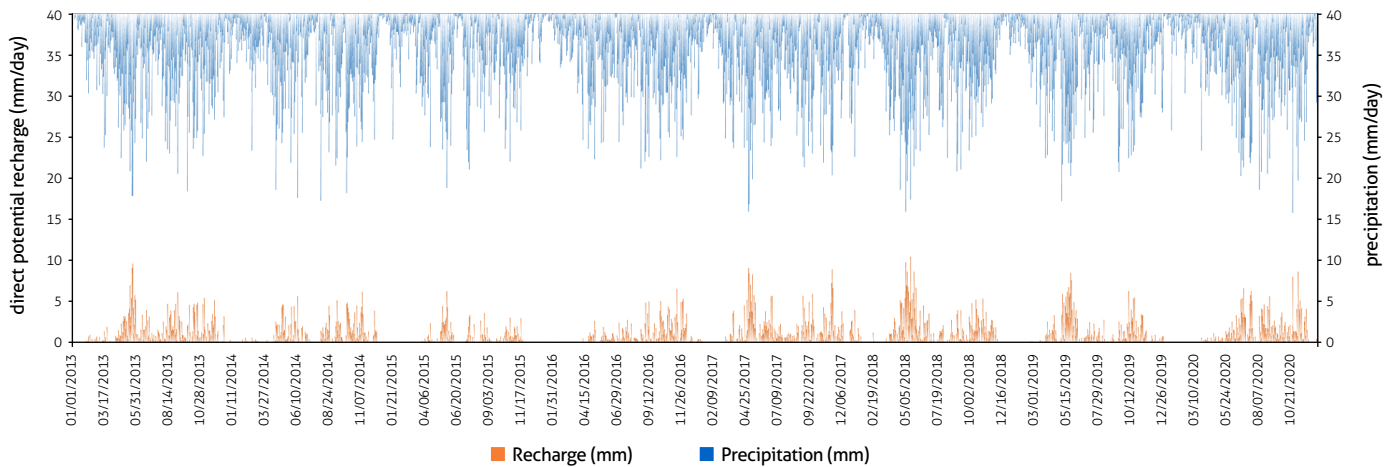


Figure 6. Daily direct potential recharge (DRP) series estimated as the spatial average for the study area (2013-2020)

noff and soil moisture) took approximately 48 hours (2 days). These execution times depend on the length of the model, the length of the study period and the computer equipment used. For this research, the model was run on a computer with 12 GB RAM and an AMD Ryzen 5 2500U processor (2.00 GHz).

The daily series of direct potential recharge (DRP) estimated with the SWB model for the spatial average of the study area (Figure 6) and the daily spatial average series for precipitation entered as a dynamic input to the model show a clear temporal coupling, which shows that the highest rates of DRP occur under the highest rates of precipitation, while in the absence of precipitation and even under the occurrence of low-magnitude precipitation, recharge flows are not generated. No temporal lag is observed in the recharge response to precipitation, which may be associated with a greater permanence of favorable soil moisture conditions in the study area.

Table 2 shows a statistical summary of the average daily recharge in the simulation period. On average, for the study area, the direct potential recharge represents 17% of the daily precipitation, while under maximum daily rainfall, the direct recharge represents 44% of the rainfall. Additionally, the great temporal variability of the DRP is highlighted as a response to the temporal variability of the rainfall and the other factors

involved in the process (evapotranspiration, antecedent moisture, storage in the soil, direct runoff, etc.). This response is reflected in the high coefficients of variation for recharge (greater than 100%) being much greater than those of precipitation.

Figure 7 shows the spatial distribution of the DRP estimated for the average of each month in the analysis period (average annual cycle for 2013-2020). The monthly DRP presents a notable seasonality, similar to the seasonality of the rainfall, indicating that the lowest monthly recharge rates (<5 mm) occur during the January-March period. The recharge is even zero in large areas of the study area, especially during February, while between May and November, monthly recharge rates are higher, with two recharge peaks, the first in May (with a spatial maximum of 370 mm/month) and the second between October and November (with a spatial maximum of 220 mm/month), with a reduction in the larger-magnitude recharge areas in August. Likewise, in December, there is a significant reduction and a predominance of low- and medium-magnitude recharge rates (between 0 mm/month and 40 mm/month).

These findings show that, similar to regional precipitation, the regional behavior of the direct potential recharge in the basins associated with the Cauca River canyon in the study area is quasi-bimodal.

Table 2. Statistical summary of the average daily potential recharge (DRP) rate in the study area

	Precipitation [mm/day]	Recharge [mm/day]	DRP/P
Average	5.6	0.9	16.70 %
Maximum	24.1	10.6	43.80 %
Minimum	0	0	-
Standard deviation	4.4	1.3	-
Coefficient of variation	78 %	141 %	-

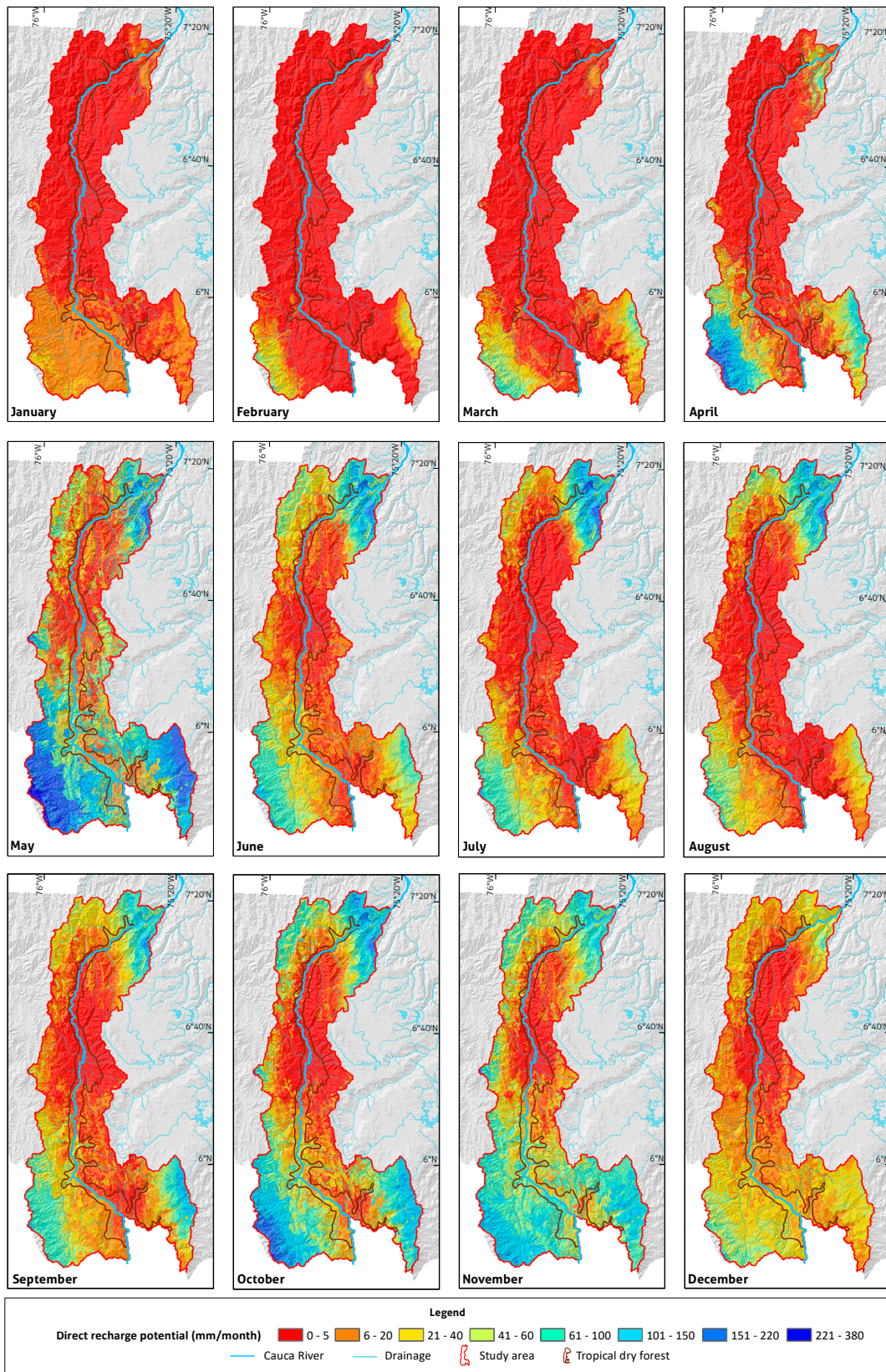


Figure 7. Spatiotemporal variability in the multiyear average monthly direct potential recharge (2013-2020) for the study area

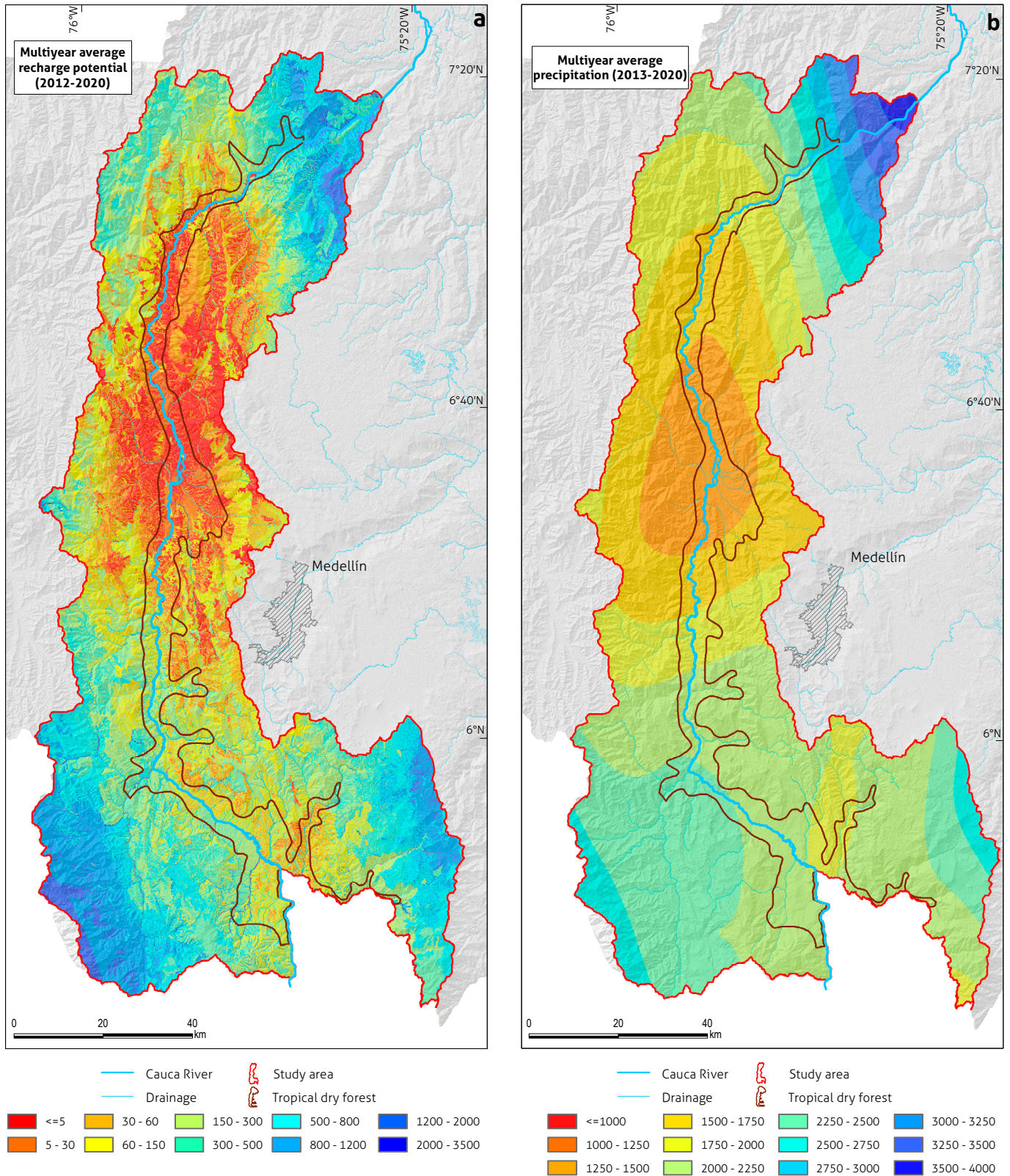
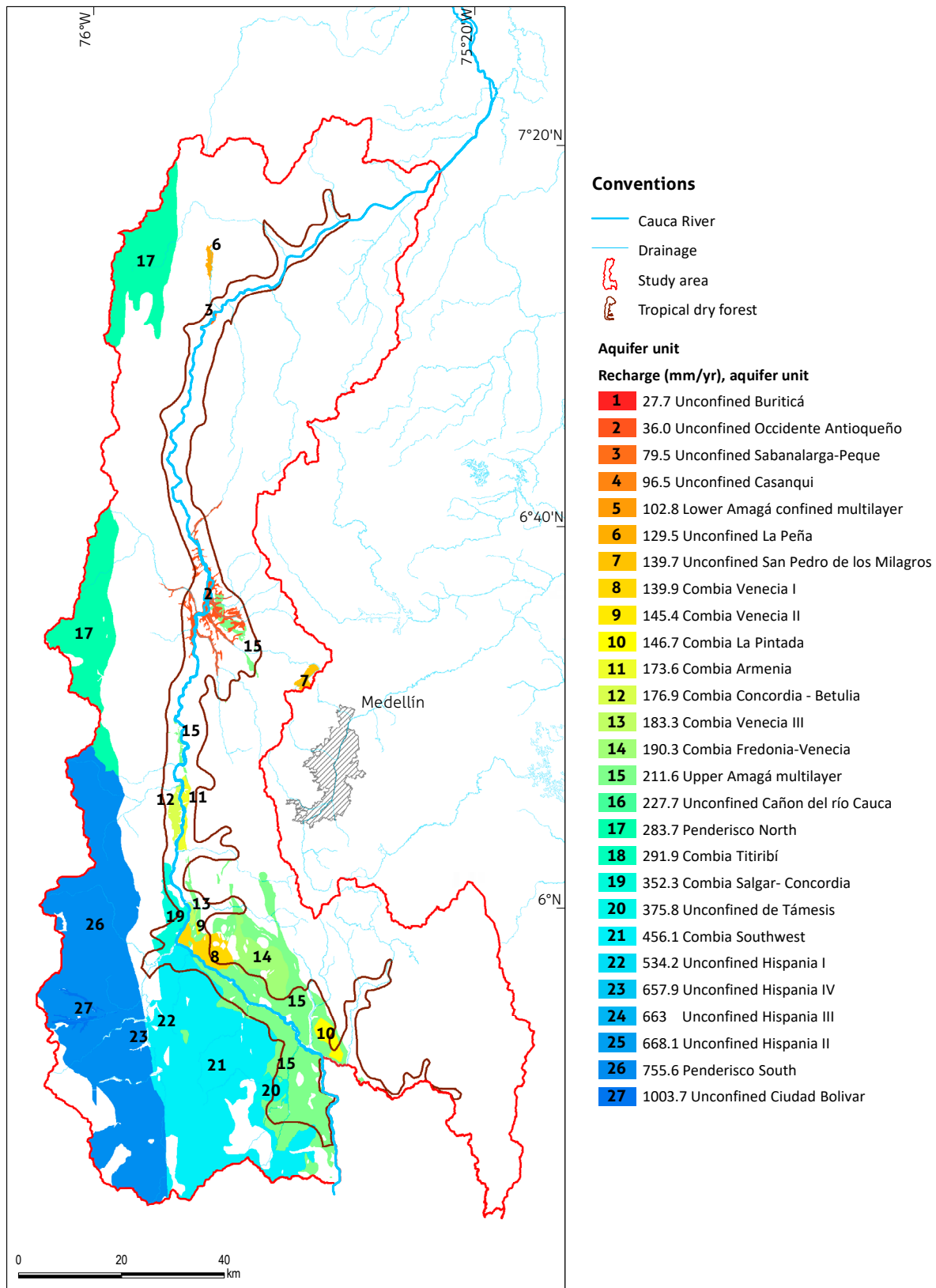


Figure 8. Spatial distribution of the average annual direct potential recharge in the study area between 2013 and 2020 and its spatial relationship with the average annual precipitation for the same period, units in mm/y



**Figure 9.** Spatial distribution of the average annual direct potential recharge (2013-2020) by hydrogeological unit in the study area. See legend in this [kmz file](#) (see in Google Earth).

Figure 8 illustrates the spatial distribution of the annual average direct potential recharge for the study area estimated between 2013 and 2020. The spatial variability of the recharge is also observed in detail, which has an important and close relationship with the spatial distribution of the average annual precipitation. Spatial patterns of the potential recharge are strongly related to the spatial variability of rainfall but also to the spatial variability of soil properties and type of land cover. It is also observed that the highest recharge rates, on the order of between 800 mm/year and 3500 mm/year, occur in the upper parts of the San Juan, Arma, Tonusco and Ituango river basins, as well as in the northern part of the study area in the municipality of Briceño and the Espiritu Santo River basin; in these areas, there is greater precipitation but also conditions of greater soil permeability and low field capacities. On the other hand, the lowest recharge rates (less than 5 mm/year) occur in the central region of the study area between the municipalities of Santa Fe de Antioquia, Olaya, Sopetrán and Liborina, mainly toward the bottom of the Cauca River canyon. In the upper part of the Aurra River basin, recharge rates are not as low, between 30 mm/year and 150 mm/year.

Regarding the spatial variability of the characterized and estimated hydrological flows, it is important to emphasize that in the direct extension of the TDF ecosystem, there are conditions of high temperatures and lower precipitation (spatial average of 1858 mm/year, compared to 2051 mm/year for the study area), high potential evapotranspiration rates (spatial average of 1793 mm/year, compared to 1591 mm/year for the study area) and low direct potential recharge rates (spatial average of 152 mm/year, compared to 342 mm/year for the study

area), so direct water availability in this area is low, especially toward the central and north-central regions of the TDF extension.

From the regional estimates of direct potential recharge performed, the representative average precipitation potential recharge was obtained for each hydrogeological unit with aquifer potential in the study area (Figure 9). Notably, the aquifers associated with the Penderisco Formation to the northwest and southwest of the study area are characterized by a medium to high annual potential recharge, between 284 mm (northwest) and 756 mm (southwest). The aquifers of the Combia Formation to the southwest register high average annual recharge rates of 456 mm, while the quaternary units in relation to the direct potential recharge are behaviorally diverse, where unconfined aquifers associated with alluvial deposits are observed, with low annual recharge values, including the Buriticá Aquifer (28 mm), the Western Aquifer in Antioquia (36 mm) and the Sabanalarga-Peque Aquifer (80 mm). Unconfined aquifers mainly associated with alluvial terraces, with high annual recharge values, include the unconfined aquifer of Tâmesis (376 mm) and the unconfined aquifers of Hispania (534 mm to 668 mm). Finally, it is noteworthy that the unconfined aquifer of the Cauca River canyon has an annual direct recharge of 228 mm, which represents a moderate magnitude.

The state variable of the distributed SWB model is soil moisture, whose spatiotemporal behavior is highly variable and is strongly related to the temporal variability of precipitation (Figure 10). In periods of high rainfall, this humidity increases up to a storage limit defined by the field capacity, and under sustained conditions of low rainfall, soil moisture de-

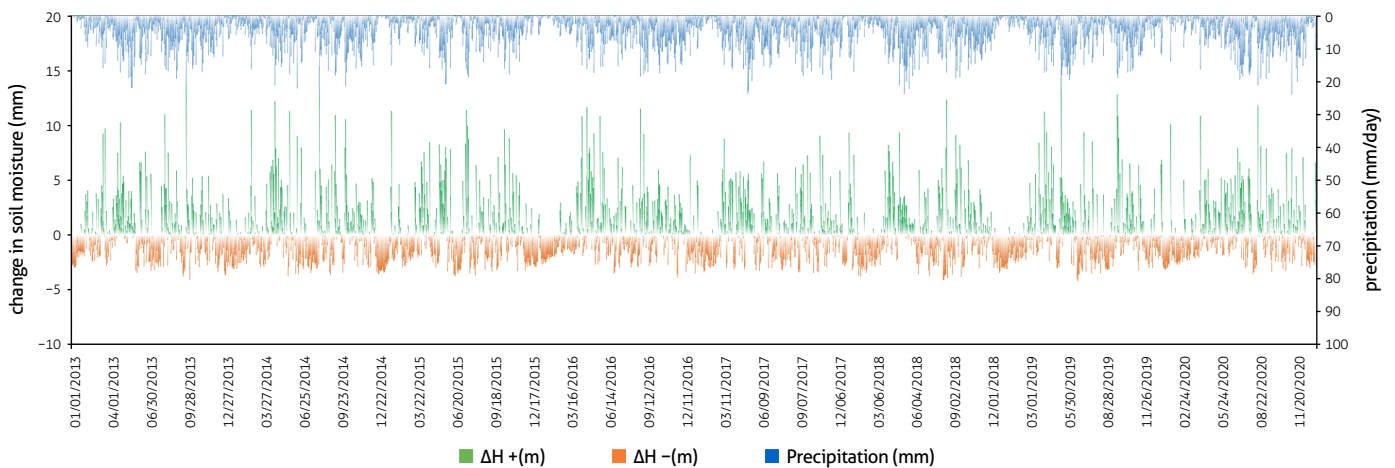


Figure 10. Daily series of soil moisture change ( $\Delta H$ ) estimated on average for the study area (2013-2020)

creases progressively and sustainably until a limit corresponding to the permanent wilting point, which shows a water discharge (negative change in storage) from the soil–plant control volume caused by the continuous requirement of the ETp.

Soil moisture and its temporal variation largely depend on the temporal variability of rainfall at the daily and monthly scales, which is also evident interannually (Figure 10). Between 2017 and 2018, characterized as wet years, there is generally higher soil moisture, with moisture conditions around field capacity for several continuous months, while between 2015 and 2016, dry years, there is generally less moisture in the soil, with considerable moisture loss mainly between December 2015 and January 2016. The positive changes in soil moisture ( $\Delta H+$ ) are generally of greater magnitude than the negative changes ( $\Delta H-$ ), which favors the generation of recharge, although the negative changes are more persistent in times of no rain, as is logical in relation to the action of the ETp.

Finally, Table 3 presents the total flows for each variable of the soil moisture balance, summarized as a percentage of precipitation. Balance closure tends to be adequate, with an approximate closure error of  $-0.4\%$  (difference between inputs and outputs), which may be associated with changes in soil moisture storage, which in long-term periods (greater than ten years) should tend to zero, and/or to the systematic uncertainties of obtaining the input variables and of the operation of the submodels (e.g., NC method, Thornthwaite and Mather method, etc.).

All the terms of the balance vary temporally with precipitation. For example, in dry years, a greater percentage of rain becomes actual evapotranspiration (ETa) and is intercepted by foliage (Inp), and less is converted into direct surface runoff (DR) and DRP, while in wet years, the opposite occurs. In addition, the main flow is the ETa, which represents on average

56% of the precipitation and, in turn, satisfies on average 72% of the ETp. The next most important flow is interception with 17.6%, which, together with the ETa, can satisfy 95% of the ETp. Finally, the DRP represents an average of 16.4% of the precipitation and the DR, that is, on average 11.1% of the precipitation.

A fundamental aspect of the water balance analysis is the water deficit, which is the difference between the ETp and the ETa. When the availability of water is not sufficient for the ETa to satisfy the conditions of the ETp (positive difference  $ETp - ETa$ ), water deficit conditions arise, which are directly related to the water stress of the plants. This research shows that the highest rates of water deficit are concentrated in the central part of the study area, at the bottom of the Cauca River canyon, mainly between Santa Fe de Antioquia, Olaya, Sopetrán and Liborina, with values between 500 mm/year and 900 mm/year of deficit, while the lowest rates of deficit are reported in the upper part of the basins, where the ETp requirements are low and the availability of water resources due to greater precipitation is high. It is important to note that, in general, the areas of high water deficit and low soil moisture coincide with the extension of TDF, so that together with the conditions of low water availability defined by lower precipitation, lower direct recharge by rain and greater ETp requirements, it is reasonable to think that the water sustainability of the TDF ecosystem cannot depend solely on direct water availability (direct recharge by rain in the polygon of the TDF ecosystem) since this source is limited.

## 5. DISCUSSION

The spatiotemporal variability of recharge in the study area is dominated by the spatiotemporal behavior of precipitation, as is

**Table 3.** Summary of the main terms (as a percentage of precipitation) that make up the soil water balance (SWB) expressed as the spatial average for the study area.

Year	Potential evapotranspiration (ETp) [mm/year]	Precipitation (P) [mm/year]	Direct potential recharge (DRP)	Actual evapotranspiration (ETa)	Surface runoff (DR)	Foliage interception (Inp)
2013	1536	2210	18.90 %	52.10 %	13.50 %	16.70 %
2014	1595	1991	15.50 %	58.60 %	9.60 %	17.90 %
2015	1686	1704	10.40 %	66.80 %	9.50 %	18.50 %
2016	1667	1966	13.20 %	56.50 %	7.70 %	18.80 %
2017	1532	2254	19.30 %	52.40 %	12.40 %	16.90 %
2018	1597	2246	19.90 %	55.00 %	13.80 %	16.60 %
2019	1568	2035	16.70 %	54.90 %	12.30 %	17.40 %
2020	1551	2001	17.70 %	54.00 %	9.70 %	17.60 %
Average	1591	2051	16.40 %	56.30 %	11.10 %	17.60 %

common in tropical areas, where the availability of precipitation is the major determinant of recharge behavior (Bastidas Osejo et al., 2019; Koïta et al., 2018). The typical range of spatiotemporal variation in the estimated regional recharge is significant, between 5 mm/year and 2000 mm/year, which is consistent with the magnitudes of the potential recharge estimated in regions with weather conditions similar to those studied in this research (Andualet et al., 2021; Bastidas Osejo et al., 2019; Dos Santos et al., 2021; Hussin et al., 2020; Koïta et al., 2018).

The application of the distributed water balance model allows the determination of the direct potential recharge present in the study area. The high spatiotemporal variability of both precipitation and recharge is highlighted, which coincides with previous studies in several parts of the study area (Servicios Hidrogeológicos Integrales S. A. S. and Corantioquia, 2014; Universidad Nacional de Colombia and Corantioquia, 2004).

Regarding the magnitude of the direct potential recharge, the distributed balance model establishes that in the central region of the study area, between the municipalities of Santa Fe de Antioquia, Olaya, Sopetrán and Liborina, mainly toward the Cauca River canyon bottom, there are recharges between 30 mm/year and 150 mm/year and between 150 mm/year and 750 mm/year on the left bank of the Cauca River, between Támesis and southern Concordia. These values are similar to those obtained in studies carried out in 2004, 2014 and 2015 by Corantioquia, Universidad Nacional de Colombia and Servicios Hidrogeológicos Integrales S. A. S.

The results of the spatiotemporal distribution of the direct potential recharge in the study area provide elements that support the hypothesis initially proposed regarding the water availability of the TDF ecosystem, since the conditions of water availability directly in the extent of the ecosystem are limited. The lowest recharge rates in the study area, the highest potential evapotranspiration rates and the highest water deficit are reported. While in the middle and upper part of the basins associated with the Cauca River canyon, the direct potential recharge rates are high, these recharge flows could become regional and lateral for the aquifers located at the bottom of the Cauca River canyon, provided that there are hydrogeological conditions conducive to such interconnection, such as the degree of fracturing of the rocks, existence of regional geological structures, degree of permeability of the hydrogeological units and favorable topographic conditions. In the study conducted by the University of Antioquia and Corantioquia in 2021, various geological rock units with hydrogeological potential were

defined, located in the upper part of the western slope of the Cauca River. Additionally, piezometric surfaces were modeled based on the data collected from a dense inventory of water points in the same study area, in which it was found that the general trends of the groundwater flow follow the topographic conditions, supporting the hypothesis that the direct potential recharge of the hydrogeological units of the upper part of the basins can become lateral and regional flows for the aquifers at the bottom of the canyon, where the TDF is located.

The recharge results in the study area are compared with those of previous hydrogeological studies in the aquifer system of western Antioquia (mainly Sopetrán, San Jerónimo and Aurra) and in the Valparaíso-La Pintada aquifer. Notably, in the case of western Antioquia, there is knowledge of the aquifers associated with alluvial deposits and the formulation of an aquifer environmental management plan (PMAA). Several areas of direct potential recharge located in the upper part of the basins of the study area, which have the potential to be areas of indirect recharge by regional flows, coincide with the location of recharge zones established in the area of Santa Fe de Antioquia and Olaya located between 1800 masl and 2400 masl and between 1100 masl to 1400 masl (Vélez and Rhenals, 2008), and in Valparaíso and La Pintada, where recharge is located in the upper parts of Cerro Amarillo and Farallones de la Pintada (Servicios Hidrogeológicos Integrales S. A. S. and Corantioquia, 2014).

The hypothesis that regional flows can feed the aquifers that provide water sustainability to the TDF finds local support from Vélez and Rhenals (2008), who, based on environmental isotopes estimated for the area between Santa Fe de Antioquia and Olaya, found the existence of regional flows from the high-elevation areas of the basin, especially from the Chico River basin.

The results of the present investigation constitute contributions at the regional scale to complement the hydrogeological knowledge of the previously studied regions, for which there are still no specific hydrogeological studies, making it possible to identify areas with greater hydrogeological potential based on their direct potential recharge. The estimates of direct potential recharge presented here should be validated through other estimation methods, such as those based on hydrographs of the surface currents receiving groundwater flows (Andualet et al., 2021; Dos Santos et al., 2021; Healy, 2010; Koïta et al., 2018; Scanlon et al., 2002; Vélez and Bastidas, 2018), those of piezometric oscillations (Bastidas Osejo et al., 2019; Dos San-

tos et al., 2021; Healy and Cook, 2002; Melo et al., 2015; Varni, 2013) and hydrogeochemicals and isotopes (Barua et al., 2021).

## 6. CONCLUSIONS

The geological synthesis shows that, given the technostructural characteristics of the central Andean region, there is a probable aquifer potential in the watersheds that demarcate the Cauca River canyon in Antioquia, which includes, in addition to the soft formations (sedimentary deposits), various units of hard fractured rocks that develop secondary permeability.

In this context, with the implementation of the distributed SWB model, it was possible to obtain estimates of direct potential recharge by precipitation in all geological units that have hydrogeological potential characteristics (which are listed and highlighted in Figure 9), in addition to understanding the spatiotemporal behavior of this recharge in the entire study area and the factors that most influence this behavior.

The high spatiotemporal variability of the potential recharge of the hydrogeological units associated with the basins of the TDF in Antioquia is confirmed, with typical ranges that oscillate between 5 mm/year and 2000 mm/year, characteristic of tropical climates, as highlighted in the discussion. This variability is mainly related to the spatial structure of rainfall and the permeability properties of soils and land cover. The interannual variability of the direct potential recharge is associated with the occurrence of the ENSO phenomenon. It is evident that under the El Niño phase, as was the case in 2015, the potential recharge tends to decrease, while under La Niña, as in 2018, the potential recharge tends to increase.

The potential recharge by precipitation shows a clearly defined spatial variability, with greater magnitudes toward the upper parts of the basins of the San Juan, Arma, Tonusco and Ituango rivers, as well as in the northern part of the study area, in the municipality of Briseño and the Espiritu Santo River basin. In these zones, greater precipitation is recorded, as are soil conditions with greater permeability and low field capacities. The lowest recharge rates occur in the central region of the study area between the municipalities of Santa Fe de Antioquia, Olaya, Sopetrán and Liborina, mainly toward the bottom of the Cauca River canyon. The spatial estimates of potential recharge allow us to conclude that the recharge in the extension of the TDF (152 mm/year on average) is much lower than that generated in the entire study area (342 mm/year on average), in which it is estimated that high recharge rates occur in

the upper and middle parts of the basins afferent to the Cauca River canyon.

The general water balance for the study area allows us to conclude that most of the precipitation is converted into actual evapotranspiration, followed by interception by foliage, potential recharge and finally direct surface runoff. All balance terms vary temporally with precipitation. This pattern indicates that dry years lead to a higher percentage of rainfall being converted into actual evapotranspiration (ETa) and intercepted by foliage (Inp), and less rainfall becomes DR and DRP, while in wet years, the opposite occurs.

The highest rates of water deficit and lowest soil moisture content are concentrated in the central part of the study area, at the bottom of the Cauca River canyon. High water deficit and low soil moisture conditions coincide with the extension of the TDF, which is important in explaining that the water sustainability of this specific ecosystem may be related to the groundwater flows that are not directly generated in that area, given the low magnitude of recharge, but rather in the middle and upper part of the associated basins.

The spatial patterns of the direct potential recharge, its magnitudes and the spatial distribution of the other terms of the water balance allow us to conclude that there is a high potential for the generation of recharge by regional flows (lateral-indirect recharge) toward the hydrogeological units that are directly related to the TDF, since in the area covered by this ecosystem, the direct recharge is low; however, in the upper part of the associated basins, there are significant direct recharges that can become regional flows, depending on the structural patterns in the area and the direction of groundwater flow.

The regional recharge hypothesis derived from this research in the study area, as well as the magnitudes of regional recharge, are consistent with the results of local recharge estimates by various methods obtained from previous investigations in aquifers that are part of the study area, such as those of western Antioquia and Valparaíso-La Pintada.

## 7. SUPPLEMENTARY DATA

Supplementary data for this article can be found online at <https://doi.org/10.32685/0120-1425/bol.geol.49.1.2022.625>

The tables S1 to S7, in the supplementary data, provide information regarding the geological legend of Figure 1 and the information of the hydrometeorological stations used for the model, the description of the soil legend presented in Figure 3

and the description of the land cover in Figure 3, in addition to the values assigned to the parameters of the SWB model (curve number, daily recharge threshold, rooting depth).

#### Available data in kmz files

Figure 1. Delimitation of the study area and geological units present

Figure 3. Graphic summary of the spatial information used for the implementation of the SWB model in the study area

Figure 4. Spatial distribution of soil textures and field capacity in the study area

Figure 9. Spatial distribution of the average annual direct potential recharge (2013-2020) by hydrogeological unit in the study area

#### ACKNOWLEDGMENTS

The authors thank the Regional Autonomous Corporation of the Center of Antioquia (Corantioquia) for allowing and financing the development of this research within the framework of the project “Aunar esfuerzos para la exploración del potencial hidrogeológico en zonas de bosque seco en el cañón del río Cauca en la jurisdicción de Corantioquia (Joining efforts for the exploration of the hydrogeological potential in areas of dry forest in the Cauca River canyon, in the jurisdiction of Corantioquia)”, developed in conjunction with the University of Antioquia. We would like to thank all the members of the Environmental Engineering and Management Research Group (GIGA) of the University of Antioquia, who actively participated in the development of this project.

#### REFERENCES

- Aguilera, H., & Murillo, J. (2009). The effect of possible climate change on natural groundwater recharge based on a simple model: a study of four karstic aquifers in SE Spain. *Environmental Geology*, 57, 963-974. <https://doi.org/10.1007/s00254-008-1381-2>
- Ahmed, A., Ranasinghe-Arachchilage, C., Alrajhi, A., & Hewa, G. (2021). Comparison of multicriteria decision-making techniques for groundwater potential recharge zonation: Case study of the willochra basin, South Australia. *Water*, 13(4), 525. <https://doi.org/10.3390/w13040525>
- Andualet, T. G., Demeke, G. G., Ahmed, I., Dar, M. A., & Yibeltal, M. (2021). Groundwater recharge estimation using empirical methods from rainfall and streamflow records. *Journal of Hydrology: Regional Studies*, 37, 100917. <https://doi.org/10.1016/j.ejrh.2021.100917>
- ASF DAAC. (2015). *ALOS PALSAR\_Radiometric\_Terrain\_Corrected\_high\_res; Includes Material* © JAXA/METI 2007. <https://doi.org/10.5067/Z97HFCNKR6VA>
- Barua, S., Cartwright, I., Evan Dresel, P., & Daly, E. (2021). Using multiple methods to investigate the effects of land-use changes on groundwater recharge in a semi-arid area. *Hydrology and Earth System Sciences*, 25(1), 89-104. <https://doi.org/10.5194/hess-25-89-2021>
- Bastidas, B. (2019). *Modelo conceptual de la recarga de aguas subterráneas en el nivel somero del Sistema Hidrogeológico Golfo de Urabá, evaluando su magnitud y variabilidad espacio-temporal* [Bachelor Thesis]. Universidad de Antioquia.
- Bastidas Osejo, B., & Betancur, T. (2019). Uso de R y el paquete Fields para la interpolación espacial recurrente de variables ambientales [presentation]. *R day Medellín*.
- Bastidas Osejo, B., Betancur, T., & Campillo, A. (2019). Analysis of water table fluctuations to improve understanding and quantification of the groundwater recharge process in the shallow aquifer of the gulf of Urabá (Colombia). In *E-Proceedings of the 38th IAHR World Congress* (pp. 76-85). <https://doi.org/10.3850/38WC092019-1010>
- Betancur, T. (2021). *Potencial y perspectivas de exploración hidrogeológica en Antioquia según criterios litoestructurales*. <https://sociedadcolombianadegeologia.org/potencial-y-perspectivas-de-exploracion-hidrogeologica-en-antioquia-segun-criterios-litoestructurales/>
- Bradbury, K., Fienen, M. N., Kniffin, M., Krause, J., Westbroek, S. M., Leaf, A. T., & Barlow, P. M. (2017). *Groundwater flow model for the Little Plover River basin in Wisconsin's Central Sands*. Wisconsin Geological and Natural History Survey. <http://pubs.er.usgs.gov/publication/70186797>
- Calle, B., & González, H. (1980). *Geología y geoquímica de la Plancha 166, Jericó. Escala 1:100 000*. Ingeominas.
- Calle, B., & González, H. (1982). *Geología y geoquímica de la Plancha 186 Riosucio. Memoria explicativa*. Ingeominas.
- Corporación Autónoma Regional del Centro de Antioquia (Corantioquia), Ministerio de Ambiente y Desarrollo Sostenible, Ministerio de Hacienda y Crédito Público y Fondo de Adaptación. (2018a). *Actualización del Plan de ordenación y manejo de la cuenca hidrográfica de los directos río Cauca*

- (Md)-río Aurra-NSS (2620-02). [https://www.corantioquia.gov.co/ciadoc/AGUA/AIRNR\\_CN\\_1605\\_48\\_2016\\_DOCUMENTO%20POMCA.pdf](https://www.corantioquia.gov.co/ciadoc/AGUA/AIRNR_CN_1605_48_2016_DOCUMENTO%20POMCA.pdf)
- Corporación Autónoma Regional del Centro de Antioquia (Corantioquia), Ministerio de Ambiente y Desarrollo Sostenible, Ministerio de Hacienda y Crédito Público y Fondo de Adaptación. (2018b). *POMCA de los directos río Cauca-río Amagá-quebrada Sinifaná-NSS (2620- 01)*. [https://www.corantioquia.gov.co/ciadoc/AGUA/AIRNR\\_1512\\_252\\_2015\\_FASE%20APRESTAMIENTO.pdf](https://www.corantioquia.gov.co/ciadoc/AGUA/AIRNR_1512_252_2015_FASE%20APRESTAMIENTO.pdf)
- Cronshey, R., McCuen, R., Miller, N., Rawls, W., Robbins, S., & Woodward, D. (1986). *Urban hydrology for small watersheds - TR-55*. U.S. Department of Agriculture, Soil Conservation Service.
- De Berg, M., Cheong, O., Kreveld, M., & Overmars, M. (2008). *Computational geometry: Algorithms and applications*. Springer. <https://doi.org/10.1007/978-3-540-77974-2>
- De Vries, J. J., & Simmers, I. (2002). Groundwater recharge: An overview of process and challenges. *Hydrogeology Journal*, 10(1), 5-17. <https://doi.org/10.1007/s10040-001-0171-7>
- Dockter, D., & Palmer, P. L. (1994). *Computation of the 1982 Kimberly-Penman and the Jensen-Haise evapotranspiration equations as applied in the U.S. Bureau of Reclamation's Pacific Northwest AgriMet Program*. <https://www.usbr.gov/pn/agrimet/aginfo/AgriMet%20Kimberly%20Penman%20Equation.pdf>
- Donato, G., & Belongie, S. (2002). Approximate thin plate spline mappings. In A. Heyden, G. Sparr, M. Nielsen & P. Johansen (eds.), *Computer Vision - ECCV 2002* (Vol. 2352, pp. 21-31). Springer-Verlag. <https://doi.org/10.1007/3-540-47969-4>
- Dos Santos, R. M., Koide, S., Távora, B. E., & De Araujo, D. L. (2021). Groundwater recharge in the cerrado biome, Brazil—A multi-method study at experimental watershed scale. *Water*, 13(1), 1-28. <https://doi.org/10.3390/w13010020>
- Dripps, W. R., & Bradbury, K. R. (2007). A simple daily soil-water balance model for estimating the spatial and temporal distribution of groundwater recharge in temperate humid areas. *Hydrogeology Journal*, 15(3), 433-444. <https://doi.org/10.1007/s10040-007-0160-6>
- Echavarría, S. B. (2013). *Modelo de simulación de funcionamiento hidráulico del sistema de drenaje del área metropolitana del valle de México. Aplicación a las políticas de operación* [Ph.D. Thesis]. Universidad Nacional Autónoma de México. <https://repositorio.unam.mx/contenidos/69328>
- Ehlers, L., Herrmann, F., Blaschek, M., Duttmann, R., & Wendland, F. (2016). Sensitivity of mGROWA-simulated groundwater recharge to changes in soil and land use parameters in a Mediterranean environment and conclusions in view of ensemble-based climate impact simulations. *Science of The Total Environment*, 543, 937-951. <https://doi.org/10.1016/j.scitotenv.2015.04.122>
- Engott, J. A., Johnson, A. G., Bassiouni, M., Izuka, S. K., & Rotzoll, K. (2017). *Spatially distributed groundwater recharge for 2010 land cover estimated using a water-budget model for the Island of O'ahu, Hawai'i*. Scientific Investigations Report (versión 1.). U.S. Geological Survey. <https://doi.org/10.3133/sir20155010>
- Fauzia, Surinaidu, L., Rahman, A., & Ahmed, S. (2021). Distributed groundwater potential recharges assessment based on GIS model and its dynamics in the crystalline rocks of South India. *Scientific Reports*, 11(1), 1-16. <https://doi.org/10.1038/s41598-021-90898-w>
- Gobernación de Antioquia. (2018). *Anuario estadístico de Antioquia*. <http://www.antioquiadatos.gov.co/index.php/anuario-estadistico-2018>
- González, H. (2001). *Memoria explicativa del mapa geológico de Antioquia, escala 1:400 000*. Ingeominas.
- Hall, R., Álvarez, J., Rico, H., & Vásquez, H. (1970a). *Mapa geológico de Colombia. Cuadrángulo H7 Ituango. Planchas 104 Ituango -115 Toledo. Cuadrángulo H-8 Yarumal, 105 Valdivia - 116 Yarumal. Escala 1:100 000. Memoria explicativa*. Ingeominas.
- Hall, R., Álvarez, J., Rico, H., & Vásquez, H. (1970b). *Memoria explicativa del mapa geomorfológico aplicado a movimientos en masa escala 1:100 000. Plancha 115 Toledo*. Ingeominas
- Hargreaves, G., & Samani, Z. (1985). Estimating potential evapotranspiration. *Journal of Irrigation and Drainage Engineering*, 108, 225-230.
- Harlow, J., & Hagedorn, B. (2018). SWB modeling of groundwater recharge on Catalina Island, California, during a period of severe drought. *Water*, 11(1), 58. <https://doi.org/10.3390/w11010058>
- Healy, R. W. (2010). *Estimating groundwater recharge*. Cambridge University Press.
- Healy, R. W., & Cook, P. G. (2002). Using groundwater levels to estimate recharge. *Hydrogeology Journal*, 10(1), 91-109. <https://doi.org/10.1007/s10040-001-0178-0>
- Herrera-Pantoja, M., & Hiscock, K. (2008). The effects of climate change on potential groundwater recharge in Great Britain. *Hydrological Processes*, 22, 73-86.

- Hussin, N. H., Yusoff, I., & Raksmei, M. (2020). Comparison of applications to evaluate groundwater recharge at lower Kelantan river basin, Malaysia. *Geosciences*, 10(8), 1-25. <https://doi.org/10.3390/geosciences10080289>
- Instituto de Hidrología, Meteorología y Estudios Ambientales (Ideam). (2010). *Leyenda nacional de coberturas de la tierra. Metodología adaptada para Colombia Escala 1:100 000*. <http://documentacion.ideam.gov.co/cgi-bin/koha/opac-detail.pl?biblionumber=10707>
- Instituto Geográfico Agustín Codazzi (IGAC) & Gobernación de Antioquia. (2007). *Estudio general de suelos y zonificación de tierras del departamento de Antioquia*. <http://documentacion.ideam.gov.co/cgi-bin/koha/opac-detail.pl?biblionumber=6777>
- Jabloun, M., & Sahli, A. (2012). *WEAP-MABIA Tutorial*. [https://www.weap21.org/WebHelp/Mabia\\_Algorithms.htm](https://www.weap21.org/WebHelp/Mabia_Algorithms.htm)
- Jasechko, S., & Taylor, R. G. (2015). Intensive rainfall recharges tropical groundwaters. *Environmental Research Letters*, 10(12). <https://doi.org/10.1088/1748-9326/10/12/124015>
- Johnson, A. G., Engott, J. A., Bassiouni, M., & Rotzoll, K. (2018). *Spatially distributed groundwater recharge estimated using a water-budget model for the Island of Maui, Hawai'i, 1978-2007*. Scientific Investigations Report (versión 1.). U.S. Geological Survey. <https://doi.org/10.3133/sir20145168>
- Koita, M., Yonli, H. F., Soro, D. D., Dara, A. E., & Vouillamoz, J. M. (2018). Groundwater storage change estimation using combination of hydrogeophysical and groundwater table fluctuation methods in hard rock aquifers. *Resources*, 7(1), 5. <https://doi.org/10.3390/resources7010005>
- Lamichhane, S., & Shakya, N. M. (2019). Alteration of groundwater recharge areas due to land use/cover change in Kathmandu Valley, Nepal. *Journal of Hydrology: Regional Studies*, 26, 100635. <https://doi.org/10.1016/j.ejrh.2019.100635>
- Mair, A., Hagedorn, B., Tillery, S., El-Kadi, A. I., Westenbroek, S., Ha, K., & Koh, G.-W. (2013). Temporal and spatial variability of groundwater recharge on Jeju Island, Korea. *Journal of Hydrology*, 501, 213-226. <https://doi.org/10.1016/j.jhydrol.2013.08.015>
- Mejía, M. (1984a). *Plancha 130. Santa Fe de Antioquia, borde occidental. Departamento de Antioquia. Escala 1:50 000. Memoria explicativa*. Ingeominas
- Mejía, M. (1984b). *Plancha 146. Medellín, borde occidental. Departamento de Antioquia. Escala 1:50 000. Memoria explicativa*. Ingeominas
- Melo, D., Wendland, E., & Guanabara, R. (2015). Estimación de la recarga de agua subterránea basada en el balance hídrico en la zona de suelo no saturado. *Revista Brasileira de Ciência do Solo*, 39, 1336-1343.
- Mockus, V. (1965). Section 4 Hydrology. In SCS (Ed.), *National Engineering Handbook* (Issue 4).
- Moeck, C., Grech-Cumbo, N., Podgorski, J., Bretzler, A., Gurdak, J. J., Berg, M., & Schirmer, M. (2020). A global-scale dataset of direct natural groundwater recharge rates: A review of variables, processes and relationships. *Science of the Total Environment*, 717, 137042. <https://doi.org/10.1016/j.scitotenv.2020.137042>
- Moreles, M. Á., & Mejía, F. (2010). Interpolación con funciones de base radial y el método del sistema diferencial para identificación de parámetros en acuíferos. *Revista Internacional de Métodos Numéricos para Cálculo y Diseño en Ingeniería*, 26(3), 241-247.
- Murphy, P. G., & Lugo, A. E. (1986). Ecology of tropical dry forest. *Annals Review of Ecology and Systematics* 17, 67-68.
- Mussa, K. R., Mjemah, I. C., & Machunda, R. L. (2021). Natural groundwater recharge response to climate variability and land cover change perturbations in basins with contrasting climate and geology in Tanzania. *Earth*, 2(3), 556-585. <https://doi.org/10.3390/earth2030033>
- NRCS-USDA. (2018). *Soil Texture Calculator*. [https://www.nrcs.usda.gov/wps/portal/nrcs/detail/soils/survey/?cid=nrcs142p2\\_054167](https://www.nrcs.usda.gov/wps/portal/nrcs/detail/soils/survey/?cid=nrcs142p2_054167)
- Nychka, D., Furrer, R., Paige, J., & Sain, S. (2015). *fields: Tools for spatial data, v. 8.4-1*. <https://doi.org/10.5065/D6W957CT>
- O'Callaghan, J. F., & Mark, D. M. (1984). The extraction of drainage networks from digital elevation data. *Computer Vision, Graphics, and Image Processing*, 28(3), 323-344. [https://doi.org/10.1016/S0734-189X\(84\)80011-0](https://doi.org/10.1016/S0734-189X(84)80011-0)
- Oliveira, P. T. S., Wendland, E., Nearing, M. A., Scott, R. L., Rosolem, R., & Da Rocha, H. R. (2015). The water balance components of undisturbed tropical woodlands in the Brazilian cerrado. *Hydrology and Earth System Sciences*, 19, 2899-2910.
- Organización de las Naciones Unidas para la Educación, la Ciencia y la Cultura (Unesco) & Oficina Regional de Ciencia y Tecnología de la Unesco para América Latina y el Caribe (Rostlac). (1982). *Guía metodológica para la elaboración del balance hídrico de América del Sur*. <https://unesdoc.unesco.org/ark:/48223/pf0000051960>

- Oviedo, L. M. (2020). *Variaciones de la recarga de agua subterránea bajo escenarios de cambio climático en el nivel somero del sistema acuífero bajo Cauca antioqueño* [Master Thesis]. Universidad Nacional de Colombia. <https://repositorio.unal.edu.co/handle/unal/79775>
- Patiño, S. M. (2021). *Análisis hidroestructural y estimación de recarga potencial por precipitación de la dunita de Medellín, sistema acuífero del valle de Aburrá* [Master Thesis]. Universidad EAFIT. <https://repositorio.eafit.edu.co/handle/10784/29585?show=full>
- Peijun, S., Yanan, H., Congying, Y., & Zhi, L. (2021). Quantitative estimation of groundwater recharge in the thick loess deposits using multiple environmental tracers and methods. *Journal of Hydrology*, 603. <https://doi.org/10.1016/j.jhydrol.2021.126895>
- Pizano, C., & García, H. (2014). *El bosque seco tropical en Colombia*. Instituto de Investigación de Recursos Biológicos Alexander von Humboldt.
- Poveda, G. (2004). La hidroclimatología en Colombia: una síntesis desde la escala interdecadal hasta la escala diaria. *Revista Académica Colombiana de Ciencias*, 28(0370-3908), 22.
- Poveda, G., & Álvarez, D. M. (2012). El colapso de la hipótesis de estacionariedad por cambio y variabilidad climática: implicaciones para el diseño hidrológico en ingeniería. *Revista de Ingeniería*, 36, 65-76. <https://doi.org/10.16924/riua.v0i36.137>
- Poveda, G., Vélez, J., Mesa, O., Hoyos, C., Salazar, L., Mejía, J., Barco, O., & Correa, P. (2002). Influencia de fenómenos macroclimáticos sobre el ciclo anual de la hidrología colombiana: cuantificación lineal, no lineal y percentiles probabilísticos. *Meteorología Colombiana*, 6, 1-10. <http://www.researchgate.net/publication/233969454>
- Ruiz, L., Varma, M. R. R., Kumar, M. S. M., Sekhar, M., Maréchal, J.-C., Desclotres, M., Riotte, J., Kumar, S., Kumar, C., & Braun, J.-J. (2010). Water balance modelling in a tropical watershed under deciduous forest (Mule Hole, India): Regolith matrix storage buffers the groundwater recharge process. *Journal of Hydrology*, 380(3-4), 460-472. <https://doi.org/10.1016/j.jhydrol.2009.11.020>
- Saxton, K. E., & Rawls, W. J. (2006). Soil water characteristic estimates by texture and organic matter for hydrologic solutions. *Soil Science Society of America Journal*, 70(5), 1569. <https://doi.org/10.2136/sssaj2005.0117>
- Scanlon, B., Healy, R., & Cook, P. (2002). Choosing appropriate techniques for quantifying groundwater recharge. *Hydrogeology Journal*, 10(2), 347-347. <https://doi.org/10.1007/s10040-002-0200-1>
- Servicio Geológico Colombiano. (1979). *Mapa geológico de Antioquia 1:500 000*.
- Servicio Geológico Colombiano. (1996). *Mapa geológico de Antioquia 1:400 000*.
- Servicios Hidrogeológicos Integrales S. A. S., & Corporación Autónoma Regional del Centro de Antioquia (Corantioquia). (2014). *Evaluación hidrogeológica en los municipios de La Pintada y Valparaiso, jurisdicción de la dirección territorial Cartama Corantioquia*. [https://www.corantioquia.gov.co/ciadoc/AGUA/GA\\_CN\\_9909\\_2013.pdf](https://www.corantioquia.gov.co/ciadoc/AGUA/GA_CN_9909_2013.pdf)
- Thorntwaite, C. W., & Mather, J. R. (1957). Instructions and tables for computing potential evapotranspiration and water balance. *Publications in Climatology*, 10, 185-311.
- Turc, L. (1961). Water requirements assessment of irrigation, potential evapotranspiration: Simplified and updated climatic formula. *Annales Agronomiques*, 12, 13-49.
- Turkeltaub, T., Kurtzman, D., Bel, G., & Dahan, O. (2015). Examination of groundwater recharge with a calibrated/validated flow model of the deep vadose zone. *Journal of Hydrology*, 522, 618-627. <https://doi.org/10.1016/j.jhydrol.2015.01.026>
- Universidad Nacional de Colombia. (2011). *Manual de usuario HidroSIG 4.0*. <https://minas.medellin.unal.edu.co/departamentos/geocienciasymedioambiente/hidrosig/es/descargas.html>
- Universidad Nacional de Colombia & Corporación Autónoma Regional del Centro de Antioquia (Corantioquia). (2004). *Evaluación del potencial acuífero en los municipios de Santa Fe de Antioquia, San Jerónimo, Sopetrán, Olaya y Liborina*. [https://www.corantioquia.gov.co/ciadoc/AGUA/AIRNR\\_AGUA\\_CD399\\_2004.pdf](https://www.corantioquia.gov.co/ciadoc/AGUA/AIRNR_AGUA_CD399_2004.pdf)
- Varni, M. R. (2013). Aplicación de varias metodologías para estimar la recarga al acuífero pampeano, Argentina. *Tecnología y Ciencias del Agua*, 4(3), 67-85. [http://www.scielo.org.mx/scielo.php?script=sci\\_arttext&pid=S2007-24222013000300004&lang=pt](http://www.scielo.org.mx/scielo.php?script=sci_arttext&pid=S2007-24222013000300004&lang=pt)
- Vela Mayorga, A. (2001). *Desarrollo de un modelo de balance de agua en los suelos de Castilla-La Mancha sobre un sistema de información geográfica: condiciones de aplicación y limitaciones* [Ph.D. Thesis]. Universidad de Castilla-La Mancha. <https://dialnet.unirioja.es/servlet/tesis?codigo=198388>
- Vélez, M., & Bastidas, B. (2018). Cuantificación de la recarga de aguas subterráneas en un acuífero transfronterizo de la cuenca amazónica Acuífero Leticia-Tabatinga. XIV Con-

- greso Latinoamericano de Hidrogeología, X Congreso Argentino de Hidrogeología y VIII Seminario Hispano Latinoamericano Sobre Temas Actuales de La Hidrología Subterránea. Salta, Argentina.
- Vélez, M., & Rhenals, R. (2008). Determinación de la recarga con isótopos ambientales en los acuíferos de Santa Fe de Antioquia. *Boletín de Ciencias de la Tierra*, 24, 37-54.
- Wang, S. J., Lee, C. H., Yeh, C. F., Choo, Y. F., & Tseng, H. W. (2021). Evaluation of climate change impact on groundwater recharge in groundwater regions in Taiwan. *Water*, 13(9). <https://doi.org/10.3390/w13091153>
- Westenbroek, S. M., Kelson, V. A., Dripps, W. R., Hunt, R. J., & Bradbury, K. R. (2010). SWB-A modified Thornthwaite-Mather Soil-Water-Balance code for estimating groundwater recharge. U.S. Geological Survey Techniques and Methods 6-A31. <https://doi.org/10.3133/tm6A31>
- Westenbroek, S. M., Engott, J. A., Kelson, V. A., & Hunt, R. J. (2018). SWB version 2.0 — A soil-water-balance code for estimating net infiltration and other water-budget components. *U.S. Geological Survey Techniques and Methods*, 6(A59). <https://doi.org/10.3133/tm6A59>
- Xie, Y., Cook, P. G., Simmons, C. T., Partington, D., Crosbie, R., & Batelaan, O. (2017). Uncertainty of groundwater recharge estimated from a water and energy balance model. *Journal of Hydrology*, 561, 1081-1093. <https://doi.org/10.1016/J.JHYDROL.2017.08.010>



Identificación de características geomorfológicas de las unidades hidrogeológicas de las formaciones Combia y Amagá en el cañón del río Cauca, Antioquia. Via Peñalisa - Jericó  
Fotografía de Teresita Betancur



This work is distributed under the Creative Commons Attribution 4.0 License.

Received: November 19, 2021

Revision received: April 28, 2022

Accepted: May 9, 2022

Published online: June 30, 2022

## Research article

# Magnetic fabric of deformed Quaternary sediments: contributions to the understanding of the neotectonic activity in the surroundings of the Aburrá Valley, Central Cordillera, Colombia

Fábrica magnética de sedimentos cuaternarios deformados: contribuciones para entender la actividad neotectónica en los alrededores del Valle de Aburrá, Colombia

Santiago Noriega-Londoño<sup>1</sup>, Duván Jaraba<sup>1</sup>, María Paula Ruiz<sup>1</sup>, María Isabel Marín-Cerón<sup>1</sup>, Sergio Andrés Restrepo-Moreno<sup>2,3</sup>

1. Environmental Geology and Tectonics Research Group, Department of Earth Sciences, Universidad EAFIT, Medellín, Colombia.

2. Department of Geosciences and Environment, Universidad Nacional de Colombia, Medellín, Colombia.

3. Department of Geological Sciences, University of Florida, Gainesville, USA.

**Corresponding author:** Santiago Noriega-Londoño, [santiagoel@gmail.com](mailto:santiagoel@gmail.com)

## ABSTRACT

The origin of the Aburrá Valley (AV) is proposed as a set of coalescent tectonic subbasins located along the northern portion of the Central Cordillera of Colombia, the Northern Andes of Colombia. The Itagüí, Medellín, Bello, and Barbosa subbasins have developed between the Romeral Shear Zone (RSZ) and the Antioqueño Batholith starting in the Late Cenozoic. The aim of this study is to contribute to the understanding of the AV neotectonic framework using the anisotropy of magnetic susceptibility (AMS) and structural analysis. For this, we measure the magnetic fabric ellipsoid shape of faulted sediments and compare them with the geometry and kinematics of fault planes to determine their relationship with the present-day stress field and the regional fault architecture. The principal directions of the elongation axes along the La Brizuela and Yarumalito sites were NE-SW, following the magnetic lineation trend and marking a normal displacement with a dextral component. A marked NW-SE magnetic cleavage was found for the La Caimana site along a strike-slip tectonic setting. Holocene ruptures of the principal displacement zone (i.e., the RSZ) and their surroundings, may indicate normal faulting, with fault bends and steps over basins controlled primarily by R' and P structures. Moreover, the active faults located to the east of the AV indicate post Plio-Pleistocene deformations with normal faulting through 90/80 to 150/70 antithetic faults. This work identifies the AMS technique as a powerful tool, for understanding the neotectonic framework along urban and surrounding areas.

**Citation:** Noriega-Londoño, S., Jaraba, D., Ruiz, M. P., Marín-Cerón, M. I., & Restrepo-Moreno, S. (2022). Magnetic fabric of deformed Quaternary sediments: contributions to the understanding of the neotectonic activity in the surroundings of the Aburrá Valley, Central Cordillera, Colombia. *Boletín Geológico*, 49(1), 103-123. <https://doi.org/10.32685/0120-1425/bol.geol.49.1.2022.634>

**Keywords:** Active tectonics, Romeral shear zone, anisotropy of magnetic susceptibility, deformation ellipsoid, seismic hazard, Colombian Andes, Aburrá Valley.

## RESUMEN

El origen del Valle de Aburrá ha sido propuesta como un conjunto de subcuencas tectónicas coalescentes, ubicadas a lo largo de la cordillera Central de Colombia, Andes del Norte de Colombia. Las subcuencas se habían desarrollado entre la zona de Cizalla romeral (ZSR) y el Batolito Antioqueño desde el Cenozoico Tardío. El objetivo de este estudio es contribuir a la comprensión del marco tectónico del Valle de Aburrá, mediante el uso de la anisotropía de la susceptibilidad magnética y el análisis estructural. Para ello, medimos la forma elipsoide de la tela magnética de los sedimentos con fallas y la comparamos con la geometría y cinemática de los planos de falla para determinar su relación con el campo de tensión actual y la arquitectura de fallas regionales. Las principales direcciones de los ejes de elongación a lo largo de los sitios de La Brizuela y Yarumalito fueron NE-SW, paralelo a la tendencia de lineación magnética y marcan un desplazamiento normal con componente dextral. Se encontró, además, una marcada escisión magnética NW-SE para el sitio de La Caimana a lo largo de un entorno tectónico de deslizamiento de golpe. Las rupturas del Holoceno de la zona de desplazamiento principal (es decir, la RSZ) y sus alrededores, pueden indicar fallas normales, con curvas de falla y paso sobre cuencas controladas principalmente por estructuras R' y P. Además, las fallas activas ubicadas al este del AV indican deformaciones posteriores al Plio-Pleistoceno con fallas normales a través de fallas antitéticas de 90/80 a 150/70. Este trabajo pone de presente la técnica de la anisotropía de la susceptibilidad magnética como una herramienta útil en la comprensión del marco neotectónico a lo largo de las áreas urbanas y circundantes.

**Palabras clave:** Tectónica activa, zona de cizallamiento Romeral, anisotropía de susceptibilidad magnética, elipsoide de deformación, peligro sísmico, Andes colombianos.

## 1. INTRODUCTION

Documenting the geometry, kinematic and last time of displacement of faults is key for neotectonic studies and seismic hazard assessment. Neotectonics is responsible for understanding the current tectonic deformation framework of a region to characterize the long-term history of active faults, i.e., faults that have registered earthquakes in the recent geological past (Stewart, 2005). Thus, neotectonic studies are classically based on fault-related geomorphic expressions, the spatial distribution of recent deposits with stratigraphic evidence of deformation, and historical and instrumental seismicity. They constitute the essential elements to characterize the history and recent activity of seismogenic faults (Burbank and Anderson, 2011; McCalpin, 2013). The minerals within the fault zone and the immediate surroundings can be mechanically rotated and re-oriented, accommodating the equilibrium conditions that mark rupture plane orientations (Passchier and Trouw, 2005). This imprints a particular fabric on the deformed minerals, with particular geometry and kinematics, due to the superimposed strain field (Parés and Pluijm, 2002).

The anisotropy of magnetic susceptibility (AMS) is a geometric representation of the shape of the magnetic fabric in the

ellipsoid as a function of the magnetic susceptibility distribution (tensor defined by the  $k_1 \geq k_2 \geq k_3$  axis) of minerals in a sample (Jelinek, 1981). The magnetic susceptibility ( $k$ ) refers to the ability of minerals to acquire induced magnetization (Bilardello, 2016; Borradaile, 1988), then the shape of the magnetic fabric ellipsoid represents how paramagnetic and magnetic minerals are distributed along space (Parés, 2015).

The Aburrá Valley (AV) is located between the Antioqueño Plateau (AP) (Arias, 1996; Restrepo-Moreno et al., 2009) and the Romeral shear zone (RSZ) (Vinasco, 2019) with an 8-25 km wide fault zone that comprises various fault traces (Correa-Martínez et al., 2020). These two first-order landforms indicate that the AV is the product of coupled tectonic and erosive processes. However, the origin and evolution of this valley (e.g., clearly tectonic and/or erosive hypotheses) have been a subject of broad scientific discussion (e.g., Aristizábal et al., 2004; Aristizábal and Yokota, 2008; García, 2006; Hermelin, 1982, 1992; Rendón, 2003; Rendón et al., 2006). However, recent tectonic geomorphology and geophysics studies demonstrate that the AV is a tectonic valley influenced by regional faults (Rendón, 2003), covered by extensive Quaternary and Pliocene deposits, which filled independent pull-apart subbasins, today grouped along the Medellín-Porce drainage system.

Fault-related neotectonic expressions are associated with changes along the river profile, the morphology of each tectonic subbasin, and the occurrence of alluvial and hill slope deposits with evidence of tectonic deformation.

Faults covered by sediments of relatively well-known ages are fundamental in neotectonic investigation because i) they allow estimating a relative age of the deformation, and ii) they can reproduce the geometry and kinematics of these faults as the tectonic structures and the magnetic fabric tend to be parallel to subparallel. Opportunities to characterize active faults by the analysis of deformed sediment demonstrate the crucial role of Quaternary deposits as key for basic seismic hazards.

The main objective of this project is to contribute to the understanding of the neotectonic activity in the surroundings of the AV, Central Cordillera, Colombia, based on the magnetic fabric of deformed Quaternary sediments. For this reason, the magnetic susceptibility anisotropy (AMS) technique was used to constrain the sediment deformation along the AV and

surroundings to characterize the magnetic fabric and deformation ellipsoids along active faults. With these data, we search to contribute to updating the tectonic evolution models of this portion of the Central Cordillera, and the evaluation of the seismic hazards in the Aburrá metropolitan area.

## 2. STUDY SITE

The AV is in the north Central Cordillera and is surrounded by the RSZ on its western side and the Antioqueño Batholith in the east and north east (Figure 1). The RSZ represents a major long-term regional structure (e.g., Chicangana, 2005; Correa-Martínez et al., 2020; Ego et al., 1996; Vinasco, 2019; Vinasco and Cordani, 2012), and the Antioqueño Batholith, is one of the major Cretaceous granitic bodies of the Central Cordillera (more than 8000 km<sup>2</sup> exposed area), which can be considered as an analogous to a backstop (i.e., large rigid block in response to deformation (Rodríguez et al., 2005; Restrepo-Mo-

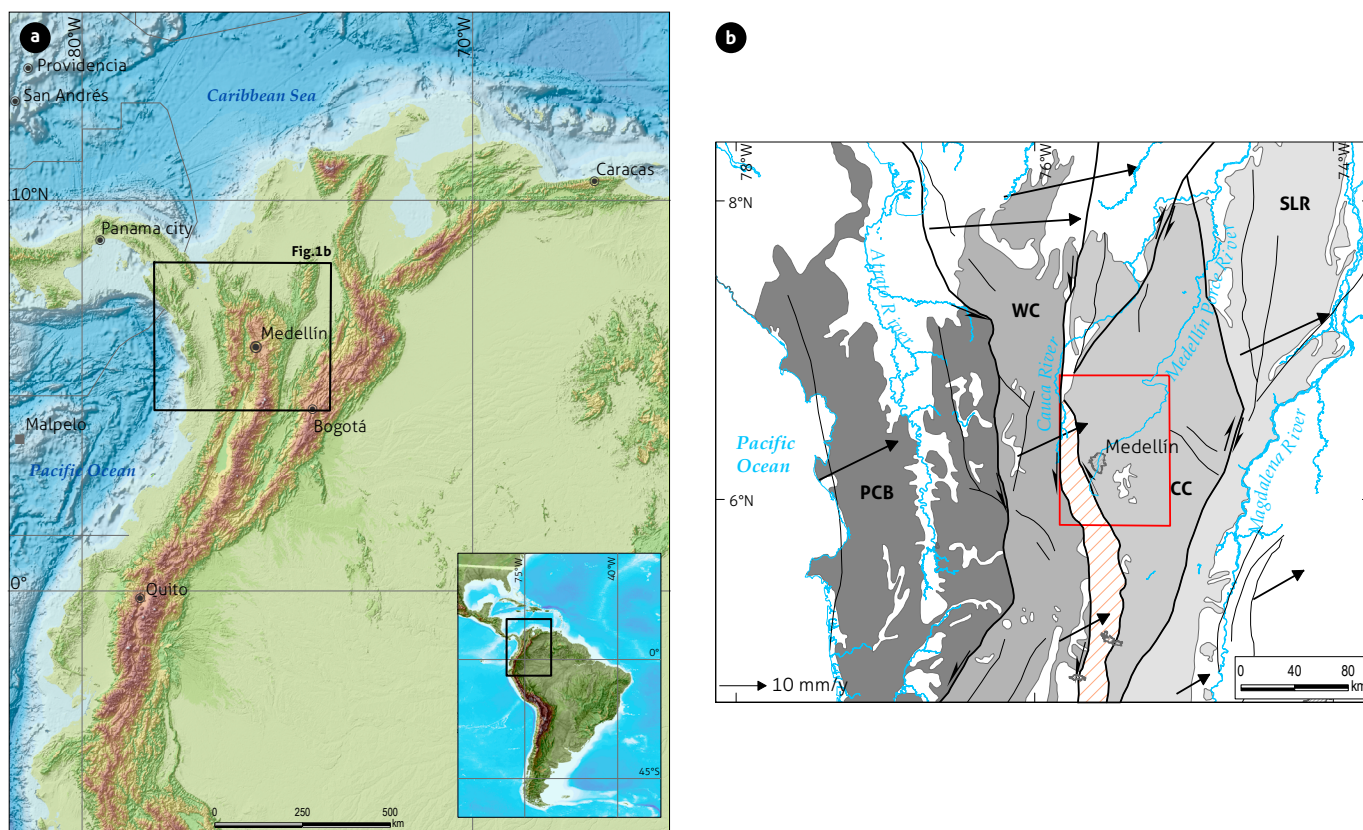


**Figure 1.** Study site location

a) The Colombian Andes in the South American and Andean context.. b) Simplified map of Northwestern Colombian Andes with main active faults at both sides of the Central Cordillera, and location of the AV. The black arrow indicates the GPS vectors relative to stable South America after Mora-Páez et al. (2020). CC = Central Cordillera, SLR = San Lucas Range, PCB = Panamá-Chocó Block, WC = Western Cordillera.

reno et al., 2009). Therefore, the AV location becomes vital to understanding the tectonic stress transfer and strain partition in relation to landscape response to late Andean orogenic pulses. The present day plate tectonic regime of the Northern Andean belt is dominated by oblique convergence of the Nazca, Caribbean and South American plates that control the behavior of major active faults and seismogenic faults in the region (Costa et al., 2020; Veloza et al., 2012). Understanding the patterns of AV landscape evolution is essential for the improvement of natural hazard assessments and successful land management strategies.

Multiple tectonic and geomorphological models of AV evolution have been proposed in recent decades (e.g., Álvarez et al., 1984; Arbeláez, 2019; Arboleda et al., 2019; Aristizábal et al., 2004; Aristizábal and Yokota, 2008; Botero, 1963; García, 2006; Henao Casas and Monsalve, 2017; Hermelin, 1982; In-

tegral, 1982, 2000; Rendón, 2003; Rendón et al., 2006; SGM, 2002; Shlemon, 1979). All these proposed models coincide with the relevance of climate and tectonic forcing processes in AV development, at least since the Late Pliocene, but the roles of mechanisms and forcing processes differ considerably.

The tectonic configuration of pull-apart basin, push-up blocks and erosive processes along the AV have been proposed partially by many authors (e.g., Botero, 1963; Hermelin, 1982) (Figure 2). Additionally, Rendón (2003), and Rendón et al. (2006) contributed to this hypothesis by integrating morphotectonic, morphostratigraphic, geophysical and geochronologic techniques demonstrating that the AV is the result of the merging of different ancient tectonic subbasins that have been active since at least Pliocene times (Henao Casas and Monsalve, 2017; Rendón et al., 2006; Toro, 1999; Toro et al., 2006). RSZ dynamics and the most recent phases of Andean Orogeny defi-

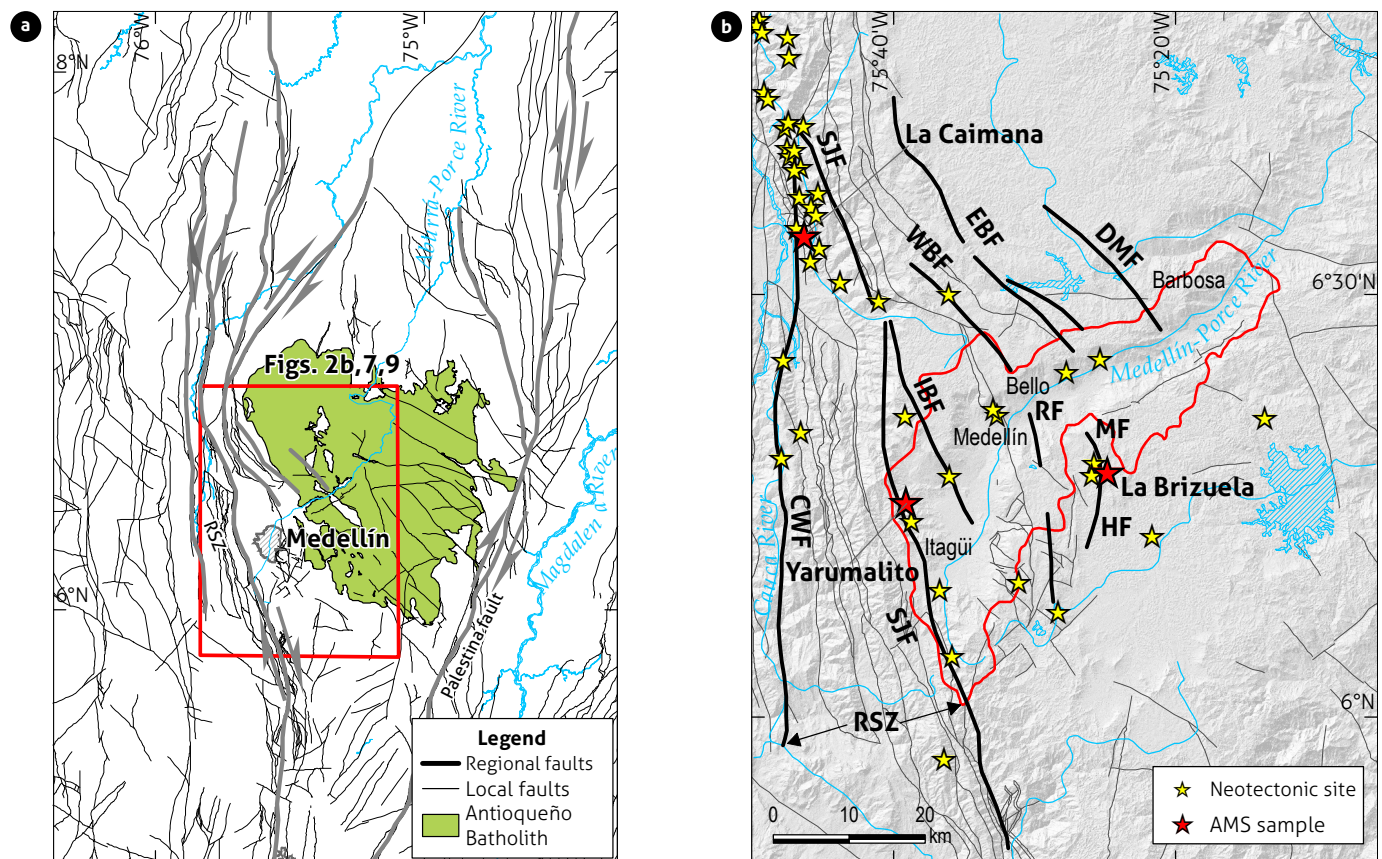


**Figure 2.** Detailed tectonic and geomorphic expression of the Central Cordillera controlling AV’s morphotectonic  
 a) Main tectonic boundaries in the Northwestern Andes (black lines) and location of the study site between the RSZ, and the Antioqueño Batholith which is shown as green polygon in the center of the Central Cordillera (Gómez-Tapias et al., 2015). b) Active faults in the surroundings of the AV, named as SIF = San Jerónimo Fault, CWF = Cauca West Fault, IBF = Iguaná-Boquerón Fault, WBF = Western Belmira Fault, EBF = Eastern Belmira Fault, RF = Rodas Fault, DMF = Don Matias Fault, MF = La Mosca Fault, and HF = La Honda Fault. Along these faults several neotectonic sites have been reported previously (see Table 1), and three of them were selected for AMS analysis.

ne a simplistic tectonic model for the AV (Arias, 1995; Rendón et al., 2006; Restrepo-Moreno et al., 2009). Faulted deposits in western, central and northeastern sites of the AV suggest that tectonic deformation is still active in the region (e.g., Rendón, 2003; Yokota and Ortiz, 2003).

Geophysical data provide clues to estimate the crustal structure of the AV, suggesting an average crustal thickness of ca. 50-55 km in the Antioqueño Batholith area (Henaó Casas and Monsalve, 2017; Poveda, 2013). This value is higher than the average of 30-40 km for the North Andean block (Ojeda and Havskov, 2001). On the other hand, Rendón (2003), using a geoelectrical survey, demonstrated that basement rocks of the AV are deformed by RSZ-related faults configuring a complex system of pull-apart basins and pop-up structures, segmenting the erosional surfaces of the Central Cordillera, just in the transition to the Antioqueño Batholith.

The tectonic geomorphology of the AV is analyzed by Rendón (2003) as a landscape response to tectonic and climatic forcing. Then, Rendón et al. (2006) and Aristizábal and Yokota (2008) propose chronostratigraphic frameworks of slope and alluvial deposits between the Late Pliocene and Late Pleistocene based on fission tracks and radiocarbon ages. These works include the previous datasets from Restrepo (1991), Silva (1999), Toro (1999) and Toro et al. (2006), improving the AV models with the implementation of quantitative geomorphic analysis and dating techniques. Several swath profiles and longitudinal river profile analyses made by Aristizábal and Yokota (2008), and Rendón (2003) indicate the knickpoints and knickzone locations of the main river and some of its tributaries.

The main knickpoints coincide with geomorphic features controlled by faults such as north Ancón and south Ancón and deformed basins previously highlighted. Although some of the faults reported as crossing the AV show deformation over recent sediments, their ages and displacement rates remain undocumented (Table 1). Future efforts on neotectonic studies need to concentrate on dating faulted or deformed sediments to quantify the timing and rates of active faults and ultimately to expand the temporal window by exploring paleoseismological and even archeoseismological records.

RSZ historical earthquakes, and hence the AV's seismic history, are documented in the area (Espinosa, 2003), but the most recent events were concentrated in the southern part of the Romeral megastructure, such as the 5.5 Mw Popayan earthquake in 1983 (Lomnitz and Hashizume, 1985); 6.4 Mw Páez earthquake in 1994 (Wilches-Chaux, 2005); and 6.2 Mw Quindío earthquake in 1999 (Gallego et al., 2005). In the northern part, close to AV, Suter et al. (2011) indicates the occurrence of pre-Hispanic Holocene earthquakes, and Caballero (2014) highlights events reported in Medellín by historians during the 18<sup>th</sup> century.

### 3. METHODOLOGY

#### 3.1. Identification and sampling of deformed sediments for AMS analysis

To constrain the tectonic imprints on recent deposits, we choose samples for AMS analysis from sites restricted to fault traces with a well-defined morphotectonic expression and previously documented Quaternary deformation (Table 1). We chose pla-

Table 1. Main features of active faults in the surroundings of the AV separating major tectonic basins

Structure	Geometry	Kinematic	Brief description	Deformed sediments	References
Romeral shear zone	N-S to NNW-SSE/ high angle to E	Predominantly inverse. Left-lateral North of 5° latitude and right-lateral to the south	Constitute the PDZ and include San Jerónimo and Romeral faults. Exhibit high geomorphic expression, control southwestern basins of Aburrá Valley	Displacement of Holocene clayed terraces in Santa Fe-Sopetrán depression, and Late Holocene alluvial deposits in Yarumalito school and Late Holocene paleosols in close to Palmitas	Toro et al. (1999), Ortiz (2002), Vinasco and Cordani (2012), Suter et al. (2011), Lalinde et al. (2009)
Belmira Fault	N-S to N30W	Inverse with left-lateral component	Control the Rio Chico catchment and show displaced deposits. It is related to Calles Fault to the east and EL Carmen Fault in the transition to the west. Its southern trace connects with Don Matias Fault	Deformed Pleistocene mudflow	Integral (1982), Mejía (1984), SGM (2002), Rendón (2003), Álvarez and Trujillo (1989)
Don Matias Fault	N30-40W	Inverse with left-lateral component	Continuity of the Belmira fault to the southeastern	Deformed Pleistocene mudflow	Integral (1982), Rendón (2003)
Rodas Fault	N-S/subhorizontal	Inverse	Fault associated with Aburrá Ophiolitic complex emplacement in the eastern hillslopes of the valley		Rendón (2003)
La Honda Fault	N-S/50-75E	Inverse/left lateral (?)	Control the Honda creeks in the east erosion surface beside the AV.	Deformed Holocene volcanic ash layers and Pleistocene fluvio-lacustrine deposits	Integral (2000), SGM (2002), Rendón (2003)
La Mosca Fault	NNW/subvertical	Inverse/left lateral (?)	Control the La Mosca creeks in the east erosion surface beside the AV.	Displacement of Holocene volcanic ash layers and Plio-Pleistocene fluvio-lacustrine deposits close the La Mosca Creek	Pages and James (1981), Rendón et al. (2015)
La Iguaña-Boquerón Fault	N-S to N12-20W/ high angle to E	Unknown	Fault associated with the Romeral shear zone	Deformed Pleistocene mudflows	Ortiz (2002), Rendón (2003)

ces from the available neotectonic sites based on: i) deformed sediments of known age, and ii) fine grain size fractions (i.e., high contents of silt and clay) to improve sampling. Prior to the sampling phase, we made geomorphologic maps at 1:10 000 scale, combining the main fault traces and Quaternary deposit distribution, which allowed us to identify the structural and morphotectonic framework of each place. Additionally, stratigraphic relationships of the deformed sediments with the surroundings were described, as well as the measurement of geological structures such as fault planes that affect the selected outcrops. Then, we sampled deformed soft-sediment material, mainly silt to clay layers, using polystyrene boxes of 8 cc. Each box was marked and fully oriented in the field using a Brunton compass and following the AGICO (2011) protocol.

### 3.2. Magnetic fabric of deformed sediments

The AMS of sedimentary samples can be represented as a magnetic fabric ellipsoid shape defined by the geometric distribution of the magnetic susceptibility tensor ( $k_1 \geq k_2 \geq k_3$  axis) of a set of minerals in a previously oriented sample. As the magnetic susceptibility ( $k$ ) refers to the ability of the minerals to acquire induced magnetization (Bilardello, 2016; Borradaile, 1988), the magnetic fabric ellipsoid shape represents how paramagnetic (e.g., pyroxenes, amphibole, biotite, etc.) and magnetic minerals (e.g., magnetite, hematite, iron, etc.) distribute in space (Parés, 2015). The magnitude of magnetic fabric can be expressed by the degree of anisotropy ( $P = k_1/k_3$ ) and the shape of the magnetic fabric ellipsoid is conveniently described by the shape parameter (Jelinek, 1981);  $1 > T > 0$  reflects oblate or planar shapes whereas  $-1 < T < 0$  reflects prolate or linear shapes (Jelinek, 1981).

In deformed environments, the textural and magnetic fabric of fine sediments is coaxial with the directions of the principal strain axes; in these cases, the AMS ellipsoid can be represented as a deformation ellipsoid (Levi et al., 2014; Parés, 2015; Parés and Pluijm, 2002). While undeformed sediments tend to show oblate shapes, during extension or compaction the AMS ellipsoid changes progressively to a prolate shapes. As the deformation continues ellipsoid shapes become oblate again showing higher degrees of anisotropy compared to in previous stages of deformation (Parés, 2015; Soto et al., 2009; Weil and Yonkee, 2009). In neotectonic analysis, magnetic foliation of samples located in active fault zones is valuable because addresses shear plane orientations while magnetic lineation ( $k_1$ ) indicates the shear direction. Due to this, the AMS

approach becomes a valuable tool to measure and characterize the magnetic fabric of brittle faults and fault-deformed soft sediments (e.g., Borradaile and Henry, 1997; Casas-Sainz et al., 2018; Hamilton et al., 2004; Levi et al., 2014, 2018; Maffione et al., 2012; Soto et al., 2009).

A total of one hundred specimens were analyzed using the AGICO MFK1-FB Multifunction Kappabridge Magnetic susceptibility meter. Magnetic fabric data were acquired using Safyr4 W software (AGICO, 2011). Measurements were made at room temperature and under an operational frequency of 976 Hz and a low-intensity magnetic field of  $200 \text{ Am}^{-1}$  at the Paleomagnetism Laboratory of the Universidad EAFIT. Fifteen default positions for measurement were conducted according to the Jelinek protocol (Jelinek, 1977). After the Kappabridge measurements, we used the advanced treatment of magnetic anisotropy data - Anisoft software version 5.1.03 (Chadima and Jelinek, 2019), to produce the susceptibility mean tensor and its statistical error and to compute the AMS parameters and graphic results, such as the Jelinek (T-Pj), Flinn (L-F), and T-L diagrams.

### 3.3. Structural analysis

Theoretically, in a Riedel shear model, the principal displacement zone (PDZ) constitutes the general trend of the major shear zone which responds to a regional stress field (Cloos, 1928; Davis et al., 2000; Riedel, 1929). A synthesis of the geometric relationship of the basic structures and their sequential development in a stress field is presented by Cloos (1928), Busby and Bassett (2007), Cosgrove (2007), Gurbuz (2010), Mann et al. (1983), Noda (2013), Passchier and Trouw (2005), Ramsay (1980), Riedel (1929), Traforti et al. (2016), among others. In this model, the synthetic Riedel fault (R) is the first to be developed at angles of ca.  $30^\circ$  with respect to the maximum stress vector ( $\sigma_1$ ). Progressively, a second structure, the antithetic Riedel fault (R'), appears with the same angle on the opposite side of the maximum stress vector plane ( $\sigma_1$ ), showing conjugate shear deformation. As deformation evolves, P and P' shears appear as minor faults located symmetrically at  $\sim 55^\circ$  to the main compressional vector ( $\sigma_1$ ). The Y shears are minor synthetic faults parallel to the PDZ, and T represents tension fractures parallel to the maximum stress vector plane ( $\sigma_1$ ).

A tectonic framework of the AV was reviewed and analyzed from theoretical models of deformation in strike-slip environments and available literature of the study site. For the first part, we applied the Riedel shear model (Riedel, 1929) to geome-

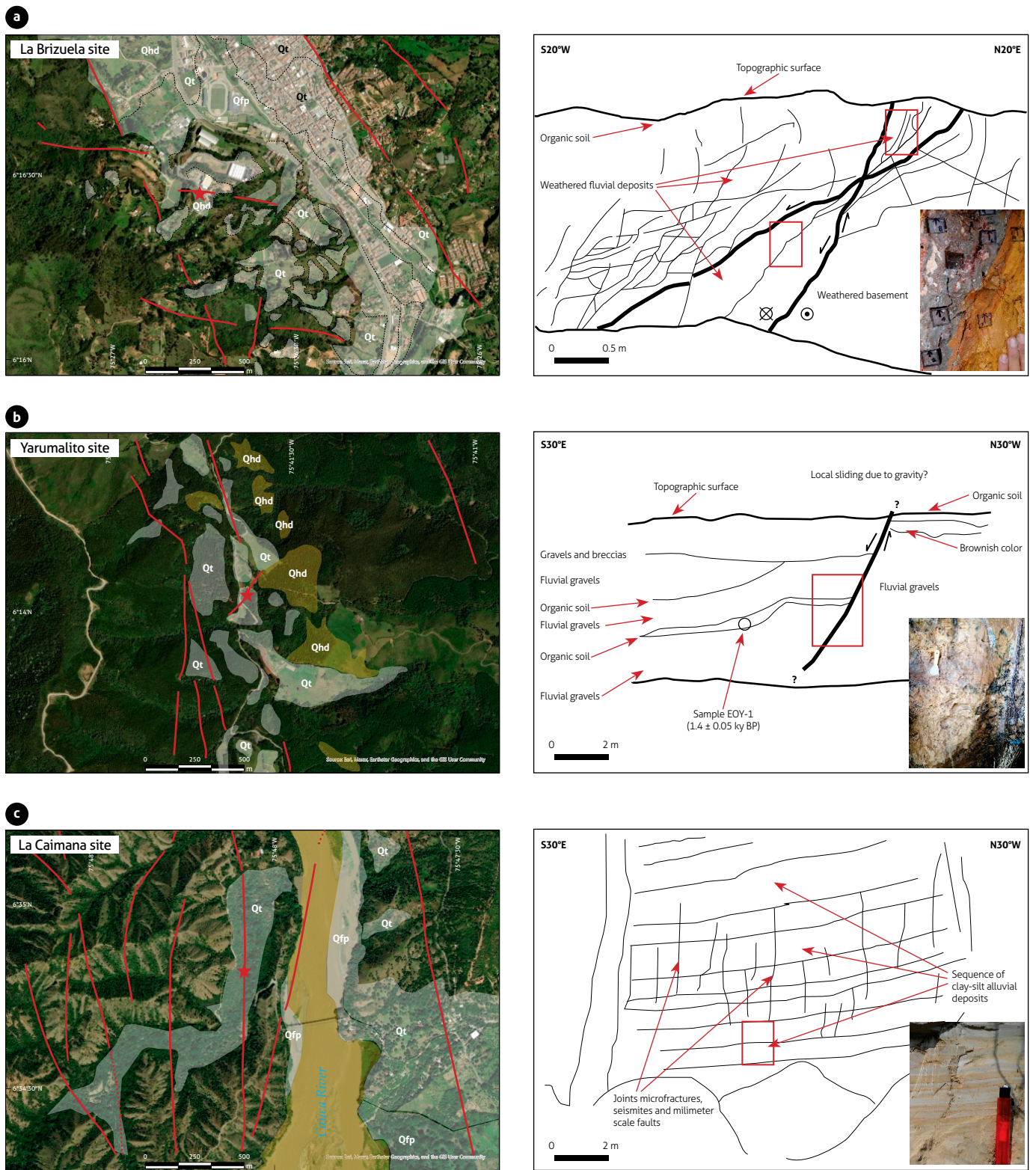


**Figure 3.** Selected sites for AMS analysis  
 a) Faulted Pleistocene (?) alluvial deposit along the La Mosca satellite Fault at the La Brizuela site. b) Faulted Holocene soil along the San Jerónimo Fault at the Yarumalito site. c) Apparently undeformed Holocene deposits covering the Cauca West Fault close to Santa Fe de Antioquia town. Red stars mark the specific location of the AMS analysis while red lines are the local faults covered by Quaternary deposits (Qt = Terrace, Qfp = Flood plain, Qhd = Hillslope deposit)

trically define the PDZ and hence estimate the kinematics of faulting and to identify neotectonic patterns in the AV that can be described by strike-slip faulting. In this stress-strain conceptual model, a hierarchy of structures can appear as the deformation evolves through time (Busby and Bassett, 2007; Mann et al., 1983; Noda, 2013). Then, we reviewed and compiled the geometry and kinematics of regional faults with neotectonic activity reported in the literature (Table 1). These faults were delineated using their geomorphic expression in a digital elevation model (DEM) with a 12.5 m spatial resolution. The DEM was downloaded from <https://www.asf.alaska.edu>, and the Topo toolbox v 2.2 (Schwanghart and Scherler, 2014) was used for longitudinal river profile extraction and knickpoint identification. In the field, mesoscale faults and structural datasets observed at the selected sites for AMS analysis were measured and compared with the magnetic fabric of deformed soft sediments. As the structural data provide the geometry of the fault plane, the AMS was used to evaluate the sense of motion of the structure. Finally, these data were compared with fault architecture derived proposed models of tectonic evolution of the AV.

## 4. RESULTS

### 4.1. Neotectonic sites and deformed sediments

The three selected sites with occurrence of Quaternary fluvio-lacustrine deposits and imprinted deformation of active faults are shown in Figures 2 and 3. They correspond to the La Brizuela (Guarne), Yarumalito (San Antonio de Prado), and La Caimana (Santa Fe de Antioquia) sites. Table 2 describe

main geologic features of each site. While the first one represents active faulting on the eastern side of the AV, the last two correspond to active faulting along the RSZ. Surface ruptures and faulted/buried sediments are characteristic at La Brizuela and Yarumalito sites, as opposed to the La Caimana site, where horizontal layers of apparently undeformed sediments cover active faults of the Cauca River Canyon. Gray-clayed sediments of the La Brizuela site exhibit inverse relief and high weathering grades, with estimated Plio-Pleistocene ages (Page and James, 1981) and deformation related to the La Mosca fault (Rendón et al., 2015). A total of 55 samples were collected at this site, with 12 samples distributed in the footwall block, 23 in the hanging wall block beside the principal fault plane, and 20 samples from apparently undeformed sediments (Figure 3a). Along the RSZ, the Yarumalito and La Caimana sites correspond to Holocene alluvial deposits (Yokota and Ortiz, 2003; García et al., 2011) covering the San Jerónimo and Cauca West faults respectively (Figures 3b and 3c). At the Yarumalito site, we collected 9 samples from the footwall and 6 from the hanging wall for a total of 15 samples. Finally, 30 samples of horizontally layered nondeformed sediments were collected at the La Caimana site.

### 4.2. AMS measurements of deformed sediments

The results of the AMS measurements are shown in Table 3. The shape parameters of the magnetic fabric ellipsoid are summarized in Figure 4. The mean susceptibility ( $k_m$ ) versus corrected anisotropy shape factor ( $P_j$ ) and the Jelinek diagram ( $P_j$ -T) are shown in Figure 5.

Table 2. Main geologic features of the selected sites for magnetic fabric analysis

Site	Structural features	Stratigraphic/ geomorphologic features	References
La Brizuela	Main structure: La Mosca Fault. Geometry: NNW/subvertical. Kinematic: Inverse/left lateral (?). Associated structures: normal faults at N85W strike. Marks the structural boundary between the Antioqueño Batholith to the east and the eastern structures of the RSZ controlling the landscape along La Mosca Creek.	Surficial formations: Alluvial terraces of the La Mosca Creek and associated slope deposits. Estimated age of deposits covering the fault: Pliocene to Pleistocene age for high elevated terraces showing high weathering grades (Bauxite). Type of deformation: Centimetric deformation along a mayor plane of displacement affecting highly weathered alluvial deposits.	Pages and James (1981); Rendón et al. (2015)
Yarumalito	Main structure: San Jerónimo Fault (RSZ). Geometry: N-S to NNW-SSE/high angle to E. Kinematic: Predominantly inverse Left-lateral North of 5° Latitude and right-lateral to the south. Associated structures: Satellite fault at 185/75 with normal movement.	Surficial formations: Alluvial deposits covered by relatively young paleosol. Estimated age of deposits covering the fault: Radiocarbon age of ca. 1400 y BP from paleosol. Type of deformation: Normal fault displaces alluvial deposits and paleosol at the Yarumalito school (San Antonio de Prado) affected by a satellite fault of the San Jerónimo Fault.	Ortiz (2002), Yokota and Ortiz (2003), Lalinde et al. (2009)
La Caimana	Main structure: Cauca West Fault (RSZ). Geometry: N10°W. Kinematic: Unknown, inferred as lateral left. There are positive flowers at mesoscale close to Santa Fe de Antioquia. Associated structures: Cauca West subparallel anastomosed faults.	Surficial formations: Alluvial and lacustrine deposits developed as consequence of Cauca's River natural damming. Estimated age of deposits covering the fault: Late Holocene radiocarbon ages from 0.1-6 ky. Type of deformation: soft sediment displacement and seismites with locally undeformed outcrop.	Suter et al. (2011); García et al. (2011)

**Table 3.** Group statistics of the anisotropy of magnetic susceptibility (AMS) from the deformed sediment samples in the surroundings of the AV

Site	Sample	N	$k_m$	sdv	k1		k2		k3		L	sdv	F	sdv	$P_j$	sdv	T	sdv
					Decl.	Incl.	Decl.	Incl.	Decl.	Incl.								
La Brizuela	All deformed samples	35	75.3	77.9	221.4	19.4	77.2	66.5	315.9	12.7	1.055	0.059	1.072	0.105	1.138	0.156	0.126	0.394
	Footwall	12	140.8	102.1	233.6	2.3	136.8	71.3	324.4	18.6	1.087	0.074	1.064	0.052	1.162	0.125	0.087	0.464
	Hanging wall	23	43.58	32.88	204.7	46.7	30.5	43.1	297.8	2.9	1.035	0.032	1.074	0.125	1.120	0.168	0.192	0.360
	Non-deformed samples	20	45.21	48.12	181.8	40.4	10.5	49.3	275.0	4.3	1.014	0.011	1.025	0.034	1.041	0.042	0.048	0.431
Yarumalito	All samples	15	450.5	202.9	38.1	71.4	219.2	18.6	129.1	0.3	1.006	0.003	1.008	0.004	1.014	0.004	0.094	0.427
	Footwall	6	491.7	253.5	52.0	68.2	254.2	20.3	161.4	7.5	1.006	0.002	1.007	0.005	1.013	0.003	0.075	0.575
	Hanging wall	9	422.9	172.4	27.7	70.7	181.8	17.5	274.3	7.9	1.006	0.002	1.008	0.004	1.015	0.005	0.107	0.333
La Caimana	Non-deformed samples	30	708.7	139.5	114.2	85.8	308.1	4.0	218.0	1.0	1.008	0.004	1.027	0.005	1.037	0.007	0.533	0.163

Notes: N = Number of analyzed samples,  $k_m$  = mean susceptibility (in  $10^{-6}$  SI units), (Decl) Declination and (Incl) inclination of the three-susceptibility axis (geographic coordinates), L = Lineation, F = Foliation,  $P_j$  = Corrected anisotropy degree, T = Shape factor of the AMS ellipsoid.

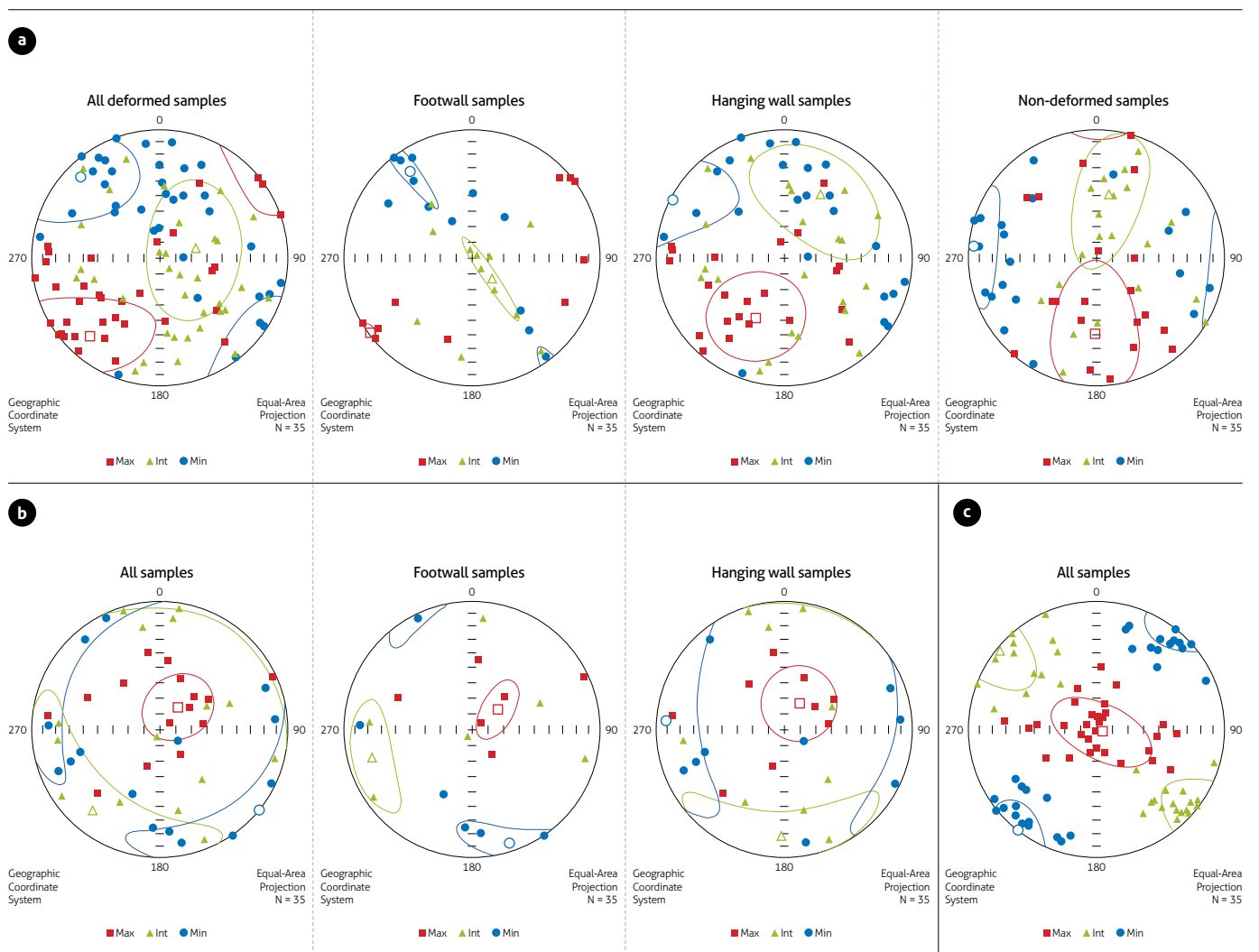


**Figure 4.** Magnetic fabrics of deformed sediments at the sites: a) La Brizuela, b) Yarumalito, and c) La Caimana

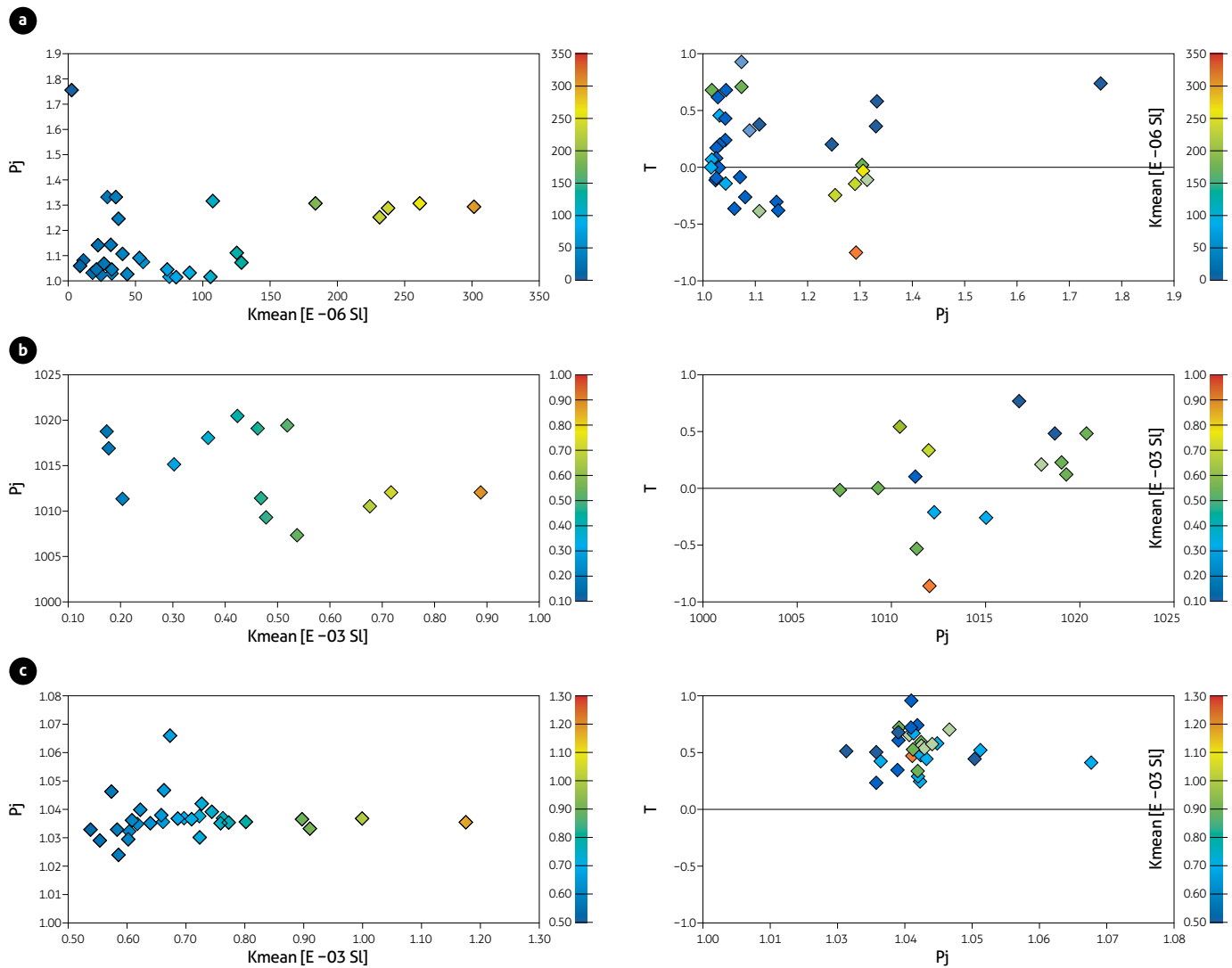


Figure 5. Mean susceptibility vs Corrected anisotropy shape factor and Jelinek diagram (Pj-T) of the deformed deposits at a) La Brizuela, b) Yarumalito, and c) La Caimana

The magnitude of the mean susceptibility ranges between 0 and  $300 \times 10^{-6}$  SI, with average values of ca.  $75.31 \times 10^{-6}$  SI at the La Brizuela site. At the Yarumalito site, the average susceptibility is  $450.5 \times 10^{-6}$  SI, with values ranging between 150 and  $900 \times 10^{-6}$  SI. The mean susceptibility values of La Caimana range between 500 and  $1200 \times 10^{-6}$  SI, with an average of  $708.7 \times 10^{-6}$  SI. In all cases, the  $k_m$  values were on the order of  $10^{-3}$  SI, except for the La Brizuela results, where  $k_m$  reached values near  $10^{-6}$  SI. The Jelinek diagram indicates that samples from La Brizuela and Yarumalito exhibit mixed prolate and oblate ellipsoid shapes with  $P_j$  values of less than 1.8, while samples from La Caimana show well grouped oblate ellipsoids with  $P_j$  values

between 1.02 and 1.07 (Figure 5). The F-L and L-T diagrams (Figure 6) show the well-defined triaxial ellipsoids of the Yarumalito and La Brizuela sites despite the large dispersion of this last sample. For the La Caimana samples, the results indicate oblate ellipsoid shapes.

#### 4.3. Structural models and magnetic fabric data

As the AV is located between the Antioqueño Batholith and the RSZ, its tectonic history needs to be a consequence of the evolution of these major geomorphic features. For our structural analysis, we define the RSZ, with a main strike of ca. N20°W, as the PDZ controls the major shear zone, which responds to the

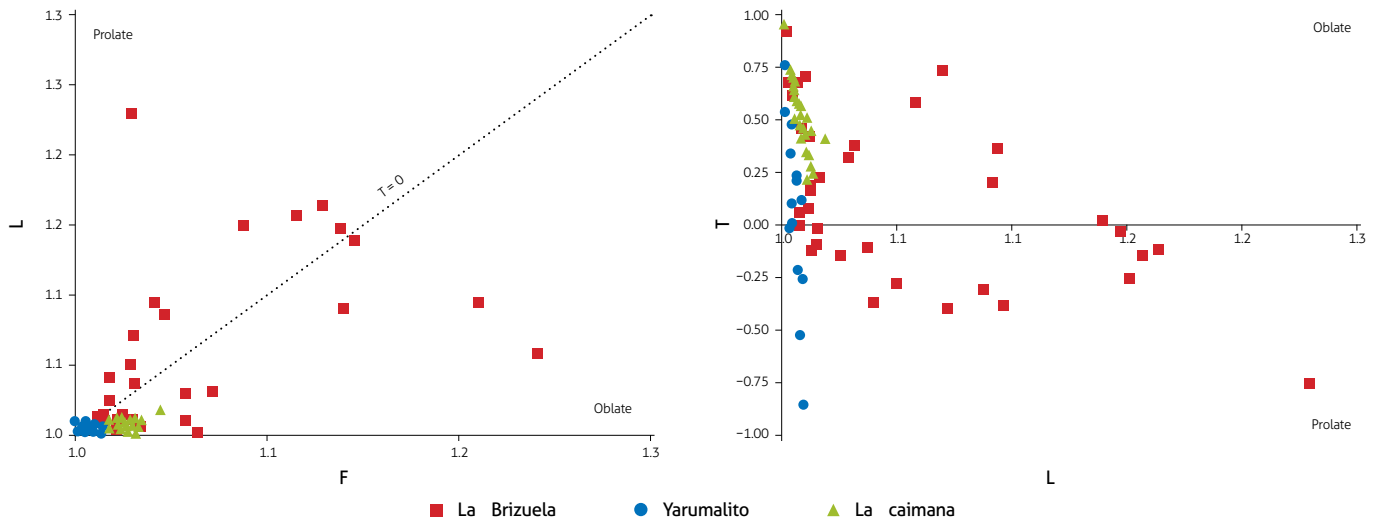


Figure 6. Shape parameters of the magnetic fabric ellipsoid and Flinn diagram for samples located in La Brizuela, Yarumalito, and La Caimana

regional stress field (Riedel, 1929; Ramsay, 1980; Davis et al., 2000). Then, assuming a left-lateral displacement of the PDZ (Gallego, 2018; Paris et al., 2000), our analysis indicates the occurrence of synthetic faults (R) with NNW strikes and left-lateral displacement along the RSZ and Antioqueño Batholith transition (Figures 2 and 7). These structures extend across the basement of the AV forming gorges (i.e., Ancones) and tectonic valleys, and exhibit their expression along the longitudinal river profile of the Medellín-Porce River as knickzones (Figure 8). Based on the spatial distribution of these faults, and tectonic/geomorphologic models proposed by Rendón (2003) and Aristizábal and Yokota (2008), we separate the AV valley into four main sections (or subbasins) named Itagüí, Medellín, Bello and Barbosa, from South to North.

The first and uppermost section includes the Itagüí tectonic subbasin with irregular depths varying between ca. 75 m to ca. 220 m, the Altavista Stock and the older and highly deformed deposits of the AV located in La Tablaza, Caldas (Rendón et al., 2006; Toro et al., 2006). This southwestern portion of the AV is directly influenced by the San Jerónimo Fault as the latter controls the Doña María creek and the headwaters of the Medellín River (Rendón et al., 2006) (Figures 2, 7 and 8). Highly dense anastomosed geometry of faults with fault bending basins (R-start displacement) appear dominating the landscape in this section of the AV.

The second section corresponds to the Medellín tectonic subbasin, located on the western-central side of the AV. In this sec-

tion, the AV exhibits a major width of ca. 10 km, following a NW trend narrow depression of ca. 240 m depth that appears related to the Boquerón-Iguaná Fault trace Rendón (2003) (Figure 7). Topographic highs located in erosion surfaces on both sides of the AV such as the Baldías (~3200 masl) and Santa Elena (~2600 masl) are included in this segment. Step-over basin geometries were identified in this section with the dominance of NW to EW striking normal faults (coaxial with antithetic R' structures).

A third section of the AV includes the Bello tectonic subbasin with less than 110 m depth and the Ovejas Stock delimited by the western Belmira Fault. This section acts as a transition to the Antioqueño Batholith domain, as well as inherited structures associated with Aburrá's ophiolitic complex (Ibáñez-Mejía et al., 2020). This section also exhibits fault-terminated basins with WNW normal faults (Rendón, 2003).

The fourth section is on the northeastern side of the AV and inside the granodiorite body of the Antioqueño Batholith. This section exhibits a completely different landscape and tectonic regime in terms of valley morphology following a well-defined NE trending V-valley shape separating the extensive erosion surfaces of the AP and vertical elevation differences of ca. 1 km. The occurrence of tectonic controls of NE strikes in this section of the AV can be related to P' structures. As a synthesis, the AV can be understood as a complex coalescence of tectonic basins located in the middle and upper sections of the AV. They appear as lazy-S shaped basins (Mann et al., 1983) immediately beside the RSZ (i.e., Caldas, La Estrella and

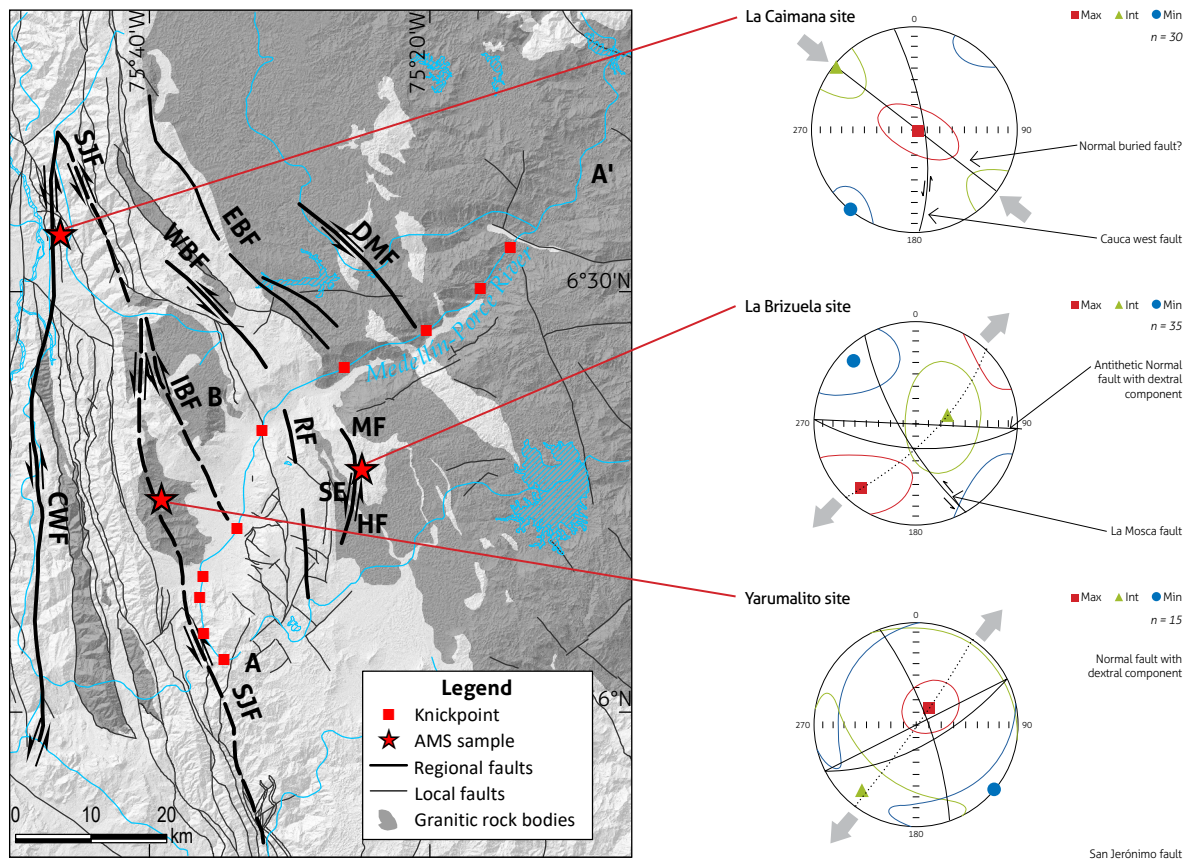


**Figure 7.** Comparison of magnetic fabric ellipsoid and structural datasets of active faults at La Caimana, La Brizuela, and Yarumalito sites, and a synthesis of the Riedel shear model indicating the occurrence of primary and secondary structures under a known strain field. Longitudinal river profile is marked from A to A'. SJF = San Jerónimo Fault, CWF = Cauca West Fault, IBF = Iguaná-Boquerón Fault, WBF = Western Belmira Fault, EBF = Eastern Belmira Fault, RF = Rodas Fault, DMF = Don Matias Fault, MF = La Mosca Fault, and HF = La Honda Fault. B = Baldías, SE = Santa Elena.

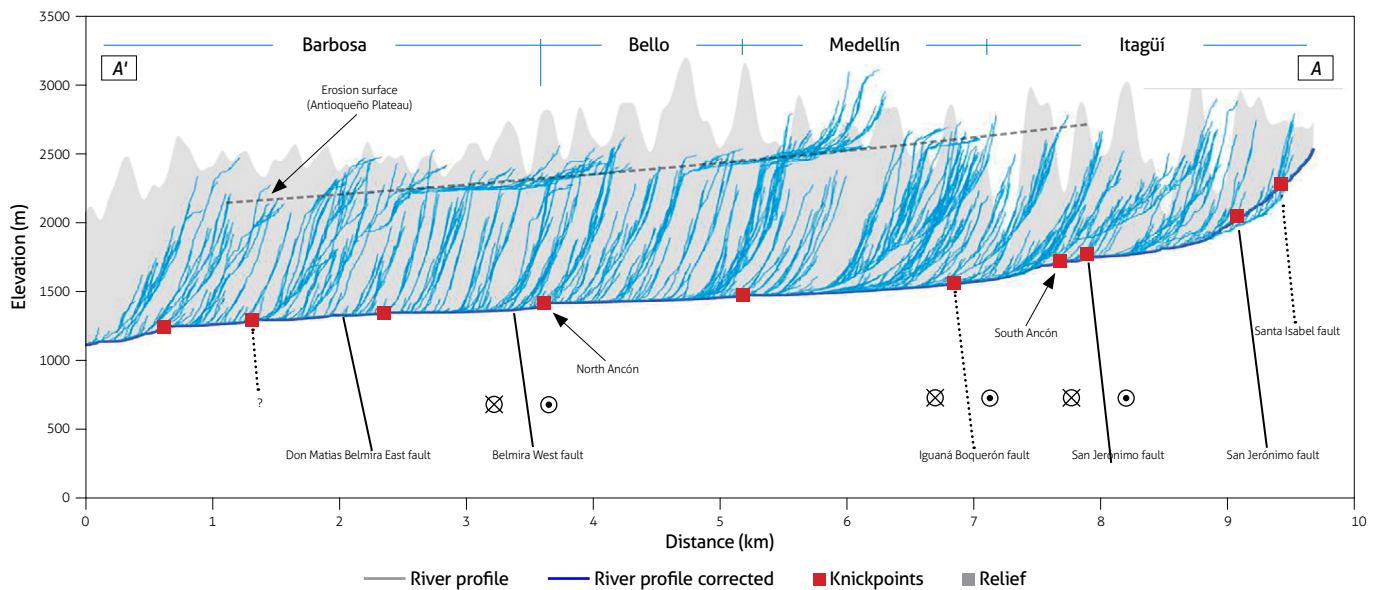


**Figure 8.** Longitudinal profile of the Medellín Porcía River indicating the spatial distribution for the four tectonic basins of the AV separated by local faults (Rendón, 2003)

San Antonio de Prado) comprising the upper AV. In the middle portion of the valley, tectonic basins appear as releasing bend step-over and/or rhomboidal shaped pull-apart basins (i.e., Bello and Medellín subbasins) (Figure 7).

The structural and magnetic fabric data obtained at the outcrop scale are presented in Table 4. In addition, Figure 7 shows the principal directions of the AMS ellipsoid integrated with the geometry and kinematics of the measured fault planes at the three selected sites for detailed analysis.

Although the La Mosca fault has a general strike of ca. N30°W, subvertical dip and left-lateral displacement, our structural data from the La Brizuela site indicate normal faulting along the 185/75 plane. The magnetic fabric ellipsoid shape shows mean values of declination/inclination of 221.4/19.4 for  $k_{max}$  and 345.9/12.7 for  $k_{min}$ . Slight differences were found between samples from both sides of the La Mosca fault, as the  $k_{max}$  magnetic lineations were ~204.7/46.7 for the hanging wall, and ~233.6/2.3 for the footwall. The results from apparently nondeformed sediments also show magnetic lineation of 181.8/40.4. In the fault zone, mixed ellipsoids between oblate and prolate shapes suggest high magnetic foliation toward the south and southeast and magnetic lineation indicating normal displacement with a dextral component along the WNW fault plane.

At the Yarumalito site, a mixed prolate-oblate ellipsoid with marked magnetic foliation ranging between 94/82 and 162/83, subparallel to the 150/70 fault plane, and subvertical lineation indicate predominantly normal faulting with a dextral component. Buried faults in the La Caimana site follow the regional trend of the RSZ (i.e., NS to NNW), although our AMS ellipsoid indicates a subvertical magnetic cleavage of 114.2/85.8 (Figure 7).

## 5. DISCUSSION

Deformed sediments are critical in active tectonic settings because they record the timing and magnitude of ancient earthquakes and provide clues for detailed palaeoseismological analysis (McCalpin, 2012). Our data provide new clues to understanding the neotectonic framework of the AV and its surroundings as well as a practical approach to tectonic geomorphology, structural geology, and AMS analysis in seismic hazard studies. Previous geophysical data indicate faults controlling AV's topographic structure and sedimentary infill (Rendón, 2003; Henao Casas and Monsalve, 2017). These structures exhibit marked geomorphic expressions along each tectonic subbasin and the whole drainage network and deform Quaternary deposits in some parts of their main traces (see Table 1).

Because the structural data from deformed sediments yield the geometry of the fault plane, the AMS provides clues on the kinematic of the fault, and  $k_{max}$  tends to align in response to the stress field, we used the obtained magnetic lineation ( $k_l$ ) as a shear direction indicator in neotectonic studies (Caricchi et al., 2016; Cho et al., 2014; Levi et al., 2014; Parés and Pluijm, 2002). In this study, all the collected samples show deformational magnetic fabric, i.e., subhorizontal  $k_{min}$  distribution even on apparently nondeformed samples of La Caimana and La Brizuela (Figure 4). The occurrence of magnetic fabric on evidently nondeformed sediments is also documented by Cifelli et al. (2004) indicating the development of a stress field during the incipient deformational phase. In addition, the obtained mean susceptibility ( $k_m$ ) values were on the order of  $10^{-3}$  SI, except for the La Brizuela results, where  $k_m$  reached values in the range of  $10^{-6}$  SI (Figure 5) suggesting that the net contri-

Table 4. Summary of the magnetic fabric and structural dataset from the analyzed sites

Fault	Site	Sample	n	AMS ellipsoid shape	Magnetic lineation ( $k_{max}$ )	Magnetic foliation	Magnetic fabric	Structural data
La Mosca	La Brizuela	All deformed samples	35	Triaxial oblate to elongate	221.4/19.4	136/76 (NE-SW)	Compressional/cleavage development	Fault plane: 185/85, 183/73, 180/74
		Footwall	12	Triaxial oblate	233.6/2.3	144/71 (N50E-S50W)	Compressional/cleavage development	
		Hanging wall	23	Triaxial	204.7/46.7	118/87 (NE-S28W)	Compressional/cleavage development	
		Nondeformed samples	20	Triaxial	181.8/40.4	95/85 (N05E-S05W)	Shear-related/deformational fabric	
San Jerónimo	Yarumalito	All samples	15	Triaxial	38.1/71.4	129/89 (N39E-S39W)	Shear-related/deformational fabric	Fault plane: 150/70
		Footwall	6	Triaxial	52.0/68.2	162/83 (N72E)	Shear-related/deformational fabric	
		Hanging wall	9	Triaxial	27.7/70.7	94/82 (N04E)	Shear-related/deformational fabric	
Cauca West	La Caimana	Nondeformed samples	30	Triaxial oblate	114.2/85.8	308/89 (N52W)	Shear-related/deformational fabric	Horizontal bedding plane. Fault plane (covered): 90/90, 270/85

bution of ferromagnetic minerals to the susceptibility and to the AMS is not considerable (Parés, 2015). Large differences in mean susceptibility for the three sampling sites may reflect some postdepositional or tectonically induced changes in magnetic mineralogy, as well as the potential effect of weathering in the older deposits of La Brizuela. In general, the AMS ellipsoids from the La Brizuela and Yarumalito sites correspond to a slightly similar extensional deformation following a NE-SW orientation, while the AMS ellipsoid from the La Caimana site shows a highly compressional/rotational system with a NW strike for the major plane (Figure 6).

Also, the AV comprises a complex valley after the coalescence of multiple tectonic subbasins in the transition zone between the AP and the RSZ morphotectonic domains. For a better understanding of the tectonic history of the AV, we discuss the structural and magnetic results for two main sections that include our AMS sites, the AV to AP transition zone under a high contrast of basement anisotropies, and the RSZ, where the PDZ marks the main trend of deformation along the study site.

### 5.1. AV-AP transition zone

The La Mosca fault (LMF) is an approximately N10°W, inverse and left lateral, high dip fault located on the eastern side of the AV (Figure 7). Its trace controls La Mosca Creek, which crosses Guarne town. Gallego (2015) indicates that the La Mosca and La Honda Faults coincide with a faulted contact between metamorphic basement and the Antioqueño Batholith. In geomorphologic terms, the La Mosca fault separates erosion surfaces and erosive scarps, as Rendón (2003) reported its correlation following the Eastern Belmira Fault (i.e., NW of AV). These structures represent the transitional expression of the strain partitioning on the farthest portion of the RSZ (i.e., Bello and Barbosa tectonic subbasins) but also seem to respond to the same regional strain field. Additionally, the northeastern part of the Medellín tectonic subbasin exhibits a fault-terminated basins with a Z-shape and basement of less than 110 m depth and a NW-SE trend (Figure 9).

At the La Brizuela site, AMS results show that the magnetic lineation of samples from the La Mosca Fault at the La Brizuela site indicates values of 205/47 to 234/03 (SW) and shear planes with poles ranging between 298/03 and 324/19 (NW). In contrast, the results from apparently undeformed samples located approximately five meters away from the fault trace (WNW) show magnetic foliation planes with a N-S trend ( $k_3 \sim 276/04$ ) and magnetic lineation of ca. 180/40. The orientation of the

main normal plane shows a dextral component of displacement related to the development of antithetic faults (R') which segment the principal trace of N10°W strike (Figure 7). This transitional section toward the AP was considered to represent relatively low neotectonic activity before the studies of Rendón et al. (2015), which showed continuous deformation along the La Mosca and La Honda Faults displacing alluvial deposits and volcanic ash layers.

AMS data from some of the alluvial deformed Quaternary deposits in the LMF support the fact of undocumented neotectonic features which creates the idea of relatively low tectonic and seismic activity but also updates the earthquake geology on the eastern side of the AV and its surroundings. This situation is caused in part due to the difficulties to find Quaternary deposits preserving fault displacements and deformation history of the region. Although that, recent studies have been updated the seismic hazard assessment in the region as new stratigraphic evidence have been documented.

Note that the structural analysis shown in Figure 9 marks the occurrence of NE structures corresponding to antithetic faults (P') which control the northern section of the AV along the low anisotropy regime of the Antioqueño Batholith, while the antithetic faults (R') cross the valley. Despite the lack of paleoseismological data from the LMF, neotectonic elements of this site mark a substantial active tectonics along a relatively low mechanical anisotropy (i.e., granitic and thermal metamorphic rocks). Note that fault-bonded granitic rock units such as Altavista and Ovejas stocks can be interpreted as segmented and transported blocks along the RSZ-related faults in its eastern side, indicating a progressive reduction in size as they approaches the main strain zone (i.e., the PDZ). Growing urbanism and concomitant modification make it difficult to document of detailed stratigraphic evidence of ancient earthquakes.

### 5.2. Romeral shear zone (RSZ)

The San Jerónimo and West Cauca faults constitute the eastern and outermost faults of the RSZ, displaying mainly NNW strike deformation. The morphological expression of fault traces and their associated morphotectonic features are well documented along this shear zone (Lalinde et al., 2009; Ortiz, 2002; Rendón, 2003). In addition, Late Holocene displacements of these faults (Yokota and Ortiz, 2003) allow us to propose and evaluate the hypothesis of this region as the PDZ.

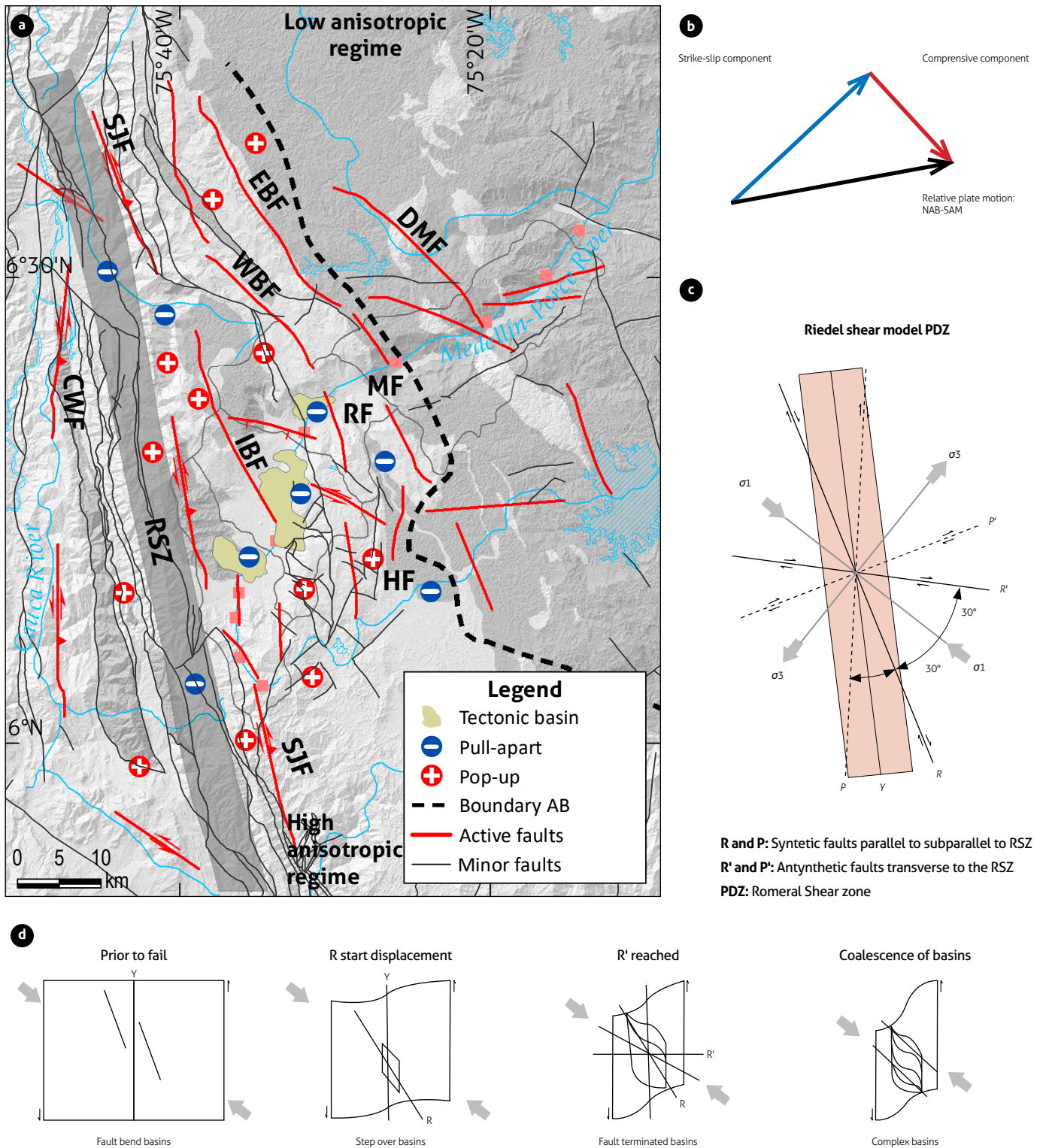


**Figure 9.** Conceptual model for a neotectonic framework of the AV  
 a) Crustal deformation models under strike-slip fault systems; b) Components of the relative plate motion between the North Andean Block (NAB) and the South America Plate (SAM). GPS vectors from Mora-Páez et al. (2020) and Noquet et al. (2014), in Kirby (2016); c) Simplified Riedel shear model under the present-day stress field and the compressive component. d) Simplified model of the evolution of coalescence transtensional/transpressive sedimentary basins (Mann et al., 1987; Noda, 2013).

The structural architecture in the Yarumalito site is defined by relatively more active faults that developed into step-over basins such as the upper Doña Maria catchment and the Medellín River headwaters, all of them in the Itagüí tectonic subbasin (Figure 9). Furthermore, a normal 150/70 satellite fault of the San Jerónimo Fault exhibits a more recent displacement (ca. 1.5 ky, from  $^{14}\text{C}$ , Yokota and Ortiz, 2003), with a similar geometry and kinematics as found in the LMF, except for a different subvertical magnetic lineation of 94/82 and 162/83 (Figure 7). This expression of the magnetic fabric in the Yarumalito site marks an important horizontal component of displacement of faults in this section, where the anisotropic regime is considerably higher in comparison with the eastern section.

On the other hand, tectonic and magnetic results on the western side of the RSZ, i.e., the La Caimana site, contrast with previous sites (Figure 7). Late Holocene fine-grained sedimentary sequences overlying the Cauca West Fault (Suter et al., 2011) do not exhibit remarkable deformation at the local scale, and the more remarkable deformation shows millimetric displacement of silt layers. Triaxial oblate magnetic ellipsoid shapes, with a magnetic lineation of 114.2/85.8 and magnetic foliation plane of 308/89 (N52W), define a shear-related/deformational fabric of the La Caimana site consequent with a previous tectonic hypothesis of strike-slip faulting controlling the Santa Fe-Sopetrán depression along a section dominated by the Cauca River Canyon and RSZ. The obtained structural and magnetic dataset marks the RSZ as a PDZ of the neotectonic model of the AV. Additionally, these results on the western section of the RSZ are in agreement with the development of NW structures in a similar structural regime along the WC, including faults such as the Cañasgordas, Abriaquí, and Arma, among others (Paris et al., 2000; Noriega and Caballero, 2015; add more refs), all of which show a left-strike kinematics and Quaternary displacements.

### 5.3. Neotectonic and recent deformation in the surroundings of the AV

Based on the compiled and measured structural data of the active faults and associated structures in the study zone, we propose an interpretation of the brittle structures along the AV and their relationship with the surrounding first order geomorphic structures, such as the Antioqueño Batholith and the RSZ. Additionally, we propose that fault bending basins controlled by synthetic faults (R) appear in the early stages of deformation.

This is what we observed in the core of the PDZ (i.e., Itagüí subbasin) as corresponding to the more active and rejuvenated structure (Figure 9). As deformation continues, antithetic faults (R') control the development of step-over basins with extended areas and deeper depocenters (Medellín and Bello subbasins). The long-term evolution of tectonic valleys creates complexes of coalescent valleys subbasins with overimprinted tectonic and erosive processes (e.g., Mann et al., 1983; Noda, 2013). In our specific case, the PDZ was defined by the RSZ, as it represents the major structure controlling the strain partition in the study site. In addition, compressional vectors estimated from the deformational magnetic ellipsoid are coherent with geodesic vectors from Mora-Páez et al. (2020), as both indicate a NW-SE orientation of the maximum compressional component ( $\sigma_1$ ), and they are consequent with the neotectonic framework of the Northern Andes (Costa et al., 2020).

Deformation in an oblique convergence tectonic setting produces strain partitioning, and hence faulting and folding, by transpression and transtensional mechanisms (Cosgrove, 2007; Ramsay, 1980). This setting is dominated by strike-slip regional faults that introduce crustal-scale heterogeneities. In this study, we assume that the massive granitic body of the Antioqueño Batholith has a different mechanical response than the surrounding fault-controlled lithologies included in the transition to the RSZ. This simplified scheme of differential mechanical response as a function of inherited anisotropy and rheology of the involved materials is coherent with the development and reactivation of faults controlling isolated tectonic basins conforming to the actual drainage system of the AV. Morphologic expression of their discontinuities appears along active faults separating tectonic basins and along the longitudinal river profile where some of them show knickpoint retreatment just upward of the main trace of the AV's transversal faults.

In the AV, brittle deformation is produced by transpressive and transtensive displacement along strike-slip structures. Along this transition between the AB and the RSZ, these faults have produced a positive relief in the form of 'pop-up' topography and negative relief in the form of tectonic basins discussed and simplified in Figure 9. As the deformation concentrates and landscape evolves, complex structures of pull-apart basins appear (see Kim and Sanderson, 2006), with the subsequent filling of basins by sediments and the reorganization of the drainage network inside tectonic valleys since the Pliocene (Aristizábal et al., 2004; Rendón et al., 2006). Additionally, higher depocenters in the Medellín and Itagüí basins correlate with

the chronostratigraphic records documented in the AV (e.g., Rendón et al., 2006; García, 2006). In evolved stages of deformation during the Quaternary, isolated tectonic subbasins could combine by means of uplift processes, rising advance of the erosion wavefronts along the Medellín-Porce River, and the coalescence of subbasins, forming broader and more complex sedimentary basins (Mann et al., 1983; Noda 2013, etc.). This last event of landscape rejuvenation corresponds to the Pleistocene pulses of Andean Orogeny and hence the actual neotectonic regime that controls seismogenic sources in the AV and their surroundings.

## 6. CONCLUSIONS

The results and interpretation of the magnetic fabric and structural datasets previously presented allow us to conclude that:

- » All the AMS data from selected neotectonic sites exhibit triaxial ellipsoids with  $k_{min}$  values distributed in a subhorizontal plane and subvertical  $k_{max}$  that define shear-related fabric and/or cleavage development. This implies that deformed and apparently undeformed sediments covering active faults record a magnetic fabric associated with the tectonic imprints of recent displacement, and it can be used as a strain indicators in further neotectonic studies.
- » Magnetic and structural data from the La Brizuela site indicate normal faulting with a dextral component along an antithetic (R') 185/85 plane with respect to the PDZ (~80/90). At this site, the magnetic lineation from Pleistocene alluvial deposits deformed by the La Mosca Fault varies between 182/40 and 234/03. A similar trend is obtained in the Yarumalito site with an antithetic (P') 150/70 plane and normal displacement of the Late Holocene paleosol. At this site, the magnetic lineation of ca. 38/70 marks a dextral component.
- » At the La Caimama site, apparently nondeformed sediments of Middle to Holocene ages covering regional faults such as the Cauca West; in the western section of the RSZ, they exhibit shear-related AMS ellipsoids with subvertical magnetic lineation of 114/85 and defining a 308/89 plane.
- » Disparities between the kinematics of active faults in the study site are related to local responses of the regional strain field conditioned by lithology and inherited mechanical anisotropy overprinted on recent markers of deformation such as Quaternary deposits.
- » The presented results show that Quaternary sedimentary deposits affected by active tectonic processes preserve the shape of the magnetic fabric ellipsoid, which is associated with the fault-plane solutions at the La Mosca, San Jerónimo and Cauca West faults. This work demonstrates the feasibility of the AMS analysis application to the characterization of active faults and neotectonic studies, and it advances a methodological approach that allows the production of data relative to past earthquakes and seismic hazards in the surroundings of the AV.

## ACKNOWLEDGMENT

We are deeply grateful for the technical and financial support for Santiago Noriega-Londoño provided by the SNL Doctoral project, Departamento de Ciencia, Tecnología e Innovación (Colciencias), the Fundación para el Futuro de Colombia (Colfuturo), and the Universidad EAFIT (Project 785-2017 number 201820001205). We thank José Duque Trujillo and Ana Lucía Pérez Calle for their support at the paleomagnetism laboratory of Universidad EAFIT, and Martin Chadima for his contributions to improve the quality of this work. The authors thank the anonymous reviewers for their valuable comments and suggestions, which helped to improve the original manuscript.

## REFERENCES

- AGICO. (2011). *User Manual SAFYR4W* (p. 45).
- Álvarez, C., Trujillo, R., & Hermelin, M. (1984). Aspectos geomorfológicos y estructurales del valle del norte de Aburrá. *Ist Confecence on Geological Hazards in the Aburrá Valley*, 1-12.
- Arbeláez, C. (2019). *Contribuciones desde la geomorfometría y la geomorfología tectónica: Valle de Aburrá, Cordillera Central de Colombia* [Bachelor Thesis]. Universidad EAFIT.
- Arboleda, M., Arbeláez, C., Noriega-Londoño, S., & Marín-Cerón, M. (2019). Evidencias del control tectónico en la evolución del Valle de Aburrá: implicaciones a partir de análisis geomorfológicos y morfoestructurales. *XVII Congreso Colombiano de Geología. IV Simposio de Exploradores*.
- Arias, A. (1995). El relieve de la zona central de Antioquia: Un palimpsesto de eventos tectónicos y climáticos. *Revista Facultad de Ingeniería: Universidad de Antioquia*, (10), 9-24. <https://revistas.udea.edu.co/index.php/ingenieria/article/view/325539>

- Arias, L. A. (1996). Altiplanos y cañones en Antioquia: Una mirada genética. *Revista Facultad de Ingeniería: Universidad de Antioquia*, 12, 84-96. <https://revistas.udea.edu.co/index.php/ingenieria/article/view/325627>
- Aristizábal, E., & Yokota, S. (2008). Evolución geomorfológica del Valle de Aburrá y sus implicaciones en la ocurrencia de movimientos en masa. *Boletín de Ciencias de La Tierra*, (24), 2008. <https://revistas.unal.edu.co/index.php/rbct/article/view/9268>
- Aristizábal, E., Yokota, S., Ohira, H., & Hagai, J. (2004). Dating of slope sediments and alluvial deposits in the Aburra Valley, Colombia. *Geoscience Reports of Shimane University*, 23, 85-88. <https://ir.lib.shimane-u.ac.jp/6148>
- Bilardello, D. (2016). Magnetic Anisotropy: Theory, Instrumentation, and Techniques. In *Reference Module in Earth Systems and Environmental Sciences*. <https://doi.org/10.1016/B978-0-12-409548-9.09516-6>
- Borradaile, G. J., & Henry, B. (1997). Tectonic applications of magnetic susceptibility and its anisotropy. *Earth-Science Reviews*, 42(1-2), 49-93. [https://doi.org/10.1016/S0012-8252\(96\)00044-X](https://doi.org/10.1016/S0012-8252(96)00044-X)
- Borradaile, G. J. (1988). Magnetic susceptibility, petrofabrics and strain. *Tectonophysics*, 156(1-2), 1-20. [https://doi.org/10.1016/0040-1951\(88\)90279-X](https://doi.org/10.1016/0040-1951(88)90279-X)
- Botero, G. (1963). *Contribución al conocimiento de la geología de la zona central de Antioquia*. Universidad Nacional de Colombia.
- Burbank, D. W., & Anderson, R. S. (2011). *Tectonic Geomorphology*. John Wiley & Sons, Ltd. <https://doi.org/10.1002/9781444345063>
- Busby, C. J., & Bassett, K. N. (2007). Volcanic facies architecture of an intra-arc strike-slip basin, Santa Rita Mountains, Southern Arizona. *Bulletin of Volcanology*, 70(1), 85-103. <https://doi.org/10.1007/s00445-007-0122-9>
- Caballero Acosta, J. H. (2014). Important forgotten earthquakes for Medellín. *Boletín de Ciencias de La Tierra*, (36), 69-70. <https://doi.org/10.15446/rbct.n36.47639>
- Caricchi, C., Cifelli, F., Kissel, C., Sagnotti, L., & Mattei, M. (2016). Distinct magnetic fabric in weakly deformed sediments from extensional basins and fold-and-thrust structures in the Northern Apennine orogenic belt (Italy). *Tectonics*, 35(2), 238-256. <https://doi.org/10.1002/2015TC003940>
- Casas-Sainz, A. M., Gil-Imaz, A., Simón, J. L., Izquierdo-Llavall, E., Aldega, L., Román-Berdiel, T., Osácar, M. C., Pueyo-Anchuela, Ó., Ansón, M., García-Lasanta, C., Corrado, S., Invernizzi, C., & Caricchi, C. (2018). Strain indicators and magnetic fabric in intraplate fault zones: Case study of Daroca thrust, Iberian Chain, Spain. *Tectonophysics*, 730, 29-47. <https://doi.org/10.1016/j.tecto.2018.02.013>
- Chadima, M., & Jelinek, V. (2019). *Anisoft5.1.03: Anisotropy data browser for Windows*. Agico, Inc.
- Chicangana, G. (2005). The Romeral fault system: a shear and deformed extinct subduction zone between oceanic and continental lithospheres in Northwestern South America. *Earth Sciences Research Journal*, 9(1), 51-66.
- Cho, H., Kim, M.-C., Kim, H., & Son, M. (2014). Anisotropy of Magnetic Susceptibility (AMS) of the Quaternary Faults, SE Korea: Application to the Determination of Fault Slip Sense and Paleo-stress Field. *The Journal of the Petrological Society of Korea*, 23(2), 75-103. <https://doi.org/10.7854/JPSK.2014.23.2.75>
- Cifelli, F., Mattei, M., Hirt, A. M., & Günther, A. (2004). The origin of tectonic fabrics in “undeformed” clays: the early stages of deformation in extensional sedimentary basins. *Geophysical Research Letters*, 31(9). <https://doi.org/10.1029/2004GL019609>
- Cloos, H. (1928). Experimente zur inneren tektonik. *Centralblatt Für Mineralogie*, 1, 609-621.
- Correa-Martínez, A., Martens, U., & García, G. (2020). Collage of tectonic slivers abutting the eastern Romeral Fault System in central Colombia. *Journal of South American Earth Sciences*, 104, 102794. <https://doi.org/10.1016/j.jsames.2020.102794>
- Cosgrove, J. W. (2007). The use of shear zones and related structures as kinematic indicators: A review. In *Deformation of the Continental Crust: The Legacy of Mike Coward*. Geological Society Special Publication, vol. 272. <https://doi.org/10.1144/GSL.SP.2007.272.01.05>
- Costa, C., Alvarado, A., Audemard, F., Audin, L., Benavente Escóbar, C., Bezerra, F., Cembrano, J., González, G., López, M., Minaya, E., Santibáñez, I., García Peláez, J. A., Arcila, M., Pagani, M., Pérez, I., Delgado, F., Paolini, M., & Garro, H. (2020). Hazardous faults of South America; compilation and overview. *Journal of South American Earth Sciences*, 104, 102837. <https://doi.org/10.1016/j.jsames.2020.102837>
- Davis, G. H., Bump, A. P., García, P. E., & Ahlgren, S. G. (2000). Conjugate Riedel deformation band shear zones. *Journal of Structural Geology*, 22(2), 169-190. [https://doi.org/10.1016/S0191-8141\(99\)00140-6](https://doi.org/10.1016/S0191-8141(99)00140-6)
- Ego, F., Sébrier, M., & Yepes, H. (1996). Is the Cauca-Patia and Romeral Fault System left or right lateral? *Geophysi-*

- cal Research Letters, 22(1), 33-36. <https://doi.org/10.1029/94GL02837>
- Espinosa, A. (2003). La sismicidad histórica en Colombia. *Revista Geográfica Venezolana*, 44(2), 271-283. <http://ecotropicos.saber.ula.ve/db/ssaber/Edocs/pubelectronicas/revistageografica/vol44num2/nota42-2-1.pdf>
- Gallego, A., Ospina, L., & Osorio, J. (2005). Sismo del Quindío del 25 de enero de 1999, evaluación morfotectónica y sísmológica. *Boletín de Geología*, 27(1), 134-150. <https://revistas.uis.edu.co/index.php/revistaboletindegologia/articulo/view/869>
- Gallego, J. (2018). *Assessment of recent tectonic activity of the Sabanalarga Fault System, Western Antioquia – Colombia* [Master thesis]. University of Bern.
- García, C. (2006). Estado del conocimiento de los depósitos de vertiente del Valle de Aburrá. *Boletín de Ciencias de La Tierra*, (19). <https://revistas.unal.edu.co/index.php/rbct/articulo/view/724>
- García, Y. C., Martínez, J. I., Vélez, M. I., Yokoyama, Y., Battarbee, R. W., & Suter, F. D. (2011). Palynofacies analysis of the late Holocene San Nicolás terrace of the Cauca paleolake and paleohydrology of northern South America. *Palaeogeography, Palaeoclimatology, Palaeoecology*, 299(1-2), 298-308. <https://doi.org/10.1016/j.palaeo.2010.11.010>
- Gómez-Tapias, J., Nivia, Á., Montes, N. E., Almanza, M. F., Alcárcel, F. A., & Madrid, C. (2015). *Notas explicativas: Mapa geológico de Colombia*. Publicaciones Geológicas Especiales 33. Servicio Geológico Colombiano.
- Gürbüz, A. (2010). Geometric characteristics of pull-apart basins. *Lithosphere*, 2(3), 199-206. <https://doi.org/10.1130/L36.1>
- Hamilton, T. D., Borradaile, G. J., & Lagroix, F. (2004). Sub-fabric identification by standardization of AMS: an example of inferred neotectonic structures from Cyprus. In *Magnetic Fabric: Methods and Applications*. Special Publications vol. 238. Geological Society of London. <https://doi.org/10.1144/GSL.SP.2004.238.01.27>
- Henao Casas, J., & Monsalve, G. (2017). Geological inferences about the upper crustal configuration of the Medellín – Aburra valley (Colombia) using strong motion seismic records. *Geodesy and Geodynamics*, 8(5), 319-327. <https://doi.org/10.1016/j.geog.2017.07.002>
- Hermelin, M. (1982). El origen del valle de Aburrá: evolución de ideas. *Boletín de Ciencias de La Tierra*, (7-8), 47-65. <https://revistas.unal.edu.co/index.php/rbct/articulo/view/94642>
- Hermelin, M. (1992). Los suelos del oriente antioqueño: un recurso no renovable. *Bulletin De L'institut Francais D'etudes Andines*, 21(1), 25-36. [https://www.persee.fr/doc/bifea\\_0303-7495\\_1992\\_num\\_21\\_1\\_1054](https://www.persee.fr/doc/bifea_0303-7495_1992_num_21_1_1054)
- Ibáñez-Mejía, M., Restrepo, J., & García-Casco, A. (2020). Tectonic juxtaposition of Triassic and Cretaceous meta-(ultra)mafic complexes in the Central Cordillera of Colombia (Medellin area) revealed by zircon U-Pb geochronology and Lu-Hf isotopes (pp. 418-443). In *Geocronologia e Evolução Tectônica do Continente Sul-Americano: a contribuição de Umberto Giuseppe Cordani*. Solaris.
- Integral. (1982). Aprovechamiento múltiple del Río Grande. Estudio geológico y evaluación preliminar del riesgo sísmico.
- Integral. (2000). Conexión Túnel Aburrá Oriente. Informe geológico final.
- Jelinek, V. (1977). *The statistical theory of measuring anisotropy of magnetic susceptibility of rocks and its application*. Geofyzika Brno.
- Jelinek, V. (1981). Characterization of the magnetic fabric of rocks. *Tectonophysics*, 79(3-4), T63-T67. [https://doi.org/10.1016/0040-1951\(81\)90110-4](https://doi.org/10.1016/0040-1951(81)90110-4)
- Kim, Y.-S., & Sanderson, D. J. (2006). Structural similarity and variety at the tips in a wide range of strike-slip faults: a review. *Terra Nova*, 18(5), 330-344. <https://doi.org/10.1111/j.1365-3121.2006.00697.x>
- Kirby, S. H. (2016). Active tectonic and volcanic mountain building as agents of rapid environmental changes and increased orchid diversity and long-distance orchid dispersal in the tropical Americas: opportunities and challenges. *Lankesteriana: International Journal on Orchidology*, 16(2), 243-254. <https://doi.org/10.15517/lank.v16i2.26027>
- Lalinde, C., González, A., & Caballero, H. (2009). Evidencia paleosísmica en el segmento de falla Sopetrán o San Jerónimo Segmento 5. *Boletín de Geología*, 31(2), 23-34. <https://revistas.uis.edu.co/index.php/revistaboletindegologia/articulo/view/347>
- Levi, T., Weinberger, R., Alsop, G. I., & Marco, S. (2018). Characterizing seismites with anisotropy of magnetic susceptibility. *Geology*, 46(9), 827-830. <https://doi.org/10.1130/G45120.1>
- Levi, T., Weinberger, R., & Marco, S. (2014). Magnetic fabrics induced by dynamic faulting reveal damage zone sizes in soft rocks, Dead Sea basin. *Geophysical Journal International*, 199(2), 1214-1229. <https://doi.org/10.1093/gji/ggu300>
- Lomnitz, C., & Hashizume, M. (1985). The Popayán, Colombia, earthquake of 31 March 1983. *Bulletin of the Seismological Society of America*, 75(5), 1315-1326. <https://doi.org/10.1785/BSSA0750051315>

- Maffione, M., Pucci, S., Sagnotti, L., & Speranza, F. (2012). Magnetic fabric of Pleistocene continental clays from the hanging-wall of an active low-angle normal fault (Altotiberina Fault, Italy). *International Journal of Earth Sciences*, (101), 849-861. <https://doi.org/10.1007/s00531-011-0704-9>
- Mann, P., Hempton, M. R., Bradley, D. C., & Burke, K. (1983). Development of pull-apart basins. *The Journal of Geology*, 91(5), 529-554. <https://doi.org/10.1086/628803>
- McCalpin, J. P. (2012). Paleoseismology, Second Edition. *Environmental & Engineering Geoscience*, 18(3), 311-312. <https://doi.org/10.2113/gseegeosci.18.3.311>
- McCalpin, J. P. (2013). Neotectonics. In *Encyclopedia of Earth Sciences Series*. Springer. [https://doi.org/10.1007/978-1-4020-4399-4\\_252](https://doi.org/10.1007/978-1-4020-4399-4_252)
- Mejía, M., Álvarez, E., González, H. & Grosse, E. (1983). Geología de la Plancha 146 Medellín Occidental. Mapa a escala 1:100.000. Ingeominas
- Mora-Páez, H., Kellogg, J. N., & Freymueller, J. T. (2020). Contributions of space geodesy for geodynamic studies in Colombia: 1988 to 2017. In Gómez, J. & Pinilla-Pachón, A. O. (eds.), *The Geology of Colombia*, vol. 4 Quaternary. Publicaciones Geológicas Especiales 38. Servicio Geológico Colombiano. <https://doi.org/10.32685/pub.esp.38.2019.14>
- Noda, A. (2013). Strike-Slip Basin – Its Configuration and Sedimentary Facies. In *Mechanism of Sedimentary Basin Formation - Multidisciplinary Approach on Active Plate Margins*. IntechOpen. <https://doi.org/10.5772/56593>
- Ojeda, A., & Havskov, J. (2001). Crustal structure and local seismicity in Colombia. *Journal of Seismology*, 5(4), 575-593. <https://doi.org/10.1023/A:1012053206408>
- Ortiz, E. A. (2002). *Evaluation of Neotectonic Activity of the Cauca-Romeral Fault System near western Medellín, Colombia* [Bachelor Thesis]. Shimane University.
- Page, W., & James, M. (1981). The Antiquity of the erosion surfaces and the Late Cenozoic deposits near Medellín, Colombia: implications to tectonics and erosion rates. *Revista CIAF*, 6(1-3), 421-454.
- Parés, J. (2015). Sixty years of anisotropy of magnetic susceptibility in deformed sedimentary rocks. *Frontiers in Earth Science*. <https://www.frontiersin.org/article/10.3389/feart.2015.00004>
- Parés, J., & Pluijm, B. A. (2002). Evaluating magnetic lineations (AMS) in deformed rocks. *Tectonophysics*, 350(4), 283-298. [https://doi.org/10.1016/S0040-1951\(02\)00119-1](https://doi.org/10.1016/S0040-1951(02)00119-1)
- Paris, G., Machette, M. N., Dart, R. L., & Haller, K. M. (2000). Map and Database of Quaternary Faults and Folds in Colombia and its Offshore Regions. *USGS Open-File Report 2000-284*. <https://doi.org/10.3133/ofr00284>
- Passchier, C. W., & Trouw, R. A. J. (2005). *Microtectonics*. Springer. <https://doi.org/10.1007/3-540-29359-0>
- Poveda, E. (2013). *Discontinuidades sísmicas en la litósfera bajo la zona andina y el occidente colombianos a partir de formas de onda de sismos distantes*. Universidad Nacional de Colombia.
- Ramsay, J. G. (1980). Shear zone geometry: A review. *Journal of Structural Geology*, 2(1-2), 83-99. [https://doi.org/10.1016/0191-8141\(80\)90038-3](https://doi.org/10.1016/0191-8141(80)90038-3)
- Rendón, A., Gallego, J., Jaramillo, J. P., González, A., Caballero, J., Lalinde, C., & Arias, L. A. (2015). Actividad neotectónica y análisis paleosismológico en el oriente cercano a la ciudad de Medellín – Colombia. *Boletín de Ciencias de La Tierra*, 37, 5-19.
- Rendón, D. (2003). *Tectonic and sedimentary evolution of the upper Aburrá Valley, northern Colombian Andes* [Master Thesis]. Shimane University.
- Rendón, D., Toro, G., & Hermelin, M. (2006). Modelo cro-noestratigráfico para el emplazamiento de los depósitos de vertiente en el Valle de Aburra. *Boletín de Ciencias de La Tierra*, (18), 103-118. <https://revistas.unal.edu.co/index.php/rbct/article/view/95934>
- Restrepo-Moreno, S., Foster, D., Stockli, D., & Parra, N. (2009). Long-term erosion and exhumation of the “Altiplano Antioqueño”, Northern Andes (Colombia) from apatite (U–Th)/He thermochronology. *Earth and Planetary Science Letters*, 278(1-2), 1-12. <https://doi.org/10.1016/j.epsl.2008.09.037>
- Restrepo, J. (1991). *Datación de algunas cenizas volcánicas de Antioquia por el método de trazas de fisión*. AGID Report 16. Universidad EAFIT.
- Riedel, W. (1929). Zur Mechanik geologischer Brucherscheinungen. *Zentralblatt Für Mineralogie, Geologie, Und Paleontologie*, 354.
- Rodríguez, G., Zapata, G., González, H. & Cossio, U. (2005). *Geología de la Plancha 147 Medellín Oriental. Mapa a escala 1:100.000*. Ingeominas
- Schwanghart, W., & Scherler, D. (2014). Short Communication: TopoToolbox 2 - MATLAB-based software for topographic analysis and modeling in Earth surface sciences. *Earth Surface Dynamics*, 2, 1-7. <https://doi.org/10.5194/esurf-2-1-2014>
- SGM. (2002). *Microzonificación sísmica de los municipios del Valle de Aburrá y definición de zonas de riesgo por movimientos en masa e inundaciones*.

- Shlemon, R. (1979). Zonas de deslizamientos en los alrededores de Medellín, Antioquia (Colombia). Ingeominas.
- Silva, D. (1999). *Datación por trazas de las tefras depositadas en los alrededores del Valle de Aburrá* [Bachelor Thesis]. Universidad EAFIT.
- Soto, R., Larrasoaña, J. C., Arlegui, L. E., Beamud, E., Oliva-Urcia, B., & Simón, J. L. (2009). Reliability of magnetic fabric of weakly deformed mudrocks as a palaeostress indicator in compressive settings. *Journal of Structural Geology*, 31(5), 512-522. <https://doi.org/10.1016/j.jsg.2009.03.006>
- Stewart, I. (2005). Neotectonics. *Encyclopedia of Geology*, 425-428. <https://doi.org/10.1016/B0-12-369396-9/00502-5>
- Suter, F., Martínez, J. I., & Vélez, M. I. (2011). Holocene soft-sediment deformation of the Santa Fe–Sopetrán Basin, northern Colombian Andes: Evidence for pre-Hispanic seismic activity? *Sedimentary Geology*, 235(3-4), 188-199. <https://doi.org/10.1016/j.sedgeo.2010.09.018>
- Toro, G. (1999). *Téphrocronologie de la Colombie centrale (département d'Antioquia et abanico de Pereira)* [Ph.D. Thesis]. Université Joseph Fourier.
- Toro, G., Hermelin, M., Schwabe, E., Posada, B. O., Silva, D., & Poupeau, G. (2006). Fission-track datings and geomorphic evidences for long-term stability in the Central Cordillera highlands, Colombia. *Zeitschrift Fur Geomorphologie, Supplementband*.
- Traforti, A., Massironi, M., & Zampieri, D. (2016). Geo-structural map of the Laguna Blanca basin (Southern Central Andes, Catamarca, Argentina). *Journal of Maps*, 12(3), 431-442. <https://doi.org/10.1080/17445647.2015.1035557>
- Veloza, G., Styron, R., & Taylor, M. (2012). Open-source archive of active faults for northwest South America. *GSA Today*, 22(10), 4-10. <https://doi.org/10.1130/GSAT-G156A.1>
- Vinasco, C. (2019). The romeral shear zone. In *Frontiers in Earth Sciences*. [https://doi.org/10.1007/978-3-319-76132-9\\_12](https://doi.org/10.1007/978-3-319-76132-9_12)
- Vinasco, C., & Cordani, U. (2012). Reactivation episodes of the Romeral fault system in the Northwestern part of Central Andes, Colombia, through 39AR-40AR and K-AR results. *Boletín de Ciencias de La Tierra*, (32), 111-124. <https://revistas.unal.edu.co/index.php/rbct/issue/view/3449>
- Weil, A., & Yonkee, A. (2009). Anisotropy of magnetic susceptibility in weakly deformed red beds from the Wyoming salient, Sevier thrust belt: Relations to layer-parallel shortening and orogenic curvature. *Lithosphere*, 1(4), 235-256. <https://doi.org/10.1130/L42.1>
- Wilches-Chaux, G. (2005). El terremoto, la avalancha y los deslizamientos de la cuenca del río Páez (Cauca), 1994. *Desastres de Origen Natural En Colombia 1979-2004*, 121-133.
- Yokota, S., & Ortíz, E. A. (2003). <sup>14</sup>C dating of an organic paleosol covering gravel beds distributed along the San Jerónimo Fault, Western Medellín, Colombia. *Geoscience Reports of Shimane University*, 22, 179-182.

---

## Boletín Geológico

# Editorial Policy and Author Guidelines

---

The Editorial Policy and the Author Guidelines are available online in the web page of the journal:  
<https://revistas.sgc.gov.co/index.php/boletingeo/index>

## CONTENTS

### 3 Editorial

Mario Maya

Research article

### 7 Petrographic, chemical and geochronological characteristics of the Onzaga Metarhyolite and its correlation with Ordovician magmatic events in the northern Andes, Colombia

Gabriel Rodríguez García

Research article

### 29 Determination of a potentially optimal zone to perform hydraulic fracturing work, Upper Magdalena Valley basin, Colombia

Carlos Fabián Sánchez, Indira Molina, Gabriel Ángel Molina

Research article

### 41 Interpretation of Palaeozoic geofoms with the use of seismic attributes in a region of the Eastern Plains, Colombia

Laura Carolina Esquivel, Fanny Villamizar, Indira Molina

Research article

### 55 Gravity Studies at the Cerro Machín volcano, Colombia

Nicolás Felipe Pedraza, Juan Diego Velásquez, Indira Molina, Andrés Pedraza

Case study article

### 67 Hydrogeological potential in soft formations and hard rocks: A case study in the Cauca River Canyon, Antioquia, Colombia

Paola Andrea Palacio, Rodrigo Alonso Díaz, María Alejandra Vela, Juliana Ossa

Case study article

### 77 Region-scale estimation of potential groundwater recharge in soft and hard rock formations through a distributed water balance in the area of influence of the tropical dry forest in the Cauca River canyon, Antioquia, Colombia

Breiner Dan Bastidas, Juliana Ossa, Cristina Martínez, María Alejandra Vela, Teresita Betancur, Arbei Osorio

Research article

### 103 Magnetic fabric of deformed Quaternary sediments: contributions to the understanding of the neotectonic activity in the surroundings in the Aburrá Valley, Central Cordillera, Colombia

Santiago Noriega-Londoño, Duván Jaraba, María Paula Ruiz, María Isabel Marín-Cerón, Sergio Andrés Restrepo-Moreno

